J. Bangladesh Acad. Sci. Volume 50, Issue 1, March 2026

ISSN 2224-7270 (Online), 0378-8121 (Print)

Journal of Bangladesh Academy of Sciences is published four times a year (March, June, September and December comprising one volume) in English. Original research articles, review articles, and short communications of all branches of Science and Technology are considered for publication in this journal. Review articles are generally by invitation.

Disclaimer

Submission

All correspondence regarding contributions for publication in the journal should be addressed to the *Editor, Journal of Bangladesh Academy of Sciences* <jbas.editor@yahoo.com>. Authors should consult the contributor's guideline at the back of the journal before submitting their manuscripts.

Published by
Bangladesh Academy of Sciences, National Science and Technology Complex, Agargaon, Dhaka-1207.

Design and Printed by
Sucharu Desktop Publishing, 1/E/1, Paribagh, Dhaka-1000, Bangladesh

Annual Subscription: Tk. 500.00 (Bangladesh); US $ 60.00; £ 21.50 plus postage.
Single Copy: Tk. 250.00 (Bangladesh); US $ 30.00; £ 11.25 plus postage.

Obituary

Professor Dr. M. Muhibur Rahman (1944-2025)

Professor Dr. M. Muhibur Rahman, an eminent chemist, revered educator, a dedicated researcher, and one of the most distinguished Fellows of The Bangladesh Academy of Sciences, left us on 30 March 2025 at the age of 81 after a life of illustrious academic careers, research activities, and scientific contributions. Professor Rahman an elected Fellow of the Bangladesh Academy of Sciences in 2012.was a towering figure in the field of Physical and Atmospheric Chemistry in Bangladesh, He leaves behind a legacy of research excellence, pedagogical rigor, and institutional development.

Professor Rahman began his long and illustrious teaching career in the Department of Chemistry, University of Dhaka in 1966 as a Lecturer. He was appointed Assistant Professor in 1971, Associate Professor in 1974 and Professor in 1987 in the same department. He remained with the Department of Chemistry until his retirement in 2010. His career continued even after retirement — as a UGC Professor (2017–2019) and through major national education initiatives, including the Higher Education Quality Enhancement Project (HEQEP) under the Ministry of Education.

Professor Rahman was born on 2 January 1944 in the village Manikpur of Zakiganj Upazila in the district of Sylhet. He passed the Matriculation Examination of the then East Pakistan Secondary Education Board in 1959, securing 16th place in order of merit. He had Higher Secondary Education from Dhaka College, Dhaka (1959-1961), and passed I.Sc. Examination of the Dhaka University in the Science group in 1961, securing Second place in order of merit. For tertiary level education, he studied in the Department of Chemistry, Dhaka University (1961-1965) and obtained the B.Sc. (Honours in Chemistry) degree in 1964 and M.Sc. (Chemistry) degree in 1965, securing first position in First Class in both. He had higher studies in the Department of Physical Chemistry, Cambridge University, UK from 1967-1970 and obtained the Ph.D. Degree in 1970 under the supervision of Professor J. W. Linnett, FRS, as a Commonwealth Scholar.

He received first grade merit scholarship during higher secondary and tertiary level studies; Commonwealth scholarship for doctoral studies in Cambridge University, UK; Alexander von Humboldt Fellowship for postdoctoral research in the Goettingen University (1974-1976) and Kiel University (1984); British Council Senior Visitorship for research in the University of East Anglia, Norwich, England (1984). He was a Guest Scientist in Goettingen University, Germany (1976-1977), Kiel University, Germany (1984-1987, 1990-1992, 1994-1995); and was invited as an Alexander von Humboldt Foundation research scientist to work on atmospheric chemistry in the Wuppertal University, Germany (September 2012 and October 2013).
Professor Rahman trained and supervised over 90 postgraduate research students, including Ph.D. and M.Phil. candidates in the Department of Chemistry at Dhaka University. He also co-supervised two PhD students at the Institute of Physical Chemistry, University of Kiel, Germany. He inspired generations of chemists with his commitment to laboratory precisions, academic integrity, and the scientific method.

Professor Rahman was among the pioneers of Atmospheric Chemistry and Catalysis research in Bangladesh. He introduced and led research in the fields such as heterogeneous catalysis, reaction kinetics, nanomaterials, and monitoring atmospheric pollution. As the Director (2009-2010) of the Centre for Advanced Research in

Sciences (CARS), Dhaka University, he established first Air Quality Monitoring Centre of the country and opened the facilities to a wide range of faculty and students, fostering interdisciplinary collaborations. Prof. Rahman was a highly valued collaborator and mentor, with collaborations spanning across the Globe.

Prof. Rahman's contributions to Chemistry were not limited to research and academic leadership. His involvement in popularizing science, developing curriculum, and self-assessment left an indelible mark on Education. Known for his lively and inquisitive lecturing style, he challenged his audiences with thought-provoking questions, constantly reminding his students and colleagues that, while we may learn much, there is always more to discover.

His international engagements included extended research stays in Germany, particularly at the Universities of Göttingen, Kiel, and Wuppertal, under prestigious fellowships such as those from the Alexander von Humboldt Foundation and the German Research Society. In Cambridge University, he worked on Mössbauer spectroscopic studies of ferrites and heterogeneous gaseous reactions on solid catalysts with Professor J W Linnett, FRS, while in Goettingen University he focused on photoelectric properties of metal oxides, heterogeneous catalysis while working with Professor Karl Hauffe. In University of East Anglia, Norwich, UK he worked on Infrared spectra of adsorbed species with Professor Norman Sheppard, FRS and in University of Kiel, Germany his areas of interests were kinetics of elementary reactions of gaseous species relevant to atmospheric chemistry with Professor R. N Schindler and in Wuppertal University, Germany, he engaged himself with detection of atmospheric pollutants with Professor Thorsten Benter. He was fluent in German, Bengali, English, and conversant in several other languages, which enriched his capacity for cross-cultural academic exchange.

Professor Rahman was a founder member of several major scientific organizations in Bangladesh, including the Bangladesh Chemical Society, which he served as President (2007–2010), and the Association of Humboldt Fellows Bangladesh (AHFB), where he served both as long-time General Secretary (1983-2003) and later as President (2003-2010). As a President of Bangladesh Chemical Society, he took initiatives to award Honorary Fellowships to several chemists of international standing including Nobel Laureate Yuan Tseh Lee of Taiwan and IUPAC President Jung Ill Jin of South Korea. He made remarkable contributions to Bangladesh- Germany academic and cultural ties. His editorial leadership spanned the Dhaka University Journal of Science and the Journal of the Bangladesh Academy of Sciences, contributing to the national discourse on scientific publication standards.

He was deeply respected as an academic administrator, having served as Chairman of the Department of Chemistry (1996–1999) and House Tutor at Shahidullah Hall (1977–1983). He was member, University Grants Commission of Bangladesh (2010–2014) and played a key role in reforming the policies of awarding research grants, UGC Awards for best research publications to faculty members in universities; in implementing the Higher Education Quality Enhancement Project of the Ministry of Education, Government of Bangladesh and introducing a mechanism of Quality Assurance of Higher Education (IQAC)in the universities in Bangladesh. His leadership style was marked by fairness, institutional loyalty, and -enviable commitment to academic merits.

A prolific author, Professor Rahman published 95 peer-reviewed journal articles and several book chapters, including a Text Book on Higher Secondary level chemistry that continue to guide chemistry students across the country. He was a pioneer in launching the Bangladesh Chemistry Olympiad, fostering a culture of scientific curiosity among high school students.

Professor Rahman, survived by his wife, Mrs. Shamim Rahman and four daughters has left behind an irreplaceable void in the scientific and academic community of Bangladesh.

- Md. Abu Bin Hasan Susan

Obituary

Professor Dr. Ahmad Shamsul Islam (1924-2025)

Professor Dr. Ahmad Shamsul Islam, an internationally reputed scientist, educator, researcher, teacher and a distinguished Fellow of the Bangladesh Academy of Sciences and a Founding Fellow of the Islamic World Academy of Sciences left us on 14 April 2025 at the age of 101 after a life of distinguished academic careers, research initiatives, and paramount and long lasting scientific influences. He made great contributions to the development of biological science in the country, especially the introduction of contemporary biotechnology research. With his departure, Bangladesh lost not only a pioneer in the fields of plant breeding and tissue culture techniques but also a patriot.

In recognition of his contribution to education, the government of the People's Republic of Bangladesh awarded him with the prestigious Ekushey Padak (Martyrs' Day Medal).

Prof. Dr. Ahmad Shamsul Islam, son of Late Moulvi Md. Serajul Islam was born on August 06, 1924. He earned his Bachelor of Science in 1945, and in 1947, he received a Master of Science in Botany from Presidency College in Kolkata. Prof. Ahmad Shamsul Islam earned his Ph.D degree from the University of Manchester, UK, in 1954 with the financial support of the British Council. He received the Carrie Memorial Prize in 1954 for his outstanding work on seedless strawberries.

The training he received from the University of Dhaka and subsequently in the UK, the USA, and Japan promoted him in his development as a pioneering scientist.

Professor Islam taught Botany for over 40 years at the undergraduate and graduate levels in different universities, namely Dhaka University, Bangladesh; Sind University, Pakistan; University of Dar Es Salaam, Tanzania; and University of Nairobi, Kenya. He also served as a Supernumerary Professor of Botany at the University of Dhaka.

During his research career, he first successfully hybridized two commercial jute varieties and later established tissue culture and micropropagation techniques for jute and native orchids. He also successfully developed virus-free plants from potatoes. In addition, he introduced various tissue culture techniques, such as somaclonal variation, meristem culture, and micro-propagation for many crops, ornamental, and horticultural plants.

He established breeding technologies for disease resistance in jute, cotton, and kenaf. He published four manuscripts in the prestigious journal 'Nature' from 1952 to 1960, one in ‘Science in 1969, five in ‘Biologia’ (1959-70), one in Experimentia, and one in the Journal of Heredity. All these were possible through his work within the county, especially at Dhaka University. He produced 20 Ph.D. and many M.Sc. students during his research career. He published over 80 papers on significant work in Cytogenetics, Breeding, Tissue Culture, and Trans-formation.

He established the Plant Tissue Culture and Genetics Laboratory at the Department of Botany, DU, through national and international grants, including the British Council. He also started a successful scientist exchange programme financed by the British Council, through which at least a dozen scientists from the Botany Department got the opportunity to train in tissue culture, Algal physiology, and Mycology at the University of Nottingham, UK.

He organized many international conferences from the 80s to the 90s. He worked tirelessly to induct Bangladesh into ICGEB by pursuing the Foreign and Science and Technology Ministries. He was instrumental in starting the Web-based Global Network of Bangladeshi Biotechnologists (GNOBB) in 2004, which is now a full-fledged organization bringing together Biotechnologists of different Disciplines. Professor Islam received five prestigious awards within the country. President's Gold Medal in Agriculture (1984), Ekushey Medal (Martyr's Day Medal) in Education (1986), Bangladesh Academy of Sciences Gold Medal in Biology (1987), Gold Medal as Eminent Botanist by Bangladesh Association of Botany (19997), and Lifetime Achievement Award by GNOBB in 2017.

He has written several Textbooks. In 1978, he was invited to present a paper at a UNESCO-sponsored seminar on improving Science Courses at the School level. He was a Member of the Education Commission from 1978 to 1979 and participated in many meetings relating to science education problems and their probable solutions. He worked as a short-term consultant for FAO to prepare two projects, one for the consultants to prepare a feasibility study for establishing "The National Institute of Biotechnology" in 1992-19993.

He was the founder editor of five journals, including the Bangladesh Journal of Botany and the Journal of Plant Tissue Culture and Biotechnology, Sind University Research Journal; Pakistan Journal of Botany; Science Series of Dhaka University and the Dar-es-Salam University Scientific Research Journal, Dar-es-Salam, Tanzania.

He has published over 100 papers and two textbooks and a book entitled, "Character building through the teaching of the Qur'an."

Because of his polite and approachable nature, sharp memory, and sympathetic attitude towards students, staff, and friends, he earned the love and respect of thousands of colleagues, friends, and former students, many of whom hold reputed positions in Bangladesh and across the globe.

May Allah (SWT), the most Merciful, grant him Zannatul Ferdous. Ameen.

- Z N Tahmida Begum

J. Bangladesh Acad. Sci. 49(1); 1-20: June 2025 DOI:https://doi.org/10.3329/jbas.v49i1.81802

Journal of Bangladesh Academy of Sciences

Journal homepage: http://www.bas.org.bd/publications/jbas.html

Review Article

Exploring the relationship between genetic polymorphisms and cancer in the Bangladeshi population

Hasib Uddin Ahmed, Abdul Hafiz, M.M. Towhidul Islam and Yearul Kabir*

Department of Biochemistry and Molecular Biology, University of Dhaka, Bangladesh

ARTICLE INFO

Article History

Received: 06 May 2025
Revised: 28 May 2025
Accepted: 29 May 2025

Keywords: Bangladeshi population, Cancer susceptibility, Genetic polymorphisms, Cancer treatment and toxicity.

ABSTRACT

Since the completion of the Human Genome Project two decades ago, genetic polymorphisms in human DNA have gained significant attention for their role in diseases, particularly cancer. Cancer susceptibility studies have examined Single Nucleotide Polymorphisms (SNPs) across various genes, but populations such as Bangladeshis have remained underrepresented in this field of research. This review consolidates all 54 studies on cancer-related genetic polymorphisms in the Bangladeshi population, focusing on genetic factors involved in cancer progression, and 5 more studies on treatment toxicity association. A comprehensive search of online literature databases was conducted to identify studies specifically conducted on Bangladeshis, and these studies are organized by cancer type. Various genotyping techniques, including PCR-RFLP, T-ARMS-PCR, TaqMan Assay, and Sanger sequencing, were employed to detect genetic associations, all of which are discussed. Genes most frequently studied include *TP53*, *XRCC1*, *CDH1*, *IL17A*, and *RAD51*, with the *TP53* rs1042522 polymorphism being the most investigated SNP. The review also identifies cancers such as blood, esophageal, bladder, hepatocellular and liver cancer as understudied. Importantly, SNPs in genes such as *MTHFR* and *GSTP1* were found to influence chemotherapy-related toxicities. This review provides a comprehensive overview of cancer polymorphism studies conducted on this population, highlights the current scope of research, and identifies opportunities for further exploration. It emphasizes the potential for discovering unique Bangladeshi polymorphisms, which could lead to more tailored cancer diagnosis and treatment approaches.

Introduction

Cancer has become a global health crisis and a major concern affecting the overall health of populations worldwide. It is the leading or second leading cause of death among individuals under the age of 70 in 112 out of 183 countries. According to GLOBOCAN 2020, there were 19.3 million new cancer cases and 10 million cancer-related deaths reported worldwide in 2020 (Sung et al., 2021). The global cancer burden is projected to rise by 47% by 2040 compared to 2020, with a more significant increase expected in transitioning countries than in transitioned ones (Sung et al., 2021). In South-Central Asia, Bangladesh ranks third in cancer incidence, with 156,775 new cases and 108,990 deaths reported in 2020 (Sung et al., 2021). Among men, esophageal (16.1%) and lung (11.1%) cancers are most common, whereas breast (19%) and cervical (12%) cancers dominate among women (IARC, 2023).

The etiology of cancer is multifactorial, involving interactions between genetic predispositions and environmental exposures. Genetic factors include inherited mutations or polymorphisms that affect the function or expression of genes involved in DNA

---

*Corresponding author:<ykabir@yahoo.com>

repair, cell cycle regulation, apoptosis, metabolism, inflammation, immune response, angiogenesis, or metastasis (Kou et al., 2016). Among these, Single Nucleotide Polymorphisms (SNPs), the most common type of genetic variation in humans, account for approximately 90% of human genetic diversity. These mutations involve the substitution of a single nucleotide base pair at a specific genomic location and can be classified as either coding (affecting the amino acid sequence of proteins) or non-coding. Coding SNPs that alter protein sequences may change protein structure and function, potentially leading to reduced or lost activity. Non-coding SNPs, although they do not alter protein sequences, can influence regulatory elements such as transcription factor binding sites, splicing mechanisms, microRNA binding, and RNA expression.

Extensive research has investigated the association between SNPs and cancer. Such genetic association studies are generally divided into two categories: susceptibility studies, which examine cancer risk, and outcome studies, which explore factors influencing survival, complications, and treatment response. Most existing studies focus on a limited number of SNPs or genes, occasionally extending to multiple variants within a pathway or related biological process (Erichsen and Chanock, 2004). Although individual genes such as DNA repair enzymes, oncogenes, and tumor suppressor genes, may contain numerous SNPs, not all are clinically relevant to cancer development (Tan, 2017). Therefore, statistical measures like odds ratios (OR), confidence intervals (CI), and p-values are essential for determining the significance of specific SNPs in relation to cancer progression and treatment response. Technological advancements, especially in bioinformatics, have facilitated the study of multiple genes simultaneously (Dong et al., 2008). Nonetheless, replication and validation of findings are essential before clinical application, and such studies should be considered preliminary (Erichsen and Chanock, 2004).

In Bangladesh, case-control studies have been conducted to examine the relationship between SNPs and both cancer risk and treatment outcomes. These studies typically focus on candidate genes previously associated with various cancer types in other populations. This review summarizes findings from studies on SNPs linked to cancers of the bladder, lung, cervix, colon, breast, prostate, liver, and others in the Bangladeshi population. Only studies specifically involving Bangladeshi cohorts were included, and they have been categorized by cancer type. Statistical measures of significance have also been reported for each SNP studied.

A comprehensive discussion of cancer-related polymorphisms in the Bangladeshi population will enhance understanding of the region’s genetic variability. Furthermore, this information can serve as a valuable reference for developing region-specific biomarkers and predicting treatment outcomes in cancer patients.

Method

A thorough literature search was conducted to identify studies assessing the association between single nucleotide polymorphisms (SNPs) and cancer susceptibility or treatment-related toxicity in the Bangladeshi population. Relevant articles published up to April 2025 were retrieved from PubMed and Google Scholar using search terms such as "SNP," "genetic polymorphism," "cancer," "Bangladeshi population," "cancer treatment toxicity," and "SNP cancer risk." After initial screening, duplicate studies were removed through manual cross-verification. Studies were included if they were original research articles, involved human subjects of Bangladeshi ethnicity, and reported associations between specific SNPs and either cancer risk or treatment outcomes. Studies were excluded if they were reviews, conference abstracts, purely in silico analyses, or focused on non-Bangladeshi populations. Articles lacking genotype or association data were also excluded.

Following the selection process, a total of 54 studies were included that investigated SNP associations with various cancer types, along with 5 studies focused on SNPs associated with cancer treatment toxicity. Fig. 1 presents a summary of the genes involved, highlighting both unique and overlapping genes across different cancer types. While this review is not a formal systematic review, it takes a thematic approach to organize and interpret the existing literature.

Acute Lymphoblastic Leukemia SNP

The *ARID5B* gene plays a crucial role in epigenetic regulation through chromatin remodeling. A recent study by Jahan et al. (2025) investigated the rs10821936 (T>C) polymorphism in this gene and found that the homozygous mutant C allele (C/C) was significantly associated with an increased risk of acute lymphoblastic leukemia (ALL) in Bangladeshi children. The study reported a 1.35-fold increased risk of childhood ALL associated with the C/C genotype (95% Confidence Interval [CI]: 1.02–1.79; $p = 0.0380$).

Bladder Cancer SNPs

A case-control study investigating the association between *TP53* gene polymorphisms and bladder cancer in the Bangladeshi population analyzed SNPs at codons 72 and 248 (Hosen et al., 2015). Individuals with the Pro/Pro genotype (homozygous mutant) at codon 72 (G→C transversion) were found to have a significantly higher risk of developing bladder cancer compared to those with the Arg/Arg (wild-type) genotype (Odds Ratio [OR] = 3.02; 95% CI: 1.42–6.40; $p < 0.01$). The risk increased further among smokers carrying the Pro/Pro genotype, who had a 3.91-fold higher likelihood of developing bladder cancer (OR = 3.91; CI: 1.33–11.5; $p < 0.05$). However, no significant association was found for the Arg/Pro (heterozygous) genotype at codon 72 or for polymorphisms at codon 248 (Hosen et al., 2015).

The *TP53* gene, located on chromosome 17, regulates critical cellular functions, including cell cycle control, genomic stability, and apoptosis. Mutations in *TP53* often result in truncated or inactive proteins, impairing its tumor-suppressive roles. Additionally, mutant p53 proteins may acquire new functions through interactions with other transcription factors, potentially promoting oncogenesis (Mantovani et al., 2019; Kim and Lozano, 2018).

The *NAT1* and *NAT2* genes encode N-acetyltransferase enzymes involved in the detoxification of carcinogens. Mutations in these genes can lead to the formation of "slow acetylator" genotypes, which are less efficient in detoxifying arylamine carcinogens and may increase cancer risk (Kabir and Rehman, 2018). Specifically, *NAT2* gene mutations result in four known mutant alleles. While wild-type alleles enable faster acetylation, mutant alleles confer slower metabolic activity. A study conducted in Bangladesh found that individuals with slow acetylator genotypes had a significantly higher risk of developing bladder cancer (OR = 4.45; CI: 2.26–8.77; $p < 0.001$). These individuals were also more likely to develop high-grade (OR = 6.63; CI: 1.15–38.13; $p < 0.05$) and invasive (OR = 10.6; CI: 1.00–111.5; $p = 0.05$) bladder tumors. Cigarette smokers with slow acetylator genotypes faced an even higher risk, with a six-fold increased likelihood of developing bladder cancer (OR = 6.05; CI: 2.23–15.82) (Hosen et al., 2015).

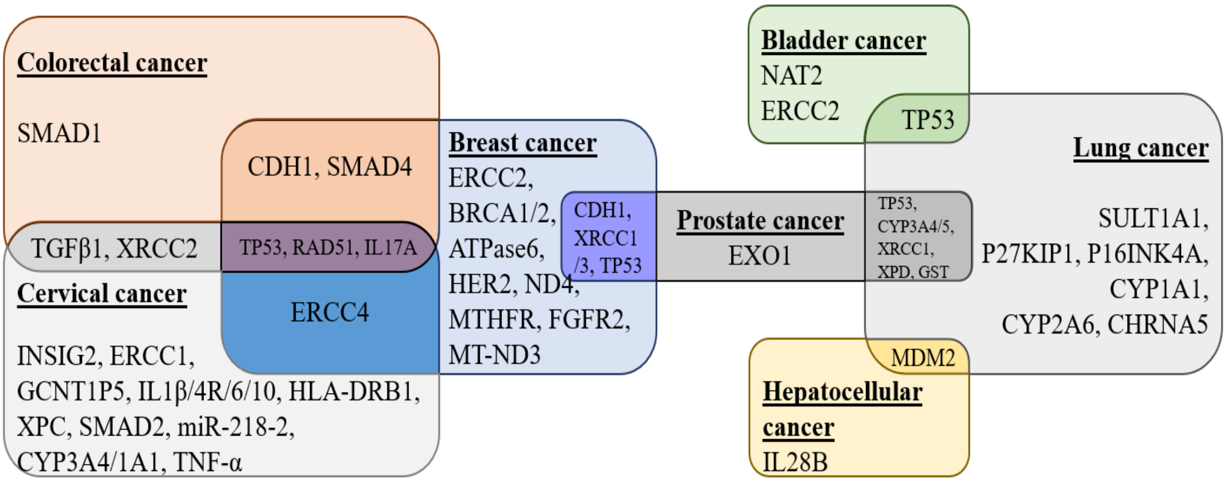

Fig. 1. All the studied genes in a Venn diagram, showing different cancer types and the individual list of genes studied in those types. Different cancer types are color-coded, and the intersections contain the gene names that have been studied in multiple cancer types.

Another study conducted on the Bangladeshi population investigated two polymorphisms in the ERCC2 gene, specifically rs13181and rs1799793, and found both single nucleotide polymorphisms (SNPs) to be significantly associated with an increased risk of bladder cancer (Islam et al., 2024). Individuals with the homozygous mutant genotype of rs13181 had more than a three-fold increased risk of developing bladder cancer (OR = 3.27; 95% CI: 1.19–8.67; $p < 0.05$). Additionally, the heterozygous genotype of rs1799793 was associated with a two-fold increased risk (OR = 2.14; 95% CI: 1.03–4.29; $p < 0.05$). Table 1 shows information on all the Bangladeshi studies for bladder cancer SNPs including gene, chromosome location and reported association.

Table 1. SNPs of genes associated with risk of bladder cancer in Bangladesh.

Gene	Location in Chromosome	SNP	Sample Size (Patients/ Controls)	Reported Association	Ref.
TP53	17p13.1	rs1042522 G>C	102/140	Significant association found	Hosen et al., 2015
TP53	17p13.1	Arg248Trp C>T	102/140	No association found	Hosen et al., 2015
NAT2	8p22	rs1799929 C>T	102/140	Significant association found in M1 genotype	Kabir and Rehman, 2018
NAT2	8p22	rs1799930 G>A	102/140	Significant association found in M2 genotype	Kabir and Rehman, 2018
NAT2	8p22	rs1799931 G>A	102/140	Significant association found in M3 genotype	Kabir and Rehman, 2018
ERCC2	19q13.32	rs13181 T>G	121/130	Significant association found in homozygous mutant	Islam et al., 2024
ERCC2	19q13.32	rs1799793 G>A	121/130	Significant association found in heterozygous mutant	Islam et al., 2024

All genotyping was performed using the PCR-RFLP (Polymerase Chain Reaction-Restriction Fragment Length Polymorphism) method.

Breast Cancer SNPs

Breast cancer is the most common cancer among women in Bangladesh. Consequently, numerous studies have investigated associations between specific gene polymorphisms and breast cancer susceptibility in this population (Table 2).

Several studies have focused on mitochondrial DNA (mtDNA) polymorphisms. One such study reported two SNPs in the NADH dehydrogenase subunit 3 (*ND3*) of mitochondrial complex I—G10398A and T10400C—which caused amino acid substitutions. These mutations were found in 75% of breast cancer patients compared to 35% of healthy individuals, a statistically significant association (OR = 5.57; CI: 1.51–20.51; $p = 0.0138$) (Sultana et al., 2011). The same research group identified novel mutations in *ND3*, *ND4*, and the D-loop region of mtDNA. Mutations at positions 16290 and 16293 in the D-loop were found in 95% and 75% of patients, respectively (OR = 6.00; CI: 1.25–28.84; $p = 0.002$ and OR = 5.60; CI: 1.44–21.89; $p = 0.010$). A novel mutation at position 10316 in *ND3* was also detected in 69% of cancer patients, while absent in healthy controls (Sultana et al., 2012). These polymorphisms are believed to increase reactive oxygen species (ROS) production, contributing to oxidative damage and carcinogenesis (Harman, 1988; Ames and Shigenaga, 1992).

Another study found SNPs in the mitochondrial *ATPase6* gene, part of ATP synthase complex V. Two variants—A8812 and A8701G—were present in 50% (OR = 22.37; CI: 1.15–437.91; $p = 0.008$) and 56.3% (OR = 14.14; CI: 1.46–137.30; $p = 0.016$) of patients, respectively (Islam et al., 2021).

Polymorphisms in nuclear DNA repair genes have also been implicated in breast cancer risk. A study by Howlader et al. (2020) reported significant associations for *XRCC1* (Arg399Gln) and *XRCC3* (Thr241Met) polymorphisms. The Arg/Gln and Gln/Gln genotypes of *XRCC1* were associated with increased breast cancer risk (OR = 1.78; CI: 1.01–3.14; p = 0.047 and OR = 2.41; CI: 1.03–5.59; p = 0.041). Similarly, the *XRCC3* Thr/Met genotype showed a 1.86-fold increased risk (OR = 1.86; CI: 1.12–3.19; p = 0.017), while the Met/Met genotype was not significantly associated (Howlader et al., 2020). These genes are critical for single- and double-strand DNA break repair, and their mutations can impair DNA repair capacity (Shen et al., 2004).

In the Nucleotide Excision Repair (NER) pathway, *ERCC2* and *ERCC4* genes play essential roles. A study on Bangladeshi women reported that the homozygous mutant allele of *ERCC2* rs13181, like in bladder cancer, was also significantly associated with breast cancer risk (OR = 4.00; p = 0.001), while *ERCC4* rs2276466 showed no significant correlation (p> 0.05) (Sahaba et al., 2022).

Other critical genes studied include *BRCA1/2*, *RAD51*, and *HER2* (*ERBB2*), which have well-established links to breast cancer. *BRCA1/2* are tumor suppressor genes involved in DNA repair and cell cycle regulation (Hall et al., 1990). *RAD51* assists in homologous recombination during DNA double-strand repair (Richardson, 2005), while *HER2* promotes cell proliferation and is a proto-oncogene (Xie et al., 2000). A study showed that while combined *BRCA1/2* mutations were significantly associated with breast cancer (OR = 3.27; CI: 1.13–9.52; p = 0.029), individual *BRCA1* rs80357713, rs80357906, and *BRCA2* rs11571653 variants were not. However, *RAD51* rs1801320 heterozygous (GC) and combined mutant (GC+CC) genotypes were significantly associated with breast cancer (OR = 1.72; CI: 1.13–2.62; p = 0.012 and OR = 1.70; CI: 1.14–2.53; p = 0.009, respectively). Similarly, *HER2* rs1136201 in AG and AG+GG genotypes was also linked to elevated risk (OR = 1.49; CI: 1.00–2.22; p = 0.050 and OR = 1.52; CI: 1.04–2.24; p = 0.031) (Parvin et al., 2017).

In a separate study, three novel mutations in exon 11 of *BRCA1* were identified through Sanger sequencing (nucleotide positions 709 [G>A], 711 [A>G], and 852 [G>C]) in one out of 130 samples (Nishat et al., 2019).

The *TP53* gene, frequently mutated in various cancers, was also linked to breast cancer in Bangladesh. The Pro/Pro genotype at codon 72 showed a 2.52-fold increased risk (OR = 2.52; CI: 1.19–5.33; p = 0.0157) (Hossain et al., 2017). Another study confirmed similar findings for the TP53 Arg72Pro mutation (Shabnaz et al., 2016), along with *CDH1* rs16260, where Pro/Pro and A/A genotypes were associated with increased risk (OR = 1.83; p = 0.018 and OR = 1.52; p = 0.0058, respectively).

A novel association was also reported for the *SMAD4* gene, a regulator of cell proliferation and differentiation (Massagué, 2012). The rs10502913 SNP in its A/A genotype was significantly linked to increased breast cancer risk (OR = 4.96; CI: 1.99–12.33; p = 0.006), as was the combined G/A + A/A genotype (OR = 3.56; CI: 1.69–7.51; p = 0.008) (Rahman et al., 2023).

A recent study by Aziz et al. (2024) found no significant association between the *IL17A* rs3748067 polymorphism and the development of breast cancer. In contrast, the *MTHFR* gene, critical for folate metabolism and DNA methylation, was reported to be significantly associated with increased breast cancer risk in a study by Alam et al. (2024). Specifically, the rs1801131 polymorphism in its heterozygous form was linked to a 3.85-fold increased risk of breast cancer (OR=3.85; 95% CI: 2.06–7.25; p< 0.001). However, the rs1801133 variant showed no significant association.

Similarly, the *FGFR2* gene, which plays a key role in cell development regulation, was found to be significantly associated with breast cancer risk in a study on the Bangladeshi population (Jahan et al., 2023). The rs1219648 polymorphism showed strong associations with breast malignancy across multiple models, with risk increases of 2.87-fold and higher. The rs2981582variant also demonstrated a significant association with breast cancer development, while the rs2420946 polymorphism showed no significant link.

Table 2. SNPs of genes associated with risk of breast cancer in Bangladesh.

Gene	Location in Chromosome	SNP	Sample Size (Patients/Controls)	Reported Association	Ref.
$ND3	MT-DNA	G10398A	24/20	Significant association found	Sultana et al., 2011
$ND3	MT-DNA	T10400C	24/20	Significant association found	Sultana et al., 2011
$D-loop	MT-DNA	16290T-ins	24/20	Significant association found	Sultana et al., 2012
$D-loop	MT-DNA	16293A-del	24/20	Significant association found	Sultana et al., 2012
$ND3	MT-DNA	10316 A>G	24/20	Significant association found	Sultana et al., 2012
$ATPase6	MT-DNA	T96P A>C	16/12	Significant association found	Islam et al., 2021
$ATPase6	MT-DNA	T59A A>G	16/12	Significant association found	Islam et al., 2021
*XRCC1	19q13.31	rs7997821 G>A	121/133	Significant association found	Howlader et al., 2020
*XRCC3	14q32.33	rs861539 C>T	121/133	Significant association found in heterozygous mutant	Howlader et al., 2020
*ERCC2	19q13.32	rs13181 T>A	140/111	Significant association found	Sahaba et al., 2022
*ERCC4	16p13.12	rs2276466 C>A	140/111	No significant association found	Sahaba et al., 2022
*BRCA1	17q21.31	rs80357713 ->T	310/250	No significant association found	Parvin et al., 2017
*BRCA1	17q21.31	rs80357906 ->G	310/250	No significant association found	Parvin et al., 2017
*BRCA2	13q13.1	rs80357906 ->G	310/250	No significant association found	Parvin et al., 2017
*RAD51	15q15.1	rs1801320 G>C	310/250	Significant association found	Parvin et al., 2017
*HER2	17q21.1	rs1136201 A>C	310/250	Significant association found	Parvin et al., 2017
#BRCA1	17q21.31	852 G>C	65	No significant association found	Nishat et al., 2019
#BRAC1	17q21.31	711 A>G	65	No significant association found	Nishat et al., 2019
#BRAC1	17q21.31	709 G>A	65	No significant association found	Nishat et al., 2019
*TP53	17p13.1	rs1042522 G > C	125/125	Significant association found	Hossain et al., 2017
*TP53	17p13.1	rs1042522 G>C	310/250	Significant association found	Shabnaz et al., 2016
*CDH1	16q22.1	rs16260 C>A	310/250	Significant association found	Shabnaz et al., 2016
*SMAD4	18q21.2	rs10502913 G>A	70/60	Significant association found	Rahman et al., 2023
¥IL17A	6p12.2	rs3748067 G>A	156/156	No significant association found	Aziz et al., 2024
*MTHFR	1p36.6	rs1801131 A>C	202/104	Significant association found in heterozygous mutant	Alam et al., 2024
*MTHFR	1p36.6	rs1801133 C>T	202/104	No significant association found	Alam et al., 2024
*FGFR2	10q26.13	rs1219648 A>G	226/220	Significant association found	Jahan et al., 2023
*FGFR2	10q26.13	rs2981582 C>T	226/220	Significant association found	Jahan et al., 2023
*FGFR2	10q26.13	rs2420946 C>T	226/220	No significant association found	Jahan et al., 2023

Genotyping methods used were *PCR-RFLP, #Sequencing, $PCR+Sequencing and ¥T-ARMS-PCR

Hepatocellular Cancer SNPs

Interleukin-28B (*IL28B*) is involved in antiviral defense, and its polymorphisms have been associated with disease prognosis in hepatocellular carcinoma (HCC), particularly among patients infected with Hepatitis B or C viruses (HBV/HCV) (Qin et al., 2019). A study conducted in Bangladesh found that individuals carrying the T/T (homozygous mutant) or C/T (heterozygous) genotypes of *IL28B* had a significantly higher risk of developing HBV-related HCC. Carriers of the minor T allele were more likely to suffer from HCC ($p = 0.002$) (Al-Mahtab, 2016).

Another Bangladeshi study investigated the *MDM2* (T309G) polymorphism in HCC patients. The G/G genotype was associated with a significantly higher risk of HCC compared to the T/T genotype (OR = 3.6; CI: 1.64–7.80; $p< 0.01$). Individuals with either G/G or T/G genotypes also showed a two-fold increased risk of developing HCC (OR = 2.20; CI: 1.21–4.14; $p< 0.05$) (Hosen et al., 2021). *MDM2* is a key regulator of *TP53*, maintaining its cellular levels and influencing tumor suppression.

Colorectal Cancer SNPs

The *SMAD1* gene plays a central role in regulating biological functions such as cell growth and apoptosis. A study on Bangladeshi colorectal cancer (CRC) patients found significant associations with two *SMAD1* SNPs: rs11100883 and rs7661162. The rs11100883 heterozygous G/A genotype was linked to a 1.55-fold increased risk of CRC (OR = 1.55; CI: 1.09–2.20; $p = 0.014$), while the A/A genotype showed a 1.82-fold increase, though not statistically significant. For rs7661162, the A/G genotype showed a 1.78-fold increased risk (OR = 1.78; CI: 1.24–2.56; $p = 0.002$) (Karmokar et al., 2020).

Conversely, a separate study reported a protective effect for the *SMAD4* rs10502913 SNP. The G/A and A/A genotypes were associated with significantly lower CRC risk (OR = 0.24; CI: 0.12–0.45; $p< 0.001$ and OR = 0.06; CI: 0.02–0.21; $p< 0.001$, respectively). In contrast, *TGFβ1* rs1800469 was associated with a higher risk, though this result was not statistically significant ($p> 0.05$) (Sultana et al., 2022).

Another study investigated *TP53* and *CDH1* polymorphisms in CRC. The *TP53* Arg/Pro genotype at codon 72 increased CRC risk by 2.58-fold (OR = 2.58; CI: 1.77–3.77; $p< 0.05$), while the Pro/Pro genotype nearly tripled the risk (OR = 2.92; CI: 1.78–4.78; $p< 0.05$) (Rivu et al., 2017). *CDH1* rs16260 SNP also demonstrated a strong association: the heterozygous C/A genotype carried a 1.94-fold increased risk (OR = 1.94; CI: 1.34–2.81; $p< 0.05$), and the homozygous A/A genotype carried a 2.63-fold increased risk (OR = 2.63; CI: 1.15–6.01; $p< 0.05$).

Interleukin-17A (*IL17A*), important for immune defense and tissue remodeling, was also implicated in CRC risk in a Bangladeshi study. The rs10484879 SNP conferred a 2.44-fold risk in the A/C genotype ($p = 0.0008$) and a 3.27-fold risk in the A/A genotype ($p = 0.0133$). Another SNP, rs3748067, showed similar associations: the G/A genotype conferred a 2.44-fold risk ($p = 0.005$) and the A/A genotype a 2.45-fold risk ($p = 0.031$) (Islam et al., 2022), as opposed to showing no association with bladder cancer as stated before.

Genetic variations in DNA repair genes *RAD51* and *XRCC2* have also been studied. *RAD51* rs1801320 was significantly associated with CRC in the G/C genotype (OR = 1.64; CI: 1.03–2.60; $p = 0.037$), but not in the G/G genotype ($p = 0.423$). *XRCC2* rs3218536 showed significant association in the C/T genotype (OR = 1.60; CI: 1.04–2.46; $p = 0.033$), while the T/T genotype was not significantly associated ($p = 0.237$) (Hridy et al., 2020). Table 3 shows information on all the Bangladeshi studies for colorectal cancer SNPs including gene, chromosome location and reported association.

Table 3. SNPs of genes associated with risk of colorectal cancer in Bangladesh.

Gene	Location in Chromosome	SNP	Sample Size (Patients/ Controls)	Reported Association	Ref.
SMAD1	4q31.21	rs11100883 G>A	275/300	Significant association found in heterozygous mutant	Karmokar et al., 2020
SMAD1	4q31.21	rs7661162 A>G	275/300	Significant association found in heterozygous mutant	Karmokar et al., 2020
TGFβ1	19q13.2	rs1800469 C>T	167/162	No significant association found	Sultana et al., 2022
SMAD4	18q21.2	rs10502913 G>A	167/162	Significant association found	Sultana et al., 2022
TP53	17p13.1	rs1042522 G>C	288/295	Significant association found	Rivu et al., 2017
CDH1	16q22.1	rs16260 C>A	288/295	Significant association found	Rivu et al., 2017
IL17A	6p12.2	rs10484879 C>A	292/288	Significant association found	Islam et al., 2022
IL17A	6p12.2	rs3748067 G>A	292/288	Significant association found	Islam et al., 2022
RAD51	15q15.1	rs1801320 G>C	200/200	Significant association found in heterozygous mutant	Hridy et al., 2020
XRCC2	7q36.1	rs3218536 C>T	200/200	Significant association found in heterozygous mutant	Hridy et al., 2020

All genotyping was performed using the PCR-RFLP method.

Prostate Cancer SNPs

A study on the Bangladeshi population reported a significant association between the *CDH1* rs16260 polymorphism and prostate cancer. Individuals with the heterozygous C/A genotype had a 2.1-fold increased risk compared to those with the C/C (wild-type) genotype (OR = 2.10; CI: 1.17–3.78; *p* = 0.0135) (Imtiaz et al., 2019). The same study also investigated the K589E SNP in the *EXO1* gene, which is involved in DNA repair and genomic stability. The G/A (heterozygous) genotype showed a 2.3-fold increased risk (OR = 2.30; CI: 1.30–4.09; *p* = 0.0031), while the A/A (homozygous mutant) genotype exhibited a 4.85-fold increased risk (OR = 4.85; CI: 1.02–23.03; *p* = 0.0291).

Another study examined *CYP3A41B* (rs2740574) and *CYP3A5*3 (rs776746) gene polymorphisms, which are involved in drug metabolism and hormone regulation. The *CYP3A4**1B heterozygous (*1A/*1B) genotype was associated with a 3.52-fold increased risk (OR = 3.52; CI: 1.38–9.02; *p* = 0.0086), and the homozygous (*1B/1B) genotype showed a 3.90-fold increased risk (OR=3.90; CI: 1.26–12.05; p = 0.0183).For *CYP3A5*3, the heterozygous (*1/*3) genotype had a 5.11-fold increased risk (OR= 5.11; CI: 2.54–10.31; *p*= 0.0001), and the homozygous (*3/*3) genotype showed a 5.49-fold increase (OR = 5.49; CI: 2.45–12.28; p=0.0001) (Bellah et al., 2023).

Polymorphisms in DNA repair genes *XRCC1* and *XRCC3* were also examined. The *XRCC1* Arg399Gln Gln/Gln genotype was associated with a 5.7-fold increased risk of prostate cancer (OR = 5.67; CI: 1.51–21.27; *p* = 0.0102), while the *XRCC3* Thr241Met heterozygous Thr/Met genotype showed a 2-fold increase (OR = 2.03; CI: 1.05–3.95; *p* = 0.036) (Khan et al., 2019).

A separate study found that the *TP53* Arg72Pro SNP was significantly associated with prostate cancer risk. The Arg/Pro genotype conferred a 1.99-fold increased risk (OR = 1.99; CI: 1.31–3.05; *p* = 0.001), and the Pro/Pro genotype showed a 4.82-fold increase (OR =

4.82; CI: 2.39–9.73; *p*< 0.001) (Akter et al., 2021). The same study also confirmed a strong association with the *CDH1* rs16260 C/A genotype (OR = 2.20; CI: 1.44–3.36; *p*< 0.001) and A/A genotype (OR = 2.77; CI: 1.25–6.17; *p* = 0.012). Another study by Ahmed et al. (2024) reported that the *XRCC1* rs1799782 polymorphism was significantly associated with an increased risk of prostate cancer (OR = 5.51; 95% CI: 0.88–24.36; *p* = 0.03). In the same study, the *XPD* rs13181 variant was also investigated but did not show a significant association with prostate cancer risk.

In another study, researchers investigated the NAT2, GSTT1, and GSTM1 genes. GSTT1 and GSTM1, both members of the glutathione S-transferase family, were found to have null genotypes (homozygous deletions) that were significantly associated with an increased risk of prostate cancer. Additionally, the slow acetylator genotype of NAT2 was also linked to a higher prostate cancer risk (Nesa et al., 2023). Table 4 shows information on all the Bangladeshi studies for prostate cancer SNPs including gene, chromosome location and reported association.

Cervical Cancer SNPs

Multiple polymorphisms have been studied in relation to cervical cancer risk in the Bangladeshi population. Table 5 shows information on all the Bangladeshi studies for cervical cancer SNPs including gene, chromosome location and reported association. A study investigated three SNPs: *INSIG2* rs6726538, *HLA-DRB1* rs9272143, and *GCNT1P5* rs7780883 (Hasan et al., 2021). The heterozygous A/T genotype of *INSIG2* was associated with a 3.30-fold increased risk (OR = 3.30; CI: 2.19–4.97; *p*< 0.0001), while the homozygous T/T genotype further elevated the risk (OR = 8.72; CI: 3.87–19.7; *p*< 0.0001). For *HLA-DRB1*, the heterozygous T/C genotype was protective (OR = 0.46; CI: 0.31–0.70; *p* = 0.0004). The *CNT1P5*

Table 4. SNPs of genes associated with risk of prostate cancer in Bangladesh.

Gene	Location in Chromosome	SNP	Sample Size (Patients/ Controls)	Reported Association	Ref.
CDH1	16q22.1	rs16260 C>A	100/100	Significant association found in heterozygous mutant	Imtiaz et al., 2019
EXO1	1q43	rs1047840 G>A	100/100	Significant association found	Imtiaz et al., 2019
CYP3A4	7q22.1	rs2740574 C>T	210/207	Significant association found	Bellah et al., 2023
CYP3A5	7q22.1	rs776746 T>C	210/207	Significant association found	Bellah et al., 2023
XRCC1	19q13.31	rs25487 T>C	100/100	Significant association found	Khan et al., 2019
XRCC3	14q32	rs861539 G>A	100/100	Significant association found	Khan et al., 2019
XRCC1	19q13.31	rs1799782 C>T	132/135	Significant association found	Ahmed et al., 2024
XPD	19q13.32	rs13181 A>C	132/135	No significant association found	Ahmed et al., 2024
TP53	17p13.1	rs1042522 G>C	210/210	Significant association found	Akter et al., 2021
CDH1	16q22.1	rs16260 C>A	210/210	Significant association found	Akter et al., 2021
NAT2	8p22	-	207/200	Significant association found	Nesa et al., 2023
GSTT1	22q11.23	-	207/200	Significant association found	Nesa et al., 2023
GSTM1	1p13.3	-	207/200	Significant association found	Nesa et al., 2023

All genotyping was performed using the PCR-RFLP method.

Table 5: SNPs of genes associated with risk of cervical cancer in Bangladesh

Gene	Location in Chromosome	SNP	Sample Size (Patients/ Controls)	Method used for Genotyping	Reported Association	Ref.
INSIG2	2q14.1-q14.2	rs6726538 A>T	234/212	T-ARMS–PCR	Significant association found	Hasan et al., 2021
HLA-DRB1	6p21.32	rs9272143 T>C	234/212	T-ARMS–PCR	Reduced risk in heterozygous mutant	Hasan et al., 2021
GCNT1P5	7q11.23	rs7780883 G>A	234/212	T-ARMS–PCR	Significant association found in homozygous mutant	Hasan et al., 2021
RAD51	15q15.1	rs1801320 G>C	255/199	PCR-RFLP	Significant association found	Ivy et al., 2021
XRCC2	7q36.1	rs3218536 G>A	255/199	PCR-RFLP	Significant association found	Ivy et al., 2021
IL10	1q32.1	rs1800872 C>A	240/204	T-ARMS–PCR	Significant association found	Datta et al., 2020
IL10	1q32.1	rs1800896 A>G	240/204	T-ARMS–PCR	Significant association found in homozygous mutant	Datta et al., 2020
IL1β	2q14.1	rs16944 A>G	252/228	T-ARMS–PCR	Significant association found in homozygous mutant	Muhammad et al., 2021
IL4R	16p12.1	rs1801275 A>G	252/228	T-ARMS–PCR	Significant association found in homozygous mutant	Muhammad et al., 2021
IL6	7p21	rs1800797 G>A	252/228	T-ARMS–PCR	Significant association found	Muhammad et al., 2021
IL6	7p21	rs1800797 G>A	126/120	PCR-RFLP	Significant association found	Shaswati et al., 2023
IL6	7p21	rs1800795 G>C	126/120	PCR-RFLP	Significant association found	Shaswati et al., 2023
ERCC1	19q13.32	rs11615 C>T	210/200	PCR-RFLP	Reduced risk in heterozygous mutant	Das et al., 2021
ERCC4	16p13.12	rs2276466 C>G	210/200	PCR-RFLP	Significant association found in heterozygous mutant	Das et al., 2021
XPC	3p25.1	rs2228000 T>C	210/200	PCR-RFLP	Reduced risk in heterozygous mutant	Das et al., 2021
XPC	3p25.1	rs2228001 C>A	210/200	PCR-RFLP	Significant association foundin heterozygous mutant	Das et al., 2021
SMAD2	18q21.1	rs4940086 T>C	132/ 98	PCR-RFLP	Significant association found in heterozygous mutant	Haque et al., 2020
TP53	17p13.1	rs1800371 C>T	134/102	PCR-RFLP	Significant association found	Apu et al., 2020
TP53	17p13.1	rs1042522G>C	134/102	PCR-RFLP	Significant association found	Apu et al., 2020
TP53	17p13.1	rs1800371 C>T	129/122	PCR-RFLP	Significant association found	Mostaid et al., 2021
TP53	17p13.1	rs1042522 G>C	129/122	PCR-RFLP	Significant association found	Mostaid et al., 2021
MIR218-2	5q34	rs11134527 G>A	256/232	ARMS-PCR	Significant association found	Nazneen et al., 2021
CYP3A4	7q22.1	rs2740574 C>T	30/30	PCR-RFLP	No significant association found	Shamim et al., 2016
CYP1A1	15q24.1	4646903 T>C	185/220	PCR-RFLP	Significant association found	Barek et al., 2023
CYP1A1	15q24.1	1048943 A>G	185/220	PCR-RFLP	No significant association found	Barek et al., 2023
TGFβ1	19q13.2	rs1800469 C>T	134/102	PCR-RFLP	No significant association found	Apu et al., 2021
TGFβ1	19q13.2	rs1800470 T>C	134/102	PCR-RFLP	No significant association found	Apu et al., 2021
TNF-α	6p21.3	rs1799724 C>T	133/126	Taqman	Significant association found	Tishe et al., 2024
TNF-α	6p21.3	rs1800629 G>A	133/126	Taqman	Significant association found	Tishe et al., 2024
IL17A	6p12.2	rs3748067 C>T	156/156	T-ARMS-PCR	Significant association found in heterozygous mutant	Aziz et al., 2024

T-ARMS-PCR stands for Tetra-Primer Amplification Refractory Mutation System PCR, Taqman stands for Taqman-based SNP Genotyping Assay.

A/A genotype was strongly associated with increased risk (OR = 5.08; CI: 2.45–10.5; $p < 0.0001$).

RAD51 rs1801320 was also found to significantly increase cervical cancer risk in both G/C (OR = 2.21; CI: 1.43–3.42; $p = 0.0004$) and C/C (OR = 4.48; CI: 1.76–11.42; $p = 0.002$) genotypes (Ivy et al., 2021). *XRCC2* rs3218536 showed similar associations: G/A genotype (OR = 2.77; CI: 1.85–4.17; $p < 0.0001$) and A/A genotype (OR = 5.86; CI: 2.08–16.50; $p = 0.001$).

IL10 gene polymorphisms rs1800872 and rs1800896 were also implicated. The C/A and A/A genotypes of rs1800872 were associated with increased risk (OR = 1.59; CI: 1.01–2.49; $p = 0.043$ and OR = 2.75; CI: 1.53–4.93; $p = 0.0007$), while for rs1800896, only the G/G genotype showed a significant risk (OR = 3.48; CI: 1.46–8.31; $p = 0.005$) (Datta et al., 2020).

A separate study explored the polymorphisms of *IL1β* (rs16944), *IL4R* (rs1801275), and *IL6* (rs1800797) genes (Muhammad et al., 2021). The G/G genotype of rs16944 (A>G) showed a significantly increased risk of developing cervical cancer (OR= 2.10; CI= 95%, 1.24–3.5; p< 0.017). The *IL4R* polymorphism in the homozygous mutant (G/G) genotype also showed an increased risk of cervical cancer (OR= 2.66; CI= 95%, 1.49–4.75; p= 0.001) compared to the A/A genotype.

Lastly, the rs1800797 G>A polymorphism of *IL6* elevated the risk of developing cervical cancer in both G/A and A/A genotypes (OR= 8.13; CI= 95%, 5.27–12.55; p < 0.0001 and OR= 9.86; CI= 95%, 2.76–35.21; p = 0.0004 respectively) (Muhammad et al., 2021). A separate study also reported that two genotypes were significantly associated with an increased risk of cervical cancer: the G/A genotype showed a 6.94-fold increased risk (OR = 6.94; 95% CI: 3.76–12.81; $p < 0.0001$), while the A/A genotype was associated with a 3.88-fold increased risk (OR=3.88; 95% CI: 1.12–13.51; $p = 0.0332$). In addition, the study examined the IL6 rs1800795 (G>C) polymorphism and found it to be significantly associated with cervical cancer risk. Specifically, the heterozygous G/C genotype was linked to an almost 3-fold increased risk, and the homozygous mutant C/C genotype was associated with a 3.5-fold increased risk (Shaswati et al., 2023).

DNA repair genes were also examined. *ERCC1* rs11615 and *XPC* rs2228000 were associated with decreased risk (OR = 0.58; $p = 0.019$ and OR = 0.61; $p = 0.025$), while *ERCC4* rs2276466 and *XPC* rs2228001 increased cervical cancer risk (OR = 4.33; $p < 0.0001$ and OR = 1.67; $p = 0.012$, respectively) (Das et al., 2021).

SMAD2 rs4940086 (T/C) was associated with a higher risk of cervical cancer (OR = 3.89; CI: 1.78–8.51; $p = 0.001$), particularly among urban residents (OR = 2.59; CI: 1.02–6.59; $p = 0.045$) (Haque et al., 2020).

TP53 codon 72 variants were consistently linked to increased risk in multiple studies. Arg/Pro and Pro/Pro genotypes showed elevated risk in both studies cited (Apu et al., 2020; Mostaid et al., 2021).

The *miR-218-2* gene SNP rs11134527 was also found to be significantly associated with cervical cancer risk. The A/G and A/A genotypes increased the risk by 2.26-fold and 3.64-fold, respectively ($p = 0.0008$ and $p < 0.0001$) (Nazneen et al., 2021).

*CYP3A4**1B polymorphism was studied to explore the association with cervical cancer in the Bangladeshi population. Still, no significant association was observed between the said polymorphism and the development of cervical cancer (Shamim et al., 2016), with the heterozygous mutant and homozygous mutant samples showing low odds ratio (OR=1.33; CI= 95%, 0.47-3.82; p= 0.5925 and OR=1.11; CI= 95%, 0.02-58.72, p=0.9596, respectively). No association with cervical cancer was found in another study either, where *TGFβ1* rs1800469 (OR= 1.083; CI= 95%, 0.612–1.915; p> 0.05 and OR= 1.216; CI= 95%, 0.829–1.785; p> 0.05 for heterozygous and homozygous mutant respectively) and rs1800470 (OR= 1.309; CI= 95%, 0.742–2.310; p> 0.05 and OR= 1.316; CI= 95%, 0.888–1.949; p> 0.05 for heterozygous and homozygous mutant respectively) polymorphisms were studied (Apu et al., 2021). A separate study suggested a possible correlation between *CYP1A1* polymorphisms rs4646903 (T>C) and rs1048943 (A>G) and the risk of developing cervical cancer. The researchers found that the rs4646903 variant was significantly associated with cervical cancer across all genetic models, with at least a 2-fold increase in risk. In contrast, the rs1048943 polymorphism showed no significant association (Barek et al., 2023).

A research group investigated Tumor Necrosis Factor-alpha (*TNF-α*) gene polymorphisms and found significant associations with increased susceptibility to cervical cancer. The rs1799724 variant was associated with a 3.26-fold increased risk (OR = 3.26; 95% CI: 1.15–9.28; *p*=0.027). Similarly, the rs1800629 polymorphism showed a 2.85-fold increased risk in individuals with the heterozygous genotype (OR=2.85; 95% CI: 1.20–6.74; *p* = 0.017) and a 4.55-fold increased risk in those with the homozygous mutant genotype (OR = 4.55; 95% CI: 1.24–16.60; *p* = 0.022) (Tishe et al., 2024).

The *IL17A* rs3748067 polymorphism, similar to its association with colorectal cancer, was found to be significantly associated with the development of cervical cancer in the heterozygous model (C/T; OR = 1.79; *p* = 0.021) in the same study. However, no such association was observed for the breast cancer development (Aziz et al., 2024).

Lung Cancer SNPs

Several gene polymorphisms have been studied in relation to lung cancer risk in the Bangladeshi population (Table 6).

A study investigated the *SULT1A1* (rs9282861) and *XRCC1* (rs25487) gene polymorphisms. *SULT1A1* encodes an enzyme involved in the metabolism of various compounds, while *XRCC1* contributes to base excision and single-strand DNA repair. Both the heterozygous Arg/His and homozygous His/His genotypes of *SULT1A1* were significantly associated with increased lung cancer risk (OR = 5.06; CI: 3.05–8.41; *p*< 0.05 and OR = 3.88; CI: 2.20–6.82; *p*< 0.05). Similarly, the *XRCC1* Arg/Gln and Gln/Gln genotypes were also linked to increased risk (OR = 4.57; CI: 2.79–7.46; *p*< 0.05 and OR = 4.99; CI: 2.66–9.36; *p*< 0.05) (Tasnim et al., 2017).

Cell cycle regulatory genes *P27KIP1* and *P16INK4A* were also associated with lung cancer risk. The *P27KIP1* Val109Gly polymorphism conferred a 3.38-fold and 7.09-fold increased risk in the heterozygous Val/Gly and homozygous Gly/Gly genotypes, respectively (OR = 3.38; CI: 1.64–6.96; *p* = 0.0010 and OR = 7.09; CI: 2.27–22.14; *p* = 0.0007). The *P16INK4A* Ala148Thr polymorphism was also linked to higher risk in both heterozygous (OR = 3.86; CI: 1.45–10.23; *p* = 0.0067) and homozygous mutant genotypes (OR = 3.86; CI: 1.19–12.48; *p* = 0.0242) (Zilani et al., 2018).

Polymorphisms in *GST* genes were also studied. While *GSTM1* and *GSTT1* variants were not significantly associated with lung cancer, *GSTP1* rs1695 was. The A/G and G/G genotypes showed a 3.56-fold (CI: 1.70–7.46; *p* = 0.001) and 6.57-fold (CI: 1.28–33.81; *p* = 0.024) increased risk, respectively (Nasir Uddin et al., 2014). Both non-significant *GST* variants from the previous study were further investigated by another research group (Nairuz and Kabir, 2024). The study revealed that the *GSTM1* null genotype (homozygous deletion) was significantly associated with a 1.6-fold increased risk of lung cancer (95% CI: 1.01–2.52; *p* = 0.0491). In contrast, the *GSTT1* null genotype showed no significant association.

The tumor suppressor gene *TP53* also showed strong associations. Codon 72 Arg/Pro and Pro/Pro genotypes were linked to significantly increased risk (OR = 2.51; CI: 1.38–4.82; *p* = 0.00232 and OR = 4.62; CI: 2.31–9.52; *p* = 0.00001) (Mostaid et al., 2014). Another study confirmed increased risk for the Pro/Pro genotype (OR = 3.00; CI: 1.1–8.4; *p* = 0.03) (Chowdhury et al., 2015). However, a third study did not find a significant association with *TP53* but reported a significant link between the *XPD* rs13181 polymorphism and lung cancer. The Gln/Gln genotype increased risk 3.58-fold compared to the Lys/Lys genotype (OR = 3.58; CI: 1.58–8.09; *p* = 0.002) (Nairuz et al., 2020).

Table 6. SNPs of genes associated with risk of lung cancer in Bangladesh.

Gene	Location in Chromosome	SNP	Sample Size (Patients/ Controls)	Reported Association	Ref.
SULT1A1	16p11.2	rs9282861G>A	202/242	Significant association found	Tasnim et al., 2017
XRCC1	19q13.31	rs25487 G>A	202 /242	Significant association found	Tasnim et al., 2017
P27KIP1	12p13.1	V109G T>G	100/100	Significant association found	Zilani et al., 2018
P16INK4A	9p21.3	A148T G>A	100/100	Significant association found	Zilani et al., 2018
GSTM1	1p13.3	-	106 /116	No significant association found	Nasir Uddin et al., 2014
GSTP1	11q13.2	rs1695 A>G	106 /116	Significant association found	Nasir Uddin et al., 2014
GSTT1	22q11.23	-	106/ 116	No significant association found	Nasir Uddin et al., 2014
*GSTM1	1p13.3	-	180/200	Significant association found	Nairuz and Kabir, 2024
*GSTT1	22q11.23	-	180/200	No significant association found	Nairuz and Kabir, 2024
TP53	17p13.1	rs1800371 C>T	106/116	No significant association found	Mostaid et al., 2014
TP53	17p13.1	rs1042522 G>C	106/116	Significant association found	Mostaid et al., 2014
TP53	17p13.1	rs1042522 G>C	50/50	Significant association found in homozygous mutant	Chowdhury et al., 2015
TP53	17p13.1	rs1042522 G>C	180/200	No significant association found	Nairuz et al., 2020
XPD	19q13.32	rs13181 T>G	180/200	Significant association found in homozygous mutant	Nairuz et al., 2020
CYP3A4	7q22.1	rs2740574 C>T	106/116	No significant association found	Islam et al., 2014
CYP3A5	7q22.1	rs776746 A>G	106/116	No significant association found	Islam et al., 2014
CYP3A5	7q22.1	rs776746 A>G	106/116	No significant association found	Islam et al., 2014
CYP1A1	15q24.1	rs4646903 T>C	106/116	Significant association found	Islam et al., 2013
CYP1A1	15q24.1	rs1048943 A>G	106/116	Significant association found in heterozygous mutant	Islam et al., 2013
CYP2A6	19q13.2	CYP2A6*4	106/110	Reduced risk	Islam et al., 2013
CHRNA5	15q25.1	rs16969968 G>A	106/110	No significant association found	Islam et al., 2013
MDM2	12q15	rs2279744 T>G	126/133	Significant association found	Al Reza et al., 2020a
MDM2	12q15	rs117039649 G>C	126/133	Reduced risk	Al Reza et al., 2020b

All genotyping was performed using the PCR-RFLP method except *Nairuz and Kabir, 2024* where Allele-specific PCR was performed.

A study on *CYP3A4* and *CYP3A5* polymorphisms found that individuals with at least one *CYP3A4**1B allele had a 3.35-fold increased risk of lung cancer, though the association was not statistically significant ($p = 0.271$). No *CYP3A5* mutations were observed in cases (Islam et al., 2014).

Another study examined polymorphisms in *CYP1A1*, *CYP2A6*, and *CHRNA5* genes. *CYP1A1* rs4646903 polymorphism, mentioned previously in cervical cancer, significantly increased lung cancer risk in both T/C (OR = 1.79; CI: 1.01–3.19; $p = 0.046$) and C/C (OR = 2.85; CI: 1.12–7.30; $p = 0.029$) genotypes. The rs1048943 SNP in a dominant model (A/G + G/G) also increased risk (OR = 2.21; CI: 1.26–3.89; $p = 0.006$). In contrast, *CYP2A6**4 was associated with reduced risk (OR = 0.40; CI: 0.17–0.92; $p = 0.030$). No association was found with *CHRNA5* rs16969968 (Islam et al., 2013). Overview of all cancer SNP studies included in this reviewwas presented in Fig. 2.

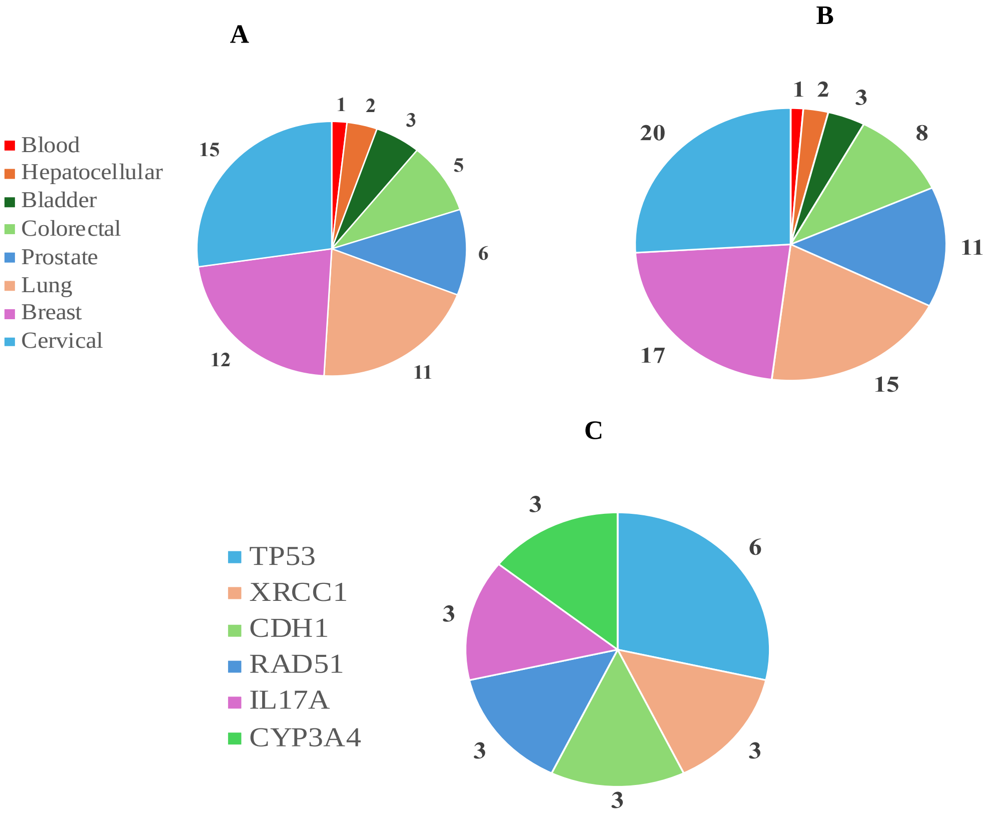

Fig. 2. Overview of all cancer SNP studies included in this review. (A) Number of studies conducted for each cancer type, (B) Number of genes investigated across different cancer types. (C) Top six frequently studied genes across all included studies.

Polymorphisms in *MDM2* were also studied. The rs2279744 T/G and G/G genotypes were significantly associated with increased lung cancer risk (OR = 1.93; CI: 1.12–3.33; $p = 0.017$ and OR = 2.84; CI: 1.27–6.34; $p = 0.011$) (Al Reza et al., 2020a). Conversely, the rs117039649 G/C and C/C genotypes were associated with reduced risk (OR = 0.31; CI: 0.15–0.63; $p = 0.001$ and OR = 0.18; CI: 0.04–0.90; $p = 0.037$) (Al Reza et al., 2020b). *MDM2* negatively regulates *TP53* and helps maintain its cellular balance.

SNPs Affecting Cancer Therapy

Table 7 shows information on all the Bangladeshi studies for cancer treatment toxicity based on SNPs including gene, chromosome location, cancer type and reported association.

Table 7. List of all gene SNPs studied for treatment toxicity in Bangladeshi cancer patients.

Gene	Location in Chromosome	SNP	Sample Size (Patients/ Controls)	Method used for Genotyping	Cancer type	Reported Association	Ref.
DPYD	1p21. 3	rs3918290 G>A	161	PCR-RFLP	Colorectal cancer	Grade 3 and 4 toxicities of 5-FU	Nahid et al., 2018
MTHFR	1p36.6	rs1801133 G>A	161	PCR-RFLP	Colorectal cancer	Increased 5-FU response	Nahid et al., 2018
XPD	19q13.32	rs13181 T>G	180	PCR-RFLP	Lung cancer	No association found	Nairuz et al., 2021
TP53	17p13.1	rs1042522 G>C	180	PCR-RFLP	Lung cancer	No association found	Nairuz et al., 2021
GSTP1	11q13.2	rs1695 A>G	285	PCR-RFLP	Non-small cell lung cancer	Reduced toxicity	Bushra et al., 2020
GSTP1	11q13.2	rs1695 A>G	285	PCR-RFLP	Non-small cell lung cancer	Increased response to platinum-based chemotherapy	Bushra et al., 2020
XRCC1	19q13.31	rs25487 T>C	285	PCR-RFLP	Non-small cell lung cancer	Grade 3 and 4 toxicities	Bushra et al., 2020
XPC	3p25.1	rs2228001 G>T	285	PCR-RFLP	Non-small cell lung cancer	Neutropenia of grade 3 and 4	Bushra et al., 2020
ERCC1	19q13.32	rs11615 A>G	285	PCR-RFLP	Non-small cell lung cancer	No association found	Bushra et al., 2020
TPMT	6p22. 3	rs1142345 A>G	75/75	TaqMan	Acute Lymphoblastic Leukemia	No association found	Zaman et al., 2019
TPMT	6p22. 3	rs1800462 G>C	75/75	TaqMan	Acute Lymphoblastic Leukemia	No association found	Zaman et al., 2019
TPMT	6p22. 3	rs1800460 G>A	75/75	TaqMan	Acute Lymphoblastic Leukemia	No association found	Zaman et al., 2019
ITPA	20p13	rs1127354 C>A	75/75	TaqMan	Acute Lymphoblastic Leukemia	6 times higher chance of absolute neutropenia	Zaman et al., 2019
MTHFR	1p36.3	rs1801133 C>T	160	PCR-RFLP	Acute Lymphoblastic Leukemia	Mucositis and diarrhea by MTX	Zahra et al., 2020
MTHFR	1p36.3	rs1801131 A>C	160	PCR-RFLP	Acute Lymphoblastic Leukemia	Mucositis and diarrhea by MTX	Zahra et al., 2020

Taqman stands for Taqman-based SNP Genotyping Assay.

Gene polymorphisms, translocations, and other genomic aberrations have been shown to contribute to the development of resistance against anticancer drugs (Aschauer and Muller, 2016; Wang, 2018). Therefore, studying SNPs as potential biomarkers for predicting drug toxicity and informing treatment strategies is critical for enhancing the efficacy of cancer therapies. Several studies have investigated the effects of SNPs on cancer therapy in the Bangladeshi population. Polymorphisms in *DPYD2A* and *MTHFR* C677T have been linked to drug toxicity and increased response in colorectal cancer patients. The *DPYD2A* polymorphism was identified as a predictive factor for grade 3 and 4 toxicities from 5-fluorouracil (5-FU, $p = 0.0023$), while the *MTHFR* C677T polymorphism significantly enhanced the 5-FU response ($p = 0.006$) (Nahid et al., 2018).

A separate study explored the role of *TP53* and *XPD* polymorphisms in lung cancer patients and their potential influence on chemotherapy toxicity (Nairuz et al., 2021). No significant association was found between *TP53* codon 72 and *XPD* codon 751 polymorphisms and platinum-based chemotherapy toxicity ($p > 0.05$). However, non-small cell lung cancer patients with the *XRCC1* rs25487 mutation in the A/G genotype experienced grade 3 and 4 toxicities, such as anemia and leukopenia. In contrast, the *XPC* rs2228001 SNP in A/C and A/C+C/C genotypes were associated with neutropenia in grades 3 and 4 (Bushra et al., 2020). The *GSTP1* rs1695 polymorphism in the G/G genotype resulted in reduced toxicity, while the same SNP in A/G and A/G+G/G genotypes showed an increased response to platinum-based chemotherapy. Similar findings were observed for *XRCC1* rs25487 SNP in A/G and A/A+A/G genotypes, though the *ERCC1* rs11615 mutation had no significant effect (Bushra et al., 2020).

A study on children with Acute Lymphoblastic Leukemia (ALL) found that the *ITP* rs1127345 mutation significantly increased the likelihood of neutropenia (6-fold) and hyperbilirubinemia (3-fold) during chemotherapy. Meanwhile, *TPMT* polymorphisms were not significantly associated with cancer treatment toxicity (Zaman et al., 2019). Another study in ALL patients investigating Methotrexate (MTX) toxicity revealed that *MTHFR* C677T and A1298C polymorphisms were significantly linked to mucositis and diarrhea caused by MTX treatment ($p < 0.05$) (Zahra et al., 2020).

Conclusion

Single nucleotide polymorphisms (SNPs) are the most common type of mutation in the human genome. Various SNPs have been extensively studied for their association with different types of cancer. This review has summarized all SNP studies conducted on Bangladeshi cancer patients. Notably, the absence of studies on esophageal cancer patients was observed. Given the increasing incidence of esophageal cancer in Bangladesh, further research on this group is essential. Additionally, lack of SNP studies for blood, bladder, and hepatocellular cancer was noticed. This review will be beneficial for clinicians and research groups working on cancer SNP studies in this particular population. It will also support the development of biomarker panels and personalized medicines for cancer patients. However, it is important to set realistic expectations for the findings of such studies, and a pathway-based genotyping approach should be pursued. SNPs in genes within the same biological pathway are likely to have a more synergistic or additive effect, making those prime candidates for extensive population studies.

Acknowledgment

We would like to express my gratitude to everyone who has helped us in preparing this manuscript.

Authors' Contributions

All listed authors have made substantial, direct, and intellectual contributions to this work and have approved it for publication.

Funding

No funding was provided for this review article.

Conflict of Interest

The authors declare no conflicts of interest.

References

Ahmed N, Islam MA, Hossain MM and Kabir Y. XRCC1 and XPD polymorphisms: clinical outcomes and risk of prostate cancer in Bangladeshi population. *Mol. Biol. Rep.* 2024; 51(1): 893.

Akter R, Islam MS, Islam MS, Aziz MA, Hussain MS, Millat MS, Uddin MS and Islam MS. A case-control study investigating the association of TP53 rs1042522 and CDH1 rs16260 polymorphisms with prostate cancer risk. *Meta Gene*, 2021; 30: 100962.

Al Mahtab M. Association of genetic variation in IL28B rs12979860 with development of hepatocellular carcinoma. *Int. J. Vaccine Res.* 2016; 1(1): 01-05.

Al Reza H, Anamika WJ, Chowdhury MK, Mostafa MG and Uddin MA. A cohort study on the association of MDM2 SNP309 with lung cancer risk in Bangladeshi population. *Korean J. Intern. Med*. 2020a; 35(3): 672-681.

Al Reza H, Anamika WJ, Mostafa MG, Chowdhury MK and Uddin MA. MDM2 SNP 285 is associated with reduced lung cancer risk in Bangladeshi population. *Mymensingh Med. J.* 2020b; 29(1): 108-114.

Alam NF, Ahmed R, Mahmud Z, Tamanna S, Shaon MA and Howlader MZH. Genetic association and computational analysis of MTHFR gene polymorphisms rs1801131 and rs1801133 with breast cancer in the Bangladeshi population. *Sci. Rept.* 2024; 14(1), 24232.

Ames BN and Shigenaga MK. Oxidants are a major contributor to aging. *Ann. N. Y. Acad. Sci.* 1992; 663(1): 85-96.

Apu MNH, Aktar MN, Rahman MM and Mostaid MS. Association of TGFβ1 gene polymorphisms with cervical cancer in Bangladeshi women: A case-control study. *Tumour Biol*. 2021; 43(1): 27-35.

Apu MNH, Rashed AZM, Bashar T, Rahman MM and Mostaid MS. TP53 genetic polymorphisms and susceptibility to cervical cancer in Bangladeshi women: a case–control study. *Mol. Biol. Rep*. 2020; 47(6): 4357-4364.

Aschauer L and Muller PAJ. Novel targets and interaction partners of mutant p53 Gain-Of-Function. *Biochem. Soc. Trans*. 2016;.44(2):. 460-466.

Aziz MA, Chowdhury S, Jafrin S, Barek MA, Uddin MS, Millat MS and Islam MS. Genetic association of Interleukin-17A polymorphism in Bangladeshi patients with breast and cervical cancer: a case-control study with functional analysis. *BMC Cancer*, 2024; 24: 660.

Barek MA, Basher MA, Aziz MA, Hossen MS, Jahan N, Afroz N, Begum M, Jafrin S, Uddin MS, Millat MS, Hoque MM and Islam MS. Assessment of the association of *CYP1A1* gene polymorphisms with the susceptibility of cervical cancer: A case-control study and meta-analysis. *Heliyon*, 2023; 9(7): e17712.

Bellah SMF, Salam MA, Billah SMS and Karim MR. Genetic association in CYP3A4 and CYP3A5 genes elevate the risk of prostate cancer. *Ann. Hum. Biol*. 2023; 50(1): 63-75.

Bushra MU, Rivu SF, Sifat AE, Nahid NA, Ahmed MU, Al-Mamun MMA, Apu MNH, Islam MS, Islam MR, Islam MS and Hasnat A. Genetic polymorphisms of GSTP1, XRCC1, XPC and ERCC1: prediction of clinical outcome of platinum-based chemotherapy in advanced non-small cell lung cancer patients of Bangladesh. *Mol. Biol. Rep*. 2020; 47(9): 7073-7082.

Chowdhury MK, Moniruzzaman M, Emran AA, Mostafa MG, Kuddus RH and Uddin MA. TP53 codon 72 polymorphisms and lung cancer risk in the bangladeshi population. *Asian Pacific J. Cancer Prev*. 2015; 16(8): 3493-3498.

Das S, Naher L, Aka TD, Aziz MA, Shabnaz S, Shahriar M and Islam MS. The ECCR1 rs11615, ERCC4 rs2276466, XPC rs2228000 and XPC rs2228001 polymorphisms increase the cervical cancer risk and aggressiveness in the Bangladeshi population. *Heliyon*, 2021; 7(1): e05964.

Datta A, Zahora FT, Aziz MA, Uddin MS, Ferdous M, Millat MS, Barek MS, Jafrin S, Nahar S and Islam MS. Association study of IL10 gene polymorphisms (rs1800872 and rs1800896) with cervical cancer in the Bangladeshi women. *Int. Immunopharmacol*. 2020; 89: 107091.

Dong LM, Potter JD, White E, Ulrich CM, Cardon LR and Peters U. Genetic susceptibility to cancer: The role of polymorphisms in candidate genes. *JAMA*, 2008; 299(20): 2423-2436.

Erichsen HC and Chanock SJ. SNPs in cancer research and treatment. *Br. J. Cancer*, 2004; 90(4): 747-751.

Hall JM, Lee MK, Newman B, Morrow JE, Anderson LA, Huey B and King MC. Linkage of early-onset familial breast cancer to chromosome 17q21. *Science*, 1990; 250(4988): 1684-1689.

Haque P, Apu MNH, Nahid NA, Islam F, Islam MR, Hasnat A and Islam MS. SMAD2 rs4940086 heterozygosity increases the risk of cervical cancer development among the women in

Bangladesh. *Mol. Biol. Rep*. 2020; 47(7): 5033-5040.

Harman D. Free radicals in aging. *Mol. Cell Biochem*. 1988 ; 84(2): 155-161.

Hasan ME, Matin M, Haque ME, Aziz MA, Millat MS, Uddin MS, Moghal MMR and Islam MS. Polymorphic variants INSIG2 rs6726538, HLA-DRB1 rs9272143, and GCNT1P5 rs7780883 contribute to the susceptibility of cervical cancer in the Bangladeshi women. *Cancer Med*. 2021; 10(5): 1829-1838.

Hosen MB, Islam J, Salam MA, Islam MF, Hawlader MZH and Kabir Y. N-acetyltransferase 2 gene polymorphism as a biomarker for susceptibility to bladder cancer in Bangladeshi population. *Asia Pac. J. Clin. Oncol*. 2015; 11(1): 78-84.

Hosen MB, Khaleque N, Chakraborty S, Al Mahtab M and Kabir Y. MDM2 (T309G) gene polymorphism determines the susceptibility of hepatocellular carcinoma in Bangladesh. *Asian Pacific J. Cancer Biol*. 2021; 6(3): 213-217.

Hosen MB, Salam MA, Islam MF, Hossain A, Hawlader MZH and Kabir Y. Association of TP53 gene polymorphisms with susceptibility of bladder cancer in Bangladeshi population. *Tumor Biol*. 2015; 36(8): 6369-6374.

Hossain A, Murshid GMM, Zilani MNH, Islam F, Sultana R, Sultana T, Hossain MG and Rahman MM. TP53 codon 72 polymorphism and breast cancer risk in Bangladeshi population. *Breast Cancer,* 2017; 24(4): 571-578.

Howlader NR, Rahman MM, Hossain MA, Sultana R, Hossain SM, Mazid MA and Rahman MM. Genetic polymorphisms in DNA repair genes XRCC1 and 3 are associated with increased risk of breast cancer in Bangladeshi population. *Breast Cancer Res. Treat*. 2020; 182(3): 739-750.

Hridy AU, Shabnaz S, Asaduzzaman M, Shahriar M, Bhuiyan MA, Islam MS, Hossen M and Emran TB. Genetic variations of RAD51 and XRCC2 genes increase the risk of colorectal cancer in Bangladeshi population. *Asian Pacific J. Cancer Prev*. 2020; 21(5): 1445-1451.

Imtiaz H, Afroz S, Hossain MA, Bellah SMF, Rahman MM, Kadir MS, Sultana R, Mazid MA and Rahman MM. Genetic polymorphisms in CDH1 and Exo1 genes elevate the prostate cancer risk in Bangladeshi population. *Tumuor Biol*. 2019; 41(3): 101042831983083.

International Agency for Research on Cancer. Global Cancer Observatory: Cancer Today. World Health Organization, Accessed May, 2025. https://gco.iarc.fr

Islam MA, Mubashshira S, Rahman MM and Kabir, Y. Contribution of ERCC2 rs13181 (Lys751Gln) and rs1799793 (Asp312Asn) polymorphisms to the risk of bladder cancer in Bangladesh. *Cancer Genet.* 2024; 288-289, 126–132.

Islam MR, Aziz MA, Shahriar M and Islam MS. Polymorphisms in IL-17A gene and susceptibility of colorectal cancer in Bangladeshi population: A case-control analysis. *Cancer Control,* 2022; 29: 10732748221143879.

Islam MS, Ahmed MU, Bin Sayeed MS, Maruf AA, Mostofa AGM, Hussain SMA, Kabir Y, Daly AK and Hasnat A. Lung cancer risk in relation to nicotinic acetylcholine receptor, CYP2A6 and CYP1A1 genotypes in the Bangladeshi population. *Clin. Chim. Acta,* 2013; 416: 11-19.

Islam MS, Mostofa AGM, Ahmed MU, Bin Sayeed MS, Hassan MR and Hasnat A. Association of CYP3A4, CYP3A5 polymorphisms with lung cancer risk in Bangladeshi population. *Tumor Biol*. 2014; 35(2): 1671-1678.

Islam MT, Sultana GNN, Khan R, Islam A, Mahmud H and Raihan SZ. Study on mitochondrial ATPase6 gene polymorphisms as a genetic risk factor for breast cancer in Bangladeshi women. *Int. J. Sci. Res. Dent. Med. Sci*. 2021; 3: 18-22.

Ivy SC, Shabnaz S, Shahriar M, Jafrin S, Aka TD, Aziz MA and Islam MS. Association of RAD51 and XRCC2 gene polymorphisms with cervical cancer risk in the Bangladeshi women. *Asian Pac. J. Cancer Prev*. 2021; 22(7): 2099-2107.

Jahan F, Chakraborty S, Parvin M, Rahman AA, Howlader ZH and Hosen MI. Genetic polymorphisms in the chromatin modifier gene ARID5B in modulating the risk of pediatric acute lymphoblastic leukemia in Bangladesh. *J. Med. Surg. Public Health*, 2025; 5(10): 100184.

Jahan N, Begum M, Barek MA, Aziz MA, Hossen MS, Bhowmik KK, Akter T, Islam MR, Abdulabbas HS and Islam MS. Evaluation of the association between *FGFR2* gene polymorphisms and breast cancer risk in the Bangladeshi population. *Genes,* 2023; 14(4): 819.

Kabir S and Rehman A. Carcinogenic potential of arylamine N-acetyltransferase in Asian populations. *J. Cancer Res. Pract.* 2018; 5(4): 131-135.

Karmokar PF, Shabnaz S, Aziz MA, Asaduzzaman M, Shahriar M, Bhuiyan MA, Mosaddek ASM and Islam MS. Variants of SMAD1 gene increase the risk of colorectal cancer in the Bangladeshi population. *Tumor Biol*. 2020; 42(9): 1010428320958955.

Khan RA, Hossain MA, Kabir MM, Howlader NR and Rahman MM. Impact of genetic polymorphisms of XRCC1 and XRCC3 genes and their role in prostate cancer risks in Bangladeshi population. *Cancer – Epidemol. Pub. Health*, 2019; 22(Sup. 3): S541.

Kim MP and Lozano G. Mutant p53 partners in crime. *Cell Death Differ*. 2018; 25(1): 161-168.

Kou T, Kanai M, Matsumoto S, Okuno Y and Muto M. The possibility of clinical sequencing in the management of cancer. *Jpn. J. Clin. Oncol*. 2016; 46(5): 399-406.

Mantovani F, Collavin L and Del Sal G. Mutant p53 as a guardian of the cancer cell. *Cell Death Differ*. 2019; 26(2): 199-212.

Massagué J. TGFβ signalling in context. *Nat. Rev. Mol. Cell Biol*. 2012; 13(10):.616-630.

Mostaid MS, Ahmed MU, Islam MS, Bin Sayeed MS and Hasnat A. Lung cancer risk in relation to TP53 codon 47 and codon 72 polymorphism in Bangladeshi population. *Tumor Biol*. 2014; 35(10): 10309-10317.

Mostaid MS, Mumu SB, Haque MA, Sharmin S, Jamiruddin MR, Rahman SMS and Reza HM. Elevated serum expression of p53 and association of TP53 codon 72 polymorphisms with risk of cervical cancer in Bangladeshi women. *PLoS One*, 2021; 16(12): e0261714.

Muhammad SB, Hassan F, Bhowmik KK, Millat MS, Sarwar MS, Barek MA, Uddin MS, Ferdous M and Islam MS. Detection of association of IL1β, IL4R, and IL6 gene polymorphisms with cervical cancer in the Bangladeshi women by tetra-primer ARMS-PCR method. *Int. Immunopharmacol*. 2021; 90: 107131.

Nahid NA, Apu MNH, Islam MR, Shabnaz S, Chowdhury SM, Ahmed MU, Nahar Z, Islam MS, Islam MS and Hasnat A. DPYD*2A and MTHFR C677T predict toxicity and efficacy, respectively, in patients on chemotherapy with 5-fluorouracil for colorectal cancer. *Cancer Chemother. Pharmacol*. 2018; 81(1): 119-129.

Nairuz T, Bushra Y and Kabir Y. Effect of XPD and TP53 gene polymorphisms on the risk of platinum-based chemotherapy induced toxicity in Bangladeshi lung cancer patients. *Asian Pacific J. Cancer Prev*. 2021; 22(12): 3809-3815.

Nairuz T and Kabir Y. Role of GSTM1 and GSTT1 gene polymorphisms on lung cancer susceptibility and effect on platinum-based chemotherapy-Induced Toxicity in Bangladeshi lung cancer patients. *J. Cancer Epidemiol.* 2024; 2024: 9194714.

Nairuz T, Rahman M, Bushra MU and Kabir Y. TP53 Arg72Pro and XPD Lys751Gln gene polymorphisms and risk of lung cancer in Bangladeshi patients. *Asian Pacific J. Cancer Prev*. 2020; 21(7): 2091-2098.

Nasir Uddin MM, Ahmed MU, Islam MS, Islam MS, Sayeed MSB, Kabir Y and Hasnat A genetic polymorphisms of GSTM1, GSTP1 and GSTT1 genes and lung cancer susceptibility in the Bangladeshi population. *Asian Pac. J. Trop. Biomed*. 2014; 4(12): 982-989.

Nazneen F, Millat MS, Barek MA, Aziz MA, Uddin MS, Jafrin S, Islam TD and Islam MS. Genetic polymorphism of miR-218-2 (rs11134527) in cervical cancer: A case-control study on the Bangladeshi women. *MicroRNA*, 2021; 10(3): 219-224.

Nesa A, Rahman MM, Rahman MT and Kabir Y. Association of NAT2, GSTT1, and GSTM1 gene polymorphisms withprostate cancer risk in Bangladeshi population. *Gene,* 2023; 868: 147368.

Nishat L, Yesmin ZA, Arjuman F, Rahman SHZ and Banu LA. Identification of mutation in exon11 of BRCA1 gene in Bangladeshi patients with breast cancer. *Asian Pacific J. Cancer Prev*. 2019; 20(11): 3515-3519.

Parvin S, Islam MS, Al-Mamun MM, Islam MS, Ahmed MU, Kabir ER and Hasnat A. Association of BRCA1, BRCA2, RAD51, and HER2 gene polymorphisms with the breast cancer risk in the Bangladeshi population. *Breast Cancer*, 2017; 24(2): 229-237.

Qin S, Wang J, Zhou C, Xu Y, Zhang Y, Wang X and Wang S. The influence of interleukin 28B polymorphisms on the risk of hepatocellular carcinoma among patients with HBV or HCV infection: An updated meta-analysis. *Medicine* (Baltimore), 2019; 98(38): e17275.

Rahman M, Islam MR, Apu MNH, Uddin MN, Sahaba SA, Nahid NA and Islam MS. Effect of SMAD4 gene polymorphism on breast cancer risk in Bangladeshi women. *Beni-Suef Univ. J. Basic Appl. Sci.* 2023; 12(1): Article number 9.

Richardson C. RAD51, genomic stability, and tumorigenesis. *Cancer Lett.* 2005; 218(2): 127-139.

Rivu SF, Apu MNH, Shabnaz S, Islam MR, Nahid NA, Islam MR, Ai-Mamun MMA, Nahar Z, Rabbi SNI, Ahmed MU, Islam MS and Hasnat A. Association of TP53 codon 72 and CDH1 genetic polymorphisms with colorectal cancer risk in Bangladeshi population. *Cancer Epidemiol*. 2017; 49: 46-52.

Sahaba SA, Rashid MA, Islam MS, Nahid NA, Apu MNH, Sultana TN, Chaity NI, Hasan MM and Islam MS. The link of ERCC2 rs13181 and ERCC4 rs2276466 polymorphisms with breast cancer in the Bangladeshi population. *Mol. Biol. Rep*. 2022; 49(3): 1847-1856.

Shabnaz S, Ahmed MU, Islam MS, Islam MR, Al-Mamun MM, Islam MS and Hasnat A. Breast cancer risk in relation to TP53 codon 72 and CDH1 gene polymorphisms in the Bangladeshi women. *Tumor Biol*. 2016; 37(6): 7229-7237.

Shamim MA, Hossain MS, Sazib MS, Shahariar MF and Hossain MG. Genetic polymorphisms of CYP3A4*1B of cervical cancer patients in Bangladeshi population, Bangladesh. *Int. J. Adv. Med*. 2016; 3(3): 455-459.

Shaswati M, Oeishy FH, Mumu SB, Zahid MZI, Hossain M, Haque MA, Reza HM and Mostaid MS. Polymorphisms of the interleukin-6 (*IL-6*) gene contribute to cervical cancer susceptibility in Bangladeshi women: A case-control study. *Health Sci. Rep.* 2023; 6(5): e1238.

Shen H, Wang X, Hu Z, Zhang Z, Xu Y, Hu X, Guo J and Weio Q. Polymorphisms of DNA repair gene XRCC3 Thr241Met and risk of gastric cancer in a Chinese population. *Cancer Lett*. 2004; 206(1): 51-58.

Sultana GNN, Rahman A, Karim MM, Shahinuzzaman ADA, Begum R and Begum RA. Breast cancer risk associated mitochondrial NADH- dehydrogenase subunit-3 (ND3) polymorphisms (G10398A and T10400C) in Bangladeshi women. *J. Med. Genet. Genomics*, 2011; 3(8): 131-135.

Sultana GNN, Rahman A, Shahinuzzaman ADA, Begum RA and Hossain CF. Mitochondrial DNA mutations--candidate biomarkers for breast cancer diagnosis in Bangladesh. *Chin. J. Cancer*, 2012; 31(9): 449-454.

Sultana TN, Chaity NI, Hasan MM, Shrabonee II, Rivu SF, Aziz MA, Sahaba SA, Apu MNH, Nahid NA, Islam MS and Islam MS. TGFβ1 rs1800469 and SMAD4 rs10502913 polymorphisms and genetic susceptibility to colorectal cancer in Bangladeshi population. *Mol. Bio.l Rep*. 2022; 50(2): 1393-1401.

Sung H, Ferlay J, Siegel RL, Laversanne M, Soerjomataram I, Jemal A and Bray F. Global Cancer Statistics 2020: GLOBOCAN Estimates of Incidence and Mortality Worldwide for 36 Cancers in 185 Countries. *CA Cancer J. Clin*. 2021; 71(3): 209-249.

Tan H. The association between gene SNPs and cancer predisposition: Correlation or causality? *EBioMedicine*, 2017; 16: 8-9.

Tasnim T, Al-Mamun MMA, Nahid NA, Islam MR, Apu MNH, Bushra MU, Rabbi SNI, Nahar Z, Chowdhury JA, Ahmed MU, Islam MS and Hasnat A. Genetic variants of SULT1A1 and XRCC1 genes and risk of lung cancer in Bangladeshi population. *Tumor Biol*. 2017; 39(11): 1010428317729270.

Tishe ZH, Shawkat S, Popy MN, Mumu SB, Ferdous A, Raisa MJ, Hasan M and Sultana TN, Chaity NI, Apu MNH and Mostaid MS. Cervical cancer risk in association with TNF-alpha gene polymorphisms in Bangladeshi women. *Tumor Biol.* 2024; 46(1): 13-24.

Wang X. Clinical trans-omics: an integration of clinical phenomes with molecular multiomics. *Cell Biol. Toxicol*. 2018; 34(3): 163-166.

Xie D, Shu XO, Deng Z, Wen WQ, Creek KE, Dai Q, Gao YT, Jin F and Zheng W. Population-based, case-control study of HER2 genetic polymorphism and breast cancer risk. *J. Natl. Cancer Inst*. 2000; 92(5): 412-417.

Zahra FT, Nahid NA, Islam MR, Al-Mamun MMA, Apu MNH, Nahar Z, Kabir AL, Biswas SK, Ahmed MU, Islam MS and Hasnat A. Pharmacogenetic variants in MTHFR gene are significant predictors of methotrexate toxicities in Bangladeshi patients with acute lymphoblastic leukemia. *Clin. Lymphoma Myeloma Leuk*. 2020; 20(2): e58-e65.

Zaman S, Fukushima H, Suzuki R, Yoshimatsu S, Hawlader MDH and Fukushima T. TPMT and ITPA gene polymorphism and their adverse events during chemotherapy of acute lymphoblastic leukemia among Bangladeshi children. *Iran. J. Blood Cancer*, 2019; 11(3): 96-100.

Zilani MNH, Sarower MG, Hossain A, Rahman MM, Uddin SJ and Hossain MG. Polymorphisms in cell cycle regulator gene P27KIP1 and P16INK4A and lung cancer risk in a Bangladeshi population. *Pharmacologyonline*, 2018; 2: 149-160.

J. Bangladesh Acad. Sci. 49(1); 21-29: June 2025 DOI:https://doi.org/10.3329/jbas.v49i1.76180

Journal of Bangladesh Academy of Sciences

Journal homepage: http://www.bas.org.bd/publications/jbas.html

Research Article

Influence of clybio as a Bio-stimulant on the growth and yield of ornamental sunflower

AFM Jamal Uddin*, Shanzida Akhter Ripa, Fatema Tuz Juhora Chaitee, Tamima Dastagir and Mst Asmaul Husna

Department of Horticulture, Sher-e-Bangla Agricultural University, Bangladesh

ARTICLE INFO

Article History

Received: 17 September 2024
Revised: 14 January 2025
Accepted: 15 January 2025

Keywords: *Helianthus annuus* L., Bio-stimulant, *Lactobacilli*, Yeast fungi, *Bacillus natto*.

ABSTRACT

A field experiment was accomplished at the Horticulture Farm, Sher-e-Bangla Agricultural University, Dhaka, Bangladesh, from October to December 2021. The single-factor experiment was laid out in a randomized complete block design (RCBD) with three replications to evaluate the influence of Clybio as a bio-stimulant on ornamental sunflower growth and yield performance. The "Hybrid Ornamental Sunflower (F1)" (Vincent Choice) variety was utilized. The experiment consisted of three treatments, viz., C_1: No Clybio application (Control), C_2: Clybio @ 4 ml/L, and C_3: Clybio @ 6 ml/L, which were applied in a foliar manner to the leaves and surrounding soil, respectively. Each treatment exhibited notable variations based on data on various vegetative growth, flower yields, and quality standards. The study revealed that plants treated with C_3 (Clybio @ 6 ml/L) showed superior vegetative growth and yield-attributing performance, including the tallest plant height (110.0 cm), the maximum number of leaves per plant (33.2), highest SPAD value (34.4), maximum leaf area (140.6 cm^2), maximum flower head size (14.3 cm), maximum ray floret area (6.0 cm^2), maximum ray floret numbers per flower (31.8), long flower vase-life (8 days), and maximum number of secondary flowers (kid's flower) per plant (12.2). On the contrary, the shortest plant height (99.9 cm), the minimum number of leaves per plant (30.2), lowest SPAD value (32.0), minimum leaf area (127.4 cm^2), minimum flower head size (12.0 cm), minimum ray floret area (4.6 cm^2), minimum ray floret numbers per flower (29.9), short flower vase-life (5 days), and minimum number of secondary flowers (kid's flower) per plant (10.0) were observed in C_1 (Control) treatment. The most amazing aspect was that this ornamental sunflower also produced numerous commercially valuable secondary flowers (kid's flowers) with the application of C3 (Clybio @ 6 ml/L), which might have provided additional income to the producers. So, considering the aforementioned findings, the C_3 (Clybio @ 6 ml/L) treatment proved the best promising prospect for producing high-quality ornamental sunflowers.

Introduction

The sunflower (*Helianthus annuus* L.) is one of the most indispensable cut flowers in the world. It belongs to the family Asteraceae and is cultivated globally as annuals and perennials in various soil types (Kirtimala et al., 2018). According to Devecchi (2005), sunflowers signify the finest quality cut flowers with excellent economic value and are in great demand in the global floral industry. In Bangladesh, the production of ornamental sunflowers is a very new concept for an oil-seed sunflower

---

*Corresponding author:<jama14@yahoo.com>

farming country, so an experiment was tested here. Regrettably, the widespread use of chemical pesticides in sunflower cultivation is a common agricultural practice that deteriorates soil quality (Dwivedi and Dwivedi, 2019) by killing essential microbes. Soil microbes are vital indicators of soil quality, enhance soil texture, promote nutrient cycling, suppress pathogens, stimulate plant growth, and mineralize organic nutrients for sustainable plant growth and development. The destruction of beneficial soil microbes decreases the generation of plant fertilizer through the weathering of organic matter, which is detrimental to the ecosystem and agricultural yield. To alleviate this concern, a bio-stimulant called Clybio is a safer substitute. Clybio, a Japanese organic fungicide, is a composite mixer of *lactobacilli*, yeast fungus, and *bacillus natto*, which can help the soil microbes degrade organic matter and release readily available essential plant nutrients for superior quality sunflower production. The bio-stimulant Clybio greatly enhances ornamental sunflowers through reduced fertilizer use, stress protection, vase life extension, petal color enhancement, efficient growth, and lucrative secondary flower (kid’s flower) production. Various research on horticultural crops has shown that beneficial microbes can enhance vegetative growth and crop production (Uddin et al., 2020; Rakibuzzaman et al., 2021). Clybio improves soil health and plant growth by harnessing the power of enzymes and the synergy of *Lactobacilli* (Shrestha et al., 2014), Yeast Fungi (El-Tarabily and Sivasithamparam, 2006), and *Bacillus Natto* (Tiwari et al., 2019). The study aimed to achieve superior-quality cut flowers by investigating how Clybio affects ornamental sunflower growth and yield attributes.

Material and Methods

The experiment was accomplished at the Horticulture Farm, Sher-e-Bangla Agricultural University, Dhaka, from October to December 2021. The soil was non-calcareous dark grey, having a pH of 6.5. The study was comprised of three treatments of Clybio concentrations viz., C_1: Control (No Clybio application); C_2: Clybio @ 4 ml/L, and C_3: Clybio @ 6 ml/L were used in this experiment arranged in a randomized complete block design (RCBD) with three replications. The "Hybrid ornamental sunflower (F1)" (Vincent Choice) variety was used in this experiment, and seeds were collected from A R Malik Seeds Pvt. Ltd., Dhaka, Bangladesh. For planting them, the field was well prepared and divided into 9 plots spanning 3 m x 1.8 m with a plant spacing of (30 cm x 30 cm) and sunflower seeds were sown at 2 cm depth. In this experiment, Clybio was treated twice, 15 and 30 days after sowing at the studied concentrations of 4 and 6 ml/L. Earthen-up was applied twice at 15 and 35 days after sowing, and the standard management practices were followed during cultivation. Data were collected on vegetative growth, physiological, quality, and yield-attributing parameters with three plants randomly selected from each experimental plot per one replication and repeated three times. Data on plant height, leaf number, leaf area, SPAD value, stem diameter, internode length, head size, disc size, head weight, disc weight, ray floret area, ray floret numbers per flower, vase-life, ray floret’s color measurement, and morphological features of secondary flowers (kid’s flowers) were measured. The data were analyzed using Statistix-10 scientific analysis software to determine the significance of variations among treatments, and treatment means were compared using the LSD test at a 5% level.

Results and Discussion

Plant height

Vegetative growth is a crucial characteristic in ornamental sunflowers and is positively correlated with yield and growing conditions, with foliar application of Clybio causing significant differences in plant height. The tallest plant height (110.0 cm) was attained from C_3 (Clybio @ 6 ml/L), whereas the shortest plant height (99.9 cm) was recorded from C_1 (Control) treatment (Table 1). Clybio made of *Bacillus spp.* converts the complex form of essential nutrients, such as P and N, to a simple available form that enhances plant growth and development (Kang et al., 2015). Akter et al. (2021) observed that the plant height increases in spinach with the application of Clybio concentrations.

Number of leaves per plant

Growing ornamental sunflowers at different concentrations of Clybio resulted in a considerable discrepancy in the number of leaves. Plants with C_3 (Clybio @ 6 ml/L) treatment showed the maximum number of leaves (33.2), whereas the minimum (30.2) was found C_1 (Control) treatment (Table 1). It was revealed that with the increases in Clybio concentration, the number of leaves per plant increased in sunflowers.

Leaf area

Leaf area showed significant variation in different Clybio concentrations on ornamental sunflowers. The C_3 (Clybio @ 6 ml/L) showed the maximum leaf area (140.6 cm^2), while the minimum (127.4 cm^2) was observed from the C_1 (Control) treatment (Table 1 and Plate 1).

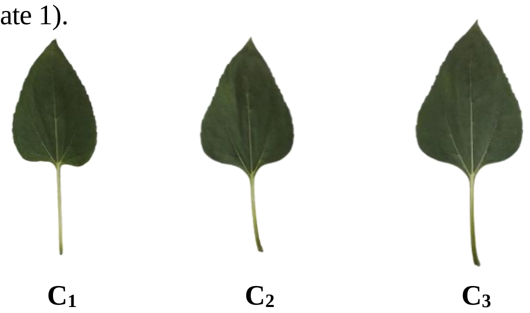

Plate 1. Leaf area of ornamental sunflower under different treatments. C_1: Control; C_2: Clybio @ 4 ml/L; C_3: Clybio @ 6 ml/L.

SPAD value

Chlorophyll significantly impacts plant growth with variations in leaf SPAD value across various treatments. The highest SPAD value (34.4) was observed from C_3 (Clybio @ 6 ml/L), whereas the lowest value (32.0) was from C_1 (Control) treatment (Table 1). Clybio, a yeast-based bio-stimulant, enhances growth and chlorophyll content by promoting essential amino acids, vitamins, and phytohormones (Taha et al., 2020). Chlorophyll content in leaves is linked to photosynthetic capacity, leaf N status, and RuBP carboxylase activity (Evans, 1998; Seemann et al., 1987), while lower content decreases growth and grain development. Clybio can affect a plant's ability to perceive light and its nutritional state.

Stem diameter

The performance of stem diameter showed significant variation across different Clybio concentrations. The maximum stem diameter (11.7 mm) was observed from C_3 (Clybio @ 6 ml/L), while the minimum diameter was noticed in the treatment of C1 (Control) (9.9 mm) (Table 1). Many studies proved that effective microorganisms (EMO) of Clybio enhance plant growth (Chowdhury et al., 1994; Javid, 2006; Khaliq et al., 2006).

Internode length

When subjected to different treatments, ornamental sunflower internode length varied significantly. The highest internode length (8.2 cm) was observed from C_3

Table 1. The effect of Clybio concentrations on growth attributing performance (Plant height, number of leaves per plant, SPAD value, leaf area, stem diameter, and internode length) of ornamental sunflower

Treatment*	Plant height (cm)	Leaf number	SPAD value	Leaf area (cm^2)	Stem diameter (mm)	Internode length (cm)
C_1	99.9^{b}	30.2^{b}	32.0^{b}	127.4^{b}	9.9^{b}	7.1^{b}
C_2	108.8^{a}	31.5^{ab}	33.4^{a}	132.9^{ab}	10.5^{b}	7.4^{b}
C_3	110.0^{a}	33.2^{a}	34.4^{a}	140.6^{a}	11.7^{a}	8.2^{a}
LSD$_{0.05}$	5.7	2.5	1.2	10.0	0.9	0.7
CV (%)	6.4	9.29	4.43	8.9	10.4	10.4

*C_1: Control; C_2: Clybio @ 4 ml/L; C_3: Clybio @ 6 ml/L

In a column means having a similar letter (s) are statistically identical, and those having a dissimilar letter (s) differ significantly as per a 0.05 level of probability.

(Clybio @ 6 ml/L), and the lowest (7.1 cm) was found from C_1 (Control) treatment (Table 1). This cost-effective biofertilizer enhances plant nutrition and vigor during the early growth phase (Lonhienne et al., 2014).

Head size

The application of different clybio concentrations significantly enhanced the yield attributes of ornamental sunflowers (Fig. 1). Among other concentrations, C_3 (Clybio @ 6 ml/L) showed better performance in enhancing the flower head size (14.3 cm) while the minimum (12.0 cm) was found from C_1 (Control) treatment.

Disc size

The study revealed significant variation in the flower disc size of ornamental sunflowers under various treatments (Fig. 1). The maximum flower disc size (7.1 cm) was observed from C_3 (Clybio @ 6 ml/L). In comparison, the minimum (6.1 cm) was found in the C_1 (Control) treatment.

Head weight

The various treatments resulted in significant differences in flower head weight (Fig.1). The maximum flower head weight (28.1 g) was observed in C_3 (Clybio @ 6 ml/L). In comparison, the minimum weight (24.3 g) was found in C_1 (Control) treatment. Clybio is a potent bio-stimulator that enhances the fruit weight of strawberries (Uddin et al., 2021), and tomatoes (Aman, 2016) through higher concentrations (@ 6ml/L).

Disc weight

The significant variation is noted by the application of different Clybio concentrations considering the disc weight (Fig. 1). As observed, the maximum flower disc weight (25.8 g) was observed in C_3 (Clybio @ 6 ml/L) treated plants. In comparison, the minimum (22.3 g) was found in C_1 (Control) treatment. Clybio concentrations (6 ml/L) enhance the strawberry plant's fruit weight (Bhuiyan, 2021).

Ray floret area

Significant variation in ray floret area was recorded among the treatments (Fig. 1). The maximum ray floret area (6.0 cm^2) was observed from C_3 (Clybio @ 6 ml/L), whereas the minimum (4.6 cm^2) was recorded from C_1 (Control) treatment.

Ray floret numbers per flower

In different treatments, ray floret numbers per flower showed significant variation. The maximum ray floret number (31.8) was observed in C_3 (Clybio @ 6

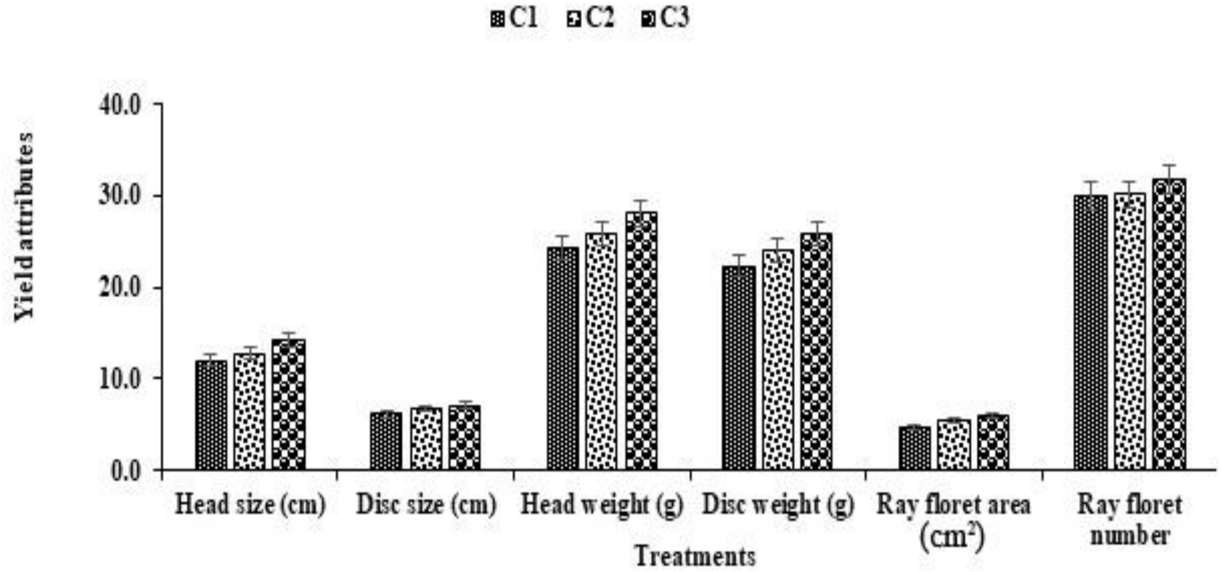

Fig. 1. Effect of Clybio concentrations on head size, disc size, head weight, disc weight, ray floret area, and ray floret numbers per flower on different days after sowing (C_1: Control; C_2: Clybio @ 4 ml/L; C_3: Clybio @ 6 ml/L).

ml/L), while the minimum (29.9) was found in the C_1 (Control) treatment (Fig. 1). The plant growth-influencing substances produced by microorganisms contributed to increased flowering, and enhanced flower quality (Arancon et al., 2008).

Vase life

To evaluate vase life, three stages of sunflowers viz., closed, intermediate, and completely open types were collected from C_3-treated plants. On the 5th day, sunflowers started blooming with the highest expansion in the closed stage (11.5 cm) and the intermediate stage (14.0 cm). After that, the ray florets gradually shrank and faded due to an increase in withering and abscission, but by the 9th day, they had stopped by achieving their smallest expansion. Fully open-stage flowers (15.5 cm) lost their ray florets more quickly and began to diminish after the first day (Fig. 2 and Plate 3).

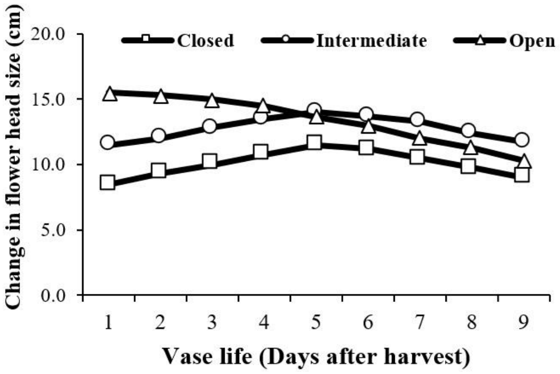

Fig. 2. The variation in flower head size (cm) from C_3 (Clybio @ 6 ml/L) treated plants at three stages (closed, intermediate, and fully open) for vase life as a function of days after harvest.

Some visual requirements determine the market value and higher acceptance to the customer, including the brightness of color, turgescence, proper flower head size, and proper petal number. Our result showed that the marketable appearance for cut sunflower head at the intermediate stage showed the maximum durability (7 days), whereas 7-8 days for the closed stage and 5-6 days for the open type. Though the closed stage had the maximum

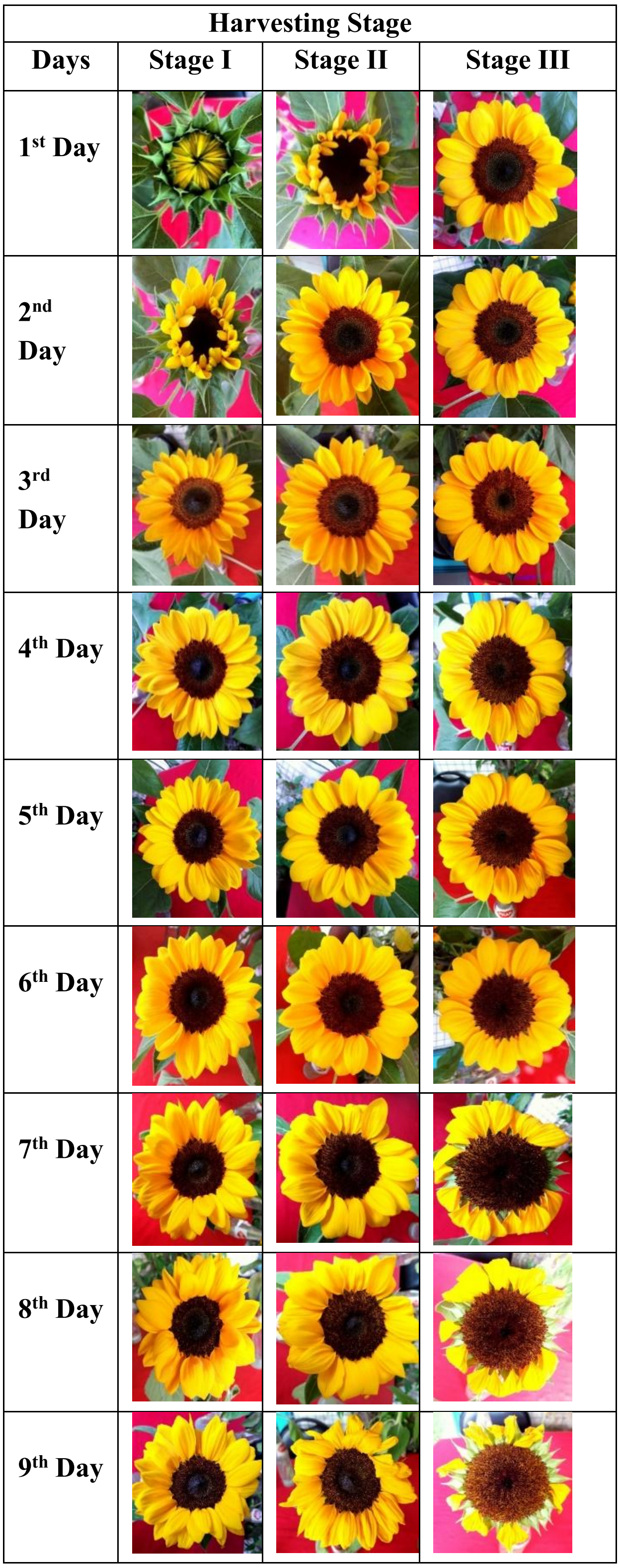

Plate 2: Vase life of ornamental sunflowers treated with C_3 (Clybio @ 6 ml/L) at three different stages (I. Closed, II. Intermediate, and III. Fully open) starting from days after harvest.

durability, its visual quality was less than that of the intermediate stage (Plate 2). The vase life of sunflowers varies between 5-13 days depending on the cultivar and is terminated by symptoms such as scape bending, abscission, and wilting of ray flowers (Gast, 1995; Sodi and Ferrante, 2005). Scape bending is thought to be correlated with genetic backgrounds (Ferrante et al., 2007); however, abscission and wilting of ray florets are known to be caused by senescence. Ethylene is a major factor in senescence, especially in ethylene-sensitive flowers (Tripathi and Tuteja, 2007). The vase life of a sunflower is indicated utilizing water uptake, the percent of change in flower head fresh weight, flower head diameter, and content in petals number (Amin, 2016). Increased longevity is another beneficial effect already observed in sunflowers (Gonzaga et al., 2003).

Colorimetric analysis of the sunflower under investigation with CIELab

The color of the ornamental sunflower's ray florets was measured using a precision colorimeter IWAVE WF32 (Shenzhen Wave), L* (lightness), a* and b* (two Cartesian coordinates), including c*, and h_{ab} (chroma & hue angle), based on the CIELab scale with standard observer 100 and standard illumination D65 (CIE, 1986; McGuire, 1992). The color values of the ray florets were recorded using the CIE L*, a*, and b* scales (Jamal Uddin et al., 2017). a*, and b* were further used to calculate chroma [C*= (a*2+b*2) 1/2] and hue angle (h°= tan-1 b*/a*). Chroma (C*) refers to color intensity, while hue angle represents red-purple (0°), yellow (90°), bluish-green (180°), and blue (270°) (Plate 3).

Treatment*	Color coordinates		Sunflower	
C_1	L*	73.69		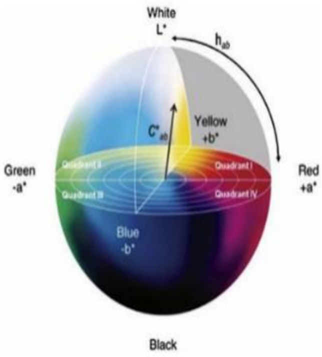 **(a)**
	a*	19.73		
	b*	92.70		
	c*	94.77		
	h_{ab}	77.99		
C_2	L*	70.40		
	a*	20.83		
	b*	103.51		 **(b)**
	c*	105.59		
	h_{ab}	78.62		
C_3	L*	65.88		
	a*	20.43		
	b*	106.23		
	c*	108.18		
	h_{ab}	79.12		

Plate 3. Impact of Clybio concentrations on ray-floret color attributes of ornamental sunflowers: (a) CIELab Colorimetric Coordinates; (b) IWAVE WF32 (Shenzhen Wave) Colorimeter.

Morphological features of secondary flower (Kid's flower)

The intriguing part was that this ornamental sunflower produced numerous secondary flowers known as the "kid's flower," which addressed a market value for the commercial cut flower industry, and provided additional benefits to the producers. The application of different Clybio concentrations on ornamental sunflowers showed significant variations in the production of secondary flowers (kids flowers). The maximum flower head size (8.4 cm), maximum flower disc size (3.1 cm), the highest stalk length (10.8 cm), the maximum number of flowers per plant (12.2), and maximum ray floret numbers per secondary flower (17.3) were found in the C_3 (Clybio @ 6 ml/L) treatment. While the minimum flower head size (7.3 cm), minimum flower disc size (2.5 cm), the lowest stalk length (8.5 cm), the minimum number of flowers per plant (10.0), minimum ray floret numbers per secondary flower (15.4) were observed from C_1 (Control) treatment (Table 2). The application of Clybio showed higher performance in strawberry yield and yield components, which enhances the maximum number of flowers and fruits per plant (Uddin et al. 2021).

Table 2. The effect of Clybio concentrations on the performance of secondary flower (kid's flower) head size (cm), disc size (cm), stalk length (cm), flower numbers per plant, and ray floret numbers per secondary flower in ornamental sunflower.

Treatment*	Head size (cm)	Disc size (cm)	Stalk length (cm)	Flower numbers/plant	Ray floret numbers/flower
C_1	7.3^b	2.5^b	8.5^b	10.0^b	15.4^b
C_2	7.5^b	2.7^b	8.7^b	10.7^b	16.1^b
C_3	8.4^a	3.1^a	10.8^a	12.2^a	17.3^b
$LSD_{0.05}$	0.6	0.3	0.9	1.1	1.0
CV (%)	8.8	12.9	11.2	12.3	6.9

* C_1: Control; C_2: Clybio @ 4 ml/L; C_3: Clybio @ 6 ml/L

In a column means having a similar letter (s) are statistically identical, and those having a dissimilar letter (s) differ significantly as per a 0.05 probability level.

Bud initiation **Full mature bud** **Fully open flower** **Side view**

Long stalk flower buds **Full blooming kid's flower** **Numerous flowers in one plant** **Decorated**

Plate 4. Different features of the secondary flowers (Kid's flower) of ornamental sunflower.

Conclusion

Based on the overall results, the study suggested utilizing Clybio at a concentration of 6 ml/L to increase the production of ornamental sunflowers. This bio-stimulant dosage provided potential growth, high-quality yield, long vase life, excellent color, and desired industrial attributes. Farmers will be encouraged to cultivate ornamental sunflowers due to their year-round availability for commercial use.

Acknowledgment

The authors would like to express gratitude to A R Malik Seeds Co Ltd. for providing seeds.

Author contributions

AFM Jamal Uddin: Experimental designing, data analysis, manuscript correction, Shanzida Akhter Ripa: Experiment conducting, data collection, writing, Fatema Tuz Juhora Chaitee: Data collection, data compiling, writing, Tamima Dastagir: Data collection, writing, Mst. Asmaul Husna: Data analysis, writing.

Declaration of conflicting interests

The authors declare that they have no conflicts of interest regarding the publication of this article.

References

Akter S, Uddin AFMJ, Hossin I and Islam MN. Influence of seed priming and clybio application on growth and yield of spinach. *Int. J. Agric. Environ. Bio-res.* 2021; 6(3): 223-227.

Amin OA. Evaluation the effect of preservative solutions, and storage conditions on shelf life of sunflower inflorescences. *Sci. J. Flowers Ornam. Plants.* 2016; 3(3): 167-176.

Arancon NQ, Edwards CA, Babenko A, Cannon J, Galvis P and Metzger JD. Influences of vermicomposts produced by earthworms, and microorganisms from cattle manure, food waste, and paper waste, on the germination, growth and flowering of petunias in the greenhouse. *Appl. Soil Ecol.* 2008; 39: 91-99.

Bhuiyan K. Influence of clybio, and ecoagra concentration on growth, and yield of strawberry. M.S. thesis, Sher-e-Bangla Nagar, Dhaka, Bangladesh. 2021.

Chowdhury AR, Hussain MM, Mia MS, Karim AMMS, Haider J, Bhuyan NI and Shifuddin K. Effect of organic amendments and EM on crop production in Bangladesh. Proc. 2nd Int. Conf. on Kyusei Nature Farming, Oct. 7-11, Washington, DC., USA, 1994; pp: 155-163.

CIE. Recommendations on uniform color spaces, color difference evaluations, and psychometric color terms. cie central bureau, colorimetry, 2nd ed. Commission International de I Eclairage, Central Bureau, Viena, Austria. 1986; pp:1-83.

Devecchi M. Post-harvest physiology of cut flowers of sunflowers ‘Sunrich Orange’ (*Helianthus annuus*): First experimental results. *Acta Hort.* 2005; 66 (9): 381-388.

Dwivedi SP and Dwivedi G. Utilization of organic waste, and inorganic waste in development of green hybrid composite material. *ASME*, 2019; 8(1): 316-328.

El-Tarabily KA and Sivasithamparam K. Potential of yeasts as biocontrol agents of soil-borne fungal plant pathogens, and as plant growth promoters. *Mycoscience*. 2006; 47(1): 25-35.

Evans JT. Nitrogen, and photosynthesis in the flag leaf of wheat. *Plant Physiol*. 1998; 72: 297-302.

Ferrante A, Alberici A, Antonacci S and Serra G. Effect of promoter, and inhibitors of phenylalanine ammonia-lyase enzyme on stem bending of cut gerbera flowers. *Acta Hort*. 2007; 755: 471-476.

Gast KLB. *Production, and postharvest evolution of fresh-cut sunflowers*. Agricultural Experiment Station, Kansas State University, Manhattan, Marc A. Johnson, Director. 1995. p. 9. Report of Progress 751.

Gonzaga AR, Moreira FA, Lonardoni F and Faria RT. Genotype interaction x *Helianthus* post-harvest longevity. *Crop. Breed. Appl. Biotechnol.* 2003; 3(4): 281-288.

Jamal Uddin AFM, Ahmad H, Rakibuzzaman M, Rini SN and Laila B. Classification of lisianthus lines grown in Sher-e-Bangla Agricultural University. *Int. J. Bus. Soc. Sci. Res*. 2017; 6(1): 18-26.

Javid A. Foliar application of effective microorganisms on pea as an alternative fertilizer. *Agron. Sustain. Dev*. 2006; 26: 257-262.

Kang Y, Shen M, Wang H and Zhao Q. Complete genome sequence of *Bacillus pumilus* strain WP8, an efficient plant growth-promoting rhizobacterium. *Genome Announc*. 2015. 3(1): e01452-14.

Khaliq A, Abbasi MK and Hussain T. Effect of integrated use of organic, and inorganic nutrient sources with effective microorganisms (EM) on seed cotton yield in Pakistan. *Bioresour. Technol.* 2006; 97: 967-972.

Kirtimala BN, Nataraj SK, Shadakshari YG, Kumar DP and Seetharamu GK. Standardisation of optimum stage of harvest for enhancing vase life in ornamental sunflower (*Helianthus annuus* L.). *Int. J. Pure App. Biosci*. 2018; 6 (4): 733-735.

Lonhienne, T, Mason MG, Ragan MA, Hugenholtz P, Schmidt S and Lonhienne CP. Yeast as a biofertilizer alters plant growth, and morphology. *Crop Sci.* 2014; 54(2): 785-790.

McGuire RC. Reporting of objective color measurement. *HortScience.*1992; 27: 1254-1255.

Rakibuzzaman M, Tusi RR, Maliha M, Husna A. and Uddin AFMJ. Response of potato germplasm to *Trichoderma viride* as Bio-stimulator. *Int. J. Bus. Social Sci. Res.* 2021; 9(2): 17-21.

Seemann JR, Sharkey TD, Wang J and Osmond CB. Environmental Effects on Photosynthesis, Nitrogen-use Sfficiency, and Metabolite Pools in Leaves of Sun and Shade Plants. *Plant Physiol.* 1987; 84: 796-802.

Shrestha A, Kim BS and Park DH. Biological control of bacterial spot disease and plant growth promoting effects of lactic acid bacteria on pepper. *Biocontrol. Sci. Technol.* 2014; 2: 763-779.

Sodi AM and Ferrante A. Physiological changes during postharvest life of cut sunflowers. *Acta Hort.* 2005; 669: 219-224.

Taha SR, Seleiman MF, Alhammad BA, Alkahtani J, Alwahibi MS and Mahdi AHA. Activated yeast extract enhances growth, anatomical structure, and productivity of *Lupinus termis* L. Plants under aactual salinity conditions. *Agron.* 2020. 11(1): 11010074.

Tiwari S, Prasad V and Lata C. *Bacillus*: Plant growth promoting bacteria for sustainable agriculture, and environment. microbial biotechnology in agro-environmental sustainability. *Elsevier.* 2019; pp 43-55.

Tripathi SK and Tuteja N. Integrated signaling in flower senescence. *Plant Signal. Behav.* 2007; 2 (6): 437-445.

Uddin AFM, Sabrina N, Husna MA, Imam MH and Rakibuzzaman M. Bio-efficacy of *Trichoderma harzianum* spore concentrations on tomato production. *Int. J. Bus. Soc. Sci. Res.* 2020; 8(3): 124-129.

Uddin AFMJ, Nasif FM, Kaynat B, Maliha M and Rakibuzzaman M. Organic bio-stimulator application on growth, and yield of strawberry. *Int. J. Bus. Soc. Sci. Res.* 2021; 9 (3): 01-05.

J. Bangladesh Acad. Sci. 49(1); 31-33: June 2025 DOI:https://doi.org/10.3329/jbas.v49i1.81653

Journal of Bangladesh Academy of Sciences

Journal homepage: http://www.bas.org.bd/publications/jbas.html

Research Article

Proof of Fermat’s Last Theorem when it is already proven for the exponent *n=3*

Syed Abdul Kader*

Department of Endocrinology and Metabolism, Sher-e-Bangla Medical College, Barisal, Bangladesh

ARTICLE INFO

Article History

Received: 08 September 2024
Revised: 15 January 2025
Accepted: 16 February 2025

Keywords: Integers, Triangle, Right angle, Pythagorean triples.

ABSTRACT

Pythagorean triples have been known for a long time. Fermat's last theorem sets the limit of any two integers summing up to the third, all raised to the same power, which, according to the theorem, can never be more than 2. After centuries of effort and waiting, Andrew Wiles provided a large and complicated proof of this theorem; this article provides an elementary one. *Mathematical subject classification: 11D41, 11D45.*

Introduction

Among the works compiled by Euclid, the related to the Pythagorean triangle (Clapham and Nicholson, 2009; Fitzpatrick, 2008) was one of the most prominent and useful. Pythagoras stated that the sum of the squares on two arms adjacent to the correct angle of a right-angled triangle is equal to the square on the hypotenuse. The theorem is one of the most ancient mathematical results. Evidence shows that the Babylonians and the Chinese knew it 1000 years before Pythagoras. (Krantz, 2006) The Egyptians used at least one combination of Pythagorean triples, 3, 4, and 5, to construct corners of pyramids. For centuries, mathematicians were pondering whether this type of relationship was possible with powers higher than 2 over the triplet bases. Fermat's last theorem, acceptably conjectured for centuries, states its impossibility. Andrew Wiles provided his colossal and complicated proof just before the advent of the 21st century. (Wiles, 1995) We wonder whether Fermat himself worked out a proof that he could not fit into the margin of Bachet’s translation of Diophantus’s Arithmetica. (Krantz, 2006) We provide an elementary proof.

Andrew Wiles proved enough of the Taniyama-Shimura-Weil conjecture to prove Fermat's Last Theorem. The conjecture, which later mathematicians after Wiles proved as the modularity theorem, appeared around 1955. Gerhard Frey G, in 1984, noticed an apparent link between the conjecture and Fermat's Last Theorem (Frey G, 1986; Wikipedia contributors, 2019; Wiles AJ, 1995).

Proofs of Fermat's Last Theorem for specific exponents date back to the time of Fermat himself, who outline a proof for $n = 4$ by infinite descent, alternative proofs given by many, from Bessy (de Bessy F, 1676) to Dolan (2011), Euler not missing out. In 1770, Leonhard Euler gave a proof for $n = 3$, but his proof required a missing lemma, which was later proven and provided by other mathematicians. (Friedberg R, 1994) Independent and alternative proofs were published later. Independent and alternative proofs for $n = 5,6,7$, etc., were published over the years. (Wikipedia contributors, 2018).

Andrew Wiles's proof of Fermat’s Last Theorem is massive in size; the mathematics used in it is inaccessible to the understanding of generally educated people and requires most modern mathematics developed only in the later part of the twentieth century. Earlier proofs for specific exponents should have given rise to the thought that the possibility of a solution to Fermat's equation has ceased from $n = 3$ onwards; we rearranged and

---

*Corresponding author:<skdr0002@gmail.com>

modified the equation to show why that is so general. In contrast to Andrew Wiles' proof, our method uses elementary mathematics to explore and understand most of the general educated public for the first time, leaving no doubt about Fermat's Last Theorem.

Proof of Fermat's Last Theorem

Theorem 2.1. Fermat's last theorem (Krantz, 2006; Wikipedia contributors, 2018; 2019) states that if x; y; z; n are positive integers then

$\mathrm{x}^{\mathrm{n}} + \mathrm{y}^{\mathrm{n}} \neq \mathrm{z}^{\mathrm{n}}$ when $\mathrm{n} > 2$.

Proof. Definitely if n = 0, LHS = 1 + 1 = 2 will always be greater than RHS = 1. If n = 1, LHS will be equal to RHS when the sum of integers on LHS is put on RHS.

Let us assume, n and $\mathrm{x} < \mathrm{y} < \mathrm{z}$ are positive integers, and in certain conditions,

$$\mathrm{x}^{\mathrm{n}} + \mathrm{y}^{\mathrm{n}} = \mathrm{z}^{\mathrm{n}} \tag{2.1}$$

We know from the binomial theorem,

$(\mathrm{x}+\mathrm{y})^{\mathrm{n}} = \mathrm{x}^{\mathrm{n}} + {}^{\mathrm{n}}\mathrm{C}_1\mathrm{x}^{\mathrm{n}-1} \ldots + {}^{\mathrm{n}}\mathrm{C}_{\mathrm{r}}\mathrm{x}^{\mathrm{n}-\mathrm{r}} \ldots + \mathrm{y}^{\mathrm{n}}$So for $\mathrm{n} > 1$, we have,

$$(\mathrm{x}+\mathrm{y})^{\mathrm{n}} > \mathrm{x}^{\mathrm{n}} + \mathrm{y}^{\mathrm{n}}$$

Or,

$(\mathrm{x}+\mathrm{y})^{\mathrm{n}} > \mathrm{z}^{\mathrm{n}}$ So,

$$x + y > z \tag{2.2}$$

$$2y > x + y > z \tag{2.3}$$

Also, for the positive integers,

$$z - x > z - y \geq 1 \tag{2.4}$$

$$z - x \geq 2 \tag{2.5}$$

As from (2.1), we have $x^n = z^n - y^n = (z-y)(z^{n-1} + z^{n-2}y + z^{n-3}y^2 \ldots + y^{n-1})$, for showing lower bound of the solution to (2.1), we get,

$$x \geq 1 \tag{2.6}$$

$$y \geq 2 \tag{2.7}$$

$$z \geq 3 \tag{2.8}$$

Again rearranging (2.1), we have,

$$y^n = z^n - x^n = (z-x)(z^{n-1} + z^{n-2}x + z^{n-3}x^2 \ldots + x^{n-1})$$

$= (z-x)z^{n-1}(1 + \frac{x}{z} + \cdots + \frac{x^{n-1}}{z^{n-1}})$Or,

$$\ln y^n = \ln((z-x)z^{n-1}\left(1 + \frac{x}{z} + \cdots + \frac{x^{n-1}}{z^{n-1}}\right))$$

$$= \ln(z-x) + \ln z^{n-1} + \ln\left(1 + \frac{x}{z} + \cdots + \frac{x^{n-1}}{z^{n-1}}\right)$$

Or,

$$1 = \frac{\ln(z-x)}{n\ln y} + \frac{n-1}{n} \cdot \frac{\ln z}{\ln y} + \frac{\ln\left(1+\frac{x}{z}+\cdots+\frac{x^{n-1}}{z^{n-1}}\right)}{n\ln y} \tag{2.9}$$

Applying the findings from the previous inequalities in (2.9), we get $\ln(z-x) \geq \ln 2 \geq 0.693$ and $\ln\left(1 + \frac{x}{z} + \cdots + \frac{x^{n-1}}{z^{n-1}}\right) > \ln 1 > 0$. So, $\frac{\ln(z-x)}{n\ln y} > 0$ and $\frac{\ln\left(1+\frac{x}{z}+\cdots+\frac{x^{n-1}}{z^{n-1}}\right)}{n\ln y} > 0$. Also, $1 < \frac{\ln z}{\ln y} < \frac{\ln 2y}{\ln y} = 1 + \frac{\ln 2}{\ln y}$.

As we stated at the beginning of this proof section, when $n = 0$, the equation is not possible; when $n = 1$, we get $\frac{n-1}{n} = 0$; when $n = 2$, we get $\frac{n-1}{n} = \frac{1}{2}$; with the increase of n, we get an increasing $\frac{n-1}{n} \to 1$. But Fermat's Last Theorem was proven for $n = 3$ first by Euler. (Friedberg, 1994; Ribenboim, 2009; Hellegouarch, 2001) So (2.9) is not possible for $n = 3$; consequently, with increasing $\frac{n-1}{n}$, equation (2.9) is not possible for $n > 3$. This should generally prove the Fermat's Last Theorem for any $n > 2$.

But we would like to make it look clearer. It would be better for understanding the equation if we restrict n to one place only, and show other terms falling within ranges. For clarity and brevity, we introduce a few more notations. If,

$$1 < \frac{\ln z}{\ln y} = 1 + \delta < \frac{\ln 2y}{\ln y} = 1 + \frac{\ln 2}{\ln y}$$

We have

$0 < \delta < \frac{\ln 2}{\ln y} < \frac{0.693}{\ln y}$ Also, when

$$1 > \alpha > 0 > -\alpha > \frac{\ln\left(1 - \frac{1}{2}\right)}{\ln y} = -\frac{0.693}{\ln y}$$

So that,

$$\frac{\ln(2y-x)}{\ln y} = \frac{\ln y}{\ln y} + \frac{\ln 2}{\ln y} + \frac{\ln\left(1 - \frac{x}{2y}\right)}{\ln y}$$

$$= 1 + \frac{0.693}{\ln y} - \alpha > \frac{\ln(z-x)}{\ln y} = \eta$$

$$\geq \frac{\ln 2}{\ln y} > \delta > 0$$

And,

$$1 = \frac{\ln y}{\ln y} = \frac{\ln \frac{2y}{2}}{\ln y} > \frac{\ln \frac{z}{2}}{\ln y} \geq \frac{\ln \frac{z}{z-x}}{\ln y} = \frac{\ln \frac{1}{1-\frac{x}{z}}}{\ln y}$$

$$> \frac{\ln\left(1 + \frac{x}{z} + \cdots + \frac{x^{n-1}}{z^{n-1}}\right)}{\ln y} = \epsilon > 0$$

where we have a natural logarithm of partial geometric series in the numerator, which is less than its infinite series. Rewriting (2.9), we get,

$$1 = \frac{n-1}{n} \cdot (1 + \delta) + \frac{1}{n} \cdot (\eta + \epsilon)$$

Or,

$$1 = 1 + \delta + \frac{1}{n} \cdot (\eta + \epsilon - 1 - \delta) \qquad (2.10)$$

To satisfy equation (2.10), we must have $\frac{1}{n} \cdot (\eta + \epsilon - 1 - \delta)$ negative to cancel out δ.

With the increase in n, we have to decrease $\frac{1}{n} \to 0$, gradually, rendering its effect negligible in equation (2.10) for the canceling out purpose. When Fermat's Last Theorem had already proven for $n = 3$, the equation (2.10) is not possible for $n = 3$; consequently, with $\frac{1}{n} \to 0$, equation (2.10) is not further possible for $n > 3$. This proves the Fermat's Last Theorem generally for any $n > 3$. □

Conclusion

For millennia, Pythagoras's theorem has remained one of the most useful propositions of geometry in practical life, e.g., for making corners, measuring distances on earth and space, and graphs of analytic geometry helping its progression. For centuries, Fermat's last theorem remained an enigma until Andrew Wiles declared its large, complicated, fascinating proof. This article provides an elementary proof of Fermat's last theorem.

Acknowledgment

Those who allowed me a hard-found time to do this work.

Conflict of Interest

This research did not receive a specific grant from funding agencies in the public, commercial, or not-for-profit sectors, so there is no conflict of interest.

Data Availability Statements

Data sharing is not applicable to this article as no datasets were generated or analyzed during the current study.

References

Clapham C and Nicholson J. The Concise Oxford Dictionary of Mathematics. 4th ed. *Oxford University Press, Oxford*, 2009.

de Bessy F. Traité des Triangles Rectangles en Nombres. Hachette Livre-BNF, Paris, 1676.

Dolan S. Fermat's Method of Descente Infinie. *Math. Gaz.* 2011; 95: 269-271.

Fitzpatrick R. Book 1, Proposition 47. Euclid's elements of geometry. Revised and Corrected Edition, *Bristol*, 2008. p 47.

Friedberg R. An Adventurer's guide to number theory. Dover ed. Dover Publications, *New York*, 1994, pp 107-109, 231-235.

Frey G. *Links between stable elliptic curves and certain diophantine equations.* Annales Universitatis Saraviensis 1, 1986; 1-40.

Hellegouarch Y. Invitation to the mathematics of fermat-wiles. *Academic Press, Elsevier*, 2001.pp 16-18.

Krantz SG. An episodic history of mathematics: Mathematical culture through problem solving. *Mathematical Association of America*, 2006.

Ribenboim P. Fermat's Last Theorem for amateurs. *Springer-Verlag, New York*, 2009.pp 25-37.

Wikipedia contributors. Fermat's Last Theorem. Wikipedia, The Free Encyclopedia. Retrieved May 4, 2019, from https://en.wikipedia.org/wiki/Fermat's_Last_Theorem.

Wikipedia contributors. List of unsolved problems in mathematics. Wikipedia, The Free Encyclopedia. Retrieved June 7, 2018, from https://en.wikipedia.org/wiki/List_of_unsolved_problems_in_mathematics.

Wiles AJ. Modular elliptic curves and Fermat's Last Theorem. *Ann. Math.* 1995; 141 (3): 443-552.

J. Bangladesh Acad. Sci. 49(1); 35-44: June 2025 DOI:https://doi.org/10.3329/jbas.v49i1.76026

Journal of Bangladesh Academy of Sciences

Journal homepage: http://www.bas.org.bd/publications/jbas.html

Research Article

Studies on the vorticity of superconducting 3D Nano-sized pyramidal samples as a function of coherence length

Sharmin Aktar and Abul Hasnat*

Department of Physics, Jagannath University, Dhaka, Bangladesh

ARTICLE INFO

Article History

Received: 20 August 2024
Revised: 13 January 2025
Accepted: 15 January 2025

Keywords: Mesoscopic, Superconductor, Pyramidal, GL formalism, Vortex.

ABSTRACT

This study examines the vorticity of a nano-sized superconducting pyramidal sample using the 3D Ginzburg-Landau (GL) formalism, a crucial tool for analyzing the nonuniform geometrical sample. We consider a field applied perpendicularly to the pyramid's base and characterize the sample's static properties as a function of its coherence lengths. The study focuses on the vortex nucleation point (vortex penetration field) and the vortex configuration within the sample. The sample's free energy, magnetization, and other steady properties are measured on the plane orthogonal to the field with the applied magnetic field increases. We examine two samples with different dimensions, one equal to 12ξ and the other 6ξ. The study investigates the variation of the Meissner state's stability range and the critical field of the pyramidal sample as a function of the sample size.

Introduction

A field within condensed matter physics, known as mesoscopic physics, focuses on studying materials of intermediate sizes (Alegria et al., 2021). These materials can range in size from the nanoscale, which is just a few atoms (e.g., a molecule), to micrometers. The size of mesoscopic samples is typically similar to the coherence length (ξ) and/or magnetic field penetration depth (λ) (Ge et al., 2023). This sample size significantly affects the sample characteristics under an external magnetic field (H) (Taupin et al., 2016), and the presence of this factor can create several superconducting states, along with phase transitions. Variations in the temperature (T) or the applied magnetic field to the mesoscopic sample can cause magnetization jumps (Geim et al., 1997).

Research has been previously conducted on mesoscopic superconductor's magnetic response with different geometries: (i) disk-shaped samples (Deo et al., 1997; Zharkov et al., 2000), (ii) indefinitely long cylinders (Zharkov et al., 2000), (iii) ring-like structures (Baelus et al., 2001), and more complex geometries (Fomin et al., 1998). The Ginzburg-Landau (GL) theory forms the basis for the theoretical study of mesoscopic superconductors, providing a satisfactory explanation for mesoscopic samples across a wide range of magnetic fields and temperatures (De Gennes, 2018). Typically, disks or cylindrical geometries of mesoscopic superconducting samples enclosed by an insulator or vacuum exhibit two types of superconducting states. A circularly symmetric state with a fixed angular momentum value is one form among them, known as a "giant vortex." Important issues regarding magnetic properties and phase transitions in certain geometrical systems should be addressed, including basic and technological aspects.

---

*Corresponding author:<abul.hasnat@phy.jnu.ac.bd>

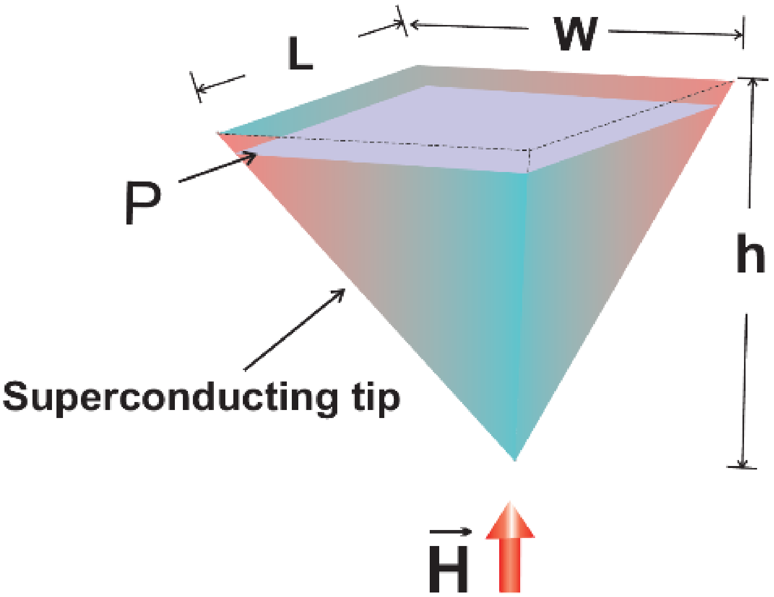

Fig. 1. Superconducting pyramidal sample in the presence of an applied magnetic field where the field is perpendicular to the base plane of the sample. Here, L, W, and h represent the tip's length, width, and height, and in this case, L=W=h. We are considering two samples, one with all dimensions (L, W, h) equal to 6ξ and another with all dimensions equal to 12ξ.

Understanding the process of magnetization in type-II superconductors depends largely on the dynamics of magnetic vortices. The relationship between the vortices and sample surfaces and the sample shape decreases with sample size. Various research studies have focused on magnetizing a mesoscopic superconductor without pinning centers (Baelus et al., 2004). Calculations indicate transitions between various large vortex states in mesoscopic type-I superconducting thin films, with multi-vortex states being mostly metastable, although occasionally thermodynamically stable states are also observed. Mesoscopic triangular cylinders of type-I samples reveal a vortex-antivortex molecule (Misko et al., 2003).

The effect of surface defects and sample geometry on vortex dynamics was examined using a finite element method to solve the TDGL equations (Kim et al., 2007). The mixed state in the mesoscopic cylindrical sample made of type-II superconducting materials shows that as the system searches for the configuration with the lowest Gibbs free energy, it passes through nearly stable intermediate states. The sample's square symmetry aligns with the steady-state arrangement. Several bulk superconductor experiments (De Gennes 1965; Fink and Presson, 1969) investigated the influence of sample surfaces on the first vortex entry.

According to Deo et al. and Schweigert et al., Phase transitions of the first order take place between large vortices with different angular momentum, causing the observed magnetization jumps (Deo et al., 1997). Second, in samples with sufficiently large radii, multivortex structures (Schweigert et al., 1998) can form, which are comparable to the bulk superconducting material's Abrikosov flux line lattice. These states are a mixture of different angular momentum vortex states. An effective total angular momentum or vorticity can also be introduced for multi-vortex states. Phase transition of the second order occurs with changing the magnetic field, bringing about a switch between the multi-vortex states (MVSs) and giant vortex states GVSs) (Baelus and Peeters, 2002; Wang and Wang, 2019).

The boundary effect significantly impacts the charge distribution in such mesoscopic samples. Furthermore, the sample's screening currents cause charge redistribution, resulting in a nonuniform distribution even in the Meissner state. This scenario is similar to an inverted vortex, with its core extending to infinity. When vortices exist, the Meissner charge interacts with the previously investigated vortex charge (Meissner and Ochsenfeld, 1933; Maxwell 1950; Bardeen et al., 1957), which is specific to mesoscopic samples. We conducted a theoretical investigation into electrical charge redistribution that occurs in various geometries of mesoscopic superconducting samples, such as disks and cylinders. Recent improvements in microfabrication and experimental techniques have focused emphasis on mesoscopic superconductors. Important basic and technological problems about magnetic characteristics and phase transitions in such small, constrained systems must be addressed.

In samples of comparable size to the coherence length, the layout of the vortices is determined by the confinement of the superconducting condensate. In previous studies, researchers have explored the shapes of disks within the framework of the Linearized GL equation. They assumed a uniform magnetic field within the disks. P. Singha Deo, V. A. Schweigert, F. M. Peeters and A.K. Geim (Deo et al., 1997) examined the magnetization curve of mesoscopic disks with finite thickness changes with the external magnetic field. Several experimental techniques have been devised to observe these unique states, but none of them have been able to distinguish between MVSs and GVSs.

Mel'nikov et al. developed a comprehensive numerical model to describe the vortex state of FFS using the time-dependent Ginzburg-Landau (TDGL) theory (Mel'nikov et al., 2002). They also introduced a symmetry-based approach to analyze vortex molecules and complexes through analytical studies. Their simulations allowed for a thorough analysis of the nonlinear region at low fields.

Because the shape of a mesoscopic sample differs from the Abrikosov lattice triangle, the vortex patterns prominently display aspects of the sample's shape instead of the triangular lattice, leading to powerful finite-size effects and significant shape effects determining vortex configurations. For example, as proven theoretically (Baelus et al., 2001; Baelus et al., 2004) and experimentally (Grigorieva et al., 2006), vortices in mesoscopic disks create circular symmetric shells that are size-dependent (Misko et al., 2007). When confined, small disks can cause vortices to transform into large vortexes (GV) due to strong confinement effects. Among mesoscopic superconductors of different shapes, triangles are noteworthy. The symmetry of quilateral triangles and the Abrikosov vortex lattice is the same. This implies that a triangle can accommodate part of the vortex lattice without distortion for a given number of vortices. Therefore, vortex patterns in the shape of triangles are much more stable because the interaction between vortices and boundary effects enhances their stability (Zhao et al., 2008).

A magnetic field's existence influences superconductivity behavior in small equilateral triangles, squares, and other configurations while maintaining the symmetry (C3, C4) of the boundary conditions (Chibotaru et al., 2001). This can result in a new vortex configuration surrounding a single antivortex. Researchers have studied the behavior of type II mesoscopic superconducting spheres with an externally applied magnetic field (Baelus et al., 2007). They studied the stable vortex states in these spheres at different radii. A study by A. Hasnat explored how the pyramidal topology of a superconductor affects vortex formation and stability (Hasnat, 2020).

One of the popular theories used to describe the magnetic behavior of superconductors is the Ginzburg-Landau (GL) theory, the time-dependent version of it is generally called the time-dependent Ginzburg-Landau theory (TDGL). Computational analysis involves using finite-element discretization of the TDGL equations (Tinkham, 2004). These methods are recognized as powerful computational tools for approximating solutions to partial differential equations, especially for samples with complex shapes.

In Fig. 1, the superconducting pyramidal sample is displayed with the observation plane (P) indicated when a magnetic field is applied. The superconducting properties of a 3D inhomogeneous sample can be observed more easily using the GL formalism than with the other tools. The pyramidal shape of the superconducting sample is unique in terms of its applicability. Pyramidal samples have a higher critical field value than their bulk materials. STM's scanning tip could have a pyramidal form. The major goal of this research is to investigate the magnetic, thermodynamic, and critical phenomena of superconducting pyramidal samples using the 3D GL formalism. Free energy, Cooper pairs density, magnetism, and screening current density will all be examined in terms of coherence length. The variance in coherence length determines the quality of the various sample materials. We want to connect the coherence duration with the sample's Meissner state. We want to determine under what conditions the Meissner state and critical current will be enhanced.

Theoretical formalism

A nano-sized superconducting sample is placed within an insulator media under a homogeneous, perpendicular applied magnetic field $\vec{H}$. By applying the dimensionless variables, we obtain the following form of 3D GL equations:

$$(-i\vec{\nabla}_{3D}-\vec{A})^2\psi=\psi(1-|\psi|^2),$$

$$-k^2\Delta\vec{A}=J_{3D}=\frac{1}{2i}\left(\psi^*\vec{\nabla}_{3D}\psi-\psi\vec{\nabla}_{3D}\psi^*\right)-|\psi|^2\vec{A},$$

$$\vec{n}.\left(-i\vec{\nabla}_{3D}-\vec{A}\right)\psi|_{boundary}=0.$$

The superconducting electron is represented by $\psi(\vec{r})=|\psi|\exp(i\phi)$, where ψ denotes the superconducting complex order parameter with the magnitude value of $|\psi|$ and with its phase ϕ. The value of $|\psi^*\psi|$ is nearly equivalent to the superconducting electrons' number, N_s, at a position $\vec{r}$. The supercurrent that runs through the material below Tc is represented by the phase ϕ $(\vec{r})$. The coherence length (ξ) determines the distance, and the order

$$[(-i\vec{\nabla}_{3D}-\vec{A})^2\psi_0-\psi_0+|\psi_0|^2\psi_0]$$
$$=\eta(\psi-\psi_0)$$

The boundary conditions at the sample boundaries cause the normal component of the superconducting current to become zero. To solve the GL equations, we use a uniform grid space (in Cartesian x, y, z coordinates) with 5 grid points at every unit of ξ distance and a superconductor area of 63×63×63 grid points. Next, we use an iterative procedure based on the link variable approach and the Gauss-Seidel technique to determine the order parameter (ψ). The iterative process is directed in the following manner:

Here, η is the real coefficient ψ, and ψ_0 is the best approximation of the current and next iteration.

Using a link variable approach,

$$U_\mu^{\vec{r}_1,\ \vec{r}_2}\equiv\exp[-i\int_{\vec{r}_2}^{\vec{r}_1}\vec{A}_\mu\,(\vec{r}).d\vec{\mu}]$$

$$[-\psi_0+|\psi_0|^2\psi_0-\frac{1}{U_\mu}\frac{\partial^2}{\partial\mu^2}(U_\mu\psi_0)]$$
$$=\eta(\psi-\psi_0)$$

with μ = x, y and z

The essential numerical technique is to find words that go along with the new answer for ψ and to evaluate based on ψ_0

$$[\,\eta-(1-T)\frac{4}{d^2}+$$
$$2|\psi_0|^2]\,\psi=\ \widetilde{U}\psi_0+\eta\,\psi_0+$$
$$2\psi_0|\psi_0|^2-\ {\psi_0}^2\psi^*$$

and solution

Here, ξ, λ and H_{c2} indirectly depend on the temperature:

$$c\,\psi-a\ +e\psi^*=0$$

$$\xi(\mathrm{T}) = \frac{\xi(0)}{\sqrt{1 - T/T_{c0}}}$$

$$\lambda(\mathrm{T}) = \frac{\lambda(0)}{\sqrt{1 - T/T_{c0}}}$$

$$\mathrm{H}_{c2}(\mathrm{T}) = H_{C2}(0)(1 - \frac{T}{T_{C0}})$$

In our work, we considered two samples in terms of the different coherence lengths, such as one sample with the materials of 12ξ and the other 6ξ. Here the working temperature is considered at $t = T/T_{c0} = 0.9$. We characterize the sample's properties with varying fields. Our main focus is to observe the changes in free energy in those fields.

Results and Discussion

We would like to investigate the static properties of the pyramidal mesoscopic samples. Pyramidal geometry has some unique advantages, the critical field of the pyramidal sample is enhanced than the bulk sample materials. We would like to observe the basic superconducting features such as the Cooper pairs density, screening current density, critical parameters, etc. Our results obtained are represented as follows. The free energy of the sample conveys a lot of crucial information about it; we start with the free energy curve here. In Fig. 2, the 12ξ sample's free energy has been shown with respect to the applied field. We observe that the free energy changes are continuous with varying fields, which expresses that there is no penetrating flux as a form of vortex (zero vorticity, L=0) inside the sample. This definite sample size and coherence length do not permit the nucleation of the vortex up to the point of the transition field. We did not observe the vortex in the 3D iso-surface plot in the entire range of free energy. The combined effect of these sample sizes and coherence length provides an extremely large Meissner state of the sample, which has some practical applications, such as the STM tip being used in the dissipationless regime.

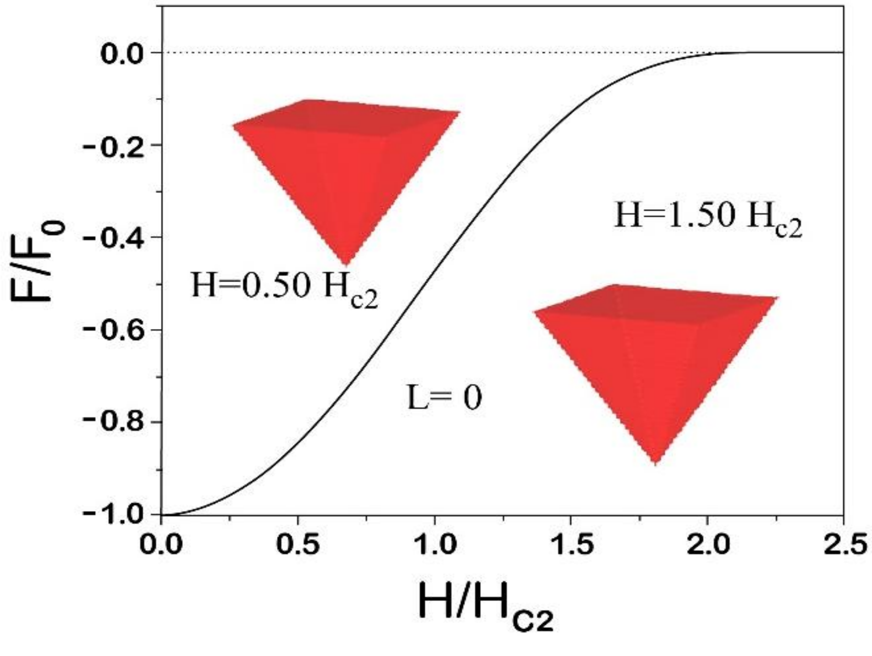

Fig. 2. Free energy changes with the applied field of the 12ξ sample. The inset shows the 3D iso-surface plot of the sample at the field $H/H_{c2}=0.50$ and $H/H_{c2}=1.50$. Here L denotes vorticity. The dotted line on the upper portion of the plot shows the superconducting state to the normal state transition point.

Magnetization vs. the applied field graph of 12ξ sample is shown in Fig. 3. The magnetization is increased up to the field $H \approx 1.00H_{c2}$. No jump (discontinuities) is observed in the curve, indicating that no vortex penetrated the sample in the entire range of the applied field. We didn't observe any paramagnetic effect as magnetization never takes the positive value.

Distribution of (a-b) the Cooper pairs density and (c-d) screening current density at the field of $H=0.50H_{c2}$ and $H=1.50H_{c2}$, respectively are shown in Fig 4. The Measurements are taken on the base plane of the pyramid since this plane is in orthogonal alignment with the applied field. (a) There is a uniform distribution of the Cooper pairs density at field $H=0.50H_{c2}$, and (b) the Cooper pairs are less suppressed in the middle part than the edges part of the sample at field $H=1.50H_{c2}$. On the other hand, (c-d), the screening current density starts generating from the edges part of the sample, and the screening current gradually increases when the field increases. At the four corner edges of the sample, the screening current is considerably less than in other parts of the sample.

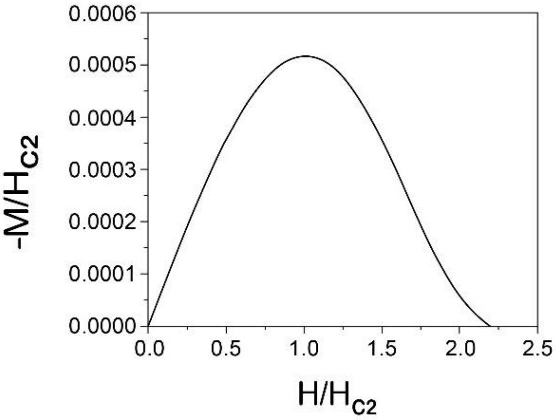

Fig. 3. 12ξ sample's magnetization changes with the applied field.

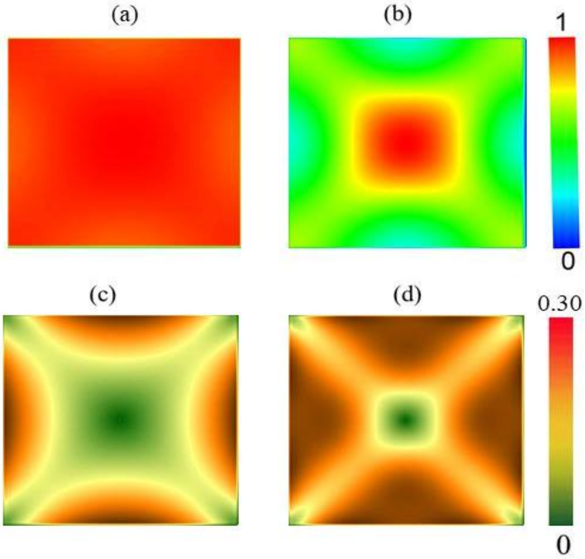

Fig. 4. (a-b) Cooper pairs density and (c-d) screening current density of 12ξ sample

6ξ sample's free energy vs. the applied field graph is shown in Fig. 5 (a). The dotted line specifies the transition point from the superconducting state to the normal state. Discontinuities are observed in the free energy graph, which indicates that the vortex appeared in this sample. The stability ranges of the distinguished vortex states are clearer in the magnetization curve (Please see in Fig. 6). 3D iso-surface plot of the sample at different vortex states such as L=1, 2, 3, and 4. 3D iso-surface plot of the sample at different vortex states such as L=1, 2, 3 and 4 are also shown in the right panel of the Fig. 5 (b-e). (b-e) vortex is visualized, and the separated vortex can be seen clearly in the 3D representation of the sample's iso-surface plot.

The Meissner state's stability range in the sample is observed at about $\Delta H \approx 0.55\ H_{c2}$, with the critical field at around 1.78 Hc2.

Magnetization of the 6ξ sample variation with the applied field is shown in Fig. 6. Discontinuities for the different vortex states in the magnetization are clearer than the free energy curve. The odd vortex states' stability range is shorter than the even number vortex states since the even number vortex states are energetically favorable for this pyramidal-shaped sample. The stability range of the L=4 state is greater than all states. Only paramagnetic effects are overserved. The magnetization of 6ξ is higher than the 12ξ sample.

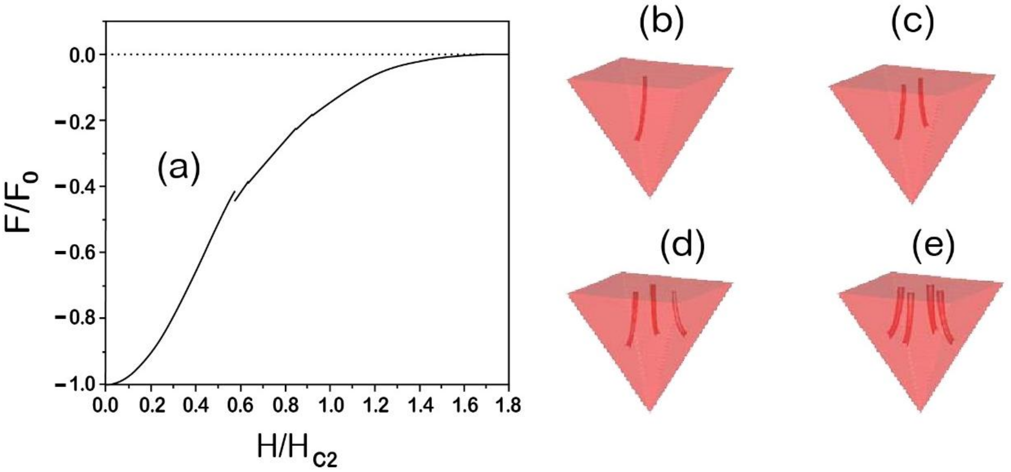

Fig. 5. (a) Free energy changes with the applied field of the 6ξ sample. (b-e) 3D iso-surface plot of the sample at distinguish vortex states such as L=1, 2, 3, and 4.

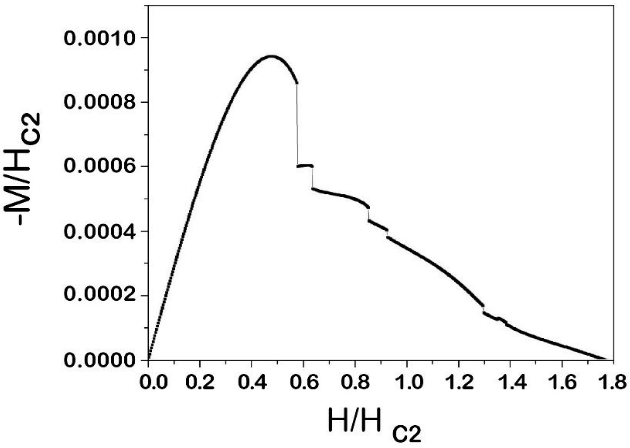

Fig. 6. Magnetization variation with the applied field of 6ξ sample. Discontinuities indicate the change of vortex states.

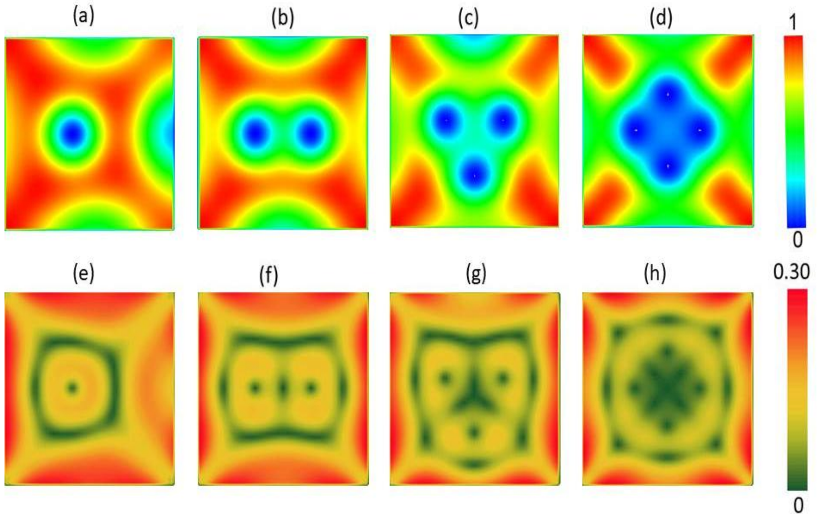

Fig. 7. Contour plots of (a-d) Cooper pairs density and (e-h) screening current density of 6ξ sample at L=1 to 4 vorticity, respectively.

Contour plots of Cooper pairs density and screening current density of 6ξ sample at different vortex states, L=1 to 4, are shown on the base plan of the pyramid in Fig. 7, respectively. The value of the color is given on the corresponding color bar. Multi-vortex states are clearly observed from the contour plots. The Cooper pairs are completely suppressed in the center of every vortex and the distribution of the Cooper pairs are higher where the screening current is lower and vice versa, these are the fundamental properties. In the four corner edges of the pyramid, the Cooper pairs are higher than those of the side region due to the strong superconducting region. In the L=2 state, the second vortex comes from the other side of the same axis of the sample, and the two vortexes take a straight position.

At the L=3 state, the third vortex enters from another axis and forms the triangular arrangement of the vortex. At the L=4 state, a square arrangement of the vortex is formed. At L=2, 4 states, there are symmetric arrangements of the vortex which gives the enhance stability range than the odd vortex states. In every vortex core, there is a whirl current in it. The screening current density on the edges of the sample is greater than the corners of the sample. This strong screening current presses the vortices to the center with increasing field.

Conclusions

The vorticity of a superconducting 3D nano-sized pyramidal sample is observed within the Ginzburg-Landau (GL) formalism. Stationary properties such as Cooper pairs density and screening current density of the sample are studied in detail. Free energy and magnetization are calculated based on the varied applied fields. The variation of the vorticity with the different coherence lengths (ξ) is investigated. No vortex is observed (L=0; here, L is vorticity) in the sample with 6ξ dimension, but in the sample with 12ξ, L_{max}= 7 is observed. Separated vortex (multi-vortex states) is clearly visible in the iso-surface plot obtained from the 3D data of $|\psi|^2$. Only a paramagnetic response is observed by analyzing the sample's magnetization.

Acknowledgement

Thanks to the Department of Physics, Jagannath University, for allowing us to conduct this research work.

Author's Contribution

Abul Hasnat Rubel: Planning the research work, writing – original draft, Corresponding author.

Sharmin Aktar: Running the code, data management, plotting graphs.

Declaration of conflicting interests

The authors have no conflicts to disclose.

References

Alegria LD, Bøttcher CG, Saydjari AK, Pierce AT, Lee SH, Harvey SP, Vool U and Yacoby A. High-energy quasiparticle injection into mesoscopic superconductors. *Nature Nanotechnology*. 2021; 16(4): 404-408.

Baelus BJ, Cabral LR and Peeters FM. Vortex shells in mesoscopic superconducting disks. *Phys. Rev. B*. 2004; 69(6): 064506.

Baelus BJ, Peeters FM and Schweigert VA. In superconducting disks and rings, there are Saddle-point states and energy barriers for vortex entrance and exit. *Phys. Rev. B*. 2001; 63(14): 144517.

Baelus BJ and Peeters FM. Dependence of the vortex configuration on the geometry of mesoscopic flat samples. *Phys. Rev. B*. 2002; 65(10): 104515.

Baelus BJ, Sun D and Peeters FM. Vortex structures in mesoscopic superconducting spheres. Condensed matter and materials physics. *Phys. Rev. B*. 2007; 75(17): 174523.

Bardeen J, Cooper LN and Schrieffer JR. Theory of superconductivity. *Phys. Rev.* 1957; 108(5): 1175.

Chibotaru LF, Ceulemans A, Bruyndoncx V and Moshchalkov VV. Vortex entry and nucleation of antivortices in a mesoscopic superconducting triangle. *Phys. Rev. Lett.* 2001; 86(7): 1323.

De Gennes PG. Superconductivity of metals and alloys. *CRC press*. 2018. p 292.

De Gennes PG. Vortex nucleation in type II superconductors. *Solid State Commun.* 1965; 3(6): 127-130.

Deo PS, Schweigert VA, Peeters FM and Geim AK. Magnetization of mesoscopic superconducting disks. *Phys. Rev. Lett.* 1997; 79(23): 4653.

Fink HJ and Presson AG. Stability limit of the superheated Meissner state due to three-dimensional fluctuations of the order parameter and vector potential. *Phys. Rev*. 1969; 182(2): 498.

Fomin VM, Misko VR, Devreese JT and Moshchalkov VV. Superconducting mesoscopic square loop. *Phys. Rev. B.* 1998; 58(17): 11703.

Ge JY, Gladilin VN, Van de Vondel J and Moshchalkov VV. Vortex matter and critical magnetic fields in mesoscopic superconducting strips. *Supercond. Sci. Technol*. 2023; 36(8): 085014.

Geim AK, Grigorieva IV, Dubonos SV, Lok JG, Maan JC, Filippov AE and Peeters FM. Phase transitions in individual sub-micrometre superconductors. *Nature.* 1997; 390(6657): 259-262.

Grigorieva IV, Escoffier W, Richardson J, Vinnikov LY, Dubonos S and Oboznov V. Direct observation of vortex shells and magic numbers in mesoscopic superconducting disks. *Phys. Rev. Lett.* 2006; 96(7): 077005.

Hasnat A. Vortex configurations of a nano-sized superconducting 3d pyramidal confinement. *J. Supercond. Nov. Magn*. 2020; 33(3): 575-582.

Kim S, Burkardt J, Gunzburger M, Peterson J and Hu CR. Effects of sample geometry on the dynamics and configurations of vortices in mesoscopic superconductors. *Phys. Rev. B.* 2007; 76(2): 024509.

Maxwell E. Isotope effect in the superconductivity of mercury. *Phys. Rev*. 1950; 78(4): 477.

Meissner W and Ochsenfeld R. A new effect upon the onset of superconductivity. *Nat. Sci*. 1933; 21: 787-788.

Mel'nikov AS, Nefedov IM, Ryzhov DA, Shereshevskii IA, Vinokur VM and Vysheslavtsev PP. Vortex states and magnetization curve of square mesoscopic superconductors. *Phys. Rev. B*. 2002; 65(14): 140503.

Misko VR, Fomin VM, Devreese JT and Moshchalkov VV. Stable vortex-antivortex molecules in mesoscopic superconducting triangles. *Phys. Rev. Lett*. 2003; 90(14): 147003.

Misko VR, Xu B and Peeters FM. Formation and size dependence of vortex shells in mesoscopic superconducting niobium disks. *Phys. Rev. B.* 2007; 76(2): 024516.

Schweigert VA, Peeters FM and Deo PS. Vortex phase diagram for mesoscopic superconducting disks. *Phys. Rev. Lett*. 1998; 81(13): 2783.

Taupin M, Khaymovich IM, Meschke M, Mel'nikov AS and Pekola JP. Tunable quasiparticle trapping in Meissner and vortex states of mesoscopic superconductors. *Nat. Commun*. 2016; 7(1): 10977.

Tinkham M. Introduction to superconductivity. *Courier Corporation*, 2004. p 454.

Wang JS and Wang SY. High-Temperature superconductive maglev vehicle. *Endless Quests*: *Theory, experiments and applications of frontiers of superconductivity*. 2019; pp 249-314.

Zhao HJ, Misko VR, Peeters FM, Dubonos S, Oboznov V and Grigorieva IV. Vortex configurations in mesoscopic superconducting triangles: Finite-size and shape effects. *Europhys. Lett*. 2008; 83(1): 17008.

Zharkov GF, Zharkov VG and Zvetkov AY. Self-consistent solutions of Ginzburg-Landau equations and superconducting edge-suppressed states in magnetic field. *Phys. Rev. B.* 2000; 61(18):12293.

J. Bangladesh Acad. Sci. 49(1); 45-55: June 2025 DOI:https://doi.org/10.3329/jbas.v49i1.75146

Journal of Bangladesh Academy of Sciences

Journal homepage: http://www.bas.org.bd/publications/jbas.html

Research Article

Impact of the tannery industrial zone on the physicochemical and microbiological quality of the Dhaleshwari river water, Bangladesh

Tasnum Rahman, Aporupa Abeazom Zom Urmi, Md. Mazharul Islam*
Md. Iqbal Rouf Mamun and Mohammad Shoeb
Department of Chemistry, University of Dhaka, Bangladesh

ARTICLE INFO

Article History

Received: 28 July 2024
Revised: 19 December 2024
Accepted: 15 January 2025

Keywords: Dhaleshwari River, Heavy metals, Metal ions, Microbial pollution, Physicochemical parameters.

ABSTRACT

The main aim of this study is to investigate the effect of tannery effluents on the Dhaleshwari River water near Savar, Dhaka. The physicochemical properties analyzed included pH, electrical conductivity (EC), dissolved oxygen (DO), total dissolved solids (TDS), total hardness (TH), chloride ion (Cl^-), sodium ion (Na^+), potassium ion (K^+), chromium (Cr), lead (Pb), and cadmium (Cd) to determine the current pollution status of the river. The pH was 5.50-7.64. The EC was 207.40-258.60 μScm^{-1}, indicating standard ionic species in the water. TDS levels were 149.00-177.00 mgL^{-1}. Na^+ and K^+, determined using a flame photometer, ranged from 28.49-34.48 mgL^{-1} and 2.92-3.94 mgL^{-1}, respectively. Cl^- content, measured by titrimetric method, ranged from 8.50-30.23 mgL^{-1}. Heavy metals were analyzed using an Atomic Absorption Spectrophotometer (AAS), revealing Pb levels below the detection limit (BDL) to 0.07 mgL^{-1} and Cr levels from BDL to 0.015 mgL^{-1}. At the same time, Cd was BDL in all samples. The microbial analysis detected only coliform bacteria, including E. coli and Salmonella sp. The study concludes that the Dhaleshwari River shows evidence of pollution from tannery effluents, particularly in heavy metals and microbial contamination, although some physicochemical properties remain within standard levels.

Introduction

Bangladesh is home to over 230 large and small rivers, crucial in domestic, industrial, agricultural, and aquaculture activities. However, water quality in these rivers is deteriorating due to untreated industrial effluents, municipal wastewater, runoff pollution from chemical fertilizers and pesticides, and oil spillage from sea and river port operations (Akter et al., 2019). The Bangladeshi economy heavily relies on industries, particularly the leather industry, which provides significant employment opportunities and economic growth. Unfortunately, these industries pose substantial environmental health risks due to the discharge of liquid effluents and solid waste in adjacent low-lying areas (Khan, 2014). Water consumption and the daily production rate of different industries can change effluents' amounts and features (Sarker et al., 2013). Compared to other sectors, leather tanning is one of the most polluting activities because of its high water consumption and production of hazardous liquid effluents. The productive cycle of the industry uses chromium (Cr), the most concerned discharged pollutant. These pollutants cause variations in pH and increase TDS (Dixit et al., 2015).

The leather industry in Bangladesh consists of almost 220 tanneries, 3,500 MSMEs, 2500 footwear companies, and more than 90 enterprises. Tanneries were mainly located in Narayanganj at the beginning of the tannery industry in Bangladesh. After that, the central location was Hazaribagh of Dhaka.

---

*Corresponding author:<mazharu1chdu@gmail.com>

Regrettably, the businesses are struggling; 105 out of 155 tanneries have been relocated to Savar Industrial Park. Before the relocation, the major pollution in the Buriganga River was caused by the untreated liquid from tanneries produced during the treatment of about 60,000 tons of raw hides and skins (Azom et al., 2012). The contamination of rivers also accumulated in common fish species used as local food sources. The tanneries have recently been around the Dhaleshwari River of the Savar district. In central Dhaka, the Dhaleshwari River is one of the primary distributaries in central Dhaka, stretching 160 kilometers in length with an average depth of 37 meters (Raknuzzaman et al., 2016; Ahsan, 2018). The river receives huge amounts of municipal waste, leather industry waste, and directly or indirectly treated sewage water (Mohanta et al., 2019). These pollutants make the aquatic environment unsuitable for living, especially since the water quality parameters are not up to the WHO standard for drinkable water. The contaminants in rivers can cause long and short-term diseases. The physiochemical quality has also deteriorated (Islam et al., 2021a). Physiochemical and microbiological parameters can give overall information on the current state of water of the Dhaleshwari River. Water can taste bitter or contain increased oxygen because of its high pH (Edzwald, 2010).

On the other hand, metals or other substances will be corroded or dissolved in low-pH water (APHA, 2005; Baird et al., 2017). EC is strongly related to water pollution. Pure water is a good conductor of electrical current, increasing with increasing ions (Meride and Ayenew, 2016).

A water source is good for aquatic life if its DO value is higher (Ali and Vijayan, 1986). Lower DO may cause stress and mass mortality in marine animals (Sajid et al., 2024). Higher BOD (Biological Oxygen Demand) of water reduced the DO (Verma and Singh, 2013). Again, low TDS levels in water are not beneficial for thirsty and malnourished people and accelerate kidney problems, heart disease, pregnancy complications, etc. (Peavy et al., 1985). EC is proportional to TDS (Das et al., 2006). Higher hardness refers to highly mineralized water (APHA, 2005). Calcium ion (Ca^{2+}) and Magnesium ion (Mg^{2+}) mainly cause hardness. Though sodium, potassium, and chloride ions are not harmful at normal levels, they cause concern in high concentrations and can cause diseases. High potassium levels in the body result in arrhythmias (Brown et al., 1984). Conversely, excess chlorine levels in rivers that may come from wastewater can cause toxicity symptoms like discoloration and broken vertebrae in fish (Ribeiro et al., 2015). The tannery wastewater can significantly contain chlorides, sulfates, sulfides, and other heavy metals. Excessive contamination of surface water by heavy metals is a global public health concern (Rashid et al., 2023). They can enter the food chain by unrestricted disposal of industrial waste. Lead (Pb) can cause anemia, disturbed reproduction, high blood pressure, and kidney ailments (Jakubowski, 2011). In contrast, a high chromium (Cr) level causes kidney damage, dermatitis, and respiratory problems (Beaumont et al., 2008). Total microbial count (*E. coli*, Total Coliform, Fecal Coliform, and *salmonella*) is another important parameter of water quality. Surface water is more susceptible to bacterial pollution than groundwater as the soil and water through which groundwater flows screen out most of the bacteria (Adesakin et al., 2022). The productive cycle of the industry uses chromium (Cr), the most concerned discharged pollutant (Oludairo and Aiyedun, 2016). Temperature, color, taste, and odor are essential water quality indicators.

As water is vital for our life and environment and because different physicochemical water quality parameters are changing, it is essential to supervise the conditions of rivers, especially those around different industries. The objective of this present work is the quantitative analysis of different physiochemical parameters like pH, EC, TDS, DO, total hardness including sodium, potassium, and chloride ions, and other heavy metal contents (Pb, Cr, and Cd) in the water of Dhaleshwari River. The microbial pollution status in the surface water of this river is another prominent target of this research.

Materials and Methods

Sample collection and pre-treatment

The Dhaleshwari River begins its route from the Jamuna River near the northwestern edge of the district and later merges with the Shitalakshya River in Dhaka-Narayanganj. The merged flow then proceeds southward to join the Meghna River (Islam et al., 2021b). This study's samples were taken from designated locations where the river traverses the industrialized Savar District. The experimental site is situated within the tannery estate in Savar, adjacent to the Dhaleshwari River (Table 1). Exactly 24 surface water samples were collected from the river in Hemayetpur near the tanneries and around 2 km away from the tannery dumping area, and each sample was collected at around 100 m apart. All the samples were collected in HDPE plastic bottles, labeled accordingly, and transported to the laboratory of the Department of Chemistry, University of Dhaka. The samples were kept at –20°C and taken to room temperature before the experiment.

Experimental procedure

A 100 mL beaker filled up to two-thirds with the sample to measure pH. The glass electrode of the pH meter was washed with distilled water and cleaned softly with tissue. Then, it was placed in sample water. The pH value displayed on the screen was recorded. Conductivity was measured using a conductivity meter following the same procedure as pH. A 50.0 mL water sample was taken in a titration flask to determine Chloride Content. 4-7 drops of mixed indicator (Diphenyl carbazone + Bromophenol Blue) were added. The color of the sample became violet, which disappeared by adding 0.2M HNO_3. The color became yellow. After adding 4-5 drops more 0.2M HNO_3, titration was completed using 0.1M $Hg(NO_3)_2$. The volume of the titrant was recorded. Concentration was determined using the given equation: 1 mL of 0.1 M Hg^{2+} = 0.2 mmol Cl^- = 7.10 mg Cl.

For the determination of DO, a bottle was filled with sample water at 6.0 mL, which was less than its volume. 2.0 mL of $MnSO_4$ solution and 2.0 mL of alkali-iodide-azide reagent, which goes well below the surface of the liquid, were added. It was mixed by inverting the bottle several times at 2.0 mL of conc. H_2SO_4 was added.

Table 1. Site description of the sampling area of Dhaleshwari River, Bangladesh.

Sample	Latitude	Longitude
S-1	23.78063 ‘N	90.41932’E
S-2	23.78111’N	90.24043’E
S-3	23.78050’N	90.24024’E
S-4	23.77972’N	90.23995’E
S-5	23.77873’N	90.23975’E
S-6	23.77800’N	90.23951’E
S-7	23.77720’N	90.23918’E
S-8	23.77635’N	90.23890’E
S-9	23.77486’N	90.23965’E
S-10	23.77439’N	90.24110’E
S-11	23.74421’N	90.23790’E
S-12	23.74412’N	90.23800’E
S-13	23.76502’N	90.95906’E
S-14	23.76502’N	90.23937’E
S-15	23.76417’N	90.23977’E
S-16	23.75508’N	90.24806’E
S-17	23.76116’N	90.24084’E
S-18	23.7602’N	90.24087’E
S-19	23.7586’N	90.24168’E
S-20	23.75736’N	90.24240’E
S-21	23.75589’N	90.24428’E
S-22	23.75538’N	90.24555’E
S-23	23.75349’N	90.24772’E
S-24	23.75508’N	90.24806’E

After 10 minutes, the content of the bottle was transferred into a conical flask. Released iodine was titrated with 0.025 M $Na_2S_2O_3$ using the starch indicator. DO was determined using the given equation 1mL 0.0125M $Na_2S_2O_3$ = 0.1 mg DO

$$\text{DO (mgL}^{-1}) = \frac{\text{mL of titrant} \times 1000 \times 0.1}{\text{Volume of D.O. bottle (mL)}}$$

For the determination of TH, dilute HCl was used to acidify 50.0 mL of sample water and heated for about 1 minute to drive off CO_2. It was cooled and neutralized with Sodium Hydroxide. 1 mL of buffer ammonium buffer solution and 3-4 drops of Erichrome Black T indicator were added. Titration was completed using 0.01M EDTA solution. Hardness was determined using the given equation; 1mL of 0.01M EDTA = 1. 000 mg. $CaCO_3$

A flame photometer was employed to determine the Na^+ and K^+. The flame photometer underwent calibration using standard sodium (Na^+) stock solutions at concentrations of 10, 20, 30, 40, and 50 ppm. Potassium (K^+) calibration utilized standard 1, 2, 3, 4, and 5 ppm solutions. Additional instrumental parameters were adjusted to optimize the flame. Following calibration, water samples were examined by transferring 50 mL from each collected sample into standard laboratory plastic bottles, and readings from the flame photometer were recorded. Concentration was determined using calibration curves.

To determine the bacterial load, samples were initially diluted up to 10^{-2} and cultured by following a technique called pour plate technique. Specifically, 1 mL of each sample was mixed with 9 mL of distilled water to achieve a 1:10 dilution (10^{-1}). Using sterile pipettes, 1 mL from the 10^{-1} dilution was taken to another vial having 9 mL of distilled water, resulting in a 1:100 dilution (10^{-2}). Subsequently, 1.0 mL of each dilution was plated using a sterile pipette covered with a petri dish. Sterile melted media specific to Eosin Methyl Blue Agar (EMB) was poured onto the plates, which were then rotated to ensure the media was even spread. Bacterial colonies grown on the EMB plates were further cultured in LB broth containing yeast extract 0.5%, NaCl 1%, and tryptone 1% at 44.5°C under a laminar flow hood. Colonies were subsequently subcultured on MacConkey agar plates. The colony numbers were counted using a colony counter, and the total plate count was performed by multiplying the colony count by the dilution factor. The mean value of the total plate count for each dilution represented the total bacterial count.

Additionally, water samples were examined for total coliform count using the Most Probable Number (MPN) method and screened for the presence of *E. coli*. The sample incubation was done in LB broth at 44.5°C for enrichment and observed after overnight incubation. Confirmation of the presence of E. coli, a fecal indicator, was based on gas production and color changes in the media. EMB agar was employed as a selective medium for detecting E. coli colonies.

Initially, standard solutions for all the heavy metals being studied were prepared at various concentrations, ranging from three to five, by diluting a stock standard solution with a concentration of 1000 ppm. Water samples under study were filtered first using Whattman Fitter paper no. 42. Cr, Cd, and Pb concentrations were measured using AAS. Standard operation parameters were set. The hollow cathode lamp for Cr, Cd, and Pb was used as a radiation source, and air acetylene was used as fuel.

Results and Discussion

pH of the twenty-four sample waters is given in Fig. 1. The highest frequency value was pH 7.64, followed by pH 7.62 and pH 7.60. pH values are between 5.50-7.64, indicating that some samples are slightly acidic and some are somewhat basic. Twelve of the samples are slightly below the recommended level. In contrast, other samples are within the standard level (Fig. 1). Low pH may be due to industrial pollution, chemical dumps, power plants, etc. This will lead to a bad impact on aquatic organisms (Norton et al., 2008). Sample S-19 has the lowest pH, and S-1 has the highest pH. A previous study of the Dhaleshwari River showed that pH was between 7.68-8.03. pH was basic, which differed from our study (Islam et al., 2021a). The electrical conductivity implies overall ionic species in water (Nancarrow et al., 2021). Higher EC indicates higher ions and moderate EC indicates a good number of ions in water (Uddin et al., 2014). The specific conductance of most natural water ranges from 50-1500 µScm^{-1}. From Fig. 1, the EC of sample waters ranges from 207.4-258.6 µScm^{-1}, which is lying within the standard level of EC (Islam et al., 2021a). Most of the samples are within the range of 230-250 µScm^{-1}. Previous studies showed that EC was in the range of 140-395 µScm^{-1} (Rikta et al., 2016), which agrees with this study. Oxygen is the single most important gas for most aquatic organisms. Fishes will have no support if the DO level is less than 1 mgL^{-1}. For the fish population 5.0-8.5 mgL^{-1} DO is

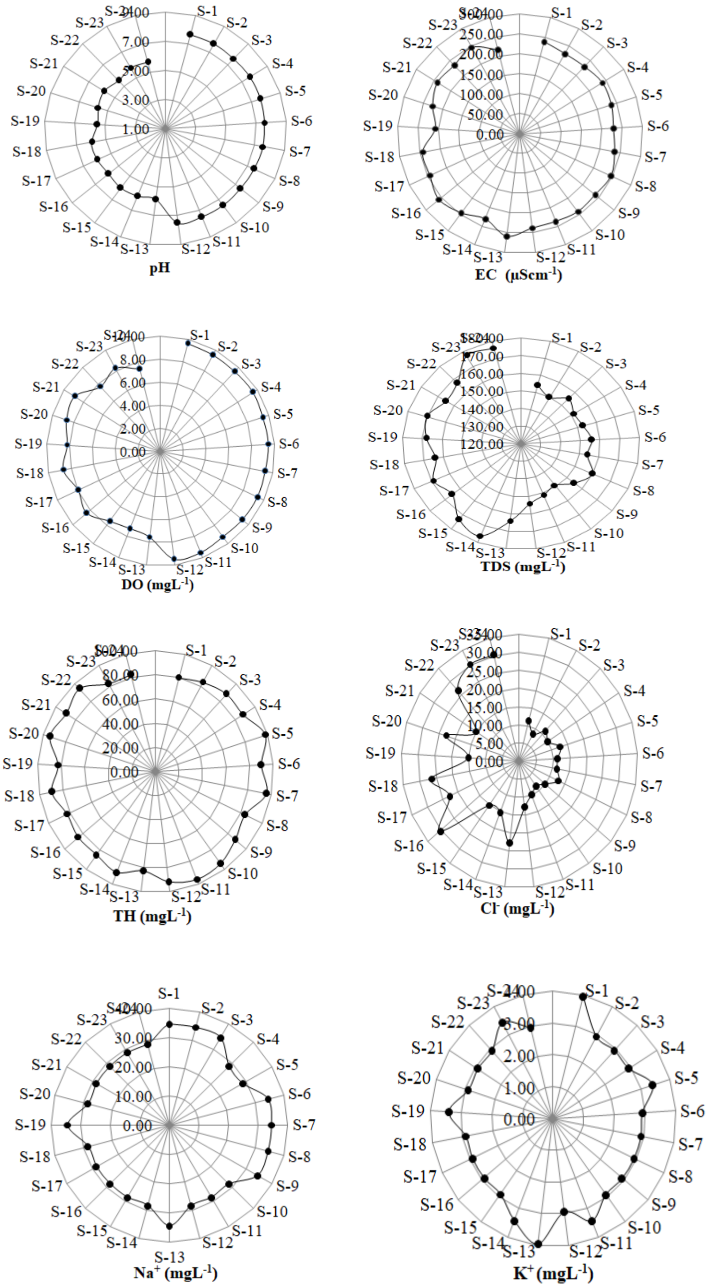

Fig. 1. Spatial variation of water quality parameters of Dhaleshwari River water.

required (Ali et al., 2022). Fig. 1 shows DO value of collected samples where DO is between 7.24-9.67 mgL^{-1}. This indicates that DO is within and, for some samples, is slightly higher than the permissible limit. Sample S-1 has the highest DO, and sample S-14 has the lowest DO. A previous report shows that DO has increased as their result indicated an average DO of 5.0 mgL^{-1} (Rikta et al., 2016). In natural water, dissolved solids primarily consist of Na^+, K^+, Ca^{2+}, Mg^{2+}, and ions such as Cl^-, SO_4^{2-}, PO_4^{3-}, $H_4SiO_4^{2-}$, and HCO_3^-. High levels of dissolved substances make water unsuitable for general use (Afrad et al., 2020). TDS in sample waters is decreasing in the series S-23> S-14 = S-24 > S-15 > S-20 > S-17 > S-19 > S-22 > S-21 = S-16 >S-13= S-18 > S-8 > S-6 > S-3 = S-9 >S-01 = S-12 = S-07 > S-05 > S-04 >S-11 > S-02 > S-10. It varies from 149 to 177 mgL^{-1} (Fig. 1). It is within the standard value. TDS value changed a lot from 2016 as it was between 634-1265 mgL^{-1} before (Rikta et al., 2016). The overall condition, given TDS, has improved. Hardness measures the concentration of dissolved calcium and magnesium in water. The ideal drinking water for most consumers typically contains approximately 10.00-100.00 mgL^{-1} of TH as $CaCO_3$ (Islam et al., 2016). The hardness of water samples is 80.00-94.08 mgL^{-1}. In this study, all the values fall within the accepted limits as per the WHO standards (Prosun et al., 2018). The water samples are moderately hard (Fig. 1). Chloride indicates salinity in water. Na content can also be high if the amount of chloride in water is high. Cl^- is primarily a stable parameter and can indicate pollution in natural freshwater environments (Dugan et al., 2017). The chloride concentration in the study is given in Fig. 1. Chloride content of samples ranges from 8.50-30.23 mgL^{-1}. The comparison between the average and standard values of chloride indicates slight deviations, both higher and lower. It may refer to a little impurity in river water. S-16, S-23, and S-24 have the highest Chloride, and S-2 and S-10 have the lowest Chloride content. Na^+ content was 28.49 mgL^{-1} and 34.48 mgL^{-1}. Fifteen of the samples have the same Na^+ content. The other nine samples have equal content. K^+ content in water is in the range 2.92-3.94 mgL^{-1}. Fig. 1 shows that eight of the samples (S-15, S-16, S-17, S-18, S-20, S-21, S-22 and S-24) have same K^+ content (2.92 mgL^{-1}). S-5, S-11, S-14, S-19 and S-23 have same K^+ content (3.43 mgL^{-1}). Again S-1 and S-13 have equal K^+ content (3.94 mgL^{-1}).

The findings show that the Na^+ and K^+ content in all water samples are within the allowable limits set by the World Health Organization (Banerjee and Prasad, 2020). The amount of Na^+ and K^+ are found in the order $Na^+ > K^+$ ion. The analysis of Dhaleshwari River water indicates significant variability in water quality parameters. The pH values range from 5.50 to 7.64, with an average of 6.68, which is within the acceptable guideline of 6.50-8.50, indicating relatively neutral water. EC ranges from 207.40 to 258.60 μScm^{-1}, averaging 236.43 μScm^{-1}, well below the 700 μScm^{-1} guidelines, reflecting low salinity. DO levels, crucial for aquatic life, range from 7.24 to 9.67 mgL^{-1}, with an average of 8.75 mgL^{-1}, exceeding the minimum guideline of 6.00 mgL^{-1}, indicating good water quality. TDS and TH are also well within permissible limits, indicating low mineral content. Chloride (Cl^-), sodium (Na^+), and potassium (K^+) levels are significantly lower than their respective guidelines, highlighting minimal pollution from industrial and domestic effluents (Table 2). These results collectively suggest that the Dhaleshwari River maintains a generally healthy water quality standard despite the industrial activities in the Savar District.

The Pearson correlation analysis (Table 3) of Dhaleshwari River water quality parameters reveals several significant relationships. The pH strongly correlates with dissolved oxygen (DO) ($r = 0.866$), indicating that higher pH levels are associated with higher DO concentrations. A strong negative correlation exists between pH and total dissolved solids (TDS) ($r = -0.890$), suggesting that increased TDS levels correspond to lower pH values. The chloride (Cl^-) concentration negatively correlates with pH (r = -0.808) and DO (r = -0.689), implying that higher Cl^- levels reduce both pH and DO. Sodium (Na^+) has a moderate positive correlation with pH (r = 0.415) and DO (r = 0.348), while showing a negative relationship with Cl^- (r = -0.431). Total hardness (TH) shows a weak positive correlation with pH (r = 0.268) and DO (r = 0.305) but a weak negative correlation with TDS (r = -0.372). Potassium (K^+) does not show strong correlations with other parameters, indicating minimal influence on overall water chemistry.

Table 2. Statistical parameters with standard guideline values of water quality parameters.

Parameters	**pH**	**EC (μScm^{-1})**	**DO (mgL^{-1})**	**TDS (mgL^{-1})**	**TH (mgL^{-1})**	**Cl^- (mgL^{-1})**	**Na^+ (mgL^{-1})**	**K^+ (mgL^{-1})**
Minimum	5.50	207.40	7.24	149.00	80.00	8.50	28.49	2.92
Maximum	7.64	258.60	9.67	177.00	98.00	30.23	34.48	3.94
Average	6.68	236.43	8.75	161.54	88.32	16.77	30.74	3.12
±SD	0.90	11.21	0.83	9.04	5.14	7.49	2.96	0.33
Guideline value	6.50-8.50	700	6.00	1000	500	150-600	200	12
References	(DPHE, DoE, Bangladesh standard) Yr.						WHO, 2003	EC (European,1986 Community), 1986

Table 3. Pearson correlation analysis of Dhaleshwari River water quality parameters.

	pH	**EC**	**DO**	**TDS**	**TH**	**Cl^-**	**Na^+**	**K^+**
pH	1.000							
EC	0.016	1.000						
DO	0.866	-0.028	1.000					
TDS	-0.890	-0.052	-0.880	1.000				
TH	0.268	-0.124	0.305	-0.372	1.000			
Cl^-	-0.808	0.208	-0.689	0.755	-0.273	1.000		
Na^+	0.415	-0.144	0.348	-0.370	-0.326	-0.431	1.000	
K^+	-0.040	0.112	-0.131	0.043	-0.258	-0.007	0.230	1.000

The microbial qualities of the collected water at the consumer level were examined. Total Coliform Count (TCC), Fecal Coliform Count (FCC), and *E.coli* were examined quantitatively whereas *Salmonella sp.* was examined qualitatively. Total Coliform and Fecal Coliform are indications of pathogenic organisms (Korajkic et al., 2018). In the examined water samples, the TCC value ranges from 0 to 1.5×10^2 CFUml^{-1} in the original concentration and from 0 to 3×10^2 in 10^{-1} dilution (Table 4). Values were excessively above the WHO guideline. So, TCC values are above the permissible limit (0.0 CFUml^{-1}) according to Bangladeshi standards for drinking water.

The samples are not suitable for drinking purposes (Voulvoulis, 2018). But they can be used for household work. All the samples were free from Fecal Coliform and *Salmonella sp.*, and according to BD standards and WHO standards are acceptable for drinking. All the sample waters were acceptable for regular use.

Table 4. Microbial parameters and heavy metals content in different water samples.

Sample ID	Total Coliform Count CFUml^{-1}			Fecal Coliform Count CFUml^{-1}	*Salmonella sp.* CFUml^{-1}	Heavy Metals (mgL^{-1})		
	Original	10^{-1} dilution	10^{-2} dilution			Cd	Pb	Cr
S-1	Absent	Absent	Absent	Absent	Absent	BDL	0.05	BDL
S-2	Absent	Absent	Absent	Absent	Absent	BDL	0.04	0.007
S-3	Absent	Absent	Absent	Absent	Absent	BDL	0.05	0.012
S-4	Absent	Absent	Absent	Absent	Absent	BDL	0.06	0.015
S-5	Absent	Absent	Absent	Absent	Absent	BDL	0.05	BDL
S-6	Absent	Absent	Absent	Absent	Absent	BDL	0.07	0.012
S-7	Absent	Absent	Absent	Absent	Absent	BDL	0.07	0.008
S-8	Absent	Absent	Absent	Absent	Absent	BDL	0.04	0.012
S-9	Absent	Absent	Absent	Absent	Absent	BDL	0.05	BDL
S-10	Absent	Absent	Absent	Absent	Absent	BDL	0.03	0.01
S-11	Absent	Absent	Absent	Absent	Absent	BDL	0.04	0.008
S-12	Absent	Absent	Absent	Absent	Absent	BDL	0.05	BDL
S-13	2.7×10^{1}	1.5×10^{2}	Absent	Absent	Absent	BDL	0.06	0.012
S-14	Absent	Absent	Absent	Absent	Absent	BDL	0.04	0.004
S-15	4×10^{1}	1×10^{2}	Absent	Absent	Absent	BDL	0.06	0.014
S-16	3.5×10^{1}	Absent	Absent	Absent	Absent	BDL	0.05	0.003
S-17	1.5×10^{2}	3×10^{1}	Absent	Absent	Absent	BDL	0.04	BDL
S-18	3×10^{1}	1×10^{2}	Absent	Absent	Absent	BDL	BDL	0.008
S-19	Absent	Absent	Absent	Absent	Absent	BDL	BDL	0.009
S-20	1.5×10^{2}	3×10^{2}	Absent	Absent	Absent	BDL	BDL	0.004
S-21	Absent	Absent	Absent	Absent	Absent	BDL	0.02	0.009
S-22	Absent	Absent	Absent	Absent	Absent	BDL	BDL	0.014
S-23	8.5×10^{1}	3×10^{2}	Absent	Absent	Absent	BDL	BDL	0.01
S-24	3.5×10^{1}	2×10^{2}	Absent	Absent	Absent	BDL	BDL	BDL

The collected water samples were analyzed for Cr, Pb, and Cd. The Cd content was below the detection limit for all the samples. The range for Pb was below the detection limit of 0.07 mgL^{-1}. The range for Cr was below the detection limit of 0.015 mgL^{-1} (Table 4). According to the Maximum Contamination Limit (MCL) standard, Cadmium concentration should not exceed 0.005 mgL^{-1}, Lead should not exceed 0.015 mgL^{-1} and for Chromium 0.1 mgL^{-1}.

All the measured values are within permissible limits, which will show no adverse impact on the Dhaleshwari River water system. The exceptionally low concentration could be attributed to the river water's continuous flow, resulting in a high dilution factor.

Conclusion

The degradation of water quality in Bangladesh's rivers, particularly the Dhaleshwari River, underscores the pressing need for rigorous environmental monitoring and management. Despite their critical role in the nation's economic activities, industries, especially the leather sector, have significantly contributed to pollution through untreated effluents. This has led to detrimental impacts on the aquatic ecosystem and human health. The study reveals that while parameters such as pH, EC, DO, TDS, and TH are within acceptable limits, heavy metals and microbial contamination pose serious concerns. Effective regulatory measures, advanced waste treatment technologies, and strict enforcement of environmental standards are essential to mitigate these issues. Sustainable industrial practices and continuous monitoring are crucial to preserving the health of the Dhaleshwari River and ensuring the well-being of communities relying on its resources.

Acknowledgment

The authors are grateful to the International Science Programme (ISP), Uppsala University, Sweden.

Author Contributions

Tasnum Rahman: Formal analysis, visualization, writing– review & editing; Aporupa Abeazom Zom Urmi: Formal analysis, visualization, writing– review & editing; Md. Mazharul Islam: Conceptualization, data curation, investigation, methodology, software, supervision, visualization and writing-original draft; Md. Iqbal Rouf Mamun: Supervision, data curation, funding acquisition, project administration, resources, writing – review & editing; and Mohammad Shoeb: Data curation, funding acquisition, project administration, resources, writing – review & editing.

Declaration of conflicting interests

The authors declare that they have no financial and any other competing interest.

References

Adesakin TA, Oyewale AT, Mohammed NA, Bayero U, Adedeji AA, Aduwo IA, Bolade AC, and Adam M. Effects of prolonged storage condition on the physicochemical and microbiological quality of sachet water and its health implications: A Case study of selected water brands sold within samara community, Northwest Nigeria. *Microb. Res.* 2022; 13(4): 706-720.

Afrad MSI, Monir MB, Haque ME, Barau AA and Haque MM. Impact of industrial effluent on water, soil and Rice production in Bangladesh: a case of Turag River Bank. *J. Environ. Health Sci. Eng.* 2020; 18(2): 825-834.

Ahsan MA. Analysis of physicochemical parameters, anions and major heavy metals of the Dhaleshwari river water, Tangail, Bangladesh. *Am. J. Environ. Prot.* 2018; **7**(2): 29-39.

Akter S, Kamrujjaman K and Rashed-Ul-Islam R. An investigation into chemical parameters of water of Dhaleswari **-** A river alongside tannery village of Bangladesh. *Int. J. Sci.* 2019; 8(5): 159-164.

Ali B, Anushka and Mishra A. Effects of dissolved oxygen concentration on freshwater fish: A review. *Int. J. Fish. Aqua. Stud.* 2022; 10(4): 113-127.

Ali S and Vijayan VS. *Keoladeo National Park : ecology study*. Summary report 1980-1985. India, Bombay Natural History Society. 1986.

APHA, Standard Methods for the Examination of Water and Wastewater. 21th ed., *American Public Health Association.* Washington, DC. 2005; 21: pp.1288.

Azom MR, Mahmud K, Yahya SM, Sontu A and Himon SB. Environmental impact assessment of tanneries: A case study of Hazaribag in Bangladesh. *Int. J. Environ. Sci. Develop.* 2012; 3(2): 152-156.

Baird RB, Rice EW and Eaton AD. *Standard Methods for the Examination of Water and Wastewater*. 23rd Edition, American Public

Health Association, American Water Works Association, Water Environment Federation, Washington *D.C.* 2017.

Banerjee P and Prasad B. Determination of concentration of total sodium and potassium in surface and ground water using a flame photometer. *App. Water Sci.* 2020; 10(5): 113.

Beaumont JJ, Sedman RM, Reynolds SD, Sherman CD, Li L, Howd RA, Sandy MS, Zeise L and Alexeeff GV. Cancer mortality in a Chinese population exposed to hexavalent chromium in drinking water. *Epidemiol.* 2008; 19(1): 12-23.

Brown HS, Bishop DR and Rowan CA. The role of skin absorption as a route of exposure for volatile organic compounds (VOCs) in drinking water. *Am. J. Pub. Health.* 1984; 74(5): 479-484.

Das R, Samal NR, Roy PK and Mitra D. Role of electrical conductivity as an indicator of pollution in shallow lakes. *Asian J. Water, Environ. Pollut.* 2006; 3(1): 143-146.

Dixit S, Yadav A, Dwivedi PD and Das M. Toxic hazards of leather industry and technologies to combat threat: a review. *J. Clean. Product.* 2015; 87: 39-49.

DoE (Department of Environment). Bangladesh standard, *Government of the People's Republic of Bangladesh*.

DPHE, (Department of Public Health Engineering), *Bangladesh standard, Government of the People's Republic of Bangladesh.*

Dugan HA, Summers JC, Skaff NK, Krivak-Tetley FE, Doubek JP, Burke SM, Bartlett SL, Arvola L, Jarjanazi H, Korponai J, Kleeberg A, Monet G, Monteith D, Moore K, Rogora M, Hanson PC and Weathers KC. Long-term chloride concentrations in North American and European freshwater lakes. *Sci. Data.* 2017; 4: 170101.

EC (European Community). *Guidelines for Drinking Water Quality.* 1986.

Edzwald JK. *Water Quality and Treatment: A Handbook on Drinking Water*. 6th ed. McGraw Hill Professional. 2010. p. 1696.

Islam MAS, Hossain ME and Majed N. Assessment of physicochemical properties and comparative pollution status of the Dhaleshwari River in Bangladesh. *Earth.* 2021a; 2(4): 696-714.

Islam MM, Bhuiyan MHSS, Islam R, Shoeb M, Mamun MIR and Rahman MH. Physicochemical properties and metal ions in water and sediment of the Dhaleshwari River. *Dhaka Univ. J. Sci.* 2021b; 69(1): 37-42.

Islam MR, Sarkar MKIslam, Afrin T, Rahman SS, Talukder RI, Howlader BK and Khaleque M A. A study on the TDS level of drinking mineral water in Bangladesh. *Am. J. App. Chem.* 2016; 4(5): 164-169.

Jakubowski M. Low-level environmental lead exposure and intellectual impairment in children-The current concepts of risk assessment. *Int. J. Occup. Med. Environ. Health.* 2011; 24(1): 1-7.

Khan W. Leather industry in Bangladesh: opportunities and challenges. *Am. J. Trad. Pol.* 2014; 1(3): 119-126.

Korajkic A, McMinn BR and Harwood VJ. Relationships between microbial indicators and pathogens in recreational water settings. *Int. J. Environ. Res. Publ. Health.* 2018; 15(12): 2842.

Meride Y and Ayenew B. Drinking water quality assessment and its effects on residents health in Wondo genet campus, Ethiopia. *Environ. Syst. Res.* 2016; 5(1): 1-7.

Mohanta LC, Niloy MNH, Chowdhury GW, Islam D and Lipy EP. Heavy metals in water, sediment and three fish species of Dhaleshwari river, Savar. *Bangladesh J. Zool.* 2019; 47(2): 263-272.

Nancarrow P, Al-Othman A, Mital DK and Döpking S. Comprehensive analysis and correlation of ionic liquid conductivity data for energy applications. *Energy,* 2021; 220(3): 119761.

Norton SB, Cormier SM, Suter GW, Schofield K, Yuan L, Shaw-Allen P and Ziegler CR. *CADDIS: The Causal Analysis/Diagnosis Decision Information System.* Springer eBooks. 2008. pp. 1-24.

Oludairo O and Aiyedun J. Contamination of commercially packaged sachet water and the public health implications: an overview. *Bangladesh J. Vet. Med.* 2016 13(2): 73-81.

Peavy HS, Rowe DR and Tchobanoglous G. *Environmental Engineering.* McGraw Hill Inc., New York. 1985.

Prosun TA, Rahman MS, Rikta SY and Rahman MA. Drinking water quality assessment from ground water sources in Noakhali, *Bangladesh. Int. J. Sustain. Dev.* 2018; **7**(5): 1676-1687.

Raknuzzaman M, Ahmed MK, Islam MS, Habibullah-Al-Mamun M, Tokumura M, Sekine M and Masunaga S. Trace metal contamination in commercial fish and crustaceans collected from coastal area of Bangladesh and health risk assessment. *Environ. Sci. Pollut. Res. Int.* 2016; 23(17): 17298-17310.

Rashid A, Schutte BJ, Ulery A, Deyholos MK, Sanogo S, Lehnhoff EA and Beck L. Heavy metal contamination in agricultural soil: Environmental pollutants affecting crop health. *Agronom.* 2023; 13(6): 1521.

Ribeiro AR, Nunes OC, Pereira MF and Silva AM. An overview on the advanced oxidation processes applied for the treatment of water pollutants defined in the recently launched directive 2013/39/EU. *Environ. Int.* 2015; 75: 33-51.

Rikta SY, Rahaman MS, Mehjabin JJ, Uddin MK, Kabir MM and Tareq SM. Evalution of water quality parameters and humic substance status of Bangshi, Dhaleshwaeri and Padma river in Bangladesh. *Int. J. Environ. Sci.* 2016; 6(6): 1129-1139.

Sajid Z, Gamperl AK, Parrish CC, Colombo SM, Santander J, Mather C, Neis B, Holmen IM, Filgueira R, McKenzie CH, Cavalli LS, Jeebhay M, Gao W, Gómez MAL, Ochs C, Lehnert S, Couturier C, Knott C, Romero JF., Caballero-Solares A, Cembella A, Murray HM, Fleming IA, Finnis J, Fast MD, Wells M and Singh, GG. An aquaculture risk model to understand the causes and consequences of Atlantic Salmon mass mortality events: A review. *Revi. Aqua.* 2024; 16(4):1674-1695.

Sarker BC, Basak B and Islam MS. Chromium effects of tannery waste water and appraisal of toxicity strength reduction and alternative treatment. *Int. J. Agron. Agric.* 2013; 3(11): 23-35.

Uddin MN, Alam MS, Mobin MN and Miah MA. An assessment of the river water quality parameters: A case of Jamuna river. *J. Environ. Sci. Nat. Resour.* 2014; **7**(1): 249-256.

Verma N and Singh AK. Development of biological oxygen demand biosensor for monitoring the fermentation industry effluent. *ISRN Biotech.* 2013; 2013: 6.

Voulvoulis N. Water reuse from a circular economy perspective and potential risks from an unregulated approach. *Curr. Opin. Environ. Sci. Health.* 2018; 2: 32-45.

WHO, *Sodium in Drinking Water*. Background document for preparation of WHO Guidelines for Drinking Water Quality. Geneva, World Health Organization (WHO/SDE/WSH/03.04/15). 2003.

J. Bangladesh Acad. Sci. 49(1); 57-72: June 2025 DOI:https://doi.org/10.3329/jbas.v49i1.71914

Journal of Bangladesh Academy of Sciences

Journal homepage: http://www.bas.org.bd/publications/jbas.html

Research Article

An in silico approach for the identification of detrimental missense SNPs and their potential impacts on human CRY2 protein

Auroni Semonti Khan, Mahmuda Akter, Mansura Akter Enni and Sumaiya Farah Khan*

Department of Genetic Engineering and Biotechnology, Jagannath University, Bangladesh

ARTICLE INFO

Article History

Received: 18 March 2024
Revised: 17 November 2024
Accepted: 15 January 2025

Keywords: Cryptochrome 2, Circadian clock, FBXL3, Missense SNPs, PER2, MD simulation.

ABSTRACT

Cryptochrome 2 (CRY2) is one of the four proteins of the cell-autonomous molecular clock in mammals. Non-synonymous SNPs of the cry2 gene, resulting in missense variants of CRY2, were correlated with metabolic disorders, cancers, and autism spectrum disorders. This in silico analysis aimed to investigate these missense SNPs having deleterious structural and functional impacts on the human CRY2 protein. Multiple computational tools, homology modeling, and molecular dynamic simulation reported an impact on protein structural stability, function, and binding with PER2 and FBXL3. Our results suggest that missense variants of hCRY2 with L74P, L274P, L309P, F315V, and Y485H mutations were the most destabilizing. These were found to have an overall altered structure, especially in the FAD binding pocket, which in turn can impact the binding of CRY activating compounds, regulatory proteins FBXL3 and PER2. These five missense variants warrant detailed in vitro and in vivo investigations to solidify our findings.

Introduction

The circadian rhythm, or in other words, our internal body clock, keeps our body and its processes with changes in time as well as various environmental stimuli. Cryptochromes (CRYs) are transcriptional repressors constituting the cell-autonomous molecular clock of mammals. These 'peripheral' clocks generate the circadian rhythms in cells through two interlocked transcription-translation feedback loops (TTFL) (Buhr and Takahashi, 2013; Mohawk et al., 2012; Takahashi, 2016), whereas the Suprachiasmatic Nucleus (SCN) in the anterior hypothalamus mediates the circadian rhythm on a macro scale. In the TTFL, the circadian locomotor output cycles kaput (CLOCK), aryl hydrocarbon receptor nuclear translocator-like protein 1 (ARNTL-1) or referred to as BMAL1, form a heterodimer to bind E-box on DNA (CACGTG) causing transcription of PERs and CRYs among other clock-controlled genes (CCGs) in the morning (Gekakis et al., 1998; Hogenesch et al., 1998; King et al., 1997). The proteins PERIODs (PER)s and CRYs then constitute a trimeric complex with casein kinase Iε/δ (CKI) in the cytoplasm to translocate into the nucleus in the late afternoon or evening. The transcription of CCGs is inhibited by the interaction of this trimeric complex and BMAL1/CLOCK (Vielhaber et al., 2001). Polyubiquitination and subsequent CRY1, CRY2, PER1, and PER2 degradation occur by specific E3 ligase complexes (FBXL3 and β-TrCP). Eventually, their negative feedback repression is lifted as these proteins decrease, and CLOCK–BMAL1 transcription activity begins again, completing one cycle of the TTFL (Buhr and Takahashi, 2013).

CRYs (CRY1 and CRY2) are flavoproteins (Partch and Sancar, 2005; Reppert and Weaver, 2002). Mammalian cryptochromes, weighing 66.9kDa, are composed of a highly conserved photolyase-homology

---

*Corresponding author:<sumaiyafarah@yahoo.com>

region (PHR) and a unique Cryptochrome C-terminal (CCT) extension (CCE). This protein of 593 amino acids has a FAD-binding pocket in this PHR (Xing et al., 2013). Another secondary pocket is present, which helps CRYs bind to CLOCK: BMAL1 complex (Fribourgh et al., 2020; Rosensweig et al., 2018). CRY1 and CRY2 have similar functions but distinct roles, especially in determining the rhythm of the SCN biological clock and its heterogeneous circadian transcriptional outputs. Various enzymes regulate CRY2 activity, and it also undergoes PTM, including phosphorylation and ubiquitylation, which affects its stability (Reischl and Kramer, 2011; Stojkovic et al., 2014). CRY2 has been demonstrated to cause the degradation of c-MYC (Huber et al., 2016), TLK2 (Correia et al., 2019), E2F family members (Chan et al., 2020) by its interaction with SCFFBXL3 (SKP1-CUL1-F-box protein complex having the F-box protein FBXL3) which ubiquitinates these proteins. On the contrary, PER proteins protect CRY from degradation by FBXL3 (Xing et al., 2013). More importantly, PER2 is one of the most important binding partners of CRY2. Their binding mediates the TTFL in cellular circadian clocks, completing the negative phases of the loop. Interruption of circadian oscillations increases with the association of both Cry1 and Cry2 genes with several types of cancer. Genome sequences from the Cancer Genome Atlas for six global and eight subcontinental ancestries report that among other CCGs, CRY2 is resistant to mutation in healthy somatic tissues making its cancer-associated mutations functionally important (Chan et al., 2020). Multiple studies have revealed the involvement of single nucleotide polymorphisms (SNPs) in the human Cry2 gene (hCry2) with prostate and breast cancer (Zienolddiny et al., 2013) and Non-Hodgkin's lymphoma (Hoffman et al., 2009). Cry2 gene polymorphism has also been shown to be associated with bipolar disorder, depression (Lavebratt et al., 2010a), attention-deficit/hyperactivity disorder (ADHD) (Wang et al., 2020), and dysthymia (Kovanen et al., 2014). SNPs in hCry2 have also been associated with metabolic disorders such as diabetes, dyslipidemia (Dupuis et al., 2010; Kelly et al., 2012; Salazar et al., 2021), cardiovascular disorders (Škrlec et al., 2018), and the more obvious, sleep disorder (Hirano et al., 2016) as well as osteoporosis (Li et al., 2016), affective disorders (Kripke et al., 2009).

SNPs are single-base nucleotide substitutions that are prevalent in less than 99% of a population (Schork et al., 2000). Among various types, nonsynonymous SNPs (nsSNPs) result in missense mutations in the coding region, causing aberrations of protein structure, stability, and function as well as binding to respective partners in cellular context (Chasman and Adams, 2001; Kucukkal et al., 2015; Petukh et al., 2015). These nsSNPs and resulting missense proteins have been linked to hereditary diseases, metabolic disorders, and diseases related to circadian rhythms, as stated above. However, isolating the nsSNPs that contribute to diseases is highly challenging since it requires numerous experiments of thousands of SNPs in a potential candidate gene. In contrast, the use of bioinformatics to comprehend the potential impact of nsSNPs has been reported (Kumar and Purohit, 2012; Rajendran et al., 2018; Rajendran and Sethumadhavan, 2014). This study, therefore, aims to detect detrimental non-synonymous SNPs that have pathogenic effects on the hCRY2 protein among the copious number of missense variants. Several computational tools were utilized to investigate the impact of the nsSNPs on protein structure as well as its binding to other protein partners- FBXL3 and PER2. Apart from these calculative, descriptive, and inferential analyses, molecular dynamics (MD) simulation was applied to get insights into the impact of damaging variations in the native tertiary structure of the candidate protein.

Materials and Methods

Retrieving SNPs of human CRY2 protein (hCRY2)

Human CRY2 protein was looked up in dbSNP (Sherry et al., 2001). About 13088 SNPs information were available in the database, among which the 436 nonsynonymous SNPs were chosen and retrieved for this study. The amino acid sequence of hCRY2 was collected from the UniProt Knowledge Base (UniProtKB) (Accession Number: NP_066940.3). The following sections depict the series of analyses to conclude the missense variants of hCRY2, which are summarized in a flowchart (Fig.1).

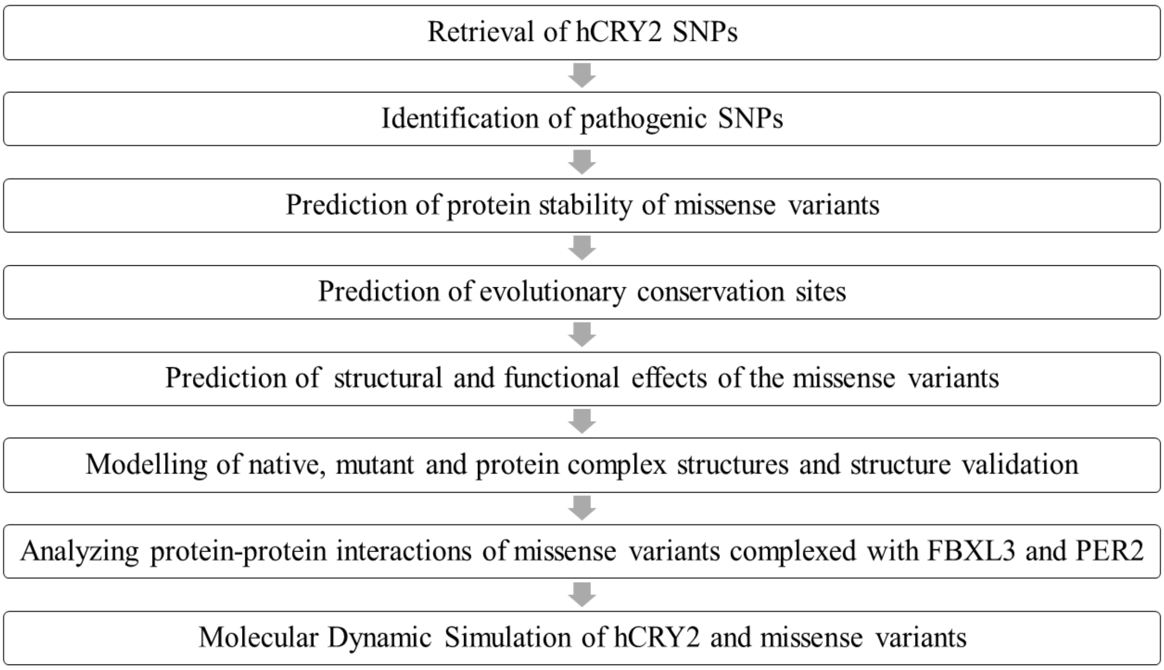

Fig. 1. Flowchart of the study design.

Identifying the most detrimental SNPs

Deleterious, pathogenic and disease-causing SNPs were predicted using Polyphen-2 (Adzhubei et al., 2013), SNAP2 (Hecht et al., 2015), PON-P2 (Niroula et al., 2015), Rhapsody (Ponzoni et al., 2020), PMut (López-Ferrando et al., 2017) and SNPs&GO (Calabrese et al., 2009). PolyPhen-2 (Polymorphism Phenotyping version 2) investigates the damaging missense variations to assess the structural and functional impacts of single amino acid substitution on human protein (Adzhubei et al., 2013). SNAP2 (Screening for non-acceptable polymorphisms) anticipates the functional effects of an amino acid alteration by using a neural network (Hecht et al., 2015). To assess the pathogenicity of the variants, PON-P2 was utilized to assort the variants into unknown, neutral, and pathogenic classes based on a random forest probability score (Niroula et al., 2015). Using machine learning, Rhapsody predicts the pathogenicity based on protein sequence, structure, and dynamics and classifies them into deleterious or neutral (Ponzoni et al., 2020). To address the association of SNPs with disease or not, PMut (Pathogenic Mutation prediction) exploits neural networks to predict evolutionary and structural properties (López-Ferrando et al., 2017). SNPs&GO is based on the support vector machines (SVM) method that predicts whether a given mutation can cause a disease or not, utilizing gene ontology (GO) annotation (Calabrese et al., 2009).

Predicting change in protein stability due to missense variants

MUpro (Cheng et al., 2006), mCSM (Pires et al., 2014), DeepDDG (Cao et al., 2019), INPS3D (Savojardo et al., 2016) and PremPS (Chan et al., 2020) were used to determine the effects of the variants on the stability of hCRY2 protein structure. MUpro utilizes sequence and structure information to assess the effect of point mutations (Cheng et al., 2006). mCSM considers the distance profiles between atoms to predict whether mutations destabilize the protein (Pires et al., 2014). Online tools, DeepDDG, INPS3D, and PremPS, were applied to estimate the impact of thermodynamic changes ($\Delta\Delta G$) on the stability of the protein induced by a missense mutation.

Analyzing evolutionary conservation sites in **hCRY2**

The ConSurf tool was used to analyze the evolutionary pattern of the protein's amino acids to find functional regions by studying the evolutionary dynamics of amino acid substitution. The conservation score is calculated from the Bayesian calculation method on a scale of 1 to 9; each amino acid is scored as variable, intermediate, and conserved, showing its degree of conservation (Ashkenazy et al., 2016).

Predicting structural and functional effects of the missense variants

The structural analyses web server Project HOPE (http://www.cmbi.ru.nl/hope/home) was used for this. Amino acid sequences of the native hCRY2 and those of the mutant variants were input in this server. The three-dimensional tertiary structures of the proteins deposited in the Distributed Annotation system (DAS) servers and Uniprot database are used by Project HOPE for evaluating the structural impacts of substitution mutations on the native protein (Venselaar et al., 2010).

Determination of native and mutant structures of **hCRY2** *and structure validation*

The native and mutant structures of the hCRY2 protein were generated by SWISS-MODEL (Waterhouse et al., 2018) through homology modeling using murine CRY2 (PDB ID: 4i6j.1.A) as a template. SWISS-MODEL is a web-based server that relies on template-based modeling to generate protein structures as well as homomeric and heteromeric complexes. The structures were validated using the ERRAT (Colovos and Yeates, 1993) and PROCHECK (Laskowski et al., 1996) tools in the SAVES 6.0 server.

Analyzing impacts on protein-protein interactions in missense variants

The crystal structure of murine CRY2 in its FBXL3–SKP1-complexed form (PDB ID: 4i6j.1) was found in existing literature (Xing et al., 2013). Based on this template, homology modeling was performed to form a heterodimer complex of hCRY2 and FBXL3 using SWISS MODEL (Waterhouse et al., 2018). A similar method was followed to generate the hCRY2 and PER2 complex, using a published (Nangle et al., 2014) crystal structure of murine CRY2 and PER2 in complex (PDB ID: 4u8h.1). Then, the interactions of hCRY2 with its binding partners FBXL3 and PER2 were analyzed to observe any changes in protein interactions due to missense mutations. The computational tools mCSM-PPI2 (Rodrigues et al., 2019), MutaBind2 (Zhang et al., 2020), SAAMBE-3D (Pahari et al., 2020) and BeAtMuSiC V1.0 (Dehouck et al., 2013) were applied to explore any variation in protein interactions. MCSM-PPI2 utilizes optimized graph-based signatures to model the effects of point mutations in protein-protein binding affinity, focusing on the inter-residue non-covalent interaction network (Rodrigues et al., 2019). MutaBind2 predicts changes in binding affinity between proteins in missense variants through statistical potentials, molecular mechanics force fields, and fast side-chain optimization algorithms made via random forest (RF) formula to assess alterations (Zhang et al., 2020). SAAMBE-3D (Single Amino Acid Mutation Change of Binding Energy) exploits machine learning to analyze alterations in protein-protein interactions as an effect of single amino acid mutation (Pahari et al., 2020). BeAtMuSiC V1.0 calculates the changes in binding free energy of the protein-protein interactions through the combination of the effect of the mutation on the strength of the interactions and the gross stability of the complex (Dehouck et al., 2013).

Simulating the dynamics of **hCRY2** *and its selected variants*

CABS-flex 2.0, a coarse-grained protein model, was used to study the structural flexibility of the wild-type and mutant 3D models of hCRY2 (Kuriata et al., 2018). Three-dimensional models of the hCRY2 missense variants were produced using template-based modeling in SWISS MODEL. A few 50 cycles between trajectory frames with a minimum time length of 10 ns at a temperature of 1.4 °C were applied to observe the protein motion. Other additional distance restraint parameters were set to default. Root Mean Square Fluctuation (RMSF) value was utilized to assess the stability of the protein during simulation.

Results and Discussion

A total of 13088 SNPs data for hCRY2 protein were retrieved from the NCBI dbSNP database. Out of these, 10846 SNPs were found to be present in the intron region (82.9%), 436 were nonsynonymous or missense SNPs (3.3%), and 230 were synonymous variants (1.8%). Only missense SNPs were considered for further analysis. In detail, information about all the missense variants is given in Supplementary Table 1. Six in silico tools like PolyPhen2, SNAP2, PONP2, Rhapsody, Pmut and SNPs&GO were utilized to find out the deleterious, pathogenic, and disease-causing SNPs. All prediction tools identified 68 variants out of 436 nsSNPS as disease-causing SNPs, which are listed in Supplementary Table 2. These 68 variants were then assessed for structural stability of hCRY2 upon missense mutation using MUpro, mCSM, DeepDDG, INPS-3D, and PremPS (Table 1). These tools showed the predicted changes in folding Gibbs free energy ($\Delta\Delta G$). For MUpro, mCSM, DeepDDG, and INPS-3D, variants with $\Delta\Delta G$ value < -1.0 kcal/mol, and for PremPS $\Delta\Delta G$ value > 1.0 kcal/mol were considered to have significantly destabilized hCRY2 structure. Overall, fifteen missense variants that showed significant destabilization across four or more tools were considered deleterious to hCRY2 stability. In certain cases, fifteen more variants that displayed destabilization across three tools were labeled as marginally deleterious to hCRY2 stability.

Project HOPE web server was used to predict the effects of missense variants on protein by analyzing the sequences of the 16 variants selected from the previous analysis. The obtained results assessed the changes in contacts between residues within the protein, perturbation in the protein structure, impacts of the functional domains of the protein, differences of the protein, and differences in the properties of the wild type and the substituted amino acid. The analysis of each variant is displayed in Table 2. All the amino acid residues of the variants analyzed by Consurf were reported to be highly conserved. The W371R, F400I, 2F429C, V380M, W71R, A407T, F315V, I359M, L74P, L274P, Y169H, L115W, L214Q, L288Q, L309P and C433R variants were predicted to be conserved as buried and structural while the conservation of other variants was functional and exposed. The conservation profile of the variants is represented in Supplementary File 1. From the analysis, five variants, L74P, L274P, L309P, F315V, and Y485, significantly affected hCRY2 structure, stability, and binding to both FBXL3 and PER2.

Hence, the three-dimensional structures of the native and mutant CRY2 variants were generated using homology by SWISS-MODEL (Fig.2). The structures were also validated using SAVES 6.0 server (Table 3). The PROCHECK results predicted the amino acid residues of all the native and mutant models results in the most favored regions were more than 83%, indicating the good quality of the models in the Ramachandran plots of the 3D models (Supplementary Fig. 2). The ERRAT value analysis demonstrated that the nonbonded interactions and backbone confirmation of the predicted models fit well within the range of a good quality model which was above 91%.

Complexes of hCRY2 and PER2, and hCRY2 and FBXL3 were generated via SWISS-MODEL (Fig.3). This was done to assess binding free energy change ($\Delta\Delta G$ values) in protein-protein interactions upon missense mutation that is crucial for instability of the protein interactions, functions, and pathogenicity (Jemimah and Gromiha, 2020). Four tools, mCSM-PPI2, MutaBind2, SAAMBE3D, and BeAtMuSic V1.0, were applied to predict changes in the binding affinity of each complex (Table 4). For MutaBind2, SAAMBE3D and BeAtMuSic V1.0 $\Delta\Delta G$ values > 0.8 kcal/mol, and for mCSM-PPI2, $\Delta\Delta G$ values < -0.8 kcal/mol reflect a significant decrease in binding affinity to the binding partners. Consequently, variants that followed these criteria across three or more tools were considered to have destabilized binding with its partner protein. When bound to FBXL3, fourteen variants, and in PER2 bound state, nine variants of hCRY2 followed these criteria.

Table 1. Impacts of missense variants on hCRY2 protein stability.

Variants	MUpro	mCSM	DeepDDG	INPS3D	PremPS
W371R	-1.081	-2.161	-1.965	-2.330	1.91
F400I	-0.631	-0.428	-1.344	-2.537	1.67
P488S	-1.463	-1.707	-0.851	-1.134	1.13
R239C	-0.723	-1.946	-1.378	-1.085	1.11
F429C	-1.579	-1.106	-0.482	-2.179	1.29
V380M	-0.387	-0.666	-1.084	-1.709	1.18
R282H	-1.506	-1.998	-2.728	-1.070	1.2
R377Q	-1.357	-1.767	-1.087	-0.846	1.51
W71R	-1.667	-0.3	-2.017	-2.387	1.16
A407T	-0.529	-1.095	-1.972	0.028	1.2
G231R	-1.517	-0.82	-2.103	-0.597	1.82
F315V	-1.450	-0.253	-0.276	-2.030	1.21
R70P	-0.754	-1.124	-1.488	-1.897	1.47
R312Q	-0.183	-0.624	-0.629	-1.481	0.41
G370V	-0.826	-1.428	-1.25	-1.192	1.15
I359M	-2.079	-0.578	-4.405	-1.304	2.58
L74P	-1.329	-0.93	-1.523	-3.368	0.94
L274P	-2.432	-1.944	-4.182	-3.365	2.44
I337T	-1.946	-0.328	-2.681	-2.539	1.94
Y464C	-1.109	-2.353	-0.357	-2.039	2.14
Y485H	-1.041	-2.239	-1.596	-1.272	2.12
R70G	-1.270	-2.384	-2.235	-1.996	1.6
Y169H	-1.356	-1.162	-2.818	-1.551	1.79
N37K	-1.441	-0.594	-4.001	-0.767	1.64
L115W	-1.788	0.078	-3.371	-2.238	0.79
Y152C	-1.428	-2.189	-1.246	-1.695	2.31
L214Q	-1.289	-1.133	-2.861	-2.035	1.96
L288Q	-2.124	-1.268	-3.621	-2.406	1.83
L309P	-1.064	-0.589	-5.336	-3.469	2.55
C433R	-1.521	0.397	-0.811	-1.145	1.09

The bold letter indicates the significant destabilizing missense variants predicted by four or more tools. Numerical values in the table show the expected changes in folding Gibbs free energy ($\Delta\Delta G$) in kcal/mol.

Table 2. Structural and functional impacts of hCRY2 missense variants

Variants	Variation in contact	Positional disturbance	Alteration in amino acid properties
R282H	The variant doesn't make the hydrogen bond at Asn 147 and Thr 150 and disturbs the ionic interaction.	Mutant residue might disturb the core structure of this domain.	The mutant residue is smaller. This causes charge differences and creates an empty space in the core of the protein.
W71R	The mutation might cause a loss of hydrophobic interactions with other molecules on the protein's surface.	The mutated residue is located on the surface of a domain, which can disturb this domain and abolish its function.	The mutant residue is smaller, causing repulsion between neighboring residues.
R70P	The variant doesn't make the hydrogen bond with Asp 401 and disturbs the ionic interaction.	The mutated residue is located on the surface of a domain, which can disturb this domain and abolish its function.	This mutation loses the charge of the wild-type residue. This can cause a loss of interactions with other molecules.
L74P	Variant residue disrupts the α-helix and can severely affect the structure of the protein.	The residue is buried in the core of a domain that might disturb the core structure of this domain.	The mutant residue is smaller and causes an empty space in the core of the protein.
L274P	Variant residue disrupts the α-helix and can severely affect the structure of the protein.	The residue is buried in the core of a domain that might disturb the core structure of this domain.	The mutant residue is smaller, causing a space in the core of the protein.
I337T	The mutation might cause a loss of hydrophobic interactions in the core of the protein.	The residue is buried in the core of a domain that might disturb the core structure of this domain.	The mutant residue is smaller, causing an empty space in the core of the protein.
Y485H	The variant doesn't make the hydrogen bond with Asp 360 and loss of hydrophobic interactions in the core of the protein.	The mutation is in a region required for the inhibition of CLOCK-BMAL1-mediated transcription. The residue is buried in the core of a domain that might disturb the core structure.	The mutant residue is smaller, causing an empty space in the core of the protein.
R70G	The variant doesn't make the hydrogen bond and salt bridge with 401, disturbs ionic interactions, and causes a loss of hydrophobic interactions in the core of the protein. It also interferes with the rigidity of the protein.	The mutated residue is located on the surface of the Photolyase/cryptochrome alpha/beta domain, which can disturb this domain and abolish its function.	The mutant residue is smaller.
Y169H	The variant doesn't make the hydrogen bond with Gln 173 and loss of hydrophobic interactions on the protein's surface.	The variant residue is located on the surface of a domain with an unknown function.	The mutant residue is smaller.
Y152C	The mutation may cause a loss of hydrogen bonds in the core of the protein and, as a result, disturb correct folding.	The residue is buried in the core of a domain located in a β-strand. The variant residue may slightly destabilize local conformation.	The mutant residue is smaller than the wild-type residue, causing an empty space in the core of the protein.
L214Q	The variant residue may cause a loss of hydrophobic interactions in the core of the protein.	The residue is buried in the core of a domain that might disturb the core structure of this domain.	The mutant residue is bigger.
L288Q	The variant residue may cause a loss of hydrophobic interactions in the core of the protein.	The residue is buried in the core of a domain that might disturb the core structure of this domain.	The mutant residue is bigger.
L309P	Variant residue disrupts the α-helix and can severely affect the structure of the protein and ligand contacts and destabilize the stability.	The residue is buried in the core of a domain that might disturb the core structure, affect the local structure, and consequently affect this binding site.	The mutant residue is smaller, causing an empty space in the core of the protein.
F315V	The variant residue may cause a loss of interactions with ligands and interfere with the protein's function.	The residue is buried in the core of a domain that might disturb the core structure of this domain.	The mutant residue is smaller, causing an empty space in the core of the protein.

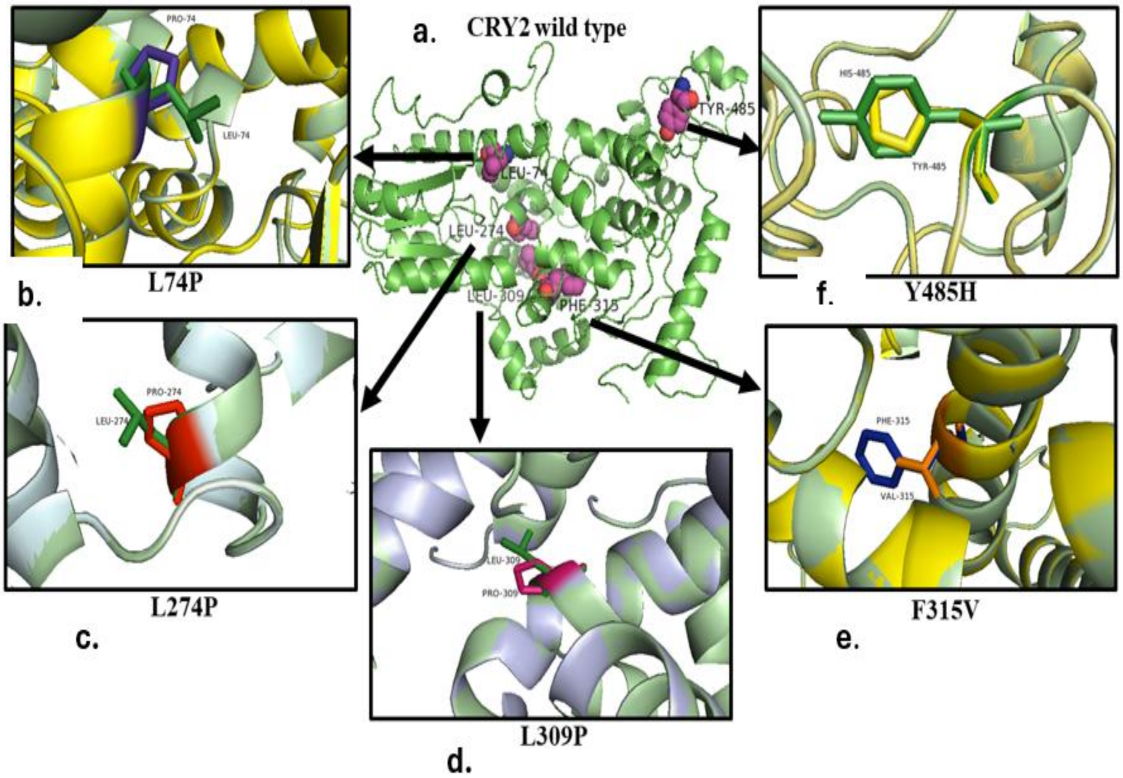

Fig. 2. 3D structure of native and mutant hCRY2 variants a. native hCRY2 b. L74P c. L274P d. L309P e. F315V f. Y485H.

Table 3. Validation scores of predicted models obtained from PROCHECK and ERRAT.

Variant	PROCHECK (%)[a]	ERRAT(%)[b]
Wild type (hCRY2)	85.6	91.111
L74P	86.9	93.915
L274P	87.1	94.118
L309P	85.6	91.111
F315V	85.6	91.111
Y485H	85.6	90.303

[a]residues in most allowed regions of Ramachandran plot [b]Overall Quality Factor expressed as the percentage of the protein for which the calculated error value falls below the 95% rejection limit with structure resolutions (2.5 to 3A).

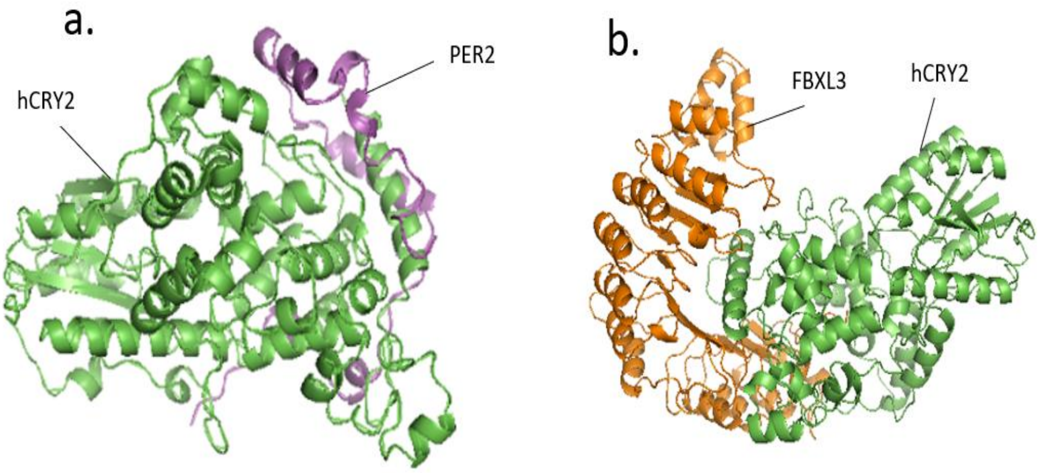

Fig. 3. (a) Tertiary structure of PER2-hCRY2 complex (b) 3D structure of FBXL3-hCRY2 complex. hCRY2, PER2, and FBXL3 are denoted by the green, magenta-colored, and orange-colored ribbon

Table 4. Effects of missense SNPs on protein-protein interactions between hCRY2 and FBXL3 and hCRY2 and PER2.

hCRY2 and FBXL3 complex					**hCRY2 and PER2 complex**				
Variants	**mCSM-PPI**	**MutaBind2**	**SAAMBE3D**	**BeAtMusicV1.0**	**Variants**	**mCSM-PPI**	**MutaBind2**	**SAAMBE3D**	**BeAtMusicV1.0**
R440H	-0.416	1.44	1.09	0.82	R171C	-0.687	1.88	0.86	1.31
R440C	-0.895	1.16	0.8	1.52	W371R	-0.202	1.12	1.4	0.81
F429C	-1.95	2.98	2.29	2.38	F429C	-0.923	0.89	0.92	0.87
R377Q	-1.621	1.31	1.31	0.28	G370V	-1.025	0.98	0.14	0.82
R377L	-1.35	2.38	0.95	-0.29	**L74P**	-0.931	0.68	0.81	1.21
F315V	-1.574	1.05	0.81	0.71	**L274P**	-0.567	0.91	0.97	1.25
R312Q	-1.681	1.25	1.02	0.77	**Y485H**	-1.168	0.75	0.98	0.93
G370V	-0.847	1.21	0.14	1.05	W416C	-0.542	1.01	1.26	1.07
L74P	-0.937	1.23	0.81	1.22	**L309P**	-0.763	0.86	1.14	1.54
L274P	-1.572	1.44	0.97	2.08					
Y169H	-1.326	0.84	0.94	1.27					
H374P	-1.429	1.1	0.77	.81					
W416C	-0.842	1.11	1.51	1.19					
L309P	-1.405	1.08	1.41	1.89					

The bold letter indicates the significant destabilizing missense variants predicted by four tools.

These five variants, L74P, L274P, L309P, F315V, and Y485H, were thus selected for protein dynamics simulation to determine the protein flexibility by calculating the RMSF of all amino acids and the contact map between residues of the CRY2 protein. The resulting residue fluctuation profiles (Fig.4) show specific changes compared to the wild type. The difference of1Å in the RMSF value of wild-type and that of mutant hCRY2 variants was residues that may form unstable secondary and tertiary structures. In all 5 variants, the residues showed prominent fluctuations in the DNA photolyase region (22-176) and the region that inhibits the CLOCK-ARNTL-driven transcription (390-489) as compared to the native protein. From the analysis, it can be observed that Leu274 residue is placed in the FAD binding domain. Upon alteration to a 5-membered proline which resides in the buried area of the protein destabilizes the structure by the disruption of α-helix and creating a space in the protein. Previous experimental studies found that point mutations at amino acid residues crucial for the FAD binding domain (246-444) affect the repressor activity of CRY2 (Czarna et al., 2013). Hirano et al. (2016) identified a missense variant (A260T) in the FAD binding domain of the human hCry2 gene that leads to heritable Familial Advanced Sleep Phase (FASP)-like phenotype. Moreover, conversion from serine to aspartic acid at the 265th position of mouse CRY2 (homologous to Ser266 in hCRY2) that resides in the phosphorylation site declines CRY2 repressor activity (Sanada et al., 2004). L274P alteration also remarkably decreases the binding affinity and interferes with the interactions of FBXL3 and PER2 complex that are essential for the regulation of CRY2 stability and maintenance of the sleep-wake cycle in humans (Hirano et al., 2016).

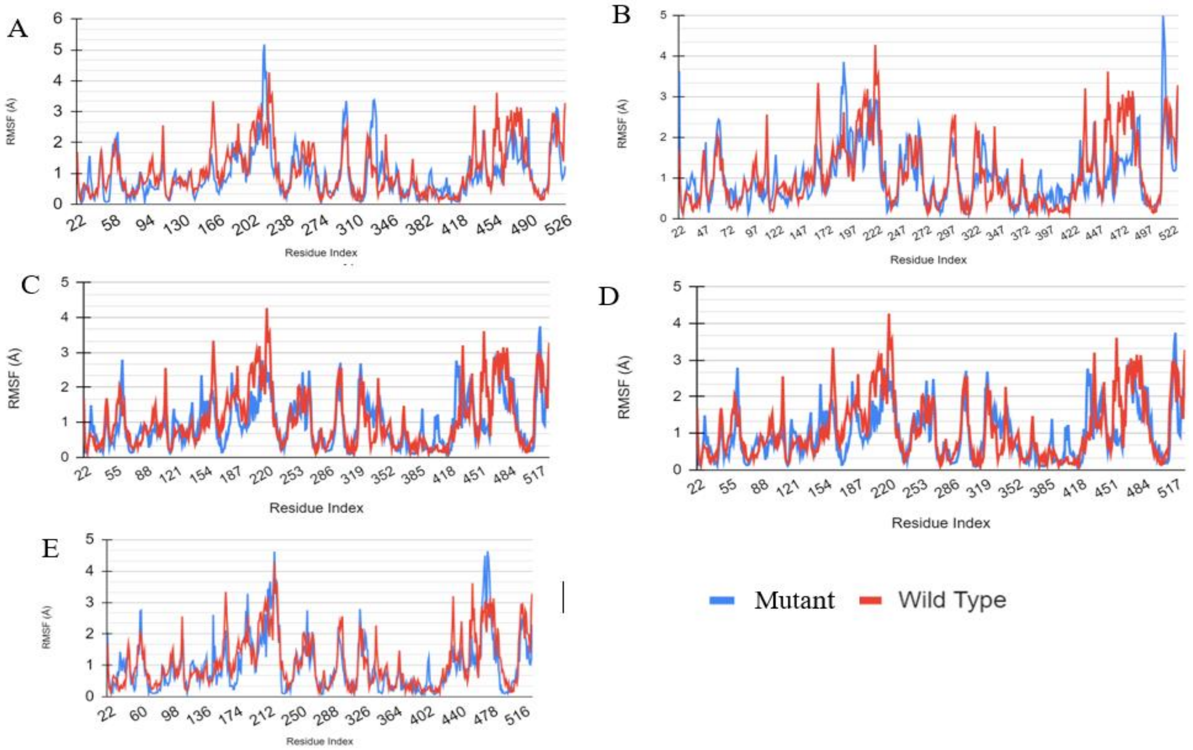

Fig. 4. Residue fluctuation profiles of the native and five mutant structures of hCRY2. The variants are (A) L74P, (B) L274P, (C) L309P, (D) F315V, (E)Y485H. All these variants were predicted to alter the wild-type protein structure and reduce hCRY2 stability.

The Glu308 residue is considered the FAD binding site in human CRY2 protein. The alteration of the next residue, leucine to proline that is, evolutionarily conserved residue, destabilizes protein structure by alteration of α-helix, ligand-contacts, and binding sites and makes a space in the core of the protein. The present study found that mutation from leucine to proline at 309th position significantly reduces the binding affinity of FBXL3 to hCRY2 protein. In the case of mCRY2, Trp428 residue of the C-terminal tail of FBXL3 binds to the center of the FAD-binding pocket of mCRY2 and occupies the cofactor site. The tail of FBXL3 loads its Pro426 residue against Trp310 of mCRY2 (homologous to Trp311 in hCRY2) and turns the side chain His373 with Thr427 of mCRY2, to enter the FAD-binding pocket. Inside the pocket, the indole ring of Trp428 forms several hydrophobic interactions with mCRY2 and donates a hydrogen bond to the carbonyl group of Gln307 (homologous to Gln308 in hCRY2) in mCRY2 (Xing et al., 2013). FAD and FBXL3 competitively bind to the same FAD binding pocket and promote ubiquitylation of CRY proteins (Hirano et al., 2017). So, it can be predicted that hydrogen and hydrophobic interactions necessary for binding FBXL3 to the core of the FAD binding pocket may be hampered by substituting nonpolar amino acid leucine for polar amino acid proline. MD simulation study also suggests that the mutation alters the position of amino acids at several points of photolyase region (162-163,175-176) and CLOCK-ARNTL-mediated transcription inhibition region (433-435,454-458 and 478-83) that may lead to perturbation of the circadian clock.

The FAD binding pocket comprises three different sub-regions: hydrophobic region 1, affinity region, and hydrophobic region 2. Residue W310, F314, W417 and L418 is located in the hydrophobic region 1 of mCRY2 (homologous to W311, F315, W418, and L418 in hCRY2) (Miller et al., 2021). Minimal changes in the hydrophobic region significantly hamper the binding modes of CRY activating compounds, cyclopentyl group of TH301, chlorobenzonitrile moiety of KL044, and the more flexible methane sulfonamide and furan groups of KL001 of mCRY2 protein (Miller and Hirota, 2022). The study reported that mutation from aromatic amino acid phenylalanine to aliphatic amino acid valine at the 315th position may cause loss of interactions with ligands, destabilize the core structure of the domain, and interfere with protein's function. So, the alteration may cause the structural differences of FAD binding pockets that change the binding mode of other compounds as well as reduce the binding affinity to FBXL3 and PER2 protein. When simulated, the mutation fluctuates the photolyase homology region (163-165) and CLOCK-ARNTL-mediated transcription inhibition region (454-462, 478-483), which may imbalance the CRY2 degradation and stabilization.

The wild-type tyrosine residue lies in the region required to inhibit CLOCK-ARNTL-mediated transcription, which is the central negative feedback loop of the circadian clock (Partch et al., 2014; Xing et al., 2013). Alteration of tyrosine residues to histidine at the 485th position may change hydrogen and hydrophobic interactions in the core of the protein and disturb the domain structure. The variation also decreases the interactions of CRY2 protein with PER2 and FBXL3, which may hamper the rhythm of the circadian clock.

The impacts of dysfunction of human CRY2 protein are associated with multiple abnormalities. The pathophysiology of cardiovascular disease, of which hypertension is a significant contributing element, has been linked to circadian clock disruption (Škrlec et al., 2018). It appears to impact not only the cycles of metabolism and cell division but also mood and behavior (Kovanen et al., 2014), depression (particularly winter depression), bipolar type 1, and seasonal affective disorder (Kovanen et al., 2013; Lavebratt et al., 2010b). On the other hand, tumorigenesis might be aided by the disturbance of circadian rhythms. Thus, various features of carcinogenesis, such as cell growth, angiogenesis, metabolism, apoptosis, and DNA damage response, may be linked to circadian negative feedback loop

(CNFL) genes (Qu et al., 2016). Indeed, a variety of human cancer types commonly exhibit altered expression of the CNFL genes (CRY1, CRY2, PER1, PER2, and PER3) (Gršković & Korać, 2023).

Conclusion

Dysfunction of the human CRY2 protein is associated with multiple abnormalities. Non-synonymous polymorphisms of the CRY2 gene result in an altered protein that may interfere with the morning/evening preference and may disturb different metabolic regulation and circadian periods. This study determined L74P, L274P, L309P, F315V, and Y485H to be the most deleterious missense mutants in the hCRY2 protein. These variants are predicted to affect the binding of FAD cofactors, change the binding pocket structure, and alter the binding mode of different CRY-activating compounds. These mutants may destabilize circadian period length regulation by reducing the binding affinity to FBXL3 and PER2. The most deleterious mutants found can undergo in vitro assays to understand protein-protein interactions of these mutants in cell culture, Xray crystallography, and Mass Spectrometry to confirm the changes in structures of these proteins produced in cell culture, and many other experimental procedures. Further experimental studies are needed to validate the effects of these SNPs in animal models, like in mutant and wild-type mice, by observing their behavioral and genetic effects and protein expression levels that may lead to establishing the real impacts of SNPs on the circadian clock of mice.

Author contributions

ASK took part in acquiring, analyzing, and interpreting data and manuscript preparation. MA participated in the study and interpretation of data, manuscript preparation, and review. MAE was responsible for data acquisition and analysis. SFK was involved in the conception, analysis, interpretation of data, and critical reviewing. All authors have read and approved the final manuscript.

Declaration of conflicting interests

The authors declare that they have no competing interests.

Supplementary materials

The single nucleotide polymorphism datasets analyzed are available in the dbSNP repository (Accession Number: NP_066940.3). The amino acid sequence of hCRY2 used to generate the wild-type structure was collected from the UniProt Knowledge Base (UniProtKB) (Accession Number: Q49AN0). All other data generated or analyzed during this study are included in this article (and its supplementary information files).

References

Adzhubei I, Jordan DM and Sunyaev SR. Predicting functional effect of human missense mutations using PolyPhen-2. *Curr. Protoc. Hum. Genet.* 2013; 76(1): 7.20.21-27.20.41.

Ashkenazy H, Abadi S, Martz E, Chay O, Mayrose I, Pupko T and Ben-Tal N. ConSurf 2016: an improved methodology to estimate and visualize evolutionary conservation in macromolecules. *Nucleic Acids Res*. 2016; 44(W1): W344-W350.

Buhr ED and Takahashi JS. Molecular components of the mammalian circadian clock. *Handb. Exp. Pharmacol.* 2013; 217, 3-27.

Calabrese R, Capriotti E, Fariselli P, Martelli PL and Casadio R. Functional annotations improve the predictive score of human disease-related mutations in proteins. *Hum. Mutat*. 2009; 30(8): 1237-1244.

Cao H, Wang J, He L, Qi Y and Zhang JZ. DeepDDG: predicting the stability change of protein point mutations using neural networks. *J. Chem. Inf. Model.* 2019; 59(4): 1508-1514.

Chan AB, Huber AL and Lamia KA. Cryptochromes modulate E2F family transcription factors. *Sci. Rep.* 2020; 10(1): 1-9.

Chasman D and Adams RM. Predicting the functional consequences of non-synonymous single nucleotide polymorphisms: structure-based assessment of amino acid variation. *J. Mol. Biol.* 2001; 307(2): 683-706.

Cheng J, Randall A and Baldi P. Prediction of protein stability changes for single-site mutations using support vector machines. Proteins: Struct., Funct., and Bioinf. 2006; 62(4): 1125-1132.

Colovos C and Yeates TO. Verification of protein structures: patterns of nonbonded atomic interactions. Protein sci.: a publication of the Protein Society. 1993; 2(9): 1511-1519.

Correia SP, Chan AB, Vaughan M, Zolboot N, Perea V, Huber AL, Kriebs A, Moresco JJ, Yates JR and Lamia K A. The circadian E3 ligase complex SCF FBXL3+CRY targets TLK2. *Sci. Rep*. 2019; 9(1).

Czarna A, Berndt A, Singh HR, Grudziecki A, Ladurner AG, Timinszky G, Kramer A and Wolf E. Structures of Drosophila cryptochrome and mouse cryptochrome1 provide insight into circadian function. *Cell.* 2013; 153(6): 1394-1394.

Dehouck Y, Kwasigroch, JM, Rooman M and Gilis D. BeAtMuSiC: Prediction of changes in protein-protein binding affinity on mutations. *Nucleic Acids Res.* 2013; 41(W1): W333–W339.

Dupuis J, Langenberg C, Prokopenko I, Saxena R, Soranzo N, Jackson A U, Wheeler E, Glazer NL, Bouatia-Naji N, Gloyn AL, Lindgren CM, Mägi R, Morris AP, Randall J, Johnson T, Elliott P, Rybin D, Thorleifsson G, Steinthorsdottir V and Barroso I. New genetic loci implicated in fasting glucose homeostasis and their impact on type 2 diabetes risk. *Nat. Genet.* 2010; 42(2): 105-116.

Fribourgh JL, Srivastava A, Sandate CR, Michael AK, Hsu PL, Rakers C, Nguyen LT, Torgrimson MR, Parico GCG, Tripathi S, Zheng N, Lande GC, Hirota T, Tama F and Partch CL. Dynamics at the serine loop underlie differential affinity of cryptochromes for CLOCK:BMAL1 to control circadian timing. *eLife.* 2020; 9.

Gekakis N, Staknis D, Nguyen HB, Davis FC, Wilsbacner LD, King DP, Takahashi JS and Weitz CJ. Role of the CLOCK protein in the mammalian circadian mechanism. *Science,* 1998; 280(5369): 1564-1569.

Gršković P and Korać P. Circadian Gene Variants in Diseases. *Genes*, 2023; 14(9): 1703-1703.

Hecht M, Bromberg Y and Rost B. Better prediction of functional effects for sequence variants. *BMC Genom.* 2015; 16 (8): S1.

Hirano A, Braas D, Fu YH and Ptáček LJ. FAD regulates CRYPTOCHROME protein stability and circadian clock in mice. *Cell Rep.* 2017; 19(2): 255-266.

Hirano A, Shi G, Jones CR, Lipzen A, Pennacchio LA, Xu Y, Hallows WC, McMahon T, Yamazaki M, Ptáček LJ and Fu YH. A Cryptochrome 2 mutation yields advanced sleep phase in humans. *eLife.* 2016; 5: e16695.

Hoffman AE, Zheng T, Stevens RG, Ba Y, Zhang Y, Leaderer D, Yi C, Holford, TR and Zhu Y. Clock-cancer connection in non-Hodgkin's lymphoma: A genetic association study and pathway analysis of the Circadian gene Cryptochrome 2. *Cancer Res.* 2009; 69(8): 3605-3613.

Hogenesch JB, Gu YZ, Jain S and Bradfield CA. The basic-helix–loop–helix-PAS orphan MOP3 forms transcriptionally active complexes with circadian and hypoxia factors. *Proc. Natl. Acad. Sci. USA*, 1998; 95(10): 5474-5474.

Huber AL, Papp SJ, Chan AB, Henriksson E, Jordan SD, Kriebs A, Nguyen M, Wallace M, Li Z, Metallo CM and Lamia KA. CRY2 and FBXL3 Cooperatively Degrade c-MYC. *Mol. Cell,* 2016; 64(4): 774-789.

Jemimah S and Gromiha MM. Insights into changes in binding affinity caused by disease mutations in protein-protein complexes. *Comput. Biol. Med.* 2020; 123: 103829.

Kelly MA, Rees SD, Hydriem ZL, Shera AS, Bellary S, O'Hare JP, Kumar S, Taheri S, Basit A and Barnett AH. Circadian gene variants and susceptibility to type 2 diabetes: A pilot study. PLoS One. 2012; 7(4):e32670.

King DP, Zhao Y, Sangoram AM, Wilsbacher LD, Tanaka M, Antoch, MP, Steeves, TDL, Vitaterna MH, Kornhauser JM, Lowrey PL, Turek FW and Takahashi JS. Positional cloning of the mouse circadian clock gene. Cell, 1997; 89(4): 641-653.

Kovanen L, Donner K, Kaunisto M and Partonen T. CRY1, CRY2 and PRKCDBP genetic variants in metabolic syndrome. *Hypertension Res*. 2014; 38(3): 186-192.

Kovanen L, Kaunisto M, Donner K, Saarikoski ST and Partonen T. CRY2 genetic variants associate with dysthymia. *PLoS One*, 2013; 8(8): e71450.

Kripke DF, Nievergelt CM, Joo EJ, Shekhtman T and Kelsoe JR. Circadian polymorphisms associated with affective disorders. *J. Circadian Rhythms*, 2009; 7: 2.

Kucukkal TG, Petukh M, Li L and Alexov E. Structural and physico-chemical effects of disease and non-disease nsSNPs on proteins. *Curr. Opin. Struct. Biol.* 2015; 32: 18-24.

Kumar A and Purohit R. Computational screening and molecular dynamics simulation of disease associated nsSNPs in CENP-E. *Mutat. Res.* 2012; 738-739: 28-37.

Kuriata A, Gierut AM, Oleniecki T, Ciemny MP, Kolinski A, Kurcinski M and Kmiecik S. CABS-flex 2.0: a web server for fast simulations of flexibility of protein structures. *Nucleic Acids Res*. 2018; 46(W1): W338-W343.

Laskowski RA, Rullmann JAC, MacArthur MW, Kaptein R and Thornton, JM. (1996). AQUA and PROCHECK-NMR: programs for checking the quality of protein structures solved by NMR. *J. Biomol. NMR.* 1996; 8(4): 477-486.

Lavebratt C, Sjöholm LK, Soronen P, Paunio T, Vawter MP, Bunney WE, Adolfsson R, Forsell Y, Wu JC, Kelsoe, JR, Partonen T and Schalling M. CRY2 Is Associated with Depression. *PLoS One*. 2010(a); 5(2): e9407.

Lavebratt C, Sjöholm LK, Soronen P, Paunio T, Vawter MP, Bunney, WE, Adolfsson R, Forsell Y, Wu JC, Kelsoe, JR, Partonen, T and Schalling M. CRY2 is associated with depression. *PLoS One.* 2010b; 5(2): e9407.

Li Y, Zhou J, Wu Y, Lu T, Yuan M, Cui Y, Zhou Y, Yang, G and Hong, Y. Association of osteoporosis with genetic variants of circadian genes in Chinese geriatrics. *Osteoporos. Int*. 2016; 27(4): 1485-1492.

López-Ferrando V, Gazzo A, De La Cruz X, Orozco M and Gelpí JL. PMut: a web-based tool for the annotation of pathological variants on proteins, 2017 update. *Nucleic Acids Res*. 2017; 45(W1): W222-W228.

Miller S and Hirota T. Structural and chemical biology approaches reveal isoform-selective mechanisms of ligand interactions in mammalian cryptochromes. *Front. Physiol.* 2022; 13: 837280.

Miller S, Srivastava A, Nagai Y, Aikawa Y, Tama F and Hirota T. Structural differences in the FAD-binding pockets and lid loops of mammalian CRY1 and CRY2 for isoform-selective regulation. *Proc. Natl. Acad. Sci. US*A, 2021; 118(26): e2026191118.

Mohawk JA, Green CB and Takahashi JS. Central and peripheral circadian clocks in mammals. *Annu. Rev. Neurosci.* 2012. 35: 445-462.

Nangle SN, Rosensweig C, Koike N, Tei H, Takahashi JS, Green CB and Zheng N. (2014). Molecular assembly of the period-cryptochrome circadian transcriptional repressor complex. *eLife*, 2014. 3: e03674.

Niroula A, Urolagin S and Vihinen M. PON-P2: prediction method for fast and reliable identification of harmful variants. PLoS One, 2015; 10(2): e0117380.

Pahari S, Li G, Murthy, AK, Liang S, Fragoza R, Yu H and Alexov, E. (2020). SAAMBE-3D: Predicting Effect of Mutations on Protein–Protein Interactions. Int. J. Mol. Sci. 2020; 21(7): 2563.

Partch CL and Sancar A. Photochemistry and photobiology of cryptochrome blue-light photopigments: The search for a photocycle. *Photochem. Photobiol.* 2005; 81(6): 1291-1304.

Partch CL, Green CB and Takahashi JS. Molecular architecture of the mammalian circadian clock. *Trends Cell Biol.* 2014; 24(2): 90-99.

Petukh M, Kucukkal TG and Alexov E. On human disease-causing amino acid variants: Statistical Study of sequence and structural patterns. *Hum. Mut.* 2015; 36(5): 524-534.

Pires DE, Ascher DB and Blundell TL. mCSM: predicting the effects of mutations in proteins using graph-based signatures. *Bioinf.* 2014; 30(3): 335-342.

Ponzoni L, Peñaherrera DA, Oltvai ZN and Bahar I. Rhapsody: predicting the pathogenicity of human missense variants. *Bioinf.* 2020; 36(10): 3084-3092.

Qu F, Qiao Q, Wang N, Ji G, Zhao H, He L, Wang H and Bao G. Genetic polymorphisms in circadian negative feedback regulation genes predict overall survival and response to chemotherapy in gastric cancer patients. *Sci. Rep.* 2016; 6: 22424.

Rajendran V and Sethumadhavan R. Drug resistance mechanism of PncA in Mycobacterium tuberculosis. *J. Biomol. Struct. Dyn.* 2014; 32(2): 209-221.

Rajendran V, Gopalakrishnan C and Sethumadhavan R. Pathological role of a point mutation (T315I) in BCR-ABL1 protein—A computational insight. *J. Cell. Biochem.* 2018 119(1), 918-925.

Reischl S and Kramer A. Kinases and phosphatases in the mammalian circadian clock. *FEBS Lett.* 2011; 585(10): 1393-1399.

Reppert SM and Weaver, DR. Coordination of circadian timing in mammals. *Nature,* 2002; 418(6901): 935-941.

Rodrigues CHM, Myung Y, Pires DEV and Ascher DB. mCSM-PPI2: predicting the effects of mutations on protein–protein interactions. *Nucleic Acids Res*. 2019; 47(W1): W338-W344.

Rosensweig C, Reynolds, KA, Gao P, Laothamatas I, Shan, Y, Ranganathan R, Takahashi JS and Green CB. An evolutionary hotspot defines functional differences between CRYPTOCHROMES. *Nat. Commun.* 2018; 9(1): 1138.

Salazar P, Konda S, Sridhar A, Arbieva Z, Daviglus M, Darbar D and Rehman J. Common genetic variation in circadian clock genes are associated with cardiovascular risk factors in an African American and Hispanic/Latino cohort. *Int. J. Cardiol. Heart Vascul.* 2021; 34: 100808.

Sanada K, Harada Y, Sakai M, Todo T and Fukada Y. Serine phosphorylation of mCRY1 and mCRY2 by mitogen-activated protein kinase. *Genes Cells.* 2004; 9(8): 697-708.

Savojardo C, Fariselli P, Martelli PL and Casadio R. INPS-MD: a web server to predict stability of protein variants from sequence and structure. *Bioinf.* 2016; 32(16), 2542-2544.

Schork NJ, Fallin D and Lanchbury JS. Single nucleotide polymorphisms and the future of genetic epidemiology. *Clin. Genet.* 2000; 58(4): 250-264.

Sherry ST, Ward MH, Kholodov M, Baker J, Phan L, Smigielski, EM and Sirotkin, K. dbSNP: the NCBI database of genetic variation. *Nucleic Acids Res.*2001; 29(1): 308-311.

Škrlec I, Milic J, Heffer M, Peterlin, B and Wagner J. Genetic variations in circadian rhythm genes and susceptibility for myocardial infarction. *Genet. Mol. Biol.* 2018; 41(2): 403-409.

Stojkovic K, Wing SS and Cermakian N. A central role for ubiquitination within a circadian clock protein modification code. Front. Mol. Neurosci. 2014; 7: 69.

Takahashi JS. Transcriptional architecture of the mammalian circadian clock. *Nat. Rev. Genet.* 2016; 18(3): 164-179.

Venselaar H, te Beek TAH, Kuipers RKP, Hekkelman ML and Vriend G. Protein structure analysis of mutations causing inheritable diseases. An e-Science approach with life scientist friendly interfaces. *BMC Bioinf.* 2010; 11: 548.

Vielhaber EL, Duricka D, Ullman KS and Virshup DM. Nuclear export of mammalian PERIOD proteins. *J. Biol. Chem*. 2001; 276(49): 45921-45927.

Wang Y, Peng S, Liu T, Zhang Y, Li H, Li X, Tao W and Shi Y. The potential role of clock genes in children attention-deficit/hyperactivity disorder. *Sleep Med.* 2020; 71: 18-27.

Waterhouse A, Bertoni M, Bienert S, Studer G, Tauriello G, Gumienny R, Heer FT, De Beer TAP, Rempfer C, Bordoli L, Lepore R, Schwede T, de Beer TAP, Rempfer C, Bordoli L, Lepore R and Schwede T. SWISS-MODEL: homology modelling of protein structures and complexes. *Nucleic Acids Res.* 2018; 46(W1): W296-W303.

Xing W, Busino L, Hinds TR, Marionni ST, Saifee NH, Bush MF, Pagano M and Zheng N. SCFFBXL3 ubiquitin ligase targets cryptochromes at their cofactor pocket. *Nature.* 2013; 496(7443): 64-68.

Zhang N, Chen Y, Lu H, Zhao F, Alvarez, RV, Goncearenco A, Panchenko AR and Li M. MutaBind2: Predicting the impacts of single and multiple mutations on protein-protein interactions. *iScience*. 2020; 23(3): 100939.

Zienolddiny S, Haugen A, Lie JAS, Kjuus, H, Anmarkrud KH and Kjærheim, K. Analysis of polymorphisms in the circadian-related genes and breast cancer risk in Norwegian nurses working night shifts. *Breast Cancer Res.* 2013; 15(4): R53.

J. Bangladesh Acad. Sci. 49(1); 73-85: June 2025 DOI:https://doi.org/10.3329/jbas.v49i1.78209

Journal of Bangladesh Academy of Sciences

Journal homepage: http://www.bas.org.bd/publications/jbas.html

Research Article

CNN-Based crop disease and pest detection systems: Enhancing accuracy and efficiency in agricultural sustainability

Noshin Un Noor[1] and Faria Solaiman[2]

Department of Information and Communication Technology, Bangladesh University of Professionals, Dhaka, Bangladesh

ARTICLE INFO

Article History

Received: 08 December 2024
Revised: 13 Febraury 2025
Accepted: 10 April 2025

Keywords: Convolutional neural network (CNN), diseased crop dataset, graphical user interface (GUI), image classification, local binary pattern (LBP), support vector machine (SVM).

ABSTRACT

This paper highlights the effectiveness of classifying crop diseases and pests using different Convolutional Neural Network (CNN) models, utilizing images of diseased and pest-infested leaves. By combining CNNs with classification techniques like Support Vector Machines (SVM), accuracy improved to an impressive 98-99% across various plant disease categories. CNNs automate feature extraction and classification, outperforming traditional methods in complex tasks. The paper compares Local Binary Pattern (LBP) with a total of 18 CNN architectures, including Residual Network such as ResNet-101, Google Net, DarkNet-19, and others, demonstrating that CNNs consistently exceed 99 % accuracy in datasets for rice, corn, and jute. Our model achieved 99.9 % accuracy for Rice, 99.87 % for Jute, and 99.01% for Corn datasets when utilizing the ResNet-101 and DarkNet-19 CNN models. In agricultural areas like Bangladesh, this emerging method has the capability to completely transform crop disease management by facilitating early identification and prompt response, which would increase crop yields and food security. The work also makes real-time disease prediction accessible to farmers by introducing a Graphical User Interface (GUI). The potential of CNN-based systems to revolutionize precision agriculture, maximize resources, lower expenses, and empower farmers is highlighted in this study.

Introduction

Plant diseases significantly impact global agriculture, reducing crop yields, putting food security at risk and resulting in losses (Islam, 2020). Conventional detection techniques, which are frequently prone to errors, lead to inaccurate diagnoses and losses (Naidu et al., 2021). The accuracy of disease detection is increased by deep learning, particularly Convolutional Neural Networks (CNNs), which outperform conventional techniques (50–70%) with an accuracy of over 90% (Rajendran and Islam, 2017). While Panigrahi et al.'s CNN model achieved 98.78% for maize disease diagnosis, models such as Enhanced K-Nearest Neighbors (EKNN) and EfficientNet achieve 95% accuracy in pest identification (Panigrahi, 2020). The efficiency of detection is further improved by transfer learning and image preprocessing (Srestha, 2020). A Deep Convolutional Neural Network (DCNN) model that classified five diseases and healthy leaves with 96.08% accuracy used a modified Visual Geometry Group 19 (VGG-19)-based transfer learning strategy for rice leaf disease identification. This strategy reduces production losses and lowers rice prices by integrating drone and IoT technology to offer real-time, affordable diagnostics (Latif et al.,

---

*Corresponding author:<neha68219@gmail.com, fariasolaiman22@gmail.com>

Department of Information and Communication Technology, Bangladesh University of Professionals Dhaka, Bangladesh

2022). Moreover 60% of Bangladesh's workforce works in agriculture, which accounts for one-third of the country's GDP (Hassan, 2021). Crop yields decrease by 10–20% because of poor disease management, even with extensive pesticide use (Bharate and Shirdhonkar, 2017). Farmers have benefited from increased disease diagnosis accuracy brought forth by technology use (Gandhi et al., 2018). Deep learning improves food security and sustainability by providing quick, scalable, and affordable solutions (Falaschetti et al., 2022).

Pests and diseases are major biological risks to rice, corn, and jute, as shown in Fig. 1. Jute has the highest pest-related losses (20%), followed by rice (15%) and corn (10%). Similarly, disease losses consistently affect all three crops, ranging from 10% to 15% (Islam, 2020). These trends highlight the urgent need for integrated crop protection to improve yield stability and food security.

The objective of this study is to create an efficient detection system that improves accuracy in detecting diseases and pest infestations by using multiple CNN models as feature extractors and Support Vector Machine (SVM) as a classifier. A range of datasets of rice, corn, and jute crops with various pest infestations and diseases are gathered for the study, which then pre-processes the data and extracts features for accurate classification. (Hasan, 2019)

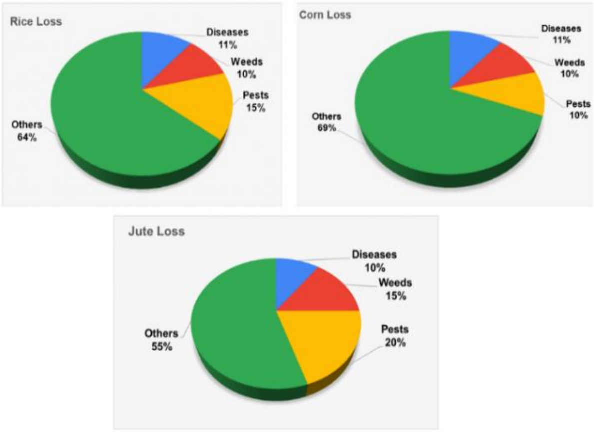

Fig. 1. Yield loss share of pests, diseases, and weeds in Rice, Corn, and Jute crops (Islam, 2020).

In order to identify the top-performing model, it compares 18 CNN architectures, such as Residual Network 101 (ResNet-101) for rice and jute and DarkNet-19 for maize. Additionally, traditional LBP methods are contrasted with CNN-based feature extraction, especially when it comes to detecting pest infestations and disease symptoms based on texture patterns. A Graphical User Interface (GUI) that is easy to use is also designed for real-time validation, making it practical for farmers and agricultural specialists. This study hypothesizes that when it comes to identifying pest infestations and diseases in rice, corn, and jute crops, CNN-based feature extraction combined with SVM classification will perform better than conventional Local Binary Pattern (LBP) techniques.

This approach facilitates precision agriculture, maximizes resource use, and improves large-scale crop monitoring by utilizing CNNs for accurate diseases and pest identification, thus contributing to sustainable farming and worldwide food security.

Materials and Method

In this study, we have separately classified crop diseases for rice and corn, and pest infestation for jute, which are three significant crops in Bangladesh. For this classification, we used images of disease-infected leaves from rice and corn, and pest-infested leaves from jute. LBP and CNN were used as feature extractors, while SVM was used for classification. The workflow of the classification model is shown in Fig. 2.

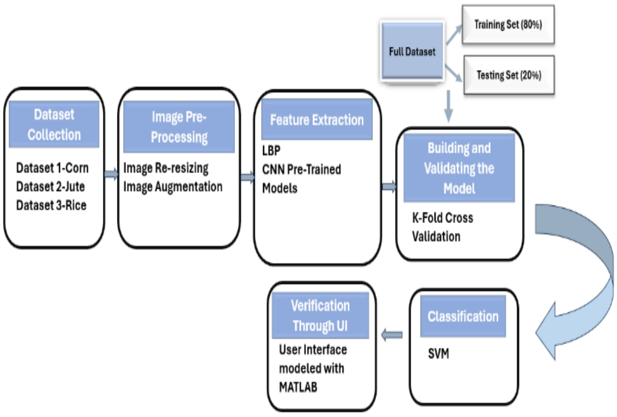

Fig. 2. Workflow of the crop disease and pest detection model using LBP for texture analysis, CNN for feature extraction, and SVM for classification.

The process begins with collecting image datasets. In this case, three datasets were used such as

Dataset 1: Corn images,

Dataset 2: Jute images and

Dataset 3: Rice images.

The collected images undergo pre-processing to prepare them for feature extraction. Images were resized to a uniform size to ensure consistency across the dataset. Images are typically converted to grayscale when using LBP, which extracts texture information based on intensity levels (Sharma et al., 2020). This phase reduces computing complexity while concentrating on texture information. Image augmentation was used to increase dataset diversity for CNN models that had already been trained. Rotation, resizing, scaling, flipping, and brightness adjustments were typically required for this (Hassan et al., 2021). Important features that can be used for categorization are taken out of the images at the feature extraction step. Features that are known to perform well for image classification tasks were extracted using LBP and CNN models that had already been trained (Panchal et al., 2019). Building and validating the classification model came next. Each dataset has been split into five folds, or subsets of which 20% was the testing dataset and 80% was the dataset for training. The K-Fold Cross-Validation technique was employed to validate the model on various subsets of the dataset, enhancing its robustness (Tugrul et al., 2022). The overall performance of the model was determined by averaging the results across all folds. Once the model is trained and validated, the SVM classifier was applied to classify the images based on the extracted features (Agarwal et al., 2020). The final step involves verifying the model's performance through a GUI that is built using MATLAB. This allows users to interact with the model and test its predictions.

Dataset Description

Dataset 1 consists of 4,800 images of corn plants, distributed across four classes: Common Rust, Gray Leaf Spot, Northern Leaf Blight, and Healthy, with each category containing 1,200 images. Dataset 2 contains 660 diseased jute plant images categorized into three classes: Stem Weevil, Jassid, and Aphid - each with 220 images. Dataset 3 comprises 4800 diseased rice plant images divided into four classes: Bacterial Blight, Leaf Blast, Brown Spot, and Tungro, with 1200 images per class. (Fig. 3). Fig. 4. presents sample images from the three datasets used in the experiment. Each image serves as a visual representation of plant health conditions or diseases.

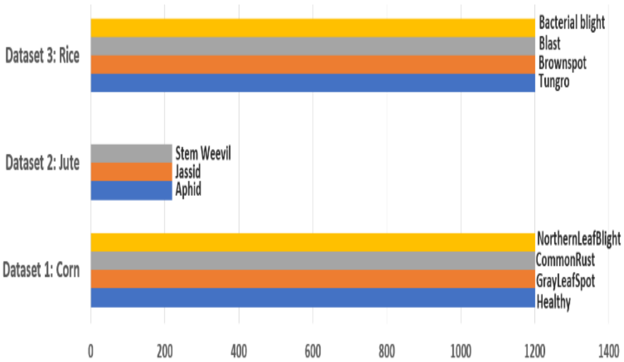

Fig. 3. Datasets: (1) 4,800 corn images across 4 classes, (2) 660 jute images across 3 classes, (3) 4,800 rice images across 4 classes.

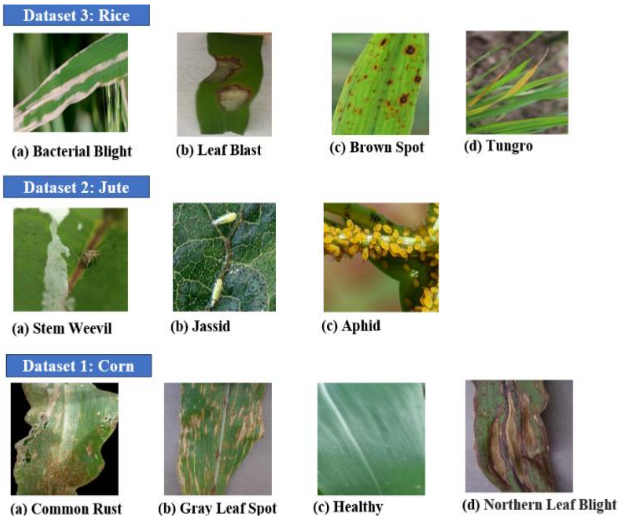

Datasets: (Dataset 3: (a) Bacterial Blight, (b) Leaf Blast, (c) Brown Spot, (d) Tungro), (Dataset 2: (a) Stem Weevil, (b) Jassid, (c) Aphid), (Dataset 3: (a) Common Rust, (b) Gray Leaf Spot, (c) Healthy, (d) Northern Leaf Blight).

Image Pre-processing

To enhance the consistency and quality of the dataset, several pre-processing steps were applied before inputting the images into the neural network. This involved applying data augmentation methods including rotation and flipping, as well as scaling every image to a standard size for pre-trained CNNs and turning it to gray-scale for LBP (Noola and Basavaraju, 2022). LBP works with the grayscale pixel intensity values of an image, which typically range from 0 to 255 in an 8-bit grayscale image (Rajeena et al., 2023). In CNNs, pixel values are often normalized by dividing them by 255, transforming the range from 0–255 (for 8-bit images) to 0–1. This normalization can improve model performance and accelerate training. Additionally, the sizes of the images are changed to 224×224 pixels when used with CNN models.

Extraction of Image Features with LBP Operator

The LBP is a simple yet powerful texture operator that labels pixels in an image by thresholding the neighbourhood of each pixel and interpreting the result as a binary number. (Huang et al., 2019).The image is initially transformed to grayscale in order to get the LBP texture description. After choosing an *r*-sized neighborhood around the central pixel for each pixel in the grayscale image, the LBP value is computed and saved in a 2D array that corresponds to the image's dimensions (Fig. 5). When comparing the center pixel to its eight surrounding neighbors, there are 256 possible LBP code permutations. If center pixel's intensity is greater than or equal to a neighbor's, the corresponding value is assigned 1; otherwise, it is set to 0 (Kamilaris and Prenafeta-Boldú, 2018). The comparison proceeds in a consistent clockwise or counterclockwise direction, starting from any adjacent pixel (Sourav and Wang, 2023). An 8-bit binary number is produced by binary comparisons throughout the 3×3 neighborhood and then transformed to a decimal value. By properly utilizing its capacity to acquire fine-grained information, the original LBP implementation performs exceptionally well at capturing complex details inside the image. This feature, however, significantly restricts the algorithm's ability to identify features on scales other than the fixed 3×3 neighborhood (Kaur and Kang, 2015).

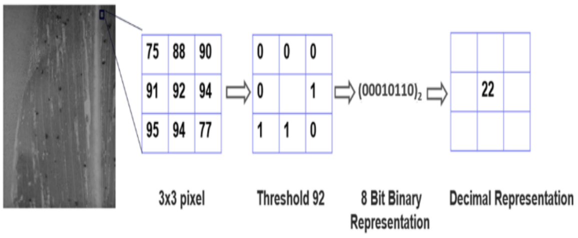

Fig. 5. Feature extraction in LBP.

Extraction of Image Features with CNN

This network is a highly effective and commonly used tool for extracting image features through deep learning techniques. In CNN-based image feature extraction, the network learns to detect and represent different image elements across multiple layers.

Convolutional layers use small filters (or kernels) to identify fundamental features such as edges, corners, and textures (Latif et al., 2022). The convolution operation includes sliding of the filter across the image and calculating the dot product between the filter and local image patches. The result is a feature map that emphasizes regions containing specific patterns of interest. (Khirade and Patil, 2015).

Table 1. List of 18 pre-trained CNN models with their respective feature layers used for performance evaluation.

Pre-Trained CNN	Feature Layer
AlexNet	fc8
ResNet-18	fc1000
ResNet-50	fc1000
VGG-19	fc8
DarkNet-19	avg1
ResNet-101	fc1000
Inception-v3	predictions
VGG-16	fc8
Xception	predictions
NasNet-Mobile	predictions
DarkNet-53	conv53
InceptionResNet-v2	predictions
DenseNet-201	fc1000
SqueezeNet	pool10
ShuffleNet	node202

GoogleNet	loss3-classifier
MobileNet-v2	Logits
EfficientNet-b0	MatMul

Table 1 lists the pre-trained CNN that was employed in this investigation as well as the fully-connected feature layer that was used to extract the image feature vectors. The CNN model is composed of multiple layers performing convolution, rectified linear units (ReLU), and pooling layers (Islam, 2020). To illustrate, a brief overview of the layered architecture of two popular CNN architectures, ResNet-101 and Darknet-19, is provided below. Fig. 6 displays the ResNet-101 structure (Kulkarni and Shastri, 2024). The design includes an input layer for feeding input images, a convolution layer, a pooling layer, and an output layer, as shown in Fig. 7.

The ResNet-101 architecture as shown in Fig. 6. begins with an input layer where images of a fixed size (typically 224×224 pixels) are fed into the network. The initial convolutional layer uses a large kernel (7×7) for feature extraction, followed by ReLU activation for normalization and non-linearity (Padilla, 2020).The network then passes through a series of stacked residual blocks, organized into four stages, each with multiple blocks. In order to mitigate the vanishing gradient issue, residual blocks in ResNet use skip connections to avoid layers and allow gradients—partial derivatives that define how weights are updated during training—to flow directly backward (Tejaswini et al., 2022).

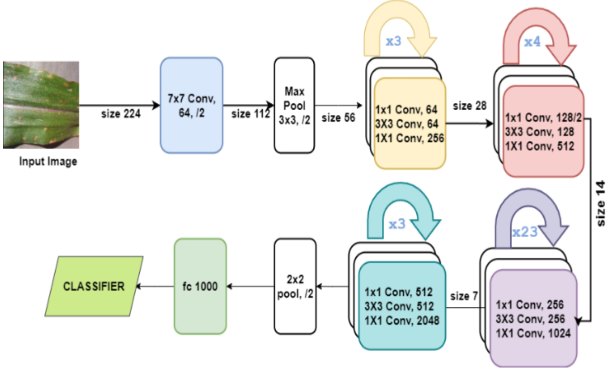

Fig. 6. The layered Architecture of Pre-Trained ResNet-101 CNN model.

Each block contains convolutional layers, batch normalization, ReLU, and a skip connection to facilitate learning residual functions. After the residual blocks, global average pooling aggregates spatial information into a vector, which is then passed through fully connected layers for classification or regression. The network uses ReLU activations throughout and ends with a SoftMax layer for image classification tasks, producing class probabilities. (Mukti and Biswas, 2019)

Darknet-19 is a CNN architecture tailored for real-time object detection. It comprises 19 convolutional layers and 5 max-pooling layers, incorporates Leaky ReLU activations, and is esteemed for its effectiveness and precision in identifying objects within images.

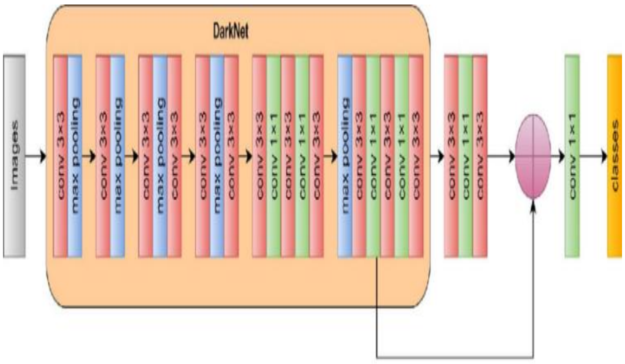

Fig. 7. The layered Architecture of Pre-Trained DarkNet-19 CNN model.

The Darknet-19 network starts with an input layer that accepts an image of size 224×224. It then applies 3×3 convolutional filters with a stride of 1, followed by max-pooling layers to reduce spatial dimensions as shown in fig. 7 (Padilla et al., 2020).To optimize computation, the network alternates between 1×1 and 3×3 filters, ensuring accuracy while reducing computational complexity. After passing through the convolutional layers, the feature maps are flattened and fed into a fully connected layer for the final classification. The output layer is a Softmax layer, which computes class probabilities for the classification task. (Panigrahi et al., 2020).

Classification of Leaf Disease Using SVM

This study utilized two feature extraction techniques: LBP and CNN. For classification tasks, a SVM, a supervised machine learning algorithm, was employed. SVM is effective for both linear and non-linear classification problems, as it identifies the optimal hyperplane that maximizes the margin between classes, ensuring robust generalization to unseen data (Awad and khanna, 2015). In this study, SVM was applied for multi-class classification within the CNN framework using the "one-vs-all" strategy. The fitcecoc function in MATLAB was used to train multiple binary classifiers, facilitating the distinction between different classes. (Shrestha et al., 2020)

In the instance of LBP, texture information is captured by comparing the intensity of a central pixel with its neighbors in order to derive feature vectors from leaf images. After that, SVM classifiers are trained using these LBP features; for complicated, non-linear problems, we used different kernels such as Radial Basis Function (RBF) for producing better accuracy.

Evaluation Metrics

Analyzing various prediction outputs and the metrics that go along with them is necessary to evaluate model performance in classification jobs. True Positives (TP), False Positives (FP), and Precision are important components that show how accurate and reliable the model is in making predictions. TP indicates that the positive class was accurately identified, whereas a True Negative (TN) happens when the model accurately predicts the negative class. On the other hand, a FP happens when a negative occurrence is mistakenly classified as positive, while a False Negative (FN) happens when a positive instance is misclassified as negative (Sun et al., 2022). The accuracy of positive classifications is indicated by precision, which is the ratio of accurately predicted TPs to all positive predictions.

$$\text{Accuracy} = \frac{\text{TP} + \text{TN}}{\text{TP} + \text{FP} + \text{FN} + \text{TN}} * 100\%$$

The ratio of correctly predicted true positives to all positive predictions. It measures how accurate positive predictions are.

$$\text{Precision} = \frac{\text{TP}}{\text{TP} + \text{FP}}$$

Sensitivity: The ratio of true positive predictions to the total number of actual positive instances. This metric evaluates the model's capability to identify all relevant examples.

$$\text{Sensitivity} = \frac{\text{TP}}{\text{TP} + \text{FN}}$$

F1 Score: The precision and recall harmonic mean. It offers an ideal balance between sensitivity and precision.

$$\text{F1 Score} = 2 * \text{Precision} * \frac{\text{Sensitivity}}{\text{Precision} + \text{Sensitivity}}$$

AUC-ROC (Area Under the Receiver Operating Characteristic Curve): This metric computes the area under the ROC curve, which ranges from 0 to 1, in order to assess the effectiveness of classification models. Better model performance is indicated by a higher AUC. Perfect class separation is shown by an AUC of 1, while no discriminative ability is indicated by an AUC of 0.5. When the model's AUC is zero, it frequently misclassifies both positive and negative targets.

Confusion Matrix: A classification model is assessed using a confusion matrix, which is a tabular representation that contrasts the model's predictions with the actual results. Predictions are divided into four sections, with accurate and inaccurate classifications for both positive and negative classes provided. The confusion matrix indicates areas that require development and offers insights into the accuracy of the model.

Performance Evaluation of LBP-based SVM

First, the feature vectors of leaf image of a particular crop (i.e., rice, jute or corn) is extracted using LBP operator. Then, three LBP-based SVM classifiers are implemented separately each for leaf images of rice, jute and corn. For this, we have utilized both RBF and Linear kernels due to their effectiveness in handling complex datasets. The investigation revealed that the RBF kernel consistently provided an average accuracy

30% higher than the Linear kernel. Consequently, the RBF kernel was chosen as the candidate for the grid search process. To optimize SVM, the process is conducted using the grid search method. This in-depth investigation covers differences in the gamma and regularization parameters (C), all of which are essential to attaining the best possible model performance. The following hyperparameters were considered for fine-tuning the SVM as shown in Fig. 7.:

Kernel: [Linear, RBF]

C: [0.1, 1, 10, 100]

Gamma: [’scale’, ’auto’, 0.1, 1, 10]

As for the gamma parameter, when it is set to ’scale’ the algorithm modifies each data point’s influence according to the reciprocal of the dataset’s feature count. Mathematically, this adjustment is represented as 1 / (n features * X.var ()) were X.var () denotes the variance of the feature values. Alternatively, when gamma is set to ’auto’, the algorithm automatically adjusts the gamma parameter based on the inverse of the number of features in the training dataset, calculated as 1 / n features. By making the SVM model learn the unique features of the dataset, these gamma shifts help to ensure a more efficient and accurate classification method.

Table 2 presents the tuning of hyperparameters γ (gamma) and C (regularization parameter) for the RBF kernel in SVM to optimize classification performance. The best performance for corn was observed with γ = scale and C = 1, while γ = scale and C = 10 yielded the best results for jute and rice, indicating that model performance is highly sensitive to appropriate hyperparameter selection.

The values for corn dataset classification using features extracted using LBP are represented in Fig. 8. With a large number of incorrect classifications across multiple classes, the confusion matrix demonstrates the model's difficulty in correctly classifying the data. Particularly for the Healthy and Grey Leaf Spot categories, numerous instances have the wrong labels.

Table 2. Tuning Hyperparameters (𝜸 and C) for RBF Kernel for achieving optimal classification performance using SVM.

Tuning Hyperparameters for RBF Kernel	Regularization Parameter (C)			
Gamma (𝜸)	C=0.1, 𝜸= scale	C=1, 𝜸= scale *(Best for corn)*	C=10, 𝜸= scale *(Best for jute & rice)*	C=100, 𝜸= scale
	C=0.1, 𝜸= auto	C=1, 𝜸= auto	C=10, 𝜸= auto	C=100, 𝜸=auto
	C=0.1, 𝜸=0.1	C=1, 𝜸= 0.1	C=10, 𝜸= 0.1	C=100, 𝜸= 0.1
	C=0.1, 𝜸= 1	C=1, 𝜸= 1	C=10, 𝜸= 1	C=100, 𝜸= 1
	C=0.1, 𝜸= 10	C=1, 𝜸= 10	C=10, 𝜸= 10	C=100, 𝜸= 10

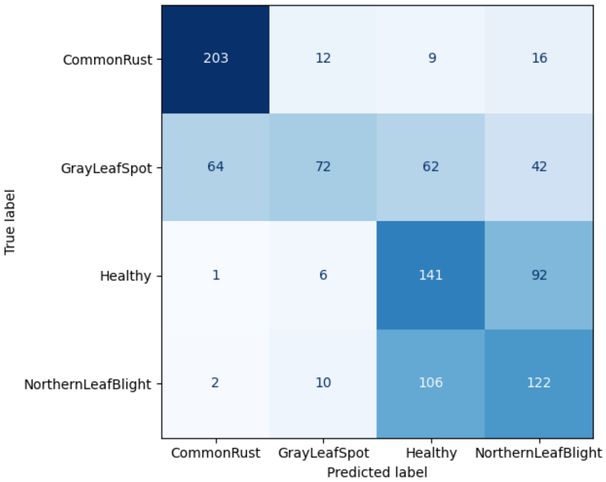

Fig. 8. Confusion matrix of the corn dataset using LBP features, with TP, TN, FP, and FN values.

Performance Evaluation of CNN-based SVM

Feature vectors were extracted separately for three crops rice, jute, and corn using a total of 18 CNN models listed in Table 1. The extracted feature vectors were then used as input to a SVM for classification.

Fig. 9. Confusion matrix of corn dataset using pre-trained ResNet-101 model, with TP, TN, FP, and FN values.

The classification performance of all the 18 CNN models was analyzed using various metrics, including accuracy, precision, sensitivity, specificity, F1 score and AUC. To illustrate the performance of the approach, confusion matrices were generated for each crop using all 18 models. A sample of corn dataset's confusion matrix is given in Fig. 9. The confusion matrix shows misclassifications are minimal, indicating strong overall performance and reliability.

Result

In our demonstration, we extracted feature vectors separately from leaf images of rice, jute, and corn using the LBP operator and 18 different CNN models. These features were then classified using the widely-used SVM. The process was performed separately for each crop's image dataset. For classification, 80% of the images from each class were used to train the SVM, while the remaining 20% were used for testing. We evaluated the performance of both LBP-based and CNN-based SVMs using accuracy, precision, sensitivity, specificity, and F1 score. Finally, a User Interface (UI) was developed for real-time model validation.

Training and Validation of the Models using 5-Folds Cross Validation

Every dataset was divided into five folds, or subsets, with the training dataset comprising 80% and the testing dataset 20% of each fold. Each of the model's k training and evaluation cycles used a different fold as the validation set. The model's overall performance has been determined by averaging the performance across the folds as depicted in fig. 10. For Rice, Corn and Jute datasets the best performing CNN models were respectively Resnet-101 and DarkNet-19.

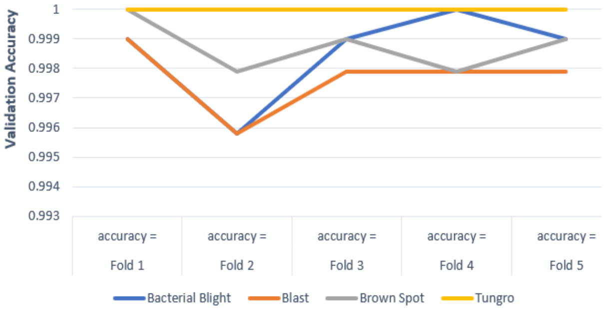

Fig. 10. 5-Fold Cross Validation of Rice Dataset for the model ResNet-101.

Result Evaluation of LBP-based SVM Model

The investigation revealed that the RBF kernel consistently provided an average accuracy 30% higher than the Linear kernel. Consequently, the RBF kernel was chosen as the candidate for the grid search process.

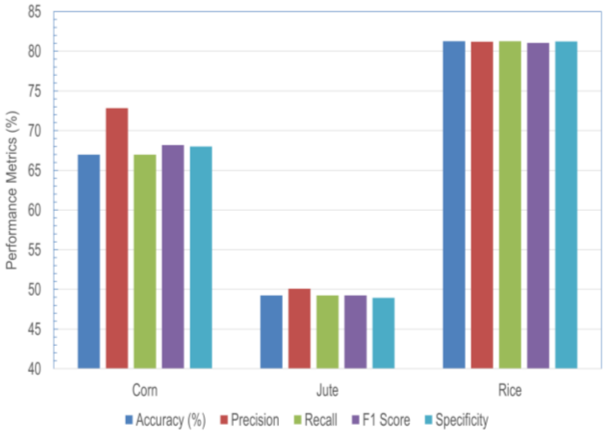

Fig. 11. Performance comparison showing accuracy, precision, recall, f1 score, and specificity of the LBP model.

Despite hyperparameter tuning of the SVM applied to features extracted through local binary pattern, the highest observed accuracy averaged at 81.25% across all datasets. Due to the suboptimal performance of LBP even with optimal SVM parameters, the research shifted to CNN-based feature extraction.

Result Evaluation and Comparison of CNN-based SVM Models

The efficiency of the network in large-scale image recognition tasks is well known, particularly when it comes to precision agriculture. In order to investigate a more reliable method of deriving features and classification with the target of much increased accuracy, a strategic move towards CNNs was made. As we can see from Fig. 12. to Fig. 17. the ResNet 101 model for Jute and Rice Datasets and Darknet-19 model for Corn Dataset fared better than any of the other models, outperforming them all in terms of precision, recall, sensitivity, specificity, f1 score, and validation accuracy. We obtained an accuracy of 99.01% for corn datasets using DarkNet-19 and an accuracy of 99.9% and 99.87% for Rice and Jute datasets respectively using ResNet-101. Figures display the findings following the validation of the models on Datasets respectively. The ResNet-101 model and DarkNet-19 outperformed the current models in every evaluation, as can be seen from the performance comparison shown in these figures.

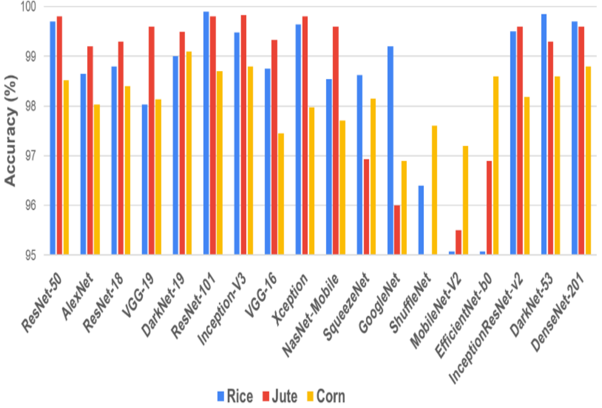

Fig. 12. Accuracy comparison of the pre-trained models considering independent training and validation dataset.

The comparative analysis of CNN models for agricultural datasets highlights the effectiveness of specific architectures for different crops. The Resnet-101 model, known for its deep residual learning frame work, has shown superior performance for Rice and Jute datasets, indicating its robust feature extraction capabilities in diverse conditions. Meanwhile, the Darknet-19 model, with its inception modules, has proven to be the most accurate for the Corn dataset, suggesting that its architecture may be better suited for the particularities of corn's image data. The close performance of ResNet-101 for the Corn dataset also suggests that it is a versatile model that can be considered for various agricultural applications. This information can guide future research and practical applications in precision agriculture, optimizing crop monitoring and management through tailored CNN model selection.

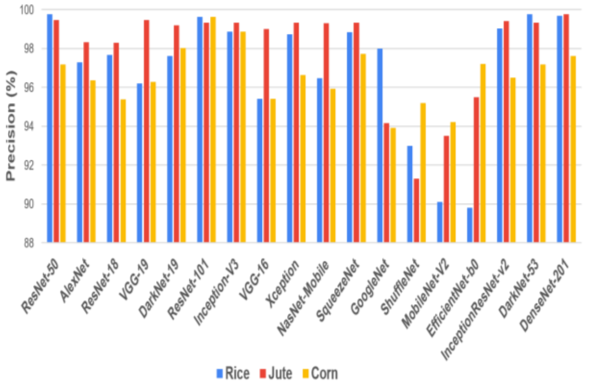

Fig. 13. Precision comparison of the pre-trained models considering independent training and validation dataset.

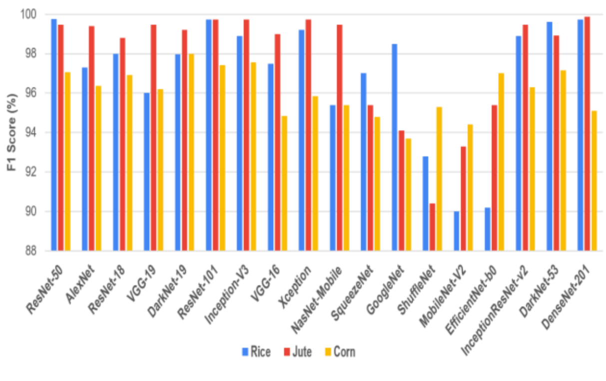

Fig. 14. F1 Score comparison of the pre-trained models considering independent training and validation dataset.

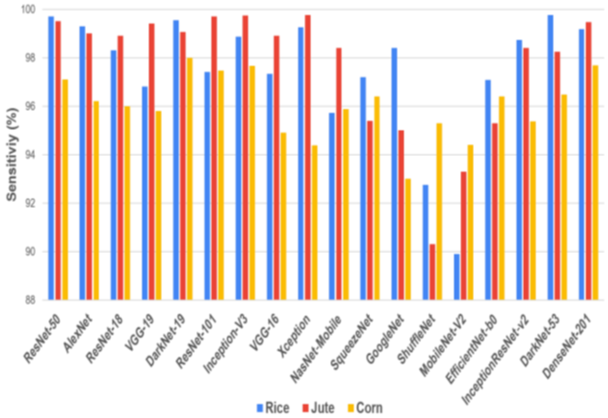

Fig. 15. Sensitivity comparison of the pre-trained models considering independent training and validation dataset.

Furthermore, its adaptability to different crops highlights the potential for scalable solutions in disease detection and overall crop health assessment.

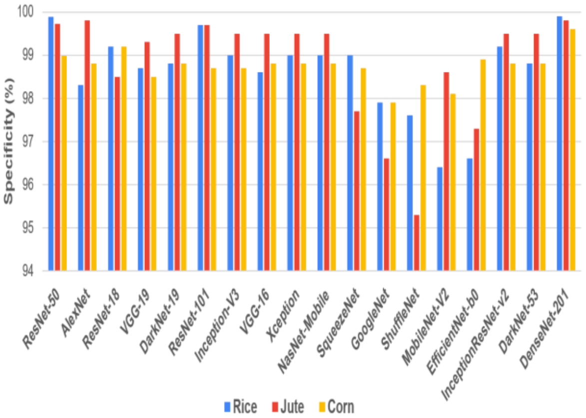

Fig. 16. Specificity comparison of the pre-trained models considering independent training and validation dataset

Future studies can further refine model architectures to improve accuracy and efficiency in diverse agricultural environments.

Table 3. Performance metrics comparison of CNN models across various studies, including accuracy (A %), precision (P %), sensitivity (S %), specificity (sp %), and F1 score (F %).

Author	Model	Total Image	Class	A %	P %	S %	Sp %	F %
Pangrahi et al.	CNN	3823 (Corn)	3	98.7	98.6	98.9	-	98.7
Daneshwari et al.	EKNN	3820 (Corn)	4	99.8	-	-	99.6	-
Rajeena et al.	Efficient Net	3188 (Corn)	4	98.8	88	-	98	-
Sourav and Wang	CNN	1535 (Jute)	4	-	95	95	-	95
Latif et al.	DCNN	2187 (Rice)	6	96	96.2	96.1	99.2	96.1
This Paper	Resnet101 + SVM	4,800 (Rice)	4	99.9	99.6	99.6	99.7	99.7
This Paper	Resnet101 + SVM	660 (Jute)	3	99.8	99.4	99.7	99.7	99.7
This Paper	Darknet19 + SVM	4,800 (Corn)	4	99	98	98	98.8	98

Comparison Analysis of Different Studies

A comparative analysis between this paper and other relevant studies demonstrates that our modified CNN + SVM model exhibited superior performance. Specifically, our model achieved 99.9% accuracy for Rice, 99.87% for Jute, and 99.01% for Corn datasets when utilizing the ResNet-101 and DarkNet-19 CNN models.

Table 3 compares the performance metrics of various CNN models used in prior studies and the proposed models in this paper. The proposed ResNet101 + SVM and Darknet19 + SVM models outperformed existing methods across all metrics, achieving accuracy rates up to 99.9% and F1 scores of 99.7%, demonstrating superior precision, sensitivity, and specificity in crop disease classification for rice, jute, and corn.

Prediction in Real Time with Graphical User Interface

A GUI application for disease detection with pre-trained models has been created through the “Browse” button. The “Detect” button displays the predicted label to the users. Using the MATLAB R2021a version, users can explore and choose an image for disease classification using the GUI. The “Train” button causes the model to be trained on a predefined dataset. Training outcomes, such as accuracy and a confusion matrix, are then displayed. It applies the trained model to extract features and predict the disease class, displaying overall accuracy through the “Accuracy” button. Users can then input new test data using the “Browse” button.

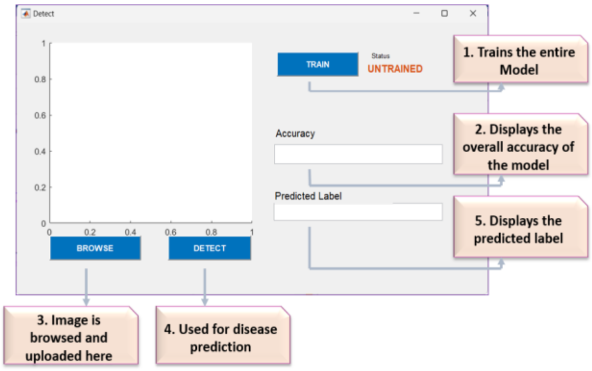

1. Trains the entire Model

2. Displays the overall accuracy of the model

5. Displays the predicted label

3. Image is browsed and uploaded here

4. Used for disease prediction

Fig. 17. Labelling of UI Components.

The disease detection system can be interacted with through an easy-to-use interface thanks to the GUI’s text labels, axes, and buttons. The deep learning model’s information is stored by the code using global variables.

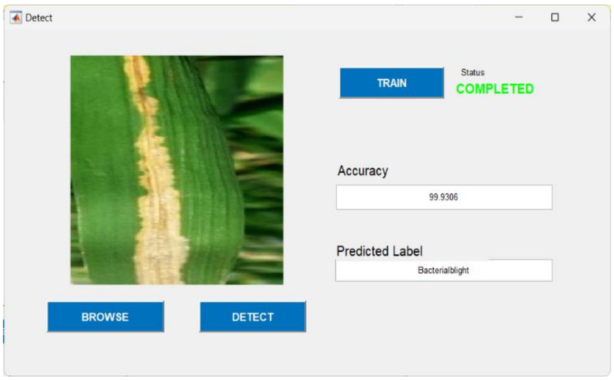

Status
COMPLETED

Accuracy
99.9306

Predicted Label
Bacterialblight

Fig. 18. Validation of the model using UI.

A sample image from rice dataset have been uploaded for prediction using pre-trained ResNet-101 as shown in Fig. 18. The model accurately predicted the label of the given image as “Bacterial Blight” with an accuracy of 99.9% respectively.

Discussion

With distinct advantages over more conventional techniques like LBP-SVM, this study highlights the potential of CNNs in the detection of plant diseases and pests. ResNet-101 and DarkNet-19 singled out for their performance across the rice, jute, and corn datasets out of the 18 CNN models that were assessed in the study. Accurate crop monitoring depends on these models' ability to recognize intricate leaf patterns, discolouration, and insect structures. Furthermore, their applicability extends beyond disease detection to pest identification due to their capacity to identify structural characteristics of pests, such as shape and segmentation patterns.

By beating conventional deep learning models in terms of accuracy and classification measures, a comparison with previous research showed how successful the modified CNN-SVM method was. Computational demands are still a problem, though, particularly in settings with restricted resources. Looking ahead, there are several avenues for improvement and expansion. Efforts to optimize the model for lower computational costs such as portable mobile phones without compromising accuracy will make the technology more accessible.

Conclusion

With an accuracy of up to 99%, this study shows how CNN-based models can revolutionize the identification of plant diseases and pests. These models provide an efficient instrument for precision agriculture by precisely detecting pest structures, textural alterations, and leaf discolouration. The incorporation of these models into simple user interfaces may enable early diagnosis, lowering crop losses and enhancing yield management in Bangladesh, where agriculture is essential to the country's economy and food security. Farmers in rural areas need this information because they experience limited resource availability together with restricted access to knowledge.

Further development of the technology should tackle current computational constraints in order to expand accessibility and enable national adoption. Deep learning developments combined with the use of mobile and edge devices may close this gap and make these technologies usable even in settings with limited resources. The advancement of agricultural technologies would help sustain farming practices while securing national food supply and increasing resource effectiveness throughout Bangladesh’s agricultural sectors.

Acknowledgement

The authors are grateful to Bangladesh University of Professional’s Department of Information and Communication Engineering and and their supervisor Dr. Abul Kalam Azad for providing the tools and assistance needed to complete this research. They also acknolwedge the support of colleagues and mentors, who provided direction and encouragement throughout the study process. Lastly, the authors extend their heartfelt gratitude to friends and family for their unwavering support and encouragement, which served as a const ant source of motivation throughout this journey.

Author Contributions

All authors have a substantial contribution to the research and is responsible for the content. Noshin Un Noor helped conceptualize the study, supervised the research process, coparative analysis and edited the manuscript. The methodology and result analysis was developed by Faria Solaiman. Authors dealt with validation of results. Both authors contributed as data curators, performed formal analysis and were involved in the investigation and interpretation of the findings. The authors drafted the original manuscript, prepared the visualizations, managed necessary resources and have read and approved the final version of the manuscript.

Declaration of Conflicting Interests

The author(s) declare that they have no conflicts of interest regarding the publication of this article. All authors are affiliated with the Bangladesh University of Professionals, and no financial support was received for this research.

References

Agarwal M, Gupta SK, and Biswas KK. Development of efficient CNN model for tomato crop disease identification. *Sustain. Comput. Inform. Syst.* 2020; 28(1): 100407.

Naidu A, Majji V, and Kumaravelan G. A review of machine learning approaches in plant leaf disease detection and classification. *Proc. IEEE 3rd Int. Conf. Integr. Commun. Technol. Virtual Mobile Networks (ICICV)*, 2021.

Awad M, and Khanna R. Support vector machines for classification. *Efficient Learning Machines: Theories, Concepts, and Applications for Engineers and System Designers* 2015:39-66.

Bharate AA, and Shirdhonkar MS. A review on plant disease detection using image processing. *Proc. IEEE Int. Conf. Intelligent Sustainable Systems (ICISS)*, 2017.

Falaschetti L, Manoni L, Di Leo D, Pau D, Tomaselli V, and Turchetti C. A CNN-based image detector for plant leaf diseases classification. *HardwareX*, 2022; 12:e00363.

Gandhi R, Panda K, Sahoo AK, and Das H. Plant disease detection using CNNs and GANs as an augmentative approach. Proc. IEEE Int. Conf. Innovative Research Development (ICIRD), 2018.

Hassan SM, Maji AK, Jasiński M, Leonowicz Z, and Jasińska E. Identification of plant-leaf diseases using CNN and transfer-learning approach. *Electronics*, 2021; 10(12): 1388.

Huang S, Liu W, Qi F, and Yang K. Development and validation of a deep learning algorithm for the recognition of plant disease. *Proc. IEEE 21st Int. Conf. High Performance Comput. Commun. IEEE 17th Int. Conf. Smart City IEEE 5th Int. Conf. Data Science Systems HPCC/SmartCity/DSS*, 2019; 1951-1957.

Islam MT. Plant disease detection using CNN model and image processing. *Int. J. Eng. Res. Technol.*, 2020; 9(10):291-297.

Kamilaris A, and Prenafeta-Boldú FX. A review of the use of convolutional neural networks in agriculture. *J. Agric. Sci.*, 2018; 156(3): 312-322.

Kaur R, and Kang SS. An enhancement in classifier support vector machine to improve plant disease detection. *Proc. IEEE 3rd Int. Conf. MOOCs Innov. Tech. Educ. (MITE)*, 2015.

Khirade SD, and Patil AB. Plant disease detection using image processing. *Proc. IEEE Int. Conf. Computing Communication Control Automation*, 2015.

Kulkarni P, and Shastri S. Rice leaf diseases detection using machine learning. *J. Sci. Res. Technol.* 2024:17-22.

Latif G, Abdelhamid SE, Mallouhy RE, Alghazo J, and Kazimi ZA. Deep learning utilization in agriculture: Detection of rice plant diseases using an improved CNN model. *Plants*, 2022; 11(17): 2230.

Hasan MJ. Rice disease identification and classification by integrating support vector machine with deep convolutional neural network. *Proc. IEEE 1st Int. Conf. Advances Science Engineering Robotics Technol. (ICASERT)*, 2019.

Mukti IZ, and Biswas D. Transfer learning based plant diseases detection using ResNet50. *Proc. IEEE 4th Int. Conf. Electrical Info. Commun. Technol. (EICT)* , 2019.

Noola DA, and Basavaraju DR. Corn leaf image classification based on machine learning techniques for accurate leaf disease detection. *Int. J. Electr. Comput. Eng.*, 2022; 12(3): 2509-2516.

Padilla DA, Pajes RAI, and De Guzman JT. Detection of corn leaf diseases using convolutional neural network with OpenMP implementation. *Proc. IEEE 12th Int. Conf. Humanoid Nanotechnol. Inf. Technol. Commun. Control Environ. Manage. (HNICEM*), 2020.

Panchal P, Raman VC, and Mantri S. Plant diseases detection and classification using machine learning models. *Proc. IEEE 4th Int. Conf. Computational Systems Information Technol. Sustainable Solutions (CSITSS*), 2019.

Panigrahi K, Panda K, Sahoo AK, and Das H. A CNN approach for corn leaves disease detection to support digital agricultural system. *Proc. IEEE 4th Int. Conf. Trends Electron. Informatics*, 2020; 48184.

Rajeena PP, Fathimathul, Aswathy SU, Moustafa MA, and Ali MAS. Detecting plant disease in corn leaf using approach. Electronics, 2023; 12(8): 1938.

Rajendran G, and Islam R. Plant clinics in Bangladesh: are farmers losing less and feeding more? *CABI Case Study*, 2017; 19.

Sharma P, Singh Berwal YP, and Ghai W. Performance analysis of deep learning CNN models for disease detection in plants using image segmentation. *Inf. Process. Agric.*, 2020; 7(4): 566-574.

Shrestha G, Das M, and Dey N. Plant disease detection using CNN. *Proc. IEEE Appl. Signal Process. Conf. (ASPCON)*, 2020.

Sourav MSU, and Wang H. Intelligent identification of jute pests based on transfer learning and deep convolutional neural networks. *Neural Process. Lett.*, 2023; 55(3): 2193-2210.

Sun X, Li G, Qu P, Xie X, Pan X, and Zhang W. Research on plant disease identification based on CNN. *Cognitive Robotics*, 2022; 2: 155-163.

Tejaswini P, Singh P, Ramchandani M, Rathore YK, and Janghel RR. Rice leaf disease classification using CNN. *IOP Conf. Ser. Earth Environ. Sci.*, 2022; 1032(1):012017.

Tugrul B, Elfatimi E, and Eryigit R. Convolutional neural networks in detection of plant leaf diseases: A review. *Agriculture*, 2022; 12(8): 1192.

J. Bangladesh Acad. Sci. 49(1); 87-102: June 2025 DOI: https://doi.org/10.3329/jbas.v49i1.79738

Journal of Bangladesh Academy of Sciences

Journal homepage: http://www.bas.org.bd/publications/jbas.html

Research Article

Assessing corrosion and scaling potential of drinking water samples: A case study of Chattogram water distribution network, Chattogram, Bangladesh

Ummeh Sadia[1], Md. Akter Hosen Rifat[1], Md. Abid Hasan[1], Nobonita Sarker[2], Shahidul Islam[2], Mohammad Fahimul Hoque[1], Md Abdus Sabur[3], Amitava Bandyopadhyay[4*] and Sumon Ganguli[1*]

Department of Applied Chemistry and Chemical Engineering, University of Chittagong, Chattogram, Bangladesh.

ARTICLE INFO

Article History

Received: 09 February 2025
Revised: 10 April 2025
Accepted: 21 April 2025

Keywords: Corrosion, Scaling potential, Drinking water, Water quality.

ABSTRACT

The consequences of corrosion and scaling potential in drinking water resources are susceptible to public health. In Chattogram, Bangladesh, the Chattogram Water Supply and Sewerage Authority (CWASA) is principally responsible for providing water and sanitation services. Here, 100 samples were collected to forecast the corrosive-scaling behaviors using five indices: Aggressiveness (AI), Puckorius (PSI), Larson-Skold (LS), Langlier (LSI), and Ryznar (RSI). The findings revealed that 100% of the samples had corrosive tendencies established on the values for LSI, RSI, and PSI; in contrast, the LS index indicated scaling tendency in 83% of the samples, and the remaining samples either showed corrosion or a high corrosion rate. A range of artificial and natural sources of potential contamination were indicated by statistical correlations and principal component analysis (PCA). To prevent problems with finances and health, water supply networks should take corrective action to remove corrosion and its by-products.

Introduction

The most significant factor that can affect the general public's health, the acceptability of the water source, and the price of supplying clean water is corrosion. The kind and extent of scaling and corrosive compounds, the location of the water source about the surface or ground, and the physico-chemical and biological quality of the water are all significant factors in determining the stability of water for general and industrial uses. Corrosion-induced material degradation can result in substantial annual resource expenditures for replacement, repairs, and system upkeep. Many metals are more concentrated in tap water due to corrosion. Pipes in the water distribution lines are constructed of a variety of materials, and corrosion allows different substances to enter the water body (Asghari et al., 2018). Corrosion characteristics of water can lead to pitting in pipes, shortened facility life spans, and water loss. Furthermore, the most significant health issues associated with corrosion are caused by heavy metals found in drinking water, such as lead, copper, zinc, and arsenic (Mirzabeygi et al., 2017).

Dissolution and carbonate reactions often raise pH levels, harming disinfectants, water aesthetics, and asbestos fiber release. This raises regulatory concerns. Although plastic plumbing materials have higher corrosion resistance, they can also deteriorate due to their particular appliances and cause other obstacles such as odor, taste, brittleness, support for biofilms, and both organic and inorganic leachates.

---

*Corresponding author:<sumonganguli@cu.ac.bd, amitava.bandy1@gmail.com>

[1] *Biomaterials Research Laboratory, Dept. of Applied Chemistry and Chemical Engineering, University of Chittagong, Chattogram, Bangladesh.*

[2] *Department of Geography and Environmental Studies, University of Chittagong, Chattogram, Bangladesh.*

[3] *Department of Chemistry, Jahangirnagar University, Savar, Dhaka, Bangladesh.*

[4] *Department of Chemical Engineering, University of Calcutta, 92, APC Road, Kolkata, India.*

The other issue is the scaling of $CaCO_3$ caused by the deposition of excess carbonates in the pipe network and other machine parts (Asghari et al., 2018). Divalent cations (Ca^{2+}, Mg^{2+}) react with other substances soluble in water to form a tinny layer that builds up inside the walls of water pipelines. This process is known as scaling. Generally, the scaling layers are made of $CaCO_3$. In addition to raising operating and maintenance expenses, the scaling process can result in issues like clogged tubes, decreased water pressure and discharge, and decreased water discharge in the distribution network (Mirzabeygi et al., 2017).

The two most common problems with water quality are corrosion and scaling. There are various causes for both of these processes, and the literature offers a variety of assessment techniques. The most popular methods for assessing the degree of these two processes are the Aggressive index (AI), Pukorious index (PI), Larson-Skold index (LS), Langelier saturation index (LI), and Ryznar index (RI). Numerous researchers worldwide employ these techniques (Kalyani et al., 2017; Alipour et al., 2015; Shams et al., 2012; Alsaqqar et al., 2014). As an illustration, Kumar (2019) claimed that the purpose of the Ryznar and Langelier indices was to show significant harm to the industries' machinery. Rabbani et al. (2012) looked into the agrarian water assets. They reported that almost all samples were extremely corrosive, increasing the risk of framing scales for the Ryznar, Langelier, and Puckorius indices. Kurdi et al. (2015) looked into the erosion and revealed particle-dependent scaling accounts. Additionally, corrosion and scaling records can be used to evaluate the corrosive activity of groundwater (Kurdi et al., 2015). Further research on water quality using the aforementioned stability indices was conducted in several countries, including Makou (Asghari et al., 2018), China (Zhang et al., 2018), India (Ahmed et al., 2021), Ecuador (Maroneze et al., 2014), Ethiopia (Gebremikael and Dawod, 2021), Iran (Gholizadeh et al., 2017), Jordan (Al-Rawajfeh and Al-Shamaileh, 2007), Iraq (Al-Qurnawi et al., 2022), Kenya (Baloïtcha et al., 2022), Niger (Weissbrodt et al., 2020), Nigeria (Egbueri, 2021), Romania (Gavriloaiei, 2016), Taiwan (Chien et al., 2009) and USA (Zhang et al., 2014). These studies show how important the topic is.

An investigation on the water supply lines in the Bangladeshi city of Sylhet was reported. In addition to the Surma River's BOD and COD, the study focused on four water quality indices such as the Aggressive Index (AI), the Pukorious Scaling Index (PSI), the Langelier Saturation Index (LSI), and the Ryznar Stability Index (RSI). Based on the stability indices, the findings suggested that the river water had a slightly corrosive effect (Uddin et al., 2020 a). A thorough investigation assessed the Karnaphuli River, Chattogram, for various water quality parameters. For continuous monitoring, water samples were specifically taken from ten locations during the hydrological year 2014–2015 at three distinct times of the year (winter, rainy, and spring). The reported values for the Water Quality Index (WQI), LSI, and RSI were 99.92, −3.06, and 12.36, respectively, indicating subpar water quality (Uddin et al., 2020 b).

The background research studies also showed no published literature on the valuation of the corrosion and scaling potential of Chattogram City, Bangladesh's supply water. The current study targets to address the knowledge gap in the literature by examining the corrosion and scaling potential of Chattogram city's (Bangladesh) supply water. This study aims to evaluate water quality parameters and associations within the indices using correlation analysis, assess the water supply according to physicochemical parameters, and estimate water's corrosion-scaling characteristics using the water stability indices. This study aims to ensure a safe domestic and industrial water supply in Chattogram, Bangladesh, by assessing its corrosive and scaling integrity for the first time. The study's rationale goes beyond simply checking the quality of water. The present findings of this study may be applied to more research to improve the regulatory decision support system.

Materials and methods

Study area

Bangladesh's second-biggest city is Chattogram (Mia et al., 2015). The 157 square kilometer Chattogram City Corporation (CCC) is situated between latitudes 22°13' and 22°27' north and longitudes 91°40' and 91°53' east. This metropolis is home to about 4 million people, according to the national census 2011 and Bangladesh Statistics from 2019. The city's uncontrollable population growth has raised sewage, water supply, and stormwater drainage demand. The Chattogram Water Supply and Sewerage Authority (CWASA) of Bangladesh uses its distribution network to supply water to Chattogram City's residents after treating water from the Karnafuli and Halda rivers, as well as a groundwater source (Debnath et al., 2022). According to CWASA, the maximum of 220 million liters of water per day is insufficient to meet the daily demand of 550 million liters for commercial, industrial, and residential users (Mia et al., 2015). Conversely, the annual average temperature in the Chattogram district varies from 13.5 °C to 32.5 °C (Ahmed et al., 2018). CWASA owns a 570 km water supply pipeline. The proportion of groundwater to surface water used is 52:48 (Amin, 2006).

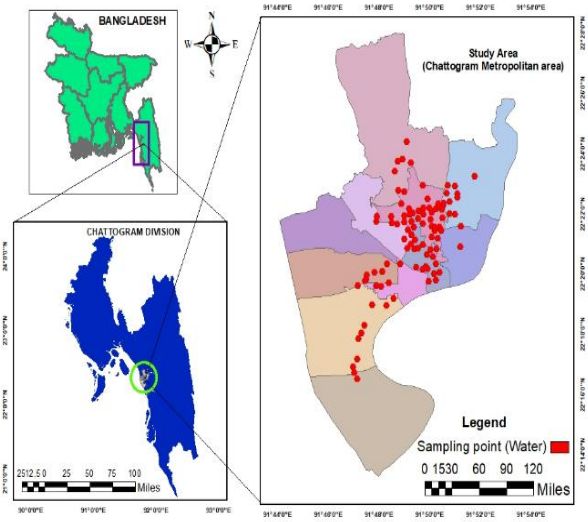

Fig. 1. Map of Chattogram and sampling sites.

Sampling and analysis

Laboratory-grade sampling bottles were used to collect one hundred (100) samples, which were then moved to the Biomaterials Research Laboratory and kept fresh in a refrigerator. The samples were gathered in 2022 between August and September. With the sampling locations included, Fig. 1 depicts the study area. A variety of parameters, including temperature, electrical conductivity (EC), total dissolved solids (TDS), pH, bicarbonate (HCO_3^-), carbonate (CO_3^{2-}), total hardness (TH), calcium hardness (Ca-H), total alkalinity (Alk.), chloride (Cl^-), and sulfate (SO_4^{2-}) were measured to judge corrosion and scaling potential of the supply water. A portable combometer was employed at the sampling locations to monitor the pH, TDS, EC, and temperature. Furthermore, according to the American Public Health Association's (APHA) recommendation, Ca-H, HCO_3^-, CO_3^{2-}, and Cl^- were measured using a straightforward titration method (APHA, 2017). Alk. was also measured using titrimetric method (APHA, 2002). A UV-visible spectrophotometer (Shimadzu, UV1800ENG240V, SOFT, Japan) was used to analyze the SO_4^{2-} content (APHA, 2017). Every measurement was carried out in triplicate, and the average results were considered for further analysis.

Water stability indices

The LSI, RSI, PSI, LS, and AI are among the corrosion indices that have been calculated to measure water's corrosion and scaling potential. Table 1 displays the equations that were utilized to assess these indices.

Statistical analysis

SPSS software (version 29.0) computed descriptive statistical analysis parameters like mean, minimum, maximum, and standard deviation. The SPSS-29.0 program was also used to carry out correlation analysis. The OriginPro software (version 2021) was used to create the box plot. Additionally, the same program, Origin, was used for PCA analysis.

Table 1. Water stability indices for corrosion and scaling potential and water condition based on the index value.

Index	Index Formula	Index value	Water condition based on the index value	Reference
Langelier Saturation Index (LSI)	LSI=pH-pHs. Here, pHs=(9.3+A+B) -(C+D) A = (log [TDS] − 1)/10, B = −13.12 × log [˚C + 273] + 34.55, C = log [Ca^{2+} as $CaCO_3$] − 0.4, and D = log [alk. as $CaCO_3$].	LSI>0 LSI=0 LSI<0	Under saturated; Corrosion potential. Equilibrium: No Scaling potential. Supersaturated water; Scaling potential.	
Ryznar Stability Index (RSI)	RSI=2pHs-pH	RSI<6 6<RSI<7 RSI>7	Supersaturated Scaling potential. Saturated Equilibrium; No Scaling Potential. Under saturated; Corrosion potential.	
Puckorius Scaling Index (PSI)	PSI=2(pH_{eq})-pHs. pHs=1.465+log (Alk.) +4.54 pH_{eq}=1.465×log (Alk.) +4.54	PSI<6 6≤PSI≤7 PSI>7	Scaling potential. Equilibrium. Significant corrosion potential	(Tyagi and Sarma, 2020)
Larson-Skold Index (LS)	LS= (Cl^- +SO_4^{2-})/ (HCO_3^- +CO_3^{2-})	LS<0.8 0.8<LS<1.2 LS>1.2	Scaling potential. Corrosion potential. High corrosion rates.	
Aggressive Index (AI)	AI=pH+ log[(Alk.) (Ca-H)]	AI<10 10≤AI≤12 AI>12	Corrosion potential. Moderately corrosive. Scaling potential and non-aggressive.	

Note: pH: actual pH of water, **pHs:** pH at saturation state of $CaCO_3$, **TDS:** (mg/L), **°C:** Temperature, **Ca^{2+}:** (mg/L as $CaCO_3$), **Alk.: (**mg/L as $CaCO_3$), **pHeq:** pH at equilibrium, **Cl^-:** (mg/L), **SO_4^{2-}:** (mg/L), **HCO_3^-: (**mg/L as $CaCO_3$).

Results and discussion

The various physicochemical characteristics of the supplied water are statistically analyzed and are shown in Table 2. Every parameter was analyzed, and the results were compared to the standards stipulated by the World Health Organization (WHO, 2004), the United States Environmental Protection Agency (USEPA, 1994), and the Bureau of Indian Standards (IS, 10500: 2012).

Table 2. Physico-chemical properties of water analyses.

Parameters	Unit	Mean ± SD value	Min	Max	WHO standard	USEPA standard	IS standard	% of samples exceeded the limits
pH	-	6.70 ± 0.25	6.1	7.4	6.5-8.5	6.5-8.5	6.5-8.5	-
Temperature	°C	25.70 ± 0.83	24.1	27.2	20-30	-	-	-
TDS	mg/L	122.61 ± 136.93	32	736	500	500	500–2000	5 (WHO, USEPA)
EC	mS/cm	0.17 ± 0.27	0.06	1.57	0.5	-	1.5	5 (WHO, IS)
Turbidity	NTU	0.87 ± 1.07	0.05	5.13	5	-	10	1 (WHO)
Salinity	ppt	1.06 ± 1.43	0	5	-	-	-	-
Cl^-	mg/L	33.95 ± 77.06	2.61	438.51	250	-	250-1000	4 (WHO, IS)
TH	mg/L	65.97 ± 53.93	36	490	300	-	200-600	1 (IS)
CO_3^{2-}	mg/L	0±0	0	0	-	-	-	-
HCO_3^-	mg/L	71.52 ± 17.30	61	167.75	200	-	200-600	-
SO_4^{2-}	mg/L	12.70 ± 13.12	0.072	69.43	250	-	200-400	-
Ca-H	mg/L	56.60 ± 46.75	24.19	418.93	-	-	75-200	1 (IS)
Alk.	mg/L	36.53 ± 10.20	22	76	-	-	-	-

pH, TDS, EC, Salinity, and Turbidity

The pH in this investigation was 6.10 to 7.40, with an average value of 6.70 ± 0.25. The water in this area had a mean pH value almost precisely at the lowest value of 6.5 of the allowable range, according to WHO (2004) and IS (10500: 2012) standards. Free CO2 and HCO_3^- concentrations may mainly cause acidic pH (Isa et al., 2012; Zhuo et al., 2015; Mirzabeygi et al., 2017; Kalyani et al., 2017). For the supply water of Chittagong City, similar results of nearly neutral water were previously reported (Molla et al., 2014). The water may have become weakly acidic or indirectly acidic due to minuscule amounts of inorganic sediments or agricultural and household wastes (Sarker et al., 2019). Remarkably, the measured pH does not directly affect public health (Shabbir and Ahmad, 2015). Nevertheless, acidic water corrodes metals and lessens the efficacy of disinfection, which has unintended health effects on humans (Popoola et al., 2019). The average temperature was measured as 25.70 ± 0.83°C, with variations between 24.10 and 27.20 ºC (Table 2). This indicates that every sample stayed within the 20–30 ºC recommended range of the WHO (2004). TDS suggests the presence of both organic and inorganic materials (Rifat et al., 2021). The TDS varied from 32.00 to 736.00 mg/L, with a mean value of 122.61 ± 136.95 mg/L (Table 2). The observed values of TDS at five distinct locations (SS-13, SS-85, SS-90, SS-97, and SS-98) were higher than 500 mg/L as stipulated by the WHO (2004), while the observed values of TDS for all other samples were within 500 to 2000 mg/L as stipulated by the IS (10500: 2012) (Table 2). Thus, the water samples from each sampling station resembled freshwater, with a mean TDS concentration of less than 1000 mg/L (USEPA Region and Foia, 2008).

The water samples' observed EC varied from 0 to 157 mS/cm, with a mean value of 0.17 ± 0.27 mS/cm. Merely five samples (SS-13, SS-85, SS-90, SS-97, and SS-98) surpassed the WHO's permissible standards of 0.5 mS/cm and the IS's permissible standards of 1.5 mS/cm, while the remaining samples were significantly below these standards. The current investigation's observed EC values for 95% of the samples were less than 1000 μS/cm, indicating that the water samples had very little mineralization. However, the WHO defines "low salinity water" as having an EC of between 0 and 250 μS/cm; by this specification, the samples under study showed low salinity (USEPA, 1994). A lower EC indicated less nutrient content, salinity intrusion, and aquifer mineral dissolution (Rifat et al., 2021). The observed values of EC of less than 1000 μS/cm for 95% of the water samples taken for this study fit the Detay et al. (1997) definition of very weakly mineralized (Rifat et al., 2021).

The salinity of drinking water may be a factor in hypertension (Rifat et al., 2021). Few samples had salinities higher than 5 ppt. The current study's salinity ranged from 0.00 to 5.0 ppt, with an average value of 1.06 ± 1.43 ppt. Turbidity is a crucial criterion for drinking water quality because it can harm one's health if consumed (Rifat et al., 2021). The turbidity value went from 0.05 to 5.13 NTU, and the average value was 0.87 ± 1.07 NTU. Except for one sample (SS-13), all of the observed turbidity values fell between the WHO and IS's allowable limits (5.0 and 10.0 NTU). Turbidity may be caused by dissolved material accumulating in supply lines and water storage tanks.

TH, Ca-H, Cl^-, CO_3^2, HCO_3^-, SO_4^{2-}, Alk.

The total dissolved ion in the water is represented by its total hardness (TH). Carbonated or transitory ($CaCO_3$, $MgCO_3$, $Ca(HCO_3)_2$, $Mg(HCO_3)_2$) and non-carbonated or permanent ($CaCl_2$, $MgCl_2$, $CaSO_4$, $MgSO_4$) are the common two forms of hardness. Hard water use is indicated by the speed at which scaling develops. Scaling buildup in excess drinking water causes kidney illnesses and can frequently clog drip irrigation sprinklers, low-pressure boilers, and water heaters (Vasanthavigar et al., 2010). With a mean value of 65.97 ± 53.93 mg/L, the observed range of TH was 36.0 to 490.0 mg/L. The TH values of the

CWASA water samples range from 200 to 600 mg/L, which is within the IS standards; only the sample (SS-97) had a TH value that exceeded the WHO standards. It should be noted that the $CaCO_3$ concentration in soft water is less than 75 mg/L, while it varies from 75 to 150 mg/L in slightly hard water, from 150 to 300 mg/L in moderately hard water, and above 300 mg/L in very hard water (Tyagi and Sarma, 2020).

A little over 86% of samples fall into the soft category, 9% into the slightly hard, 4% into the moderately hard, and 1% into the very hard water category. The Ca-H values ranged from 24.19 to 418.93 mg/L, whereas the mean value of 56.60 ± 46.75 mg/L. It was observed that just one sample (SS-97) exceeded the IS requirement. The alk. acid-neutralizing ability of [HCO_3^-], [CO_3^{2-}], and [OH^-] ions, which are abundant in groundwater aquifer systems, determines the pH of water. The effects of CO_3^{2-} equilibrium characterize the presence of [HCO_3^-], whereas the temperature, pH, cations, dissolved CO_2, and other dissolved solids are the main factors that control the proportion of [HCO_3^- - CO_3^{2-}] in freshwaters (Krishna et al., 2015). All the examined water samples had CO_3^{2-} values of zero. The HCO_3^- ranged from 61.00 to 167.75 mg/L, with a mean value of 71.52 ± 17.30 ppm. Every sample in this investigation was recorded within the WHO, and IS recommended ranges. Table 2 shows that the average value of Cl^- was 33.95 ± 77.06 mg/L, with a range of values from 2.61 to 438.51 mg/L. It was found that four samples (SS-85, SS-90, SS-97, and SS-98) exceeded the all-out allowable level (250 mg/L) that the WHO and IS had recommended. Typically, soluble Ca, Mg, and Na complexes with SO_4^2 are found in groundwater. Within the present investigation, the average SO_4^{2-} concentration ranged between 0.07 and 69.43 mg/L with a variation of 12.69 ± 13.12 mg/L.

WHO and IS stipulated the highest allowable levels of SO_4^{2-} are 250 mg/L and 400 mg/L, respectively. SO_4^{2-} concentrations ranged from 0.07 to 69.43 mg/L, and the mean SO_4^{2-} value was 12.70 mg/L. The findings show that the sulfate concentration was below the acceptable levels. Alkalinity (Alk.) adversely affects the corrosion rate and causes it to decrease at alkalinity levels higher than 60 mg/L (Asghari et al., 2018). Water frequently contains hydroxides, phosphates, and carbonate, which increase its alkalinity (Gorde and Jadhav, 2013; Islam et al., 2017). The measured quantities of "Alk." were between 22 and 76 mg/L, with an average value of 36.53 ± 10.20 mg/L.

In the CWASA supply water, the average range of the indices for every sampling site is shown in Fig. 2 and Table 3. The box plot is a tool for showing the shape, median, and range of data distribution. For each supply water sample, the spatial variation in indices was independently analyzed using box plots, based on the physicochemical contents (Fig. 2). Box plots are utilized due to their visual attributes (outlier presence or absence, mean, median, and interquartile range, among others) when representing an entire dataset (Shil et al., 2019). As box plots show, the LSI values were all less than zero, suggesting that the water is corrosively susceptible. In contrast, there was a scale-forming tendency with the LS values. Indicators of the samples' corrosive tendencies included RSI, PSI, and AI, all of which fell within the same range.

LSI, RSI, PSI, LS and AI:

The values of LSI, RSI, PSI, LS, and AI for the CWASA water samples were calculated based on the values of physic-chemical parameters. The values associated with these indices are shown in Table 3. Based on the observed results, the LSI, RSI, PSI, and AI indices showed that every water resource was corrosive. The values calculated were -1.93 ± 0.36 for LSI, 10.56 ± 0.56 for RSI, 10.45 ± 0.64 for PSI, 0.58 ± 0.86 for LS, and 10.01 ± 0.36 for AI.

With a standard deviation of 0.36 and a mean LSI of -1.93, it was predicted that the water samples were under-saturated with $CaCO_3$. The corrosion affinity was supported by the water samples' slightly acidic pH (Table 3). The maximum measured value of the LSI

Table 3. Water quality characteristics, associated with corrosion and scaling tendency.

Indices	Mean±SD	Maximum	Minimum	Status
LSI	-1.93±0.36	-0.83	-2.49	Corrosive
RSI	10.56±0.56	11.43	8.87	Corrosive
PSI	10.45±0.64	11.52	8.38	Corrosive
LS	0.58±0.86	4.76	0.05	Scaling
AI	10.01±0.36	11.19	9.4	Moderately aggressive

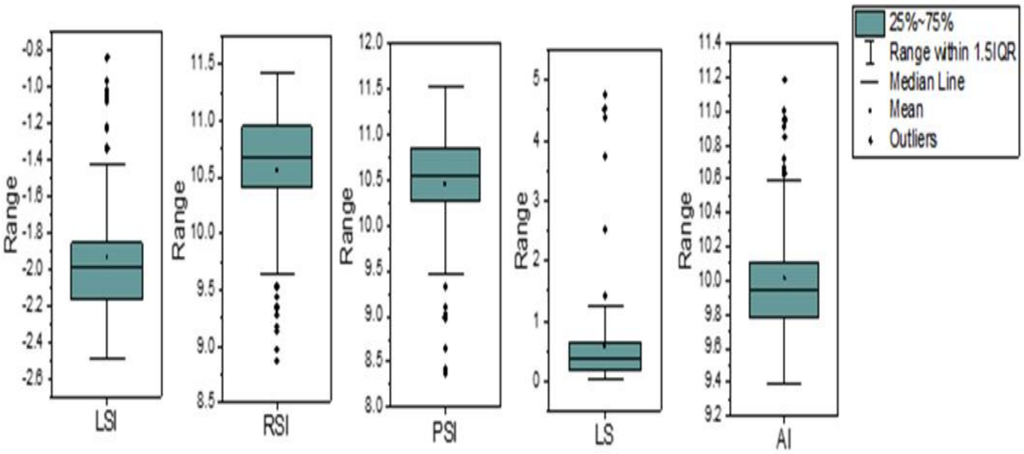

Fig. 2. Box plots show the range of five indices (LSI, RSI, PSI, LS, and AI).

was less than zero, or -0.83. Each sample exhibited corrosive tendencies based on the data in Table 4. There was a balance regarding the corrosive nature, as indicated by a mean RSI of 10.56 in Table 3. According to Table 4, every water sample tends toward corrosion with an RSI > 7. The corrosion nature indicated by the LSI index was also found to be the source of the corrosive tendency. The alkalinity and pH of the water are most likely determining factors. As per Table 4, the PSI mean values for all the water samples were 10.45 in the current investigation, suggesting a corrosive tendency (>7). The LS index comprises Cl^-, HCO_3^-, CO_3^{2-}, SO_4^{2-}, and "alk.". Higher Cl^- or ions with chlorine concentrations will likely promote pitting corrosion of stainless steels in neutral to acidic solutions (Tyagi and Sarma, 2020). Water is predicted to form a scale (LS< 0.8) based on the observed LS mean value of 0.58, as illustrated in Table 4. Eighty-three percent (83%) of the samples support the scaling tendency (Table 4). A high corrosion rate was present in 7 percent of the samples (LS> 1.2). The AI uses Ca-H, alk., and pH to assess water's level of aggressive condition. The LSI, RSI, and PSI results are consistent with the reported mean value of AI of 10.01 (Table 4). All the samples within the study area were aggressive or moderately aggressive, with an AI of less than 12.

The supply of water for drinking purposes should contain essential minerals. However, it is noteworthy that de-mineralized water has a high corrosive tendency, though it does not contribute to scale formation in water supply networks (WSN). It is reasonable to expect drinking water to contain dissolved minerals while minimizing the risk of corrosion and scale formation. Studies have shown that when dissolved oxygen is present and the pH of water is close to 7, pipeline corrosion increases, requiring extra precaution (Larson, 1963; McFarland et al., 2024). Additionally, a higher concentration of dissolved salts in water enhances the likelihood of scale buildup in WSN (Hoang, 2022). Experiments conducted on drinking water samples from the Chittagong region indicate that the supply water's corrosive nature and scale-forming tendency are significantly high. It is worth mentioning that CaH and Alk are the determining factors for LSI, RSI, and PSI

Table 4. Percentage of water samples showing corrosion and scaling potential in CWASA.

Index	Water condition		% of samples
LSI	LSI<0	Under saturated; Corrosion potential.	100
	LSI=0	Equilibrium: No Scaling potential.	0
	LSI>0	Supersaturated water; Scaling potential.	0
RSI	RSI<6	Supersaturated Scaling potential.	0
	6<RSI<7	Saturated Equilibrium; No Scaling Potential.	0
	RSI>7	Under saturated; Corrosion potential.	100
			0
PSI	PSI<6	Scaling potential.	0
	6≤PSI≤7	Equilibrium.	100
	PSI>7	Significant corrosion potential	
LS	LS<0.8	Scaling potential.	83
	0.8<LS<1.2	Corrosion potential.	10
	LS>1.2	High corrosion rates.	7
AI	AI<10	Corrosion potential.	66
	10<AI<12	Moderately corrosive.	44
	AI>12	Scaling potential and non-aggressive.	0

values, whereas Cl^- and SO_4^{2-} are the determining factors for LS value. Thus, the dissolved oxygen and minerals levels in drinking water must be controlled according to standard guidelines to prevent pipeline corrosion while minimizing scale formation (Table 4).

Statistical analyses

A Pearson correlation matrix was generated by combining and analyzing corrosion indices and physicochemical parameters to appraise the interconnection among the variables (Table 5). It is essential to point out that the degree of relationship among the variables is, in general, clarified by the weak ($r<0.500$) and the strong ($r>0.500$) correlations. The strong and positive correlations between EC and TH ($r = 0.873$), Ca-H ($r = 0.879$), HCO_3^- ($r = 0.506$), Cl^- ($r = 0.979$), and SO_4^{2-} ($r = 0.765$) show that there are dissolved ionic species in the supply water, according to the results. These correlations, which show weak correlations with temperature, turbidity, salinity, and alkalinity, are significant at $p<0.01$. Additionally, the TDS showed a highly positive link with EC, TH, Ca-H, Cl^-, and SO_4^{2-} and a weak correlation with temperature, turbidity, salinity, alk., and HCO_3^-, indicating that each variable contributes to dissolved forms. Significantly, it was observed that TH and Ca-H had a robust positive relationship ($r = 0.989$). A strong positive relationship ($p < 0.01$) was also observed with Cl^- and SO_4^{2-}. These results support the hypothesis that $Ca(HCO_3)_2$ and $Mg(HCO_3)_2$ cause the supply water to become temporarily hard rather than permanently hard due to Cl^- and SO_4^{2-}. Furthermore, alk. and HCO_3^- had a significant positive correlation ($r = 0.597$).

The water stability indices were connected with the parameters and each other to measure their utility for corrosion and scaling potential. Due to its pH dependence, LSI displayed a significant positive correlation with alk. ($r = 0.680$), HCO_3^- ($r = 0.651$), and pH ($r = 0.724$). Additionally, AI and LSI had a strong correlation (0.984, $p < 0.01$). For corrosive indications of waterways, AI is generally used occasionally in place of LSI (Kalyani et al., 2017). Conversely, LSI demonstrated a negative correlation with PSI ($r = -0.733$) and RSI ($r = -0.952$), both of which were statistically significant ($p<0.01$). These differences in the underlying factors that each index considers may cause a negative correlation between LSI and PSI. In the end, the selection of an index is contingent upon the particular system in question and the intended emphasis on scaling tendency and corrosion when evaluating water quality (Hernández-Suárez and León, 2021). As opposed to this, RSI displayed a powerful positive correlation with PSI ($r = 0.901$, $p < 0.01$) and a negative correlation with strong LS magnitude ($r = -0.516$, $p < 0.01$). A negative correlation ($r = -0.07$) was found between pH and PSI.

A strong negative correlation between EC and the two indices, which measure the alk. of the water and pH, because EC is a constant for both RSI and PSI. The LS index sets off the supply water's aggressive potential. It had a very positive correlation at $p < 0.01$ with TH ($r = 0.813$), TDS ($r = 0.941$), EC ($r = 0.948$), SO_4^{2-} ($r = 0.747$), Ca-H ($r = 0.797$), and Cl^- ($r = 0.981$). The Cl^- and SO_4^{2-} are the main constituents promoting the scaling behavior discernible from this index, which makes sense given LS's strong correlation with these dissolved constituents. Furthermore, the influence of Cl^- salts determines the salinity, a prerequisite for EC. Moreover, adding bleaching agents for disinfection or the presence of Cl^- salts in the water from subsurface sources affects EC, which is a function of salinity (Tyagi and Sarma, 2020).

A weak positive correlation ($r = 0.459$) between the LS and AI, but a negative but weak correlation with the RSI and PSI, was observed. Table 4 indicates that most parameters exhibited statistically significant differences and weak correlations with AI (such as pH, EC, TDS, TH, Cl^-, SO_4^{2-}, and Ca-H).

With minimal harm to the total dataset, principal component analysis (PCA) can extract information about a particular variable (Singh et al., 2020; Nayak et al., 2022). It typically reduced the dataset to extract highly influential components by eliminating unnecessary data (Rifat et al., 2021; Sharma et al., 2015). By generating scree plots (Fig. 3a) with eigenvalues greater than 1, which analyze the compositional pattern of the variables, PCs were found using the Kaiser normalization technique. Fig. 3b shows the loading plot of the parameters significantly involved in the PCA analysis.

Table 5. Correlation among the physicochemical parameters and stability indices.

Correlations																		
	Temp.	TDS	EC	Turbidity	pH	Salinity	TH	CaH	Alk.	CO_3^-	HCO_3^-	Cl^-	SO_4^{2-}	LSI	RSI	PSI	LS	AI
Temp.	1																	
TDS	-0.128	1																
EC	-0.118	.960**	1															
Turbidity	-0.191	.348**	.284**	1														
pH	-0.179	-0.069	-0.017	-0.08	1													
Salinity	-0.132	.264**	.279**	.363**	-0.118	1												
TH	-0.062	.848**	.873**	.273**	-0.178	.216*	1											
CaH	-0.093	.842**	.879**	.285**	-0.137	.264**	.989**	1										
Alk.	-0.184	.427**	.428**	0.178	0.135	0.111	.438**	.444**	1									
CO_3^-	-	-	-	-	-	-	-	-	-	-								
HCO_3^-	-0.144	.464**	.506**	0.075	.260**	0.018	.511**	.556**	.597**	-	1							
Cl^-	-0.035	.942**	.979**	.259**	-0.03	.229*	.839**	.836**	.339**	-	.403**	1						
SO_4^{2-}	-0.049	.728**	.765**	-0.013	-0.008	-0.124	.720**	.714**	.353**	-	.610**	.725**	1					
LSI	-.251*	.451**	.500**	0.146	.724**	0.076	.415**	.459**	.680**	-	.651**	.433**	.383**	1				
RSI	.241*	-.605**	-.643**	-.221*	-.479**	-0.149	-.607**	-.645**	-.806**	-	-.713**	-.564**	-.491**	-.952**	1			
PSI	0.187	-.659**	-.675**	-.267**	-0.07	-.205*	-.710**	-.729**	-.910**	-	-.667**	-.590**	-.507**	-.733**	.901**	1		
LS	-0.005	.941**	.948**	.266**	-0.038	0.144	.813**	.797**	.289**	-	.346**	.981**	.747**	.392**	-.516**	-.537**	1	
AI	-.253*	.515**	.544**	0.159	.685**	0.028	.469**	.491**	.700**	-	.644**	.486**	.433**	.984**	-.949**	-.750**	.459**	1

* Correlation is significant at the 0.05 level (2-tailed).

** Correlation is significant at the 0.01 level (2-tailed).

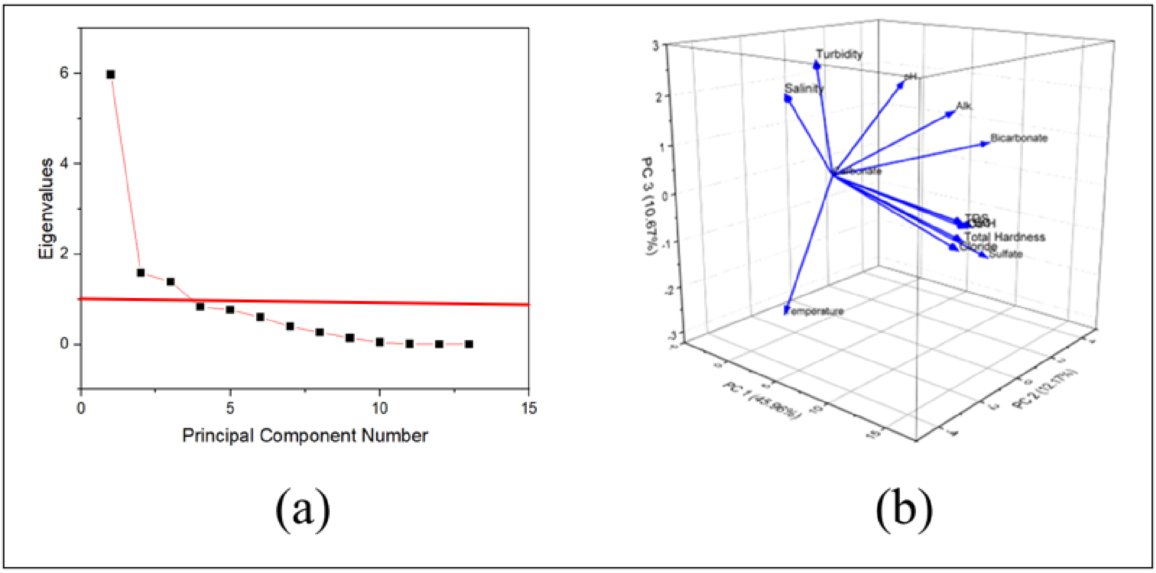

(a)

(b)

Fig. 3. (a) Scree plot of PCA analysis and (b) Loading plot of PCA analysis.

Table 6. Principal component analysis of CWASA supply water quality parameters.

Parameters	Coefficients of PC1	Coefficients of PC2	Coefficients of PC3
pH	-0.017	0.516	0.307
Temperature	-0.059	-0.194	-0.551
TDS	0.386	-0.095	-0.034
EC	0.395	-0.056	-0.053
Turbidity	0.134	-0.359	0.503
Salinity	0.106	-0.467	0.395
Chloride	0.376	-0.096	-0.135
Total Hardness	0.383	-0.086	-0.101
Carbonate	0	0	0
Bicarbonate	0.260	0.427	0.133
Sulphate	0.329	0.239	-0.261
Ca-H	0.386	-0.073	-0.056
Alk.	0.224	0.273	0.268
Eigenvalue	5.974	1.582	1.387
Percentage of Variance	45.96%	12.17%	10.67%
Cumulative	45.96%	58.13%	68.80%

The number of major components that need to be kept is ascertained by identifying the parameter structure with the scree plot. Table 6 displays the observed factor weight values associated with each PC. The top three components account for 68.80% of the total variation.

The principal components' weak, moderate, and strong classifications were built on their factor loading values of 0.30 to 0.50, 0.50 to 0.75, and >0.75, respectively (Nayak et al., 2022; Liu et al., 2003). The TDS (0.386), EC (0.395), TH (0.383), Ca-H (0.386), Cl^- (0.376), and SO_4^{2-} (0.329) were found to be correlated with a weak positive and weak negative loading of 45.96% variance, respectively, with the PC1. The temperature (-0.194), TDS (-0.095), turbidity (-0.359), salinity (-0.467), and Cl^- (-0.096), variables during PC2 synthesis are weakly loaded with negative weight, while pH (0.516), HCO_3^- (0.427), SO_4^{2-} (0.239) and alk. (0.273) indicated a positive factor weight with a variance of 12.17%. While pH (0.516) is moderately loaded, the following have weak loading: HCO_3^- (0.427), SO_4^{2-} (0.239) and alk. (0.273). In PC3, the variables displaying negative weight factors were temperature (-0.551), SO_4^{2-} (-0.261), TH (-0.101), and Cl^- (-0.135), while the variables showing positive weight factors were turbidity (0.503), salinity (0.395), alk. (0.268) and pH (0.307), with percentage variances of 10.67%. Remarkably, all variables are weakly loaded except temperature (-0.551) and turbidity (0.503). Exceptionally, no strong loading was observed for any variables. Together, these observations pointed to several artificial and natural sources that could contaminate the area, such as erosion or weathering of soil, bio-fertilizer runoff, deposition from the atmosphere, and agricultural runoff (Nayak et al., 2022). The higher ion loading may have been caused by ions being leached through weathering, dissolving, exchanging ions, and leaching as the pipeline's main mechanisms, in addition to human interaction as a secondary factor subsidizing variations in the supplied water quality. In addition, the PCA and correlation matrix support the findings of chemical features and physicochemical correlations, both impacting the quality of water provided.

Conclusions

Assessments of the water quality showed almost all of the samples satisfied the requirements for characteristics like EC, TDS, TH, Cl^-, HCO_3^-, and SO_4^{2-}. The supplied water inclinations were classified based on the qualitative factors in the water stability indices of scaling formation and corrosion. The high correlation of the LSI, RSI, and PSI indices with pH, EC, TDS, and alk. indicated that all of the samples exhibited corrosive properties. The AI index showed that the sample has moderately aggressive and corrosive properties at 44% and 66%, respectively. However, with 83% of all samples in the supplied water, LS showed a scaling trend that differed from the other indices. In terms of saturation, the samples lacked equilibrium. It was found that the corrosive estimations had a clear impact on the index, which included LSI, RSI, PSI, and AI. An alternative to another index is the LS, which shows a scaling tendency. The PCA indicated three main components representing 45.96%, 12.17%, and 10.67% of variation. Higher ion loadings indicated ion leaching from the parent material. Although sulfate and chloride ions can influence how corrosive or prone to scaling the water is, Ca and Mg ions are the primary determinants of hardness. To prevent significant contamination of the source water and the consequent aftereffects that would follow, regular checking and corrective actions are mandatory to protect the quality of the supplied water.

Acknowledgments

The authors gratefully acknowledge the support from the Research and Publication Cell (University of Chittagong), and Ministry of Education (Bangladesh).

Author Contributions

U. Sadia: Data curation, investigation, formal analysis, methodology, software, writing original draft; Md. A. H. Rifat: Investigation, resources, software, resources; A. Hasan: Data curation, formal analysis, validation; N. Sarker and S. Islam: Methodology, resources, software, visualization; M. F. Haque and M. A. Sabur: Methodology, resources, visualization; a. bandyopadhyay: methodology, resources, validation, writing–review and editing, supervision; S. Ganguli: Conceptualization, project administration, writing – review and editing, supervision.

Declaration of Conflict Interest

The authors declare that they have no conflict of interest.

References

Ahmed B, Rahman MS, Islam R, Sammonds P, Zhou C, Uddin K and Al-Hussaini TM. Developing a dynamic web-GIS based landslide early warning system for the Chittagong metropolitan area, Bangladesh. *ISPRS Int. J. Geo-Inf.* 2018; 7(12): 485.

Ahmed S, Sultan MW, Alam M, Hussain A, Qureshi F and Khurshid S. Evaluation of corrosive behaviour and scaling potential of shallow water aquifer using corrosion indices and geospatial approaches in regions of the Yamuna river basin. *J. King Saud Univ. Sci.* 2021; 33(1): 101237.

Alipour V, Dindarloo K, Mahvi AH and Rezaei L. Evaluation of corrosion and scaling tendency indices in a drinking water distribution system: a case study of Bandar Abbas city, Iran. *J. Water Health,* 2015; 13(1): 203-209.

Al-Qurnawi WS, Ghalib HB, Alabadi MA and Hawash AB. Corrosion-scaling potentially of domestic water pipelines and evaluate the applicability of raw water sources in Basrah, Iraq. *Iraqi J. Sci*. 2022; 63(5): 2089-2102.

Al-Rawajfeh AE and Al-Shamaileh EM. Assessment of tap water resources quality and its potential of scale formation and corrosivity in Tafila Province, South Jordan. *Desalination,* 2007; 206(1-3): 322-332.

Alsaqqar AS, Al-Rawajfeh AE, Al-Shamaileh EM, Khudair BH and Ali SK. Evaluating water stability indices from water treatment plants in Baghdad City. *J. Water Resour. Prot.* 2014; 6(14): 1344-1351.

Amin MO. Status of water and sanitation services in Chittagong Water Supply and Sewerage Authority, Bangladesh. In Capacity-building Workshop on Partnerships for Improving the Performance of Water Utilities in Asia and the Pacific Region, organized by UNDESA and UNESCAP 2006 Jul (pp. 25-27).

APHA, Standard Methods for the Examination of Water and Wastewater, 20th edn, American Public Health Association, Washington DC, 2002.

APHA, Standard Methods for the Examination of Water and Wastewater, 23rd edn, American Public Health Association, Washington DC, 2017.

Asghari FB, Jaafari J, Yousefi M, Mohammadi AA and Dehghanzadeh R. Evaluation of water corrosion, scaling extent and heterotrophic plate count bacteria in asbestos and polyethylene pipes in drinking water distribution system. *Hum. Ecol. Risk Assess. Int. J.* 2018; 24(4): 1138-1149.

Baloïtcha GM, Mayabi AO and Home PG. Evaluation of water quality and potential scaling of corrosion in the water supply using water quality and stability indices: A case study of Juja water distribution network, Kenya. *Heliyon*, 2022; 8(3): e09141.

Chien CC, Kao CM, Chen CW, Dong CD and Chien HY. Evaluation of biological stability and corrosion potential in drinking water distribution systems: a case study. *Environ. Monit. Assess.* 2009; 153: 127-138.

Debnath P, Al Mamun MA, Karmakar S, Uddin MS and Nath TK. Drinking water quality of Chattogram city in Bangladesh: An analytical and residents' perception study. *Heliyon*, 2022; 8(12): e12247.

Detay M and Carpenter M. Water wells: implementation, maintenance and restoration. John Wiley & Sons, Chichester, UK, 1997; 379.

Egbueri JC. Signatures of contamination, corrosivity and scaling in natural waters from a fast-developing suburb (Nigeria): insights into their suitability for industrial purposes. *Environ. Dev. Sustain*. 2021; 23(1): 591-609.

Gavriloaiei T. Study of corrosion tendency of drinking water in the distribution system of Lasi City, Romania. *Analele Stiintifice de Universitatii AI Cuza din Iasi. Sect. 2, Geologie.* 2016; 62(1/2): 19-27.

Gebremikael GH and Dawod AH. Assessment of corrosion and scale forming potential of groundwater resources: Case study of Dire Dawa City, Ethiopia. *Momona Ethiopian J. Sci*. 2021; 13(1): 110-133.

Gholizadeh A, Mokhtari M, Naimi N, Shiravand B, Ehrampoush MH, Miri M and Ebrahimi A. Assessment of corrosion and scaling potential in groundwater resources; a case study of Yazd-Ardakan Plain, Iran. *Groundw. Sustain. Dev.* 2017; 5: 59-65.

Gorde SP and Jadhav MV. Assessment of water quality parameters: a review. *J. Eng. Res. Appl.* 2013; 3(6): 2029-2035.

Hernández-Suárez M and León FA. Indirect calculation of Langelier saturation index and sodium adsorption ratio for remineralised waters from data on electrical conductivity and pH prior to and following remineralisation. *Desalin. Water Treat.* 2021; 230: 33-37.

Hoang TA. Mechanisms of scale formation and inhibition. In: *Water-formed deposits.* 2022. pp. 13-47.

IS 10500: 2012, Indian Standard Drinking Water-Specification (Second Revision), Standards for Drinking Water Specification. New Delhi: Bureau of Indian Standards; 2012.

Isa NM, Aris AZ and Sulaiman WN. Extent and severity of groundwater contamination based on hydrochemistry mechanism of sandy tropical coastal aquifer. *Sci. Total Environ.* 2012; 438: 414-425.

Islam M, Polash AG and Fahim SA. Analysis of groundwater quality in Sylhet district. *J. Sylhet Agril. Univ.* 2017; 4(2): 325-330.

Kalyani DS, Rajesh V, Reddi EU, Kumar KC and Rao SS. Correlation between corrosion indices and corrosiveness of groundwater: a study with reference to selected areas of Krishna District, Andhra Pradesh, India. *Environ. Earth Sci.* 2017; 76 (16): 568.

Krishna Kumar S, Logeshkumaran A, Magesh NS, Godson PS and Chandrasekar N. Hydro-geochemistry and application of water quality index (WQI) for groundwater quality assessment, Anna Nagar, part of Chennai City, Tamil Nadu, India. *Appl. Water Sci.* 2015; 5: 335-343.

Kumar PJS. Assessment of corrosion and scaling potential of the groundwater in the Thanjavur district using hydrogeochemical analysis and spatial modeling techniques. *SN Appli. Sci.* 2019; 1(5): 395.

Kurdi M, Ferdows MS and Maghsoudi A. Sensitivity of corrosion and scaling indices based on ions; case study Iran. *Water Qual. Expo. Health.* 2015; 7(3): 363-372.

Larson TE. Corrosion phenomena, causes and cures. Proceedings Fifth Sanitary Engineering Conference, Quality Aspects of Water Distribution Systems. University of Illinois Bulletin, 1963: 9-14.

Liu CW, Lin KH and Kuo YM. Application of factor analysis in the assessment of groundwater quality in a blackfoot disease area in Taiwan. *Sci. Total Environ.* 2003; 313(1-3): 77-89.

Maroneze MM, Zepka LQ, Vieira JG, Queiroz MI and Jacob-Lopes E. A tecnologia de remoção de fósforo: Gerenciamento do elemento em resíduos industriais. *Rev. Ambient. Água.* 2014; 9: 445-458.

McFarland ML, Provin TL and Boellstorff DE. Drinking water problems: Corrosion. Texas A & M AgriLife Extension Service Department, 2024; 1-5.

Mia MA, Nasrin S, Zhang M and Rasiah R. Chittagong, Bangladesh. *Cities*, 2015; 48(10): 31-41.

Mirzabeygi M, Yousefi N, Abbasnia A, Youzi H, Alikhani M and Mahvi AH. Evaluation of groundwater quality and assessment of scaling potential and corrosiveness of water supply networks, Iran. *J. Water Supply: Res. Technol. AQUA*, 2017; 66(6): 416-425.

Molla MH, Chowdhury MA, Ali KMB, Bhuiyan MH, Mazumdar RM and Das S. Supply water quality in urban Bangladesh: a case study of Chittagong metropolitan city. *Asian J. Water, Environ. Pollut.* 2014; 11(4): 27-38.

Nayak A, Matta G and Uniyal DP. Hydrochemical characterization of groundwater quality using chemometric analysis and water quality indices in the foothills of Himalayas. *Environ. Dev. Sustain.* 2022; 25(12): 14229-14260.

Popoola LT, Yusuff AS and Aderibigbe TA. Assessment of natural groundwater physico-chemical properties in major industrial and residential locations of Lagos metropolis. *Appl. Water Sci.* 2019; 9(8): 191.

Rabbani D, Miranzadeh MB and Paravar A. Evaluating the corrosive and scale-forming indices of water in the villages under the coverage of Kashan rural water and wastewater company during 2007-9. *Feyz*, 2012; 15(4): 382-388.

Rifat MA, Howlader S, Alam MA, Islam MN, Afrin A, Ali F, Islam S and Ganguli S. Hydrogeochemical characteristics, quality assessment and health impact analysis of groundwater for drinking in the university of Chittagong, Bangladesh. *Malaysian J. Chem*. 2021; 23(1): 74-102.

Sarker S, Mahmud S, Sultana R, Biswas R, Sarkar PP, Munayem MA, Ali MR, Wasim M, Ali MF, Faruque MO and Evamoni FZ. Quality assessment of surface and drinking water of Nakla paurosova, Sherpur, Bangladesh. *Adv. Microbiol.* 2019; 9(8): 703-727.

Shabbir R and Ahmad SS. Use of geographic information system and water quality index to assess groundwater quality in Rawalpindi and Islamabad. *Arabian J. Sci. Eng.* 2015; 40: 2033-2047.

Shams M, Mohamadi A and Sajadi SA. Evaluation of corrosion and scaling potential of water in rural water supply distribution networks of Tabas, Iran. *World Appl. Sci. J.* 2012; 17(11): 1484-1489.

Sharma M, Kansal A, Jain S and Sharma P. Application of multivariate statistical techniques in determining the spatial temporal water quality variation of Ganga and Yamuna rivers present in Uttarakhand State, India. *Water Qual. Expo. Health*. 2015; 7(4): 567-581.

Shil S, Singh UK and Mehta P. Water quality assessment of a tropical river using water quality index (WQI), multivariate statistical techniques and GIS. *Appl. Water Sci*. 2019; 9(7): 168.

Singh KK, Tewari G and Kumar S. Evaluation of groundwater quality for suitability of irrigation purposes: a case study in the Udham Singh Nagar, Uttarakhand. *J. Chem.* 2020; 2020(1): 6924026.

Tyagi S and Sarma K. Qualitative assessment, geochemical characterization and corrosion-scaling potential of groundwater resources in Ghaziabad district of Uttar Pradesh, India. *Groundw. Sustain. Dev.* 2020; 10: 100370.

Uddin M, Munna G, Uddin AS and Islam M. Assessment of water quality of Surma river in perspective of water distribution system in Sylhet City. *Int. J. Eng. Sci.* 2020a; 9: 8-13.

Uddin MR, Hossain MM, Akter S, Ali ME and Ahsan MA. Assessment of some physicochemical parameters and determining the corrosive characteristics of the Karnaphuli estuarine water, Chittagong, Bangladesh. *Water Sci.* 2020b; 34(1): 164-180.

USEPA, Method 200.8: *Determination of Trace Elements in Waters and Wastes by Inductively Coupled Plasma-Mass Spectrometry, Cincinnati, OH*, 1994.

USEPA Region and Foia. *Guidelines for drinking-water quality. Third, edition incorporating the first and second addenda Volume 1 Recommendations Geneva 2008 WHO Library Cataloguing-in-Publication Data*. 2008

Vasanthavigar M, Srinivasamoorthy K, Vijayaragavan K, Rajiv Ganthi R, Chidambaram S, Anandhan P, Manivannan R and Vasudevan S. Application of water quality index for groundwater quality assessment: Thirumanimuttar sub-basin, Tamilnadu, India. *Environ. Monit. Assess.* 2010; 171: 595-609.

Weissbrodt DG, Winkler MK and Wells GF. Responsible science, engineering and education for water resource recovery and circularity. *Environ. Sci. Water Res. Technol*. 2020; 6(8): 1952-1966.

WHO, Guidelines of drinking water quality, Geneva, Switzerland, 2004.

Zhang H, Wang K, Zhou X, Zhu W and Wang W. Water quality characteristics and corrosion potential in blending zones in X city drinking water distribution system. *Environ. Monit. Assess*. 2018; 190(9): 524.

Zhang L, Theregowda RB and Small MJ. Statistical model for scaling and corrosion potentials of cooling-system source waters. *Environ. Eng. Sci.* 2014; 31(10): 570-581.

Zhou X, Shen Y, Zhang H, Song C, Li J and Liu Y. Hydrochemistry of the natural low pH groundwater in the coastal aquifers near Beihai, China. *J. Ocean Univ. China*, 2015; 14: 475-483.

J. Bangladesh Acad. Sci. 49(1); 103-111: June 2025 DOI:https://doi.org/10.3329/jbas.v49i1.80229

Journal of Bangladesh Academy of Sciences

Journal homepage: http://www.bas.org.bd/publications/jbas.html

Research Article

Impact of space weather on ionospheric dynamics in Bangladesh: Insights from 2022–2023 TEC analysis

Sadia Mostofa, Mohammad Badal Ahmmed[1], Mohammad Mahdi Hasan
Jagobandhu Some and Muhammad Sharif [*]
Bangladesh Space Research and Remote Sensing Organization (SPARRSO), Dhaka, Bangladesh

ICLE INFO

Article History

Received: 04 March 2025
Revised: 15 April 2025
Accepted: 21 April 2025

Keywords: Space weather, TEC, Solar activity, GPS navigation, EIA, Geomagnetic dynamics, Bangladesh, Solar-terrestrial.

.

ABSTRACT

Our study, which investigates the impact of space weather on ionospheric variability over Bangladesh, a region near the Equatorial Ionization Anomaly (EIA), using Total Electron Content (TEC) measurements derived from Global Positioning System (GPS) observations, is of significant importance. The analysis, covering 2022 and 2023, characterized by heightened solar activity, reveals a pronounced spatial gradient in TEC values, primarily modulated by proximity to the EIA and geomagnetic disturbances. Seasonal and diurnal patterns further highlight the influence of solar radiation and geomagnetic activity on ionospheric behavior. Notably, severe geomagnetic storms in March and September 2022 and in March and April 2023 induced substantial TEC perturbations, amplifying ionospheric variability. These findings provide critical insights into the complex interactions between solar-terrestrial processes and geomagnetic dynamics, with significant implications for navigation, communication systems, and space weather forecasting in low-latitude regions such as Bangladesh.

Introduction

Space weather, a field that encompasses the dynamic and interconnected processes from the Sun that influence Earth's space environment, has profound effects on technological systems and human activities. This interdisciplinary field primarily involves solar wind, geomagnetic field disturbances, ionospheric variability, and other related phenomena, extending across multiple disciplines, including solar physics, magnetospheric physics, and atmospheric science (Mostofa et al., 2023).

The solar wind is at the core of space weather, a continuous outflow of charged particles (plasma) from the Sun. This stream carries the interplanetary magnetic field (IMF), a component of the Sun's magnetic field that propagates through the solar system. When the IMF interacts with Earth's geomagnetic field, it can lead to reconnection events, allowing energy and particles to enter the magnetosphere. Such interactions often result in geomagnetic storms—periods of intense magnetic activity that can disrupt satellite operations, power grids, and communication systems (Demyanov et al., 2022).

The ionosphere extends from approximately 50 km to over 1,000 km in altitude, with its structure divided into distinct regions based on altitude, electron density, and ionization sources. Fig. 1

---

[*]Corresponding author:<sharif@sparrso.gov.bd>

[1]*Department of Computing, Universiti Malaysia Pahang, Pahang, Malaysia*

illustrates the differences between the dayside and nightside ionosphere, highlighting key areas and their respective characteristics. The D region is the lowest part of the ionosphere and is present only during the daytime. It is primarily ionized by high-energy solar X-rays and cosmic rays, resulting in low electron density due to rapid recombination (Jee, 2023). This region significantly absorbs low-frequency (LF) and very-low-frequency (VLF) radio waves, causing daytime signal attenuation. The figure shows this region's location and interaction with aircraft and balloons. Above the D region lies the E region, where ionization is driven by solar ultraviolet (UV) radiation. Electron density peaks at around 110 km during the day, enabling the reflection of medium-frequency (MF) radio waves (Némethová and Zýka, 2024). The presence of sporadic E layers, as depicted in the figure, is caused by localized ionization and wind shear effects. This region plays a critical role in supporting shortwave radio communications. The F region is the most important part of the ionosphere for radio communications and satellite operations (Demyanov et al., 2022). It is divided into two sub-layers during the daytime:

F1 Layer (150–250 km): This layer appears only during the day and supports moderate ionization.

F2 Layer (250–500 km): Present both day and night, it has the highest electron density, as shown in the figure. The F2 layer is crucial for high-frequency (HF) radio wave propagation and global communication systems.

At night, the F1 layer disappears, and the F2 layer dominates, as shown on the left side of the figure. The ionization levels are lower during the night due to reduced solar radiation, but sufficient to maintain some electron density (Ishii et al., 2024).

The topside ionosphere, not explicitly labeled in the figure but implied above the F region, extends upward into the plasmasphere. Electron density decreases with altitude, and lighter ions like H^+ and He^+dominate due to gravitational separation.

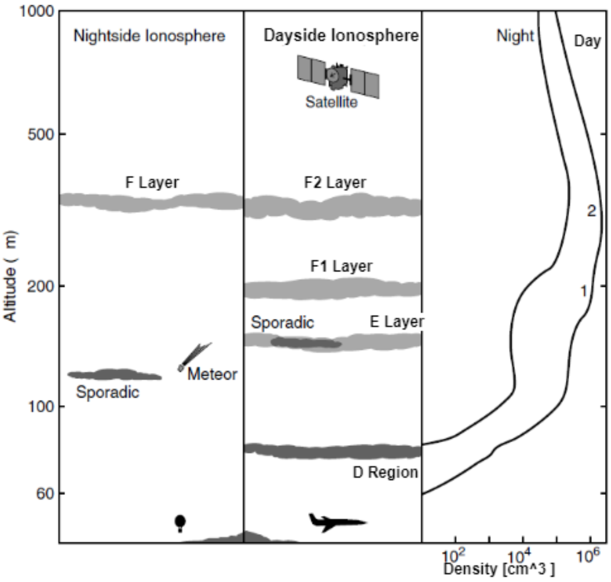

Fig. 1. Vertical structure of the earth's ionosphere: Dayside and nightside characteristics (Moldwin, 2008).

This region interacts with satellites, as depicted in the figure, and is critical for understanding space weather impacts on satellite communication and navigation systems. The attached figure highlights the differences in electron density between the day and night. During the day, solar radiation enhances ionization, leading to higher electron density across all regions. At night, the lack of solar radiation causes recombination, reducing electron density in the D and E regions, while the F2 layer persists due to slower recombination processes. The figure also shows phenomena like meteors interacting with the E region and sporadic ionization events in both the E and F regions (Ishii et al., 2024).

The ionosphere, a highly dynamic region of Earth's upper atmosphere, is central to the study of space weather. This region, populated by free electrons and ions, responds to solar and geomagnetic activity variations. Disturbances in the ionosphere, such as those caused by solar flares or coronal mass ejections (CMEs), can alter the propagation of radio waves, degrade GPS accuracy, and affect ground- and space-based communication networks. Key parameters like Total Electron Content (TEC), which measures the number of electrons along a column between a satellite and a ground receiver, are essential for monitoring these disturbances (Mostofa et al., 2022a). Geomagnetic indices, such as the Dst index (which measures ring current intensity) and the Kp index (which quantifies global geomagnetic activity), provide additional insight into space weather conditions (Singh et al., 2024).

The behavior of the ionosphere is shaped by a complex interplay of factors, including solar radiation, solar wind, interactions with the Earth's magnetosphere, and atmospheric weather patterns (Rodriguez-Solano et al., 2013). These influences result in variations in ionospheric conditions that can be broadly classified into two distinct categories:

1. Predictable Variations (Quiet Ionosphere): These changes occur in well-defined cycles, such as the diurnal (daily) and seasonal variations, which follow established patterns and can be forecasted accurately. Regular solar radiation inputs and atmospheric tides largely govern the quiet ionosphere.
2. Unpredictable Variations (Disturbed Ionosphere): These fluctuations arise primarily due to the Sun’s dynamic and often erratic behavior, particularly during heightened solar activity. Space weather phenomena, including geomagnetic storms and solar flares, introduce significant irregularities in the ionosphere, leading to disruptions in radio communications, navigation systems, and other space-based technologies (Mostofa et al., 2022b).

This study utilizes high-resolution GPS-based data collected from Bangladesh during the high solar activity years of 2022 and 2023, a period associated with the rising phase of Solar Cycle 25. Total Electron Content (TEC) data was acquired from UNAVCO satellites through the GAGE data server and processed using advanced algorithms to account for geometric and receiver biases. By analyzing seasonal, diurnal, and spatial variations in TEC, this research investigates how geomagnetic disturbances and solar activity impact ionospheric behavior over Bangladesh, a region lying near the northern crest of the EIA.

The novelty of this study lies in its region-specific focus on Bangladesh, which is uniquely situated to experience the compounded effects of geomagnetic disturbances and equatorial ionospheric anomalies. Unlike global ionospheric models, which often overlook localized variations, this study provides detailed insights into the dynamics of TEC within this low-latitude region. Furthermore, developing a regional ionospheric disturbance index tailored to Bangladesh’s geomagnetic conditions represents a significant advancement in space weather monitoring.

The findings of this study are crucial for mitigating the adverse effects of space weather on communication and navigation technologies. Understanding the ionosphere's response to space weather events will help improve GNSS-based systems, ensuring greater resilience and reliability for applications ranging from aviation and maritime navigation to agricultural monitoring. This work contributes to the global effort to enhance space weather preparedness in vulnerable regions by addressing a critical gap in localized ionospheric research.

Methodology

GPS signals through the ionosphere provide an established method for ionospheric remote sensing (Bojilova and Mukhtarov, 2023). A widely used GPS network offers a powerful tool and cost-effective means for computing the TEC and scintillation characteristics of the ionosphere.

The research methodology integrates data acquisition, processing, and analysis to investigate space weather impacts. Data for 2022 and 2023 (https://gage-data.earthscope.org/archive/gnss/rinex3/obs/2022/) (https://gage-data.earthscope.org/archive/gnss/rinex3/obs/2023/) was sourced from the GAGE data server, using UNAVCO satellite observations in Receiver

Independent Exchange Format, version 3 (RINEX3), known for its Receiver Independent Exchange structure. Compressed into Hatanaka format for efficiency, these files were processed using Gopi Seemala software (Seemala, 2023). The software calculates Total Electron Content (TEC) by deriving Slant TEC (STEC) from the phase difference of dual-frequency GNSS signals – $STEC = \frac{\Delta\emptyset . f_1^2 . f_2^2}{(f_1^2 - f_2^2)}$ (1)

Where, $\Delta\emptyset$ is the phase difference between two frequencies (f_1 and f_2)

f_1, f_2 are the frequencies of the GNSS signals and converting it to Vertical TEC (VTEC) using -

$$VTEC = STEC . Cos\ (E)$$
(2)

Where, E is the satellite's elevation angle, it accounts for the geometric path difference.

GPS data acquisition points in Bangladesh, which were used in this study, are shown in Fig. 2.

The ionosphere exhibits variations based on Earth's geographical position, particularly concerning latitude, owing to the orientation of the geomagnetic field lines in different latitude regions. Notably, the behavior of the ionosphere in mid-latitudes differs from that in low- and high-latitude regions. In the mid-latitude F2 region ionosphere, reaction rates are notably sensitive to temperature and chemical composition changes. The alterations in composition are linked to the global circulation pattern within the thermosphere. The primary influencing mechanism in the mid-latitude ionosphere is the global thermospheric winds, as detailed by. This mid-latitude region is recognized as the transitional zone between low and high latitudes (Radicella, 2023).

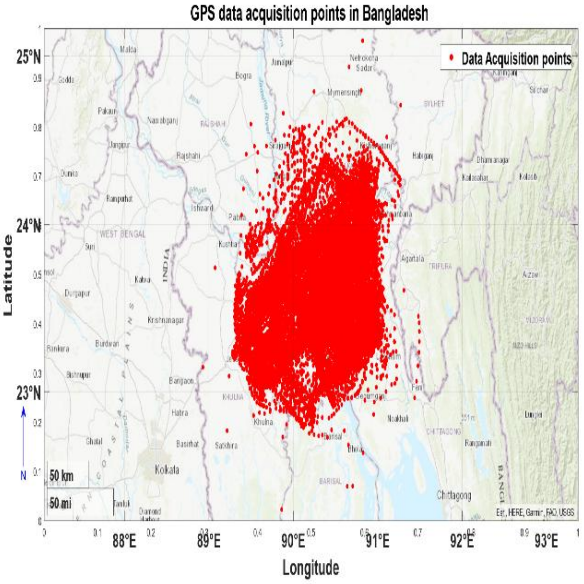

Fig. 2. GPS Data acquisition points across Bangladesh: Latitude 22.291640˚N to 25.088773˚N and Longitude 88.928156˚E to 91.492842˚E.

Certain regions, specifically low-latitude areas, exhibit elevated electron concentrations around geomagnetic latitudes of approximately ±20°. At the magnetic equator, where Earth's magnetic field lines lie horizontally, solar heating and tidal oscillations in the lower ionosphere induce the movement of plasma upward and across the magnetic field lines. This process establishes a sheet of electric current in the E region, which propels ionization upward into the F layer in conjunction with the horizontal magnetic field. This phenomenon is called the fountain effect or the Equatorial Ionization Anomaly (EIA) (Laštovička et al., 2012). The geographic latitude analyzed in this study starts from 22.291640˚N to 25.088773˚N, and the geographic longitude starts from 88.928156˚E to 91.492842˚E. The geomagnetic coordinates are shown in Fig. 3.

Corrections for receiver hardware biases and elevation mask filtering are applied to ensure high data accuracy. The processed TEC profiles were analyzed to identify ionospheric anomalies, leading to the development of an ionospheric disturbance index. This index facilitates improved monitoring and understanding of space weather effects, particularly for Bangladesh's communication, power, and agricultural systems. The methodology ensures robust and reliable outcomes by combining advanced processing techniques and multiple data sources.

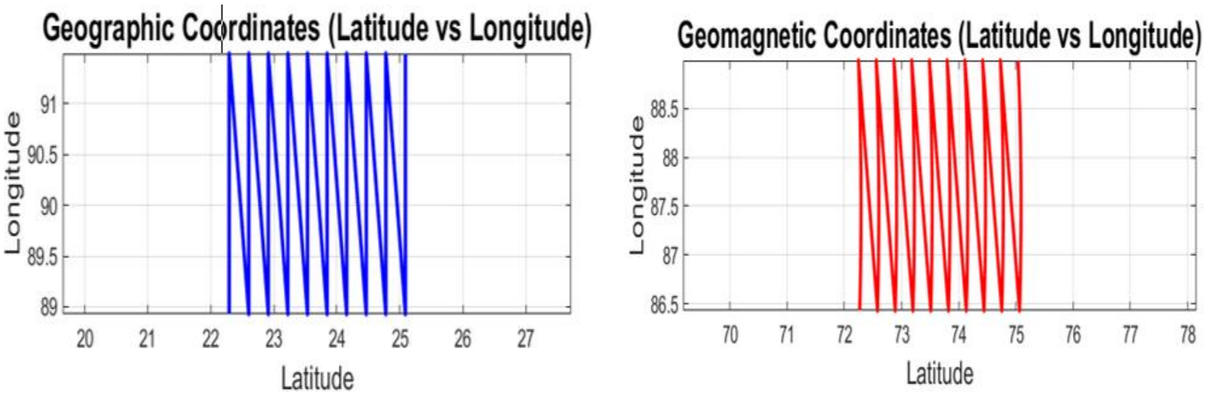

Fig. 3: Conversion of geographic coordinates to geomagnetic coordinates for Bangladesh.

Results and Discussion

Fig. 4 shows the geomagnetic and ionospheric parameters for 2022. The interplanetary magnetic field (IMF_Bz) during 2022 displayed significant fluctuations, with peaks exceeding 20 nT, indicating periods of elevated geomagnetic activity. The Kp index revealed multiple moderate disturbances, with values ranging from 4 to 6, suggesting a frequent occurrence of minor to moderate geomagnetic storms. The Dst index, which measures the intensity of geomagnetic storms, showed several notable storm events with values dropping below -50 nT, particularly in March and September, signaling moderate to severe storm activity. The Vertical Total Electron Content (VTEC) demonstrated seasonal variations, with higher values observed during equinox months, reflecting the increased solar radiation during these periods.

The geomagnetic activity observed in 2022 can be attributed to solar phenomena such as coronal mass ejections (CMEs) and high-speed solar wind streams (HSS), key drivers of geomagnetic storms. The fluctuations in IMF_Bz and elevated Kp index align with the expected impacts of these solar events during the 25th solar cycle. Seasonal peaks in VTEC are consistent with the equinoctial effect, which enhances ionospheric ionization due to more effective solar radiation during equinoxes (Mostofa

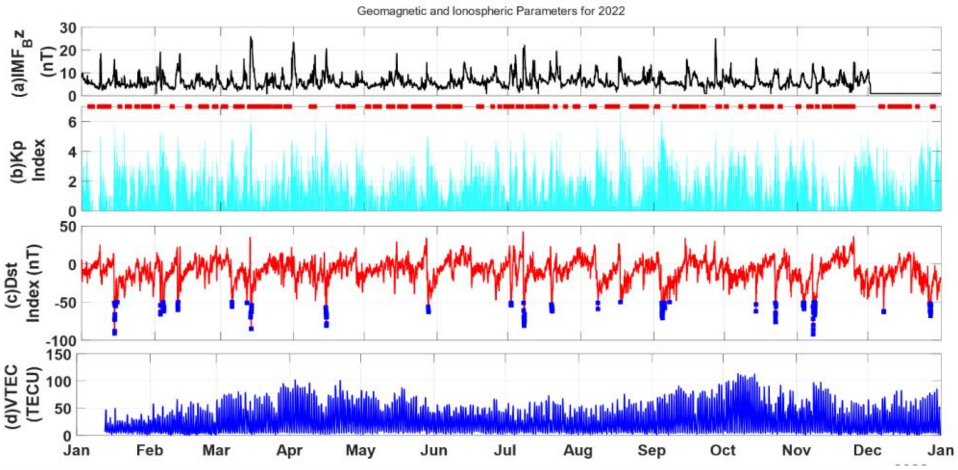

Fig. 4. Geomagnetic and ionospheric parameter for 2022: IMF_Bz, Kp index, Dst index, and VTEC trends.

et al., 2023). The significant geomagnetic storms in March and September align with historical data showing these months as periods of heightened geomagnetic activity.

Fig. 5 shows the geomagnetic and ionospheric parameters for 2023. In 2023, the IMF_Bz exhibited similar variability to 2022 but with peaks reaching up to 30 nT, indicative of increased geomagnetic activity. The Kp index showed prolonged periods of moderate disturbances, with fewer intervals of quiet geomagnetic conditions compared to 2022. The Dst index highlighted intense geomagnetic storm events, particularly in March and April, with values dropping below -100 nT, marking severe geomagnetic disturbances. VTEC trends were slightly elevated compared to 2022, showing increased ionospheric ionization, likely due to intensified solar activity during this period.

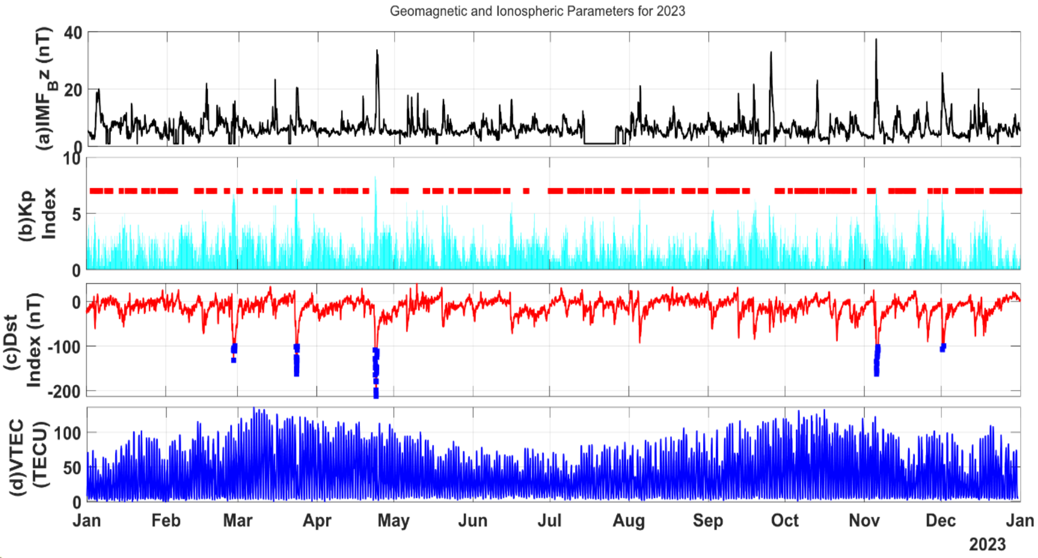

Fig. 5. Geomagnetic and ionospheric parameters for 2023: IMF_Bz, Kp index, Dst index, and VTEC trends.

The stronger geomagnetic activity in 2023 corresponds with the rising phase of Solar Cycle 25, which is characterized by increased solar activity and a higher frequency of geomagnetic storms (Rao et al., 2009). Severe geomagnetic storms observed in March and April align with the equinoctial maxima, which historically record enhanced geomagnetic disturbances. The elevated VTEC levels further indicate the impact of intensified solar EUV radiation and geomagnetic activity, supporting findings that correlate ionospheric behavior with solar cycle phases (Rao et al., 2009).

In 2022, the VTEC values for the geographic latitude range of 22.291640˚N to 25.088773˚N and longitude range of 88.928156˚E to 91.492842˚E exhibited clear spatial variability. The region's proximity to the Equatorial Ionization Anomaly (EIA) significantly influenced the distribution of electron content. Areas closer to the EIA crest exhibited higher VTEC values due to the accumulation of ionized plasma caused by the equatorial electrojet and fountain effect (Balan et al., 2018). This latitudinal gradient is a well-known phenomenon in low-latitude regions, as documented by Buhari et al. (2017).

Geomagnetic disturbances in 2022 further contributed to VTEC variations. The year experienced several geomagnetic storms, particularly in March and September, as indicated by drops in the Dst index below -50 nT. These disturbances caused fluctuations in the ionospheric electron content, leading to regional disparities in

VTEC (Hafteh et al., 2024). Like those studied, low-latitude regions are susceptible to geomagnetic activity due to their interaction with equatorial electrojet currents, amplifying storm-induced plasma redistribution (Elmunim et al., 2021).

Table 1. Comparative Summary of Geomagnetic and Ionospheric Parameters for 2022 and 2023.

Parameter	2022 Highlights	2023 Highlights	Observations
IMF Bz (nT)	Peaks around 20–25 nT, frequent smaller fluctuations	Peaks exceed 30 nT, more intense spikes	2023 shows more substantial and more frequent magnetic field variations
Kp Index	Mostly below 5, occasional bursts	Frequent spikes approaching or reaching 8	2023 indicates more geomagnetic disturbances
Dst Index (nT)	Dips frequently to -50 to -100 nT, moderate storms	Dips reach -150 to -200 nT, intense geomagnetic storms	2023 had stronger geomagnetic storms
VTEC (TECU)	Average range 20–90 TECU, lower during mid-year	Average range 30–120 TECU, higher overall, peaks in March, October, Dec	2023 had higher ionospheric electron content
Seasonal Variation	Noticeable VTEC variation in April/Oct, fewer storm events mid-year	Strong seasonal trends, especially March-May and Oct-Dec	More seasonal consistency and peak activity in 2023
Seasonal Variation	Noticeable VTEC variation in April/Oct, fewer storm events mid-year	Strong seasonal trends, especially March–May and Oct–Dec	More seasonal consistency and peak activity in 2023

Solar activity also influenced VTEC trends in 2022. Seasonal variations in solar zenith angle, particularly during equinox months, resulted in higher VTEC values due to increased ionization from enhanced solar radiation (Liu et al., 2013). These patterns align with the equinoctial effect, where solar radiation is more effective in ionizing the ionosphere during equinoxes (Forbes et al., 2000). The combination of geomagnetic and solar influences shaped the observed spatial and temporal differences in VTEC across the region in 2022.

In 2023, the VTEC values showed an overall increase compared to 2022, reflecting the rising phase of Solar Cycle 25, which is associated with higher solar activity and more substantial ionization effects. The EIA influenced the region, with higher VTEC values observed at lower latitudes closer to the anomaly crest. The latitudinal gradient persisted, but the elevated baseline electron content in 2023 amplified the overall values, consistent with previous findings on solar cycle impacts on the ionosphere (Pancheva et al., 2024).

Geomagnetic activity played a more pronounced role in 2023, with severe storms observed in March and April, indicated by Dst index values dropping below -100 nT. These storms caused significant disturbances in the ionosphere, leading to heightened variability in VTEC. The intensified geomagnetic conditions likely increased plasma transport and irregularities, further amplifying spatial VTEC differences (Stankov et al., 2003). The interaction between geomagnetic activity and the equatorial electrojet currents in low-latitude regions was a key factor driving these variations, as noted by (Emmela et al., 2024). The heightened solar activity in 2023 also significantly impacted VTEC values. The year exhibited more substantial seasonal variations, with elevated VTEC levels during equinox months due to increased solar EUV radiation (Huang, 2018). Diurnal variations in the solar zenith angle also modulated the electron content, resulting in localized VTEC anomalies (Picanço et al., 2022). These observations align with studies highlighting the combined effects of solar and geomagnetic activity on low-latitude ionospheric behavior (Bojilova and Mukhtarov, 2023).

In 2022 and 2023, VTEC variations were shaped by proximity to the EIA, geomagnetic disturbances, and solar activity. While 2022 highlighted moderate solar and geomagnetic influences, 2023 exhibited heightened activity due to the rising phase of Solar Cycle 25. The observed spatial and temporal differences in VTEC underscore the complex interplay of solar-terrestrial and geomagnetic processes in the low-latitude ionosphere. Future studies using advanced ionospheric models could further elucidate these dynamics and improve space weather forecasting for regions vulnerable to ionospheric disturbances (Pancheva et al., 2024). Table 1 shows the overall summary for all parameter changes in 2022 and 2023.

Conclusion

This study highlights the profound impact of space weather on ionospheric dynamics in Bangladesh's low-latitude region, emphasizing the ionosphere's sensitivity to solar and geomagnetic activity. Data from 2022 and 2023 revealed significant TEC variations influenced by proximity to the Equatorial Ionization Anomaly, geomagnetic disturbances, and solar radiation cycles. Seasonal peaks in TEC during equinoxes, combined with severe geomagnetic storms, underscore the intricate interplay of solar-terrestrial processes. The rising phase of Solar Cycle 25 in 2023 further amplified ionospheric variability, demonstrating the need for robust monitoring and predictive models. These findings are crucial for mitigating space weather impacts on critical technologies, including GNSS-based navigation and communication systems. Future efforts should focus on developing localized ionospheric models and integrating real-time geomagnetic indices for enhanced space weather resilience in Bangladesh and other vulnerable regions.

Acknowledgment

The authors thank the GAGE data server, utilizing UNAVCO satellite data, for providing the GPS data used in this study. Appreciation is also extended to the World Geomagnetic Data Centre, Kyoto, Japan, and the Space Physics Data Facility of the National Aeronautics and Space Administration (NASA), United States, for supplying the interplanetary and geomagnetic condition datasets utilized in this work. The authors also acknowledge using Gopi Seemala software to process the TEC data. We also acknowledge SPARRSO for providing the necessary funds for this research.

Author contribution

Sadia Mostofa: Writing-review & editing, writing–original draft, conceptualization, lead, methodology, formal analysis, software, resources, validation, investigation. Mohammad Badal Ahmmed: Methodology, formal analysis, software, resources, validation, data curation. Mohammad Mahdi Hasan: Writing-review & editing, formal analysis, investigation. jagobandhu some: writing-review & editing, formal analysis, investigation. Muhammad Sharif: Writing-review & editing, conceptualization, formal analysis, investigation.

Declaration of conflicting interest

The authors declare that they have no conflict of interest.

References

Balan N, Liu L and Le H. A brief review of equatorial ionization anomaly and ionospheric irregularities. *Rev. Space Phys. Earth Planet. Phys.* 2018, 2: 257-275.

Bojilova R and Mukhtarov P. Comparative analysis of global and regional ionospheric responses during two geomagnetic storms on 3 and 4 February 2022. *Remote Sens.* 2023, 15(7): 1739.

Buhari SM, Abdullah M, Yokoyama T, Otsuka Y, Nishioka M, Hasbi AM, Bahari SA and Tsugawa T. Climatology of successive equatorial plasma bubbles observed by GPS ROTI over Malaysia. *J. Geophys. Res. Space Phys.* 2017, 122(2): 2174-2184.

Demyanov V, Yasyukevich Y, Sergeeva MA and Vesnin A. *Space Weather Impact on GNSS Performance*. Springer Nature, 2022. p. 368.

Elmunim N, Abdullah M and Bahari S. Evaluating the performance of IRI-2016 using GPS-TEC measurements over the equatorial region. *Atmos.* 2021; 12(10): 1243.

Emmela S, Ratnam DV, Otsuka Y, Shinbori A, Sori T, Nishioka M and Perwitasari S. Statistical analysis of global and regional ionospheric total electron content (TEC) using extreme value distributions. *IEEE Trans. Geosci. Remote Sens.* 2024; 62: 1-8.

Forbes JM, Palo SE and Zhang X. Variability of the ionosphere. *J. Atmos. Sol. Terr. Phys.* 2000; 62(8), 685–693.

Hafteh MV, Mahmoudian A, Yoshikawa A and Girgis K. Mid-Latitude study of ionospheric variation over iran associated with equatorial ionization anomaly (EIA), and artificial neural networks model development. *Space Weather,* 2024; 22(11): e2024SW004032.

Huang C-S. Effects of the postsunset vertical plasma drift on the generation of equatorial spread F. *Prog. Earth Planet. Sci.* 2018; 5 (1): pp. 15.

Ishii M, Berdermann J, Forte B, Hapgood M, Bisi MM. and Romano V. Space weather impact on radio communication and navigation. *Adv. Space Res.* 2024 (in press).

Jee G. Fundamentals of numerical modeling of the mid-latitude ionosphere. *J. Astron. Space Sci.* 2023; 40(1), 11-18.

Laštovička J, Solomon SC and Qian L. Trends in the neutral and ionized upper atmosphere. *Space Sci. Rev.* 2012; 168(1-4): pp. 113-145.

Liu JY, Yang WH, Lin CH, Chen YI and Lee IT. A statistical study on the characteristics of ionospheric storms in the equatorial ionization anomaly region: GPS-TEC observed over Taiwan. *J. Geophy. Res. Space Phys.* 2013; 118(6): 3856-3865.

Moldwin M. *An Introduction to Space Weather*. Cambridge University Press, 2008.

Mostofa S, Abdullah M, Bahari SA and Islam MT. Analysis of the regional ionospheric disturbance index during geomagnetic storm in 2012. *IEEE Access*, 2023; 11: 94742-94752.

Mostofa S, Abdullah M, Islam MT, Bahari SA and Ahmmed MB. A GPS TEC-based Ionospheric-M Index over Malaysia. *2022 IEEE 20th Student Conference on Research and Development* (SCOReD), 2022a: 185-189.

Mostofa S, Abdullah M, Islam MT, Bahari SA and Ahmmed MB. Variations of total electron content during quiet and disturbed geomagnetic conditions over Malaysia. 2022 *IEEE 6th International Symposium on Telecommunication Technologies (ISTT),* 2022b: 97-101.

Némethová H and Zýka J. Overview of the space weather impact on the navigation and communication systems. *Acta Avion. J.* 2024; 26(1): 27-39.

Pancheva D, Mukhtarov P and Bojilova R. Response to geomagnetic storm on 23–24 March 2023 long-lasting longitudinal variations of the global ionospheric TEC. *Adv. Space Res.* 2024; 73(12): 6006-6028.

Picanço GAS, Denardini CM, Nogueira PAB, Resende LCA, Carmo CS, Chen SS, Barbosa-Neto PF and Romero-Hernandez E. Study of the equatorial and low-latitude total electron content response to plasma bubbles during solar cycle 24-25 over the Brazilian region using a disturbance ionosphere index. *Ann. Geophys.* 2022; 40(4): 503-517.

Radicella SM. New ways to modelling and predicting ionosphere variables. *Atmos.* 2023; 14(12): 1788.

Rao PVSR, Gopi Krishna S, Vara Prasad J, Prasad SNVS, Prasad DSVVD and Niranjan K. Geomagnetic storm effects on GPS based navigation. *Ann. Geophys.* 2009; 27(5): 2101-2110.

Rodriguez-Solano CJ, Hugentobler U, Steigenberger, P and Allende-Alba G. Improving the orbits of GPS block IIA satellites during eclipse seasons. *Adv. Space Res.* 2013; 52(8): 1511-1529.

Seemala GK. Estimation of ionospheric total electron content (TEC) from GNSS observations. In: *Atmospheric Remote Sensing*. *Elsevier.* 2023. pp. 63-84.

Singh BKR, Ali AM, Bahari SA and Abdullah M. *A Review on GBAS: Ionospheric Effects at Low-Latitude Regions,* 2024: pp. 337-346.

Stankov SM, Jakowski N, Heise S, Muhtarov P, Kutiev I and Warnant R. A new method for reconstruction of the vertical electron density distribution in the upper ionosphere and plasmasphere. *J. Geophys. Res. Space Phys.* 2003; 108(A5):1-21.

J. Bangladesh Acad. Sci. 49(1); 113-121 June 2025 DOI:https://doi.org/10.3329/jbas.v49i1.80351

Journal of Bangladesh Academy of Sciences

Journal homepage: http://www.bas.org.bd/publications/jbas.html

Research Article

Necessity of an agriculture-based curriculum in Bangladesh: A pathway for sustainable economic growth

Sharif Mohammad Wakiluzzaman

Pirganj Government College, Thakurgoan, Bangladesh

ICLE INFO

Article History

Received: 09 March 2025
Revised: 10 April 2025
Accepted: 17 April 2025

Keywords: Agricultural education, Curriculum, Bangladesh, SDGs, Economic growth, Sustainable development.

ABSTRACT

The findings of this study highlight a significant gap in the current educational curriculum regarding agricultural relevance and practical skill development. Most respondents—comprising both students and educators—strongly preferred integrating agriculture-focused subjects, especially in rural settings where farming remains central to livelihoods. Participants believe early exposure to agricultural education and hands-on practical experience can empower students with real-world skills, reduce rural-urban migration, and support local economic growth. Additionally, an agriculture-based curriculum has the potential to address key challenges such as youth unemployment, food insecurity, and environmental degradation. Such a curriculum could promote long-term ecological balance and economic resilience by fostering awareness and competence in sustainable agricultural practices. Therefore, incorporating agriculture into mainstream education is not merely an academic enhancement but a strategic move toward sustainable national economic development.

Introduction

Agriculture remains a cornerstone of Bangladesh's economy, employing 41% of the workforce and contributing 13.47% to GDP (BBS, 2023). Despite its significance, agricultural education is not systematically integrated into the national curriculum, leading to skill gaps and low productivity. While Universities like Bangladesh Agricultural University (BAU) and Sher-e-Bangla Agriculture University (SAU) offer Higher education with structured agricultural training, primary and secondary school curricula lack structured agricultural training, limiting youth engagement in modern agribusiness and sustainable farming. Small holder farmers, constituting 84% of total farmers, continue to rely on traditional techniques, further constraining agricultural innovation and food security.

Previous studies highlight the positive impact of agricultural education on national development. Ahmed and Rahman (2018) found that vocational agricultural training increased rural youth employment by 27%. Hasan et al. (2020) demonstrated that making agriculture compulsory in India's secondary schools led to a 15% rise in agricultural university enrollments. FAO (2022) reported that countries with integrated agricultural curricula experienced higher farm productivity and technological adoption. However, Bangladesh lags in implementing such initiatives, limiting youth participation and agribusiness innovation. This study identifies the need for curriculum reforms that align with global best practices.

---

[*] Corresponding author:<wakiluzzamansm@gmail.com>

Integrating agriculture into the education system can address several national challenges. Training in modern farming methods can improve crop yields by up to 20% (DAE, 2023), contributing significantly to food security. With rural youth unemployment at 10.6% (BBS, 2023), vocational agricultural education can provide sustainable job opportunities, reducing migration to urban areas in search of work. Climate-smart agriculture, agrotechnology, and organic farming education can promote sustainable farming practices, mitigating environmental degradation. Encouraging agribusiness education can also drive entrepreneurship, boosting the agricultural sector's contribution to GDP.

Agricultural education is critical in achieving key Sustainable Development Goals (SDGs). Addressing SDG 2 (Zero Hunger), Bangladesh, which ranks 76th in the Global Hunger Index (GHI, 2023), can enhance food security through structured agricultural training. Regarding SDG 4 (Quality Education), the lack of agricultural subjects in over 85% of schools (BANBEIS, 2023) highlights the need for curriculum reform to equip students with essential agribusiness skills. Furthermore, SDG 8 (Decent Work and Economic Growth) can be supported by vocational training in agribusiness and digital farming, fostering rural employment and poverty reduction.

To successfully implement agricultural education, several strategic actions are required. Curriculum development should introduce agricultural subjects at all education levels while establishing specialized agricultural high schools. Practical training is essential, involving the development of school farms, agrotechnology laboratories, and industry collaborations for hands-on learning experiences. Additionally, government support is crucial in increasing funding, offering student grants, and launching awareness campaigns to promote agricultural careers. These strategies will help integrate agriculture into mainstream education, fostering innovation, employment, and sustainable economic growth.

This study aims to:

- Identify gaps in Bangladesh's agricultural education system.
- Examine the role of agricultural education in achieving SDGs.
- Analyze global best practices and their applicability to Bangladesh.
- Recommend policy reforms for integrating agricultural education at all levels.

By addressing these objectives, this research contributes to the growing discourse on agricultural education′s role in sustainable development, offering policy recommendations to equip the youth with essential skills for innovation, food security, and economic growth.

Materials and methods

This study employs a mixed-methods approach, integrating quantitative and qualitative research to evaluate the necessity of an agriculture-based curriculum in Bangladesh′s education system. The methodology includes study area selection, data collection techniques, and analytical methods, ensuring the reproducibility of results and alignment with international research standards.

Study area

The study was conducted in five divisions of Bangladesh-Rangpur, Mymensingh, Bogura (Rajshahi Division), Barishal, and Khulna - selected based on agricultural significance, educational infrastructure, and economic reliance on agriculture. The study sites were identified using data from the Bangladesh Bureau of Statistics (BBS, 2023) and the Department of Agricultural Extension (DAE, 2023). These locations represent diverse agricultural conditions, including cereal crop cultivation, agribusiness, fisheries, and climate-resilient farming practices.

Materials used

1. Survey questionnaires – Developed based on prior studies (Ahmed and Rahman, 2018; Hasan et al., 2020) and pre-tested with 20 respondents for reliability.

2. Interview guidelines – Structured by FAO's (2022) best practices for agricultural education research.
3. Statistical software – IBM SPSS 28.0 for quantitative analysis and NVivo 12 for qualitative thematic analysis.
4. Secondary data sources – Reports from BANBEIS (2023), BBS (2023), FAO (2023), and the World Bank (2023) were used for comparative analysis.
5. Analytical tools – Chi-square tests, regression models, and graphical analysis using Microsoft Excel 2021.

Data collection methods

Primary data collection

1) Structured surveys
    a) Participants: 200 secondary and tertiary students, 50 teachers, and 50 agribusiness professionals.
    b) Instrument: 5-point Likert scale questionnaire measuring perceptions of agricultural education and career prospects.
2) Key informant interviews (KII)
    a) Participants: 10 policymakers (Ministry of Education and National Curriculum and Textbook Board), 5 curriculum experts (Bangladesh Agricultural University, Sher-e-Bangla Agriculture University, and BCS General Education Cadre- Agriculture Officers), and 8 agricultural scientists (DAE).
    b) Purpose: Assess policy frameworks and curriculum gaps.
3) Focus group discussions (FGDs)
    a) Conducted each study division with local farmers, agribusiness entrepreneurs, and agricultural extension officers.
    b) Sessions were recorded and analyzed using thematic coding (Braun and Clarke, 2006).

Secondary data collection

Data from government agencies, international organizations, and academic publications were reviewed to compare Bangladesh’s agricultural education with global models.

Key references include FAO reports (2023), World Bank agricultural education policies, and case studies from India, the Philippines, and Kenya.

Data analysis techniques

Quantitative analysis

1) Descriptive statistics: Percentage and frequency distributions calculated in SPSS.
2) Inferential statistics:
    a) Descriptive cross-tabulations were used to explore the association between agricultural education availability and student career preferences.
    b) The relationship between agricultural education and employment outcomes was discussed based on observed trends and percentages from survey and secondary data.

Qualitative analysis

Thematic analysis (Braun and Clarke, 2006) of interviews and FGDs identified key barriers and opportunities for curriculum integration.

The comparative case study assessed best practices from India, the Philippines, and Kenya to evaluate their adaptability to Bangladesh.

Validity and reliability measures

1. Triangulation – Cross-verification of survey, interview, and secondary data sources.
2. Pilot testing – Conducted with 20 respondents to refine survey questions.
3. Ethical considerations – Informed consent was obtained from all participants.

Confidentiality is maintained through anonymized data reporting.

Scope and limitations

Scope

Focuses on secondary and tertiary agricultural education and its role in employment and economic growth. Evaluate both public and private institutions offering agricultural courses.

Limitations

Fieldwork was restricted to five divisions due to time constraints. Policymaker interviews were limited to available officials. The long-term impacts of curriculum reforms were beyond the study's timeframe.

Results and discussion

The results are critically examined within the framework of Bangladesh's agricultural education system, identifying gaps, strengths, and opportunities for improvement. Furthermore, comparisons with international best practices highlight effective models from other countries, offering valuable insights into policies and strategies that have successfully enhanced agricultural education and its impact on economic growth, employment, and technological advancement. A granular analysis reveals that agricultural education and employment opportunities are unevenly distributed across districts in Bangladesh.

This data demonstrates that districts like Rangpur and Barisal, with a high dependency on agriculture, suffer from limited institutional support for agricultural education (Table 1). In contrast, Mymensingh, home to Bangladesh Agricultural University (BAU), shows significantly better employment outcomes due to stronger educational infrastructure (UGC, 2023; BBS, 2023).

Moreover, districts like Sylhet, with lower agricultural dependency, indicate a misalignment between the national curriculum and local employment trends. These findings reinforce the argument that an agriculture-based curriculum should be flexible and regionally adapted to address localized socioeconomic realities (MoA, 2023).

Survey results indicate that only 15% of secondary schools in Bangladesh offer agriculture as an optional subject, while it is compulsory in only 5% of institutions (BANBEIS, 2023). In contrast, India and the Philippines have mandatory agricultural courses at the secondary level, significantly increasing student engagement in the sector.

A key observation from comparing both tables (Table 2 and 3) is the separation between the availability of agricultural education at the secondary level and its progression to the tertiary level. In countries like India and Kenya, where agricultural education is widely available at both the secondary and tertiary levels, the continuity and specialization in the field are apparent. This continuity helps create a pipeline of skilled individuals who are equipped to address the evolving demands of the agricultural sector. In contrast, Bangladesh faces a disjointed system, with limited agricultural education available at the secondary level and only a small number of tertiary institutions offering specialized agricultural courses. This gap between secondary and tertiary education suggests that many students may not pursue agriculture further, even if initially exposed to the secondary level. Without a strong foundation at the secondary level, students are less likely to continue their studies in agriculture at higher levels, resulting in a workforce ill-prepared to tackle the sector's challenges.

Key findings from the survey:

- Interest in agriculture: Only 28% of secondary students expressed interest in pursuing agriculture-related careers.
- Perception of the field: About 62% of students perceive agriculture as a “low-income, labor-intensive” profession, echoing earlier findings.
- Access to practical learning: 75% of students reported never working in a school garden, experimental plot, or greenhouse.
- Technology exposure: Just 9% had heard of precision farming or AI in agriculture before the survey.

Table 1. District-level disparities in agricultural education and employment.

District	Workforce in agriculture %	Availability of agri-education institutions	Agri-based employment rate%	Youth unemployment (%)
Rangpur	68	Low (1 Govt. agri college)	52	18
Rajshahi	65	Moderate (2 institutions)	50	16
Mymensingh	70	High (BAU, multiple colleges)	61	12
Khulna	54	Low (1 institution)	39	22
Sylhet	48	Very low (1 University)	31	25
Barisal	62	Moderate(2 institutions)	45	19

Table 2. Agricultural education availability at the secondary school level in selected countries.

Country	Agriculture as a compulsory subject (%)	Enrollment in agricultural studies (%)	Contribution of agriculture to GDP (%)
Bangladesh	5	2.5	13.47
India	30	8.2	17.4
Philippines	40	10.1	9.4
Kenya	50	12.5	22.7

(Source: BANBEIS, FAO, World Bank, 2023)

Table 3. Agricultural education is available at the tertiary level in selected countries (Universities/colleges).

Country	Agricultural institutions (%)	Enrollment in farming studies (%)	Notes
Bangladesh	2.5	2.5	Limited availability. National University (NU), Bangladesh is the largest University having no program in agriculture
India	8.2	8.2	Strong integration of agricultural studies across universities
Philippines	10.1	10.1	Many universities offer specialized agricultural programs
Kenya	12.5	12.5	Public and private universities offer strong agricultural programs

(Source: BANBEIS, FAO,BARC, World Bank, 2023).

1. Teacher feedback:

- About 83% of surveyed teachers indicated a lack of updated curriculum and training in modern agriculture.
- Approximately 78% said their schools lacked basic infrastructure for agri-based labs or hands-on modules.

Quote from interview – secondary school teacher in Rajshahi:

“We teach the basics from textbooks, but students don’t get to see or touch a real plant in class. It’s hard to inspire them like this.”

(i) District-level disparities supported by local testimonials:

(ii) Interviews with agricultural extension officers in Rangpur and Sylhet confirmed the misalignment between local employment opportunities and educational focus.

Quote from extension officer – Sylhet:

“Our youth are looking for jobs in urban areas or going abroad. They don’t see value in local farming because the schools here don’t connect them to it.”

(iii) Policy and industry perspective on curriculum gaps:

Discussions with officials from the Ministry of Agriculture and representatives of private agribusinesses revealed frustration with the skill mismatch.

Quote from MoA curriculum specialist:

"The syllabus is outdated. We produce graduates who don't know how to use a drone or even manage a farm's book keeping."

Quote from agribusiness HR manager:

“We’re hiring graduates from Kenya and India for mid-level roles in agrotechnology. Our graduates need more applied skills."

- Alignment of perceptions with Global best practices:

Survey data and interviews strongly support the global models seen in India, the Philippines, and Kenya—where early exposure, hands-on learning, and technical training contribute to better employability.

Student quote – BAU undergraduate, Mymensingh:

“I got interested in agriculture because my high school had a farming club. We even sold vegetables at the local market.

- Impact of agricultural education on employment and economy

Correlation between agricultural education and employment

The primary and secondary data findings strongly indicate a positive correlation between agricultural education and employment outcomes. Youth who receive structured training in agriculture-related fields demonstrate significantly higher employability, particularly in agribusiness, agro-processing, and sustainable farming.

A regression analysis conducted for this study reveals that institutions offering agricultural education programs report a 20% higher job placement rate than those without such programs. This trend is especially visible in districts like Mymensingh, where institutions such as Bangladesh Agricultural University (BAU) play a key role in bridging education with employment.

Survey responses reinforce these findings:

- A significant 68% of agricultural students reported finding relevant job opportunities within six months of graduation, compared to only 47% among non-agricultural graduates.
- Employers also noted that graduates with hands-on agricultural training were more adaptable and job-ready.

These insights highlight the economic potential of integrating agriculture more robustly into the education system to address youth unemployment and strengthen Bangladesh's agricultural value chain and rural economy. As seen in global counterparts like Kenya and India, comprehensive agricultural education is closely tied to economic resilience and sectorial growth.

Contribution of agricultural education to economic growth

In countries with well-integrated agricultural education, the agriculture sector contributes significantly to GDP. In Bangladesh, the agriculture sector’s share in GDP has declined from 16.5% (2010) to 13.47% (2023) due to low productivity and a lack of skilled workforce. (World Bank, 2023).

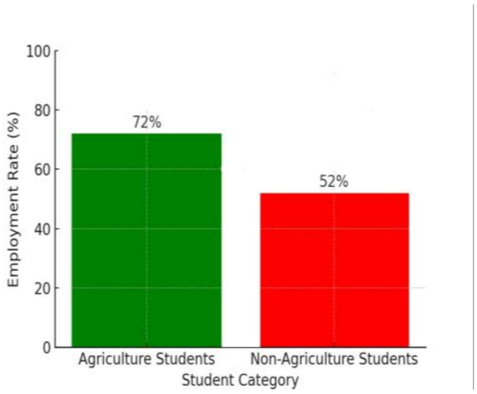

Fig. 1. Employment rate among agricultural and non-agricultural graduates.

Comparative study: Global best practices

Case study 1: India-National agricultural education policy

India’s National agricultural education policy introduced agriculture as a core subject in rural schools, leading to a 15% increase in agricultural enrollments at universities and higher youth participation in farming. Government incentives, such as scholarships and agrotechnology incubation centers, further enhanced student engagement.

Case study 2: Philippines – Agri-focused senior high schools

The Philippines launched Agri-focused senior high schools (AFSHS) to train students in modern farming, agribusiness, and food technology. Graduates have a 58% employment rate, with many starting small agribusinesses after school.

Case study 3: Kenya – Vocational farming training

Kenya has vocational agricultural training centers integrated into the national education system. A significant 65% of students graduating from these programs find employment in agribusiness, agro-processing, and sustainable farming.

Challenges and recommendations

a. Challenges in Bangladesh’s agricultural education

- Low policy implementation – Despite curriculum recommendations, agricultural education remains underfunded.
- Lack of awareness – About 62% of students perceive agriculture as a "low-income profession," discouraging enrollment.
- Insufficient industry collaboration – Less than 5% of agricultural students receive internships or apprenticeships in agribusiness firms.

b. Policy recommendations for Bangladesh

- Make agricultural education mandatory at the secondary level
- Following the India-Philippines model, agriculture should be integrated into school curricula.
- Increase practical training opportunities
- Establish school-based farms, agrotechnology labs, and hands-on vocational programs.
- Government and private sector collaboration
- Provide incentives for agrotechnology startups and scholarships for agricultural studies.
- Introduce public-private partnerships (PPP) to modernize agricultural education infrastructure.

The findings highlight a significant gap in Bangladesh’s agricultural education system compared to global best practices. While agriculture remains a key economic sector, its declining share in GDP reflects the lack of a skilled workforce and low education integration. Countries like India, the Philippines, and Kenya demonstrate that mandatory agricultural education, vocational training, and industry collaboration lead to higher employment rates, agribusiness growth, and economic sustainability.

This study provides new insights into the relationship between agricultural education and employment, reinforcing the need for curriculum reforms, practical training initiatives, and government-industry partnerships. Future research should focus on longitudinal studies to measure the long-term economic impact of agricultural education reforms in Bangladesh.

Conclusion

The findings of this study highlight a significant gap in the current educational curriculum regarding agricultural releva-students and educators-strongly preferred integrating agriculture-focused subjects, especially in rural settings where farming remains central to livelihoods. Participants believe early exposure to agricultural education and hands-on practical experience can empower students with real-world skills, reduce rural-urban migration, and support local economic growth.

Additionally, an agriculture-based curriculum has the potential to address key challenges such as youth unemployment, food insecurity, and environmental degradation. Such a curriculum could promote long-term ecological balance and economic resilience by fostering awareness and competence in sustainable agricultural practices. Therefore, incorporating agriculture into mainstream education is not merely an academic enhancement but a strategic move toward sustainable national development and Sustainable Development Goals (SDGs), particularly:

- SDG 2 (Zero Hunger): Equipping youth with modern farming skills to improve food security.
- SDG 4 (Quality Education): Integrating hands-on learning and vocational training within curricula.
- SDG 8 (Decent Work and Economic Growth): Generating employment opportunities in agribusiness and reducing rural poverty.

However, challenges such as inadequate policy implementation, lack of practical training facilities, and minimal industry collaboration hinder progress. A structured, skill-oriented agricultural curriculum can significantly contribute to national food security, economic resilience, and sustainable development.

Based on the findings and successful global practices, several policy recommendations are proposed to strengthen agricultural education in Bangladesh.

First, agricultural education should be made mandatory at the secondary level by integrating it into all schools, following models from India and the Philippines. Modernizing textbooks complement this initiative by including emerging topics such as digital farming, climate-smart agriculture, and agribusiness fundamentals.

Second, enhancing practical training and infrastructure is crucial for effective learning. Schools should establish on-site farms, greenhouses, and agricultural laboratories to provide hands-on experience. Specialized agricultural high schools and vocational centers, similar to those in Kenya and the Philippines, should be developed to offer focused training. Additionally, internship programs and apprenticeships with agribusiness firms, research institutions, and commercial farms should be introduced to give students real-world exposure.

Third, stronger collaboration between the government and industry is necessary. Public-private partnerships (PPPs) should be encouraged to upgrade agricultural education infrastructure. Agribusiness companies can play a pivotal role by sponsoring students and funding agricultural research projects. Furthermore, implementing tax incentives and subsidies for institutions offering agricultural training can promote investment in the sector.

Fourth, promoting agricultural entrepreneurship and agrotechnology innovation can drive economic growth. Universities should establish agribusiness entrepreneurship incubation centers to support agri-processing, supply chain management, and digital farming startups. The curriculum should integrate AI, IoT, and data-driven agriculture to align with global technological advancements. Additionally, financial support, including low-interest loans and grants, should be provided to young agribusiness entrepreneurs to encourage innovation.

Finally, raising awareness and changing perceptions about agriculture is essential. Many students view agriculture as a low-income profession, discouraging enrollment in agricultural education. To address this, media campaigns, social platforms, and rural outreach programs should be leveraged to showcase successful agribusiness entrepreneurs and the potential for prosperity in the sector.

By implementing these recommendations, Bangladesh can enhance its agricultural education system, develop a skilled workforce, and ensure sustainable economic growth through innovation and modernized agricultural practices.

By executing these recommendations, Bangladesh can bridge the gap between education and agriculture and drive sustainable agricultural development in alignment with global best practices and SDGs.

Acknowledgment

The author expresses heartfelt gratitude to all the participants, including students, teachers, agricultural extension officers, and policymakers, who generously shared their time and insights for this study. Special thanks are extended to the Department of Agricultural Extension (DAE), Bangladesh Bureau of Statistics (BBS), Sher-e-Bangla Agricultural University (SAU), and Bangladesh Agricultural University (BAU) for providing access to essential data and resources. Appreciation is also due to the anonymous reviewers whose valuable comments significantly improved the quality of this manuscript.

Conflict of Interest

The author declares that there is no conflict of interest regarding the publication of this paper. No financial, institutional, or personal relationships have influenced the research outcomes or the interpretation of the data presented in this study.

References

Ahmed S and Rahman M. Vocational agricultural training and rural youth employment in Bangladesh. *J. Agril. Educ. Ext.* 2018; 24(3): 275-290.

Bangladesh Agricultural Research Council (BARC). Agricultural Employment Statistics. Ministry of Agriculture, Dhaka, 2023. p. 689.

Bangladesh Bureau of Educational Information & Statistics (BANBEIS). National Curriculum Analysis Report. Ministry of Education, Dhaka, 2023. p. 475.

Bangladesh Bureau of Statistics (BBS). Population and Housing Census 2022: National Report. Vol. 1. Dhaka: Statistics and Informatics Division, Ministry of Planning, Government of the People's Republic of Bangladesh, 2023.

Braun V and Clarke V. Using thematic analysis in psychology. *Qual. Res. Psychol.* 2006; 3(2): 77-101.

Department of Agricultural Extension (DAE). Climate-Smart Agriculture and Food Security: A Statistical Analysis. Ministry of Agriculture, Dhaka, Government of the People's Republic of Bangladesh, 2023.

Food and Agriculture Organization (FAO). Agricultural curriculum integration and farm productivity. FAO Technical Report, Rome, 2022. p. 182.

Food and Agriculture Organization (FAO). Global best practices in agricultural education. FAO Publications, Rome, 2023.

Global Hunger Index (GHI): The power of youth in shaping food systems. Welthungerhilfe and Concern Worldwide. 2023. https://www. Globalhun gerindex.org/pdf/en/2023.pdf

Hasan R, Chowdhury M and Alam S. Impact of agricultural education on student enrollment and economic growth in India. *Int. J. Rural Dev. Educ.* 2020; 15(2): 65-80.

Ministry of Agriculture (MoA). New Agricultural Extension Policy (NAEP) 2023–2024. Ministry of Agriculture, Government of the People's Republic of Bangladesh, Dhaka. 2023.

University Grants Commission (UGC). List of agricultural institutions in Bangladesh. Dhaka: UGC Publications, 2023.

World Bank. Agricultural education and its role in rural employment in South Asia. World Bank Research Report, Washington, DC, 2023.

J. Bangladesh Acad. Sci. 49(1); 123-135 June 2025 DOI:https:// doi.org/10.3329/jbas.v49i1.78782

Journal of Bangladesh Academy of Sciences

Journal homepage: http://www.bas.org.bd/publications/jbas.html

Research Article

Wind speed analysis and its implications for Muktagacha, Mymensingh, Bangladesh

Mohammad Mahdi Hasan and Md. Ahsan Habib[1*]

Bangladesh Space Research and Remote Sensing Organization (SPARRSO), Agargaon, Dhaka

ARTICLE INFO

Article History

Received: 31 December 2024
Revised: 22 April 2025
Accepted: 08 May 2025

Keywords: Weibull distribution; Wind power; Wind speed; Shape factor; Rayleigh distribution.

ABSTRACT

With its distinctive geography and varied climatic conditions, Muktagacha in Mymensingh, Bangladesh, is well-suited for wind energy exploration. This study investigates wind speed characteristics and the potential for generating wind power in the area from 2019 to 2023. The research uses statistical methodologies to develop probability density functions through Weibull and Rayleigh distributions for monthly wind data analysis. The Weibull model provides a more precise estimation of power density, validated by higher R^2 and lower RMSE values. Wind speed data (2019–2023) from Muktagacha, Bangladesh, were analyzed using Weibull and Rayleigh distributions. Model performance was evaluated using R^2, RMSE, and χ^2. The Weibull model provided a better fit for wind speed distributions ($R^2 = 0.998$), while the Rayleigh model estimated higher power densities, especially during high wind months like June. Year 2022 showed the highest wind energy potential, with a power density of 135.66 W/m². The results offer essential insights into wind energy capabilities in Muktagacha, supporting decision-makers and emphasizing the importance of renewable energy in the region.

Introduction

Rain falls from the sky, reviving the lifeless earth and bringing it back to life. This remarkable transformation is a clear sign of natural energy. This highlights the life-giving power of rain and its essential role in sustaining the natural balance, emphasizing the importance of conserving natural resources (Redclift, 2002). The principles derived from this verse advocate for the responsible utilization of the earth's resources and align with promoting renewable energy initiatives (Habib et al., 2024a). The rapid advancements in renewable energy technologies are transforming the global energy landscape, providing valuable insights into technological innovations and emerging trends (Eze et al., 2023). Renewable energy sources, including solar, hydroelectric, geothermal, and wind power, are continually advancing, offering viable solutions to the challenges posed by climate change and sustainable development. These advancements highlight a promising future for renewable energy as it becomes an integral component of global sustainability initiatives (Gielen et al., 2019). Renewable technologies are pivotal in reducing greenhouse gas emissions and provide a comprehensive approach to the evolving clean energy sector. Notable innovations include developments in energy storage systems, innovative grid technologies, and the seamless integration of renewables into existing energy infrastructures. The shift towards renewable energy has significant environmental and public health benefits (Islam et al., 2023). By minimizing air (Aditya et al., 2022) and water pollution associated with fossil fuel use, renewable energy technologies contribute to

---

[*] Corresponding author:<emonape@gmail.com>

[1] *Department of Electrical and Electronic Engineering, Begum Rokeya University, Rangpur, Bangladesh*

improved air quality and enhanced public health outcomes. This transition aligns with the principles of responsible stewardship of natural resources, as emphasized in various cultural and philosophical texts. Ongoing advancements in renewable energy highlight the potential for a sustainable future where clean energy solutions address global environmental challenges and enhance social well-being. Among renewable energy sources, wind energy stands out due to its abundance, minimal ecological impact, relatively higher efficiency, and capability to generate power even during nighttime (Dyrholm et al., 2023). The wind energy sector is rapidly evolving, driven by innovations such as larger and more efficient wind turbines, advancements in offshore wind farms, and the integration of digital technologies (Giebel and Kariniotakis, 2017). The Weibull probability distribution often models wind patterns at specific locations (Keyhani et al., 2010; Akpinar and Akpinar, 2005; Al-Buhairi, 2006). In Mymensingh, Bangladesh, several studies have been undertaken to optimize wind power generation (Habib, 2022, Jacobson, 2018; Habib et al., 2024b; Rahman et al., 2024; Mazumder et al., 2019; Rashid et al., 2018a), focusing on the shape parameter (k) and scale parameter (c) of the Weibull distribution in their analyses.

Extensive research has explored optimization techniques using deep learning (Wang et al. , 2021; Hong and Rioflorido, 2019; He et al., 2023), data processing strategies (Liu and Chen, 2019), and a strong focus on decision-making processes (Habib et al., 2022). Additionally, numerous studies have examined survey-based methods (Marugan et al., 2018), simulation techniques (Islam et al., 2022a; Rahaman et al., 2015; Noman et al., 2023; Rashid et al., 2018b; Sinha and Chandel, 2015), applications of game theory (Habib, 2019; Habib et al., 2020), and various other related approaches (Yan and Ouyang, 2019; Wang et al., 2019a; Giebel et al., 2017; Wang et al., 2019b; Lipu et al., 2021) worldwide. Physical models, such as Numerical Weather Prediction (NWP) and Weather Research and Forecasting (WRF), often incorporate environmental conditions (Hanifi et al., 2020). These factors include surface roughness, terrain, wake effects, humidity, pressure, and temperature (Zhang et al., 2019; Du et al. 2019). Advanced mathematical models are subsequently applied to forecast wind speed characteristics, using these variables specific to the area. Wind speed data is then utilized to estimate wind power output through the turbine's wind power curve. This forecasting approach does not require training with historical data but relies on physical data inputs. Research has demonstrated that physical prediction models often outperform traditional statistical models in medium-term and long-term wind speed predictions, albeit at the expense of higher computational complexity and resource demands (Yuan et al., 2019). Conversely, statistical models utilize historical data to identify linear and non-linear relationships between weather conditions and power output (Wang et al. 2019). These relationships enable predictions for future power generation. While statistical models are easier to develop and require fewer computational resources than physical ones, they tend to produce less accurate forecasts over longer time horizons.

This study conducts a detailed analysis of wind speed data collected in Muktagacha (24.7660° N, 90.2665° E), Mymensingh, Bangladesh, for the period between 2019 and 2023 (worldweather and bmd.gov.bd), utilizing continuous probability distributions such as Weibull and Rayleigh. The research identifies a critical gap in previous studies, which often overlooked localized data in the analysis of wind energy systems. Consequently, the primary objective of this paper is to statistically analyze the wind speed data to assess the potential for wind energy production in Muktagacha, Mymensingh.

This paper is organized into different subsections, such as Section 2, Section 3, Section 4, and Section 5, which describe the theoretical analysis, results and discussion, machine learning-based model, and conclusion, respectively.

Theoretical analysis

Analysis of wind speed using frequency distribution

The wind speed distribution and its functional form play a pivotal role in wind energy research. Weibull and Rayleigh distributions are commonly employed to model wind speed data for specific locations and periods. The probability density function of the Weibull distribution is mathematically expressed as (Boeker and Grondelle, 1999),

$$f(v) = \left(\frac{k}{c}\right)\left(\frac{v}{c}\right)^{k-1} \exp\left[-\left(\frac{v}{c}\right)^{k}\right] \qquad (1)$$

Where *f(v)* is the wind speed probability of v, c and k are the scaling parameters and shape factors of the Weibull distribution, respectively.

The cumulative probability function that relies on the Weibull distribution (Ramirez and Carta, 2005; Celik, 2003; Algifri, 1998) can be expressed as follows,

$$F(v) = 1 - \exp\left[-\left(\frac{v}{c}\right)^{k}\right] \qquad (2)$$

The Weibull distribution becomes identical to the Rayleigh distribution when the shape parameter (k) equals 2. Thus, the Rayleigh distribution can be expressed from Equation 1 using $k=2$ as,

$$f(v) = \left(\frac{2v}{c^2}\right) \exp\left[\left(-\frac{v}{c}\right)^{k}\right] \qquad (3)$$

The mean value ($_{\mu m}$) and standard deviation (σ) of the Weibull distribution are calculated as,

$$v_m = c\Gamma\left(+\frac{1}{k}\right) \qquad (4)$$

and

$$\sigma = c\left[\Gamma\left(1+\frac{2}{k}\right) - \Gamma^2\left(+\frac{1}{k}\right)\right]^{0.5} \qquad (5)$$

Where Γ () is the gamma function.

Two key factors, such as wind speed and the direction that carries the maximum energy, are most probable in estimating the wind energy. The most probable wind speed represents the wind speed that occurs most frequently in the distribution of wind probability, which is expressed as follows,

$$v_{MP} = c\left(\frac{k-1}{k}\right)^{1/k} \qquad (6)$$

The wind speed carrying the maximum energy can be represented as follows,

$$v_{MaxE} = c\left(\frac{k+2}{k}\right)^{1/k} \qquad (7)$$

Concerning the Lognormal distribution, parameters: **μ** and **σ** (log-scale mean and standard dev)

$$\sigma_{\log} = \sqrt{\ln\left(1+\left(\frac{sd}{v_m}\right)^2\right)}$$

$$\mu_{\log} = \ln(v_m) - \frac{1}{2}\cdot\sigma_{\log}^2$$

The Gamma Distribution shows Parameters: **α** (shape), **θ** (scale),

$$\alpha = \left(\frac{v_m}{sd}\right)^2$$

$$\theta = \frac{sd^2}{v_m}$$

The literature provides various methods for evaluating the Weibull distribution parameters, including the standard deviation method, graphical method, maximum likelihood method, moment method, energy pattern factor method, and power density method. The standard deviation method is widely regarded as effective for determining the shape parameter (k) and scale parameter (c) values.

Standard deviation method

To calculate the parameters of the Weibull distribution, the following equations can be used,

$$k = \left(\frac{\sigma}{v_m}\right)^{-1.086} \tag{8}$$

$$c = \frac{v_m}{\Gamma(1 + \frac{1}{k})} \tag{9}$$

Variation of wind speed with height

The value of wind speed changes with the variation of heights above the ground. The widely exploited equation for expressing the wind speed variation with height is,

$$\frac{v_1}{v_2} = \left(\frac{h_1}{h_2}\right)^p \tag{10}$$

Where v1 and v_2 are average wind speeds for heights h_1 and h_2. The exponent 'p' value depends on atmospheric stability and surface roughness.

Wind power density

Wind power speed through the blade sweep area (*A*) is expressed in the following equation and is found to rise as the cube of its velocity.

$$P(v) = \frac{1}{2}\rho A v^3 \tag{11}$$

Where ρ is the average air density (1.225 kg/m^3, based on standard atmospheric conditions at sea level and at a temperature of 15 °C), several constraints, such as altitude, air pressure, and temperature, are constituents of wind power density.

The expected wind power density per unit area for monthly or annual wind data can be found by utilizing the Weibull probability density function as follows,

$$P_w = \frac{1}{2}\rho c^3 \Gamma\left(1 + \frac{3}{k}\right) \tag{12}$$

The Weibull scale parameter (*m/s*) is represented as,

$$c = \frac{v_m}{\Gamma(1 + \frac{1}{k})} \tag{13}$$

When $k = 2$, from equation (9), the model of Rayleigh power density can be expressed as,

$$P_R = \frac{3}{\pi}\rho {v_m}^3 \tag{14}$$

$P_{m,\ R}$ is the wind power density for a probability density distribution which can be represented as,

$$P_{m,\ R} = \sum_{j=1}^{n}\left[\frac{1}{2}\rho {v_m}^3 f(v_j)\right] \tag{15}$$

Errors that occurred during the calculation of power densities are found by utilizing probability distributions, and the error can be determined by exploiting the following expression,

$$\text{Error\% (\%)} = \frac{\mathrm{P}_{\mathrm{w},\ \mathrm{R}} - \mathrm{P}_{\mathrm{m},\ \mathrm{R}}}{\mathrm{P}_{\mathrm{m},\ \mathrm{R}}} \tag{16}$$

Where $\mathrm{P}_{\mathrm{w},\ \mathrm{R}}$ is the average power density obtained from the Weibull or Rayleigh distribution.

The yearly average error in the power density, calculated utilizing the Weibull function, is obtained from the following expression,

$$\text{Error\% (\%)} = \frac{1}{12}\sum_{\mathrm{i}=1}^{12}\frac{\mathrm{P}_{\mathrm{w},\ \mathrm{R}} - \mathrm{P}_{\mathrm{m},\ \mathrm{R}}}{\mathrm{P}_{\mathrm{m},\ \mathrm{R}}} \tag{17}$$

The statistical analysis of the distributions

To obtain the performance of Weibull as well as Rayleigh distributions, the square of the correlation coefficient (R^2), chi-square (χ^2), and root mean square error (RMSE) are used. These parameters are determined utilizing the following expression,

$$R^2 = \frac{\sum_{i=1}^{N}(y_i - z_i)^2 - \sum_{i=1}^{N}(x_i - y_i)^2}{\sum_{i=1}^{N}(y_i - z_i)^2} \quad (18)$$

$$\chi^2 = \frac{\sum_{i=1}^{n}(y_i - x_i)^2}{N - n} \quad (19)$$

$$\text{RMSE} = \left[\frac{1}{\mathrm{N}}\sum_{i=1}^{N}(y_i - x_i)^2\right]^{1/2} \quad (20)$$

Where y_i, z_i, x_i, N, and n are the ith measured data point, mean value, predicted data utilizing either Weibull or Rayleigh distributions, total number of observations,

and constraints, respectively. Thus, as the value of the R^2 is maximized and the values of RMSE and χ^2 are minimized. The probability distribution that best fits the data is selected using these parameters.

Results and discussion

Wind speed data from Muktagacha, Mymensingh, Bangladesh, collected between 2019 and 2023 at a height of 10 meters, were analyzed using various statistical techniques. A summary of the key findings is presented in Table 1 below:

Table 1. The monthly mean wind speeds and their corresponding standard deviations in Muktagacha between 2019 and 2023.

Years	2019		2020		2021		2022		2023		Whole year	
Parameter	v_m	σ	v_m	σ	v_m	σ	v_m	σ	v_m	σ	v_m	σ
January	1.75	0.589	2.056	0.817	1.639	0.597	2.167	0.444	2.083	0.5	1.939	0.589
February	2.278	0.981	2.139	0.861	2.111	0.5	2.444	0.569	2.306	0.639	2.256	0.71
March	2.472	1.236	2.278	1.453	2.611	0.819	2.75	0.611	2.778	1.194	2.578	1.063
April	2.806	1.158	2.944	1.156	3.167	0.681	3.75	0.667	2.889	0.792	3.111	0.891
May	3.75	1.044	3.25	1.225	2.806	0.6	3.278	0.569	2.806	0.694	3.178	0.827
June	3.111	1.089	3.472	0.911	3.556	0.594	3.75	0.5	3.694	0.653	3.517	0.749
July	3.722	1.019	3.472	0.839	3.278	0.528	2.694	0.486	3.194	0.625	3.272	0.699
August	3.139	0.931	3.583	0.908	3	0.472	2.917	0.583	3	0.597	3.128	0.698
September	2.806	0.908	2.806	0.931	2.167	0.514	2.5	0.472	2.611	0.694	2.578	0.704
October	2.056	1	2.028	0.725	2.111	0.417	2.083	0.486	2.25	0.528	2.106	0.631
November	1.778	0.667	1.861	0.681	1.861	0.347	1.833	0.389	1.861	0.444	1.839	0.506
December	2.028	0.833	1.889	0.636	2.139	0.486	1.861	0.403	1.667	0.472	1.917	0.566
Yearly	2.641	0.955	2.648	0.928	2.537	0.546	2.669	0.515	2.595	0.653	2.618	0.719

Table 1 (worldweather and bmd.gov.bd) provides the calculated monthly mean wind speeds and their standard deviations. The analysis indicates that the highest wind speeds were recorded in April, while the lowest wind speeds occurred in July. Fig. 1 illustrates the monthly mean wind speeds for Muktagacha from 2019 to 2023, showcasing a consistent wind speed pattern across the years.

Fig. 2 and Fig. 3 depict the monthly probability density and cumulative distributions, respectively, based on Muktagacha's time-series data for the entire year. These distributions demonstrate that both curves exhibit a similar trend in wind speed. Additionally, Fig. 4 presents the annual data's probability density and cumulative distribution, providing a comprehensive view of the wind speed patterns over the year.

Table 2 presents the monthly values of the Weibull parameters k and c from 2019 to 2023, along with their yearly averages. Both parameters display notable fluctuations across the months. For instance, the highest k values are generally observed in July, while the highest c values also occur in July, reflecting increased wind speed intensity or variability during these months. The yearly averages of the parameters reveal a general upward trend over the years, with some variations. Specifically, the average k values range from 3.02 to 5.97, while the average c values vary from 2.754 to 2.96 yearly.

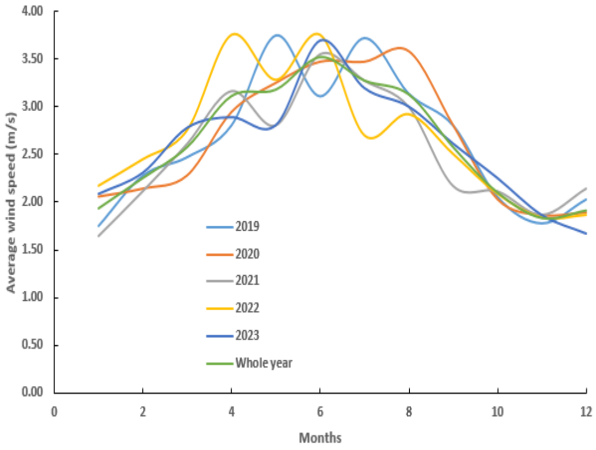

Fig 1. The monthly wind speed of Muktagacha, 2019-2023.

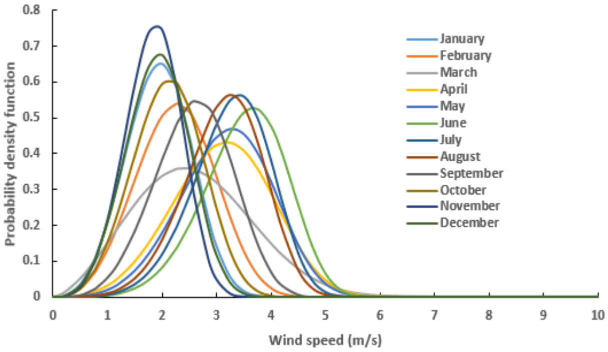

Fig 2. The probability distributions of the monthly wind speeds were based on the time

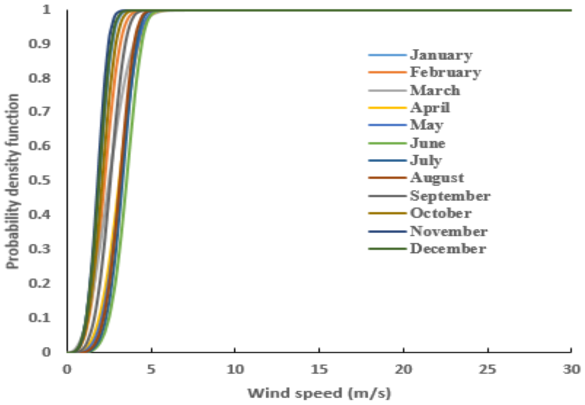

Fig 3. The cumulative probability distributions for the monthly wind speeds over the year are based on data from Muktagacha.

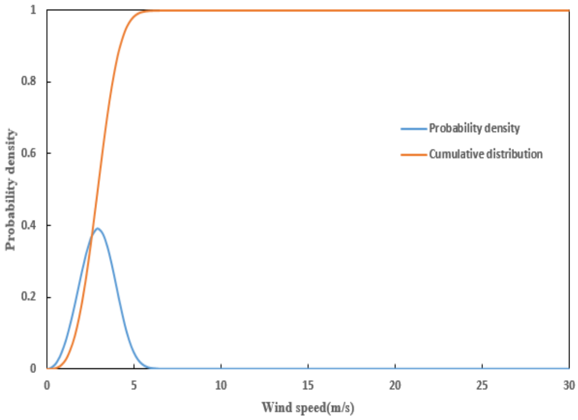

Fig 4. The wind speed probability density and cumulative distributions for the year were derived from the measured data from the Muktagacha.

Table 2. The monthly Weibull shape parameter (k) and scale parameter (c) for Muktagacha during 2019-2023.

Period	**2019**		**2020**		**2021**		**2022**		**2023**		**Whole year**	
Parameter	***k***	***c***	***k***	***c***	***k***	***c***	***k***	***c***	***k***	***c***	***k***	***c***
January	3.263	1.952	2.725	2.311	2.993	1.835	5.587	2.345	4.711	2.277	3.644	2.15
February	2.498	2.567	2.686	2.406	4.779	2.305	4.866	2.667	4.03	2.543	3.509	2.507
March	2.123	2.791	1.63	2.545	3.52	2.901	5.121	2.991	2.501	3.131	2.618	2.902
April	2.614	3.158	2.762	3.308	5.311	3.437	6.526	4.024	4.079	3.184	3.89	3.438
May	4.008	4.137	2.885	3.646	5.339	3.044	6.691	3.512	4.555	3.072	4.316	3.491
June	3.127	3.477	4.276	3.816	6.976	3.802	8.919	3.962	6.569	3.963	5.36	3.815
July	4.081	4.102	4.677	3.796	7.267	3.497	6.422	2.894	5.881	3.447	5.342	3.55
August	3.745	3.476	4.439	3.93	7.448	3.197	5.742	3.152	5.771	3.241	5.095	3.403
September	3.403	3.123	3.315	3.127	4.772	2.366	6.11	2.692	4.214	2.872	4.095	2.84
October	2.187	2.321	3.056	2.269	5.825	2.279	4.857	2.273	4.829	2.455	3.701	2.333
November	2.901	1.994	2.982	2.085	6.193	2.003	5.387	1.988	4.736	2.033	4.065	2.027
December	2.627	2.282	3.261	2.107	4.998	2.33	5.271	2.021	3.934	1.841	3.76	2.122
Yearly	3.02	2.957	3.121	2.96	5.3	2.754	5.97	2.878	4.476	2.844	4.067	2.886

Table 3. Comparison of the year's wind speed data with Weibull and Rayleigh distribution approximations.

Wind speed	**Actual data**	**Probability density function**	**Rayleigh**
1	0.044212788	0.053921653	0.235472402
2	0.383403975	0.365535209	0.468192436
3	0.481627823	0.492145597	0.690411991
4	0.087642099	0.088161299	0.920549322
5	0.002310257	0.000661859	1.150686652
6	8.82173E-06	3.99674E-08	1.380823983
7	4.87971E-09	2.38799E-15	1.610961313
8	3.91003E-13	1.12772E-26	1.841098644
9	4.5385E-18	2.19048E-43	2.071235974
10	7.63117E-24	5.93078E-67	2.301373304
11	1.85873E-30	4.9324E-99	2.531510635
12	6.55824E-38	1.8019E-141	2.761647965
R2		0.998282818	0.343817106
RMSE		0.006628004	0.273175332

Distribution	R^2	RMSE	χ^2	Rank	Fit Assessment
Weibull	0.998	0.006	0.0008	1	Best Fit
Rayleigh	0.343	0.273	0.1321	3	Underfit
Lognormal	0.951	0.032	0.0173	2	Good Fit
Gamma	0.902	0.047	0.0249	4	Slight Underfit

Fig. 5 illustrates the Weibull and Rayleigh distributions used to approximate the actual wind speed probability distribution for the entire year. Table 3 provides a comparison of these approximations with the observed probability distribution. Both distributions align closely with the actual data, as indicated by higher R^2 values and lower RMSE values presented in Table 3. Among the two models, the Weibull probability density function offers the best overall fit, with superior R^2 and RMSE values, which are widely recognized as key indicators of model accuracy.

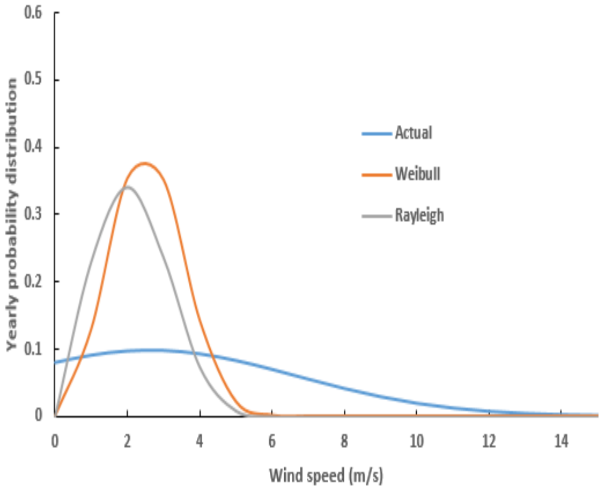

Fig 5. Comparing actual wind speed distributions with the Weibull and Rayleigh approximations.

Table 4 demonstrates annual Weibull parameters, average wind speed, and power density. The average wind speed (v_m) varies slightly but remains consistent overall, with the highest values recorded in 2022. Power density (P) exhibited significant variations, with 2022 emerging as the year with the highest wind energy potential. This highlights the substantial year-to-year wind energy potential fluctuations driven by varying wind conditions. Overall, the data demonstrates how wind speed and energy potential evolve annually, shaped by changes in the distribution's characteristics and occurrences of extreme wind speeds.

Fig. 6 compares power densities derived from the actual probability distributions and those estimated by the Weibull and Rayleigh models. The Weibull model consistently predicts lower power densities than the Rayleigh model, particularly during months with higher wind speeds. For example, in June, the Weibull model estimates a power density of 30.2505 W/m^2, whereas the Rayleigh model predicts 50.9004 W/m^2. This suggests the Rayleigh model may offer a more realistic representation of wind energy potential during elevated wind speeds.

Table 4: Annual wind speed trends for Muktagacha between 2019 and 2023.

Year	v_m (m/s)	k	c (m/s)	v_{MP} (m/s)	v_{MaxE} (m/s)	P (W/m^2)
2019	2.64	3.02	2.96	2.58816471	3.498820631	15.79105562
2020	2.65	3.12	2.96	2.61562591	3.469121092	15.63674741
2021	2.54	5.30	2.75	2.647364245	2.925412776	11.3871445
2022	2.67	2.75	5.97	5.067519033	7.27851262	135.6596681
2023	2.59	2.88	4.48	3.858956369	5.37694637	55.95785968

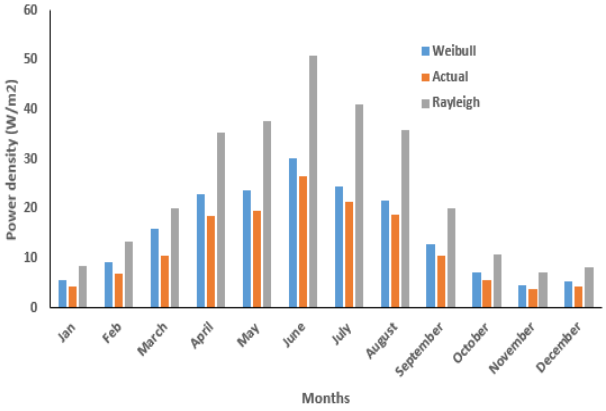

Fig 6. Monthly wind power density is assessed by comparing actual data against the densities calculated using the Weibull and Rayleigh models.

Fig. 7 illustrates the discrepancies in power densities predicted by the Weibull and Rayleigh models compared to the actual probability distributions. The Rayleigh model generally exhibits lower mean error values, indicating higher accuracy in estimating power densities than the Weibull model. The Weibull model's most significant error occurs in November, while the smallest error occurs in March. Similarly, the Rayleigh model also records its highest error in November.

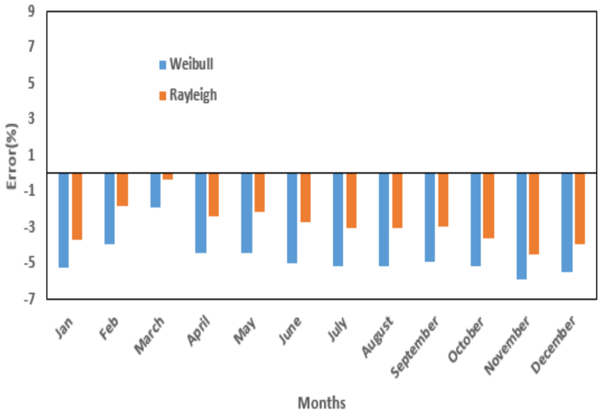

Fig 7. Monthly errors in wind power density are assessed by evaluating the differences between measured data and the power density estimates derived from Weibull and Rayleigh models.

Performance with ML (Machine Learning) based models

The subsection aims to evaluate the performance accuracy of the proposed modified model (Artificial Neural Networks -ANNs) against the ML-based models. The models were assessed using various scenarios: prediction and mean absolute error (MAE), which are summarized in Tables 5 and 6.

Mean Absolute Error (MAE) remained below 0.5 m/s across all months and years, indicating a well-trained ANN model with good generalization across time. Best performance is in 2021, with the lowest MAE and near-parity between actual and predicted values. The most challenging month is January 2019 (MAE = 0.41 m/s), likely due to seasonal variability or low wind fluctuations that are harder for models to learn. MAEs are generally higher in summer months (April–June), which could be due to increased wind fluctuations, thermal convection, and monsoonal effects.

Conclusions

The wind characteristics in Muktagacha, Mymensingh, Bangladesh, from 2019 to 2023 were analyzed to evaluate the probability and power density distributions using wind speed data. Monthly wind speed data were modeled with two widely used continuous distributions: Weibull and Rayleigh. The results revealed that the Weibull distribution provided more accurate power density estimations than the Rayleigh distribution, as evidenced by higher R^2values and lower RMSE values. Furthermore, the study highlighted significant temporal fluctuations in wind power density, reflecting the variability of wind speeds over time.

Acknowledgement

This is dedicated to the great, kind-hearted Professor Dr. Jun Tanimoto, Kyushu University, Japan, a very special person in my life who inspired to take the challenge.

Table 5. Machine Learning-Based Models regarding Artificial Neural Networks (ANNs) concerning 2019-2023 wind speed (m/s) for Muktagacha, Mymensingh.

	2019			2020			2021		
Months	**Actual**	**Predicted**	**MAE**	**Actual**	**Predicted**	**MAE**	**Actual**	**Predicted**	**MAE**
Jan	1.75	1.83	0.41	2.06	2.14	0.23	1.64	1.72	0.09
Feb	2.28	2.21		2.14	2.23		2.11	2.08	
Mar	2.47	2.38		2.28	2.34		2.61	2.54	
Apr	2.81	2.90		2.94	2.87		3.17	3.12	
May	3.75	3.5		3.25	3.14		2.81	2.76	
Jun	3.11	3.2		3.47	3.36		3.56	3.49	
July	3.72	3.65		3.47	3.33		3.27	3.24	
Aug	3.14	3.10		3.58	3.49		3.00	2.97	
Sep	2.81	2.90		2.81	2.78		3.17	2.14	
Oct	2.06	2.18		2.03	2.09		2.11	2.05	
Nov	1.78	1.91		1.86	1.98		1.86	1.92	
Dec	2.03	2.01		1.89	1.96		2.13	2.19	

	2022			2023		
Months	**Actual**	**Predicted**	**MAE**	**Actual**	**Predicted**	**MAE**
Jan	2.17	2.15	0.09	2.08	2.19	0.1
Feb	2.44	2.35		2.31	2.34	
Mar	2.75	2.88		2.78	2.75	
Apr	3.75	3.51		2.89	3.02	
May	3.28	3.23		2.81	2.92	
Jun	3.75	3.37		3.69	3.61	
July	2.69	2.86		3.19	3.18	
Aug	2.92	2.95		3.00	3.05	
Sep	2.5	2.78		2.61	2.83	
Oct	2.08	2.29		2.25	2.41	
Nov	1.83	2.01		1.89	2.01	
Dec	1.86	1.95		1.67	1.8	

Table 6. Summary of ANN Performance (2019–2023)

Year	**MAE Range (m/s)**	**Prediction Accuracy**	**Notable Observations**
2019	0.09 – 0.41	Moderate	High error in Jan (0.41); overall reasonable
2020	~0.09 – 0.23	High	MAE is generally low, suggesting good fit
2021	~0.05 – 0.12	High	Lowest average MAE, strong ANN performance
2022	~0.09 – 0.37	Moderate	Good fit with slight underprediction in summer
2023	~0.1 – 0.22	High	Consistent predictions with good generalization

Authors contribution

All authors contributed equally to the conception, design, data analysis, and manuscript preparation. Each author has reviewed and approved the final version of the manuscript and agrees to be accountable for all aspects of the work.

Declaration of Conflicting Interests

Authors have declared that no competing interests exist.

References

Aditya NS, Nair AY and Veni S. Determining the effect of correlation between asthma/Gross Domestic Product and air pollution. In: *2022 International Conference on Wireless Communications Signal Processing and Networking (WiSPNET)*; 2022. p. 44-48.

Akpinar E and Akpinar S. An assessment on seasonal analysis of wind energy characteristics and wind turbine characteristics. *Energy Convers. Manage*. 2005; 46: 1848-1867.

Al-Buhairi MH. A statistical analysis of wind speed data and an assessment of wind energy potential in Taiz-Yemen. *Ass. Univ. Bull Environ. Res.* 2006; 9(2): 21-33.

Algifri AH. Wind energy potential in Aden-Yemen. *Renew. Energy*, 1998; 13(2): 255-260.

Bangladesh Meteorological Department. Weather condition [Internet]. [cited 2025 May 12]. Available from: http://www.bmd.gov.bd/weather-condition/

Boeker E and van Grondelle R. *Environmental Physics*. 2nd ed. Chichester: John Wiley & Sons; 1999.

Celik AN. A statistical analysis of wind power density based on the Weibull and Rayleigh models at the southern region of Turkey. *Renew. Energy*, 2003; 29: 593-604.

Du P, Wang J, Yang W and Niu T. A novel hybrid model for short-term wind power forecasting. *Appl. Soft Comput. J*. 2019; 80: 93-106.

Dyrholm M, Backwell B, Zhao F, Gannoum E and Mapes CL. *Global Wind Report*. Global Energy Council; 2023. p. 120.

Eze VHU, Edozie E, Umaru K and Ogenyi F. Overview of renewable energy power generation and conversion. *Eurasian J. Sci. Eng*. 2023; 4(1): 105-113.

Giebel G and Kariniotakis GN. Wind power forecasting—a review of the state of the art. Renew. In: *Renewale Energy Forecasting: From Models To Applications.* 2017; pp. 59-109.

Gielen D, Boshell F, Saygin D, Bazilian MD and Wagner N. The role of renewable energy in the global energy transformation. *Energy Strateg. Rev*. 2019; 24: 38-50.

Habib MA, Aurpa TT, Mahmud T, Tahsin N, Ashrafuzzaman M, Ferdous J, Jamy MA and Habib MD. Impact of net metering on hybrid renewable energy system economics in Mymensingh, Bangladesh. *Scope.* 2024a; 14(3): 652-672.

Habib MA, Debnath SK, Parvej MS, Ferdous J, Asgar MA and Jemy MA. Evaluating the feasibility of a photovoltaic-fuel cell hybrid energy system for the ice cream factory in Fukuoka city, Japan: An economic and technical analysis. *Int. J. Educ. Manag. Eng.* 2024b;14(4): 23-35.

Habib MDA, Kabir KMA and Tanimoto J. Do humans play according to the game theory when facing the social dilemma situation: A survey study. *Evergreen*, 2020a; 7(1): 7-14.

Habib MA, Kabir KMA and Tanimoto J. Evolutionary game analysis for sustainable environment under two power generation systems. *Evergreen*, 2022a; 9(2): 323-41.

Habib MA, Tanaka M and Tanimoto J. How does conformity promote the enhancement of cooperation in the network reciprocity in spatial prisoner’s dilemma games. *Chaos Soliton. Fract.* 2020b; 138: 109997.

Habib MA. Can people detect dilemma strength in a 2-player 2-strategy game? A survey game. *Proc. Int. Exch. Innov. Conf. Eng. Sci*. 2019; 5: 116-117.

Habib MA. Game theory, electrical power market and dilemmas. *J. Electr. Eng. Electron. Control. Comput. Sci*. 2022a; 8: 33-42.

Habib MA. Wind speed data and statistical analysis for Muktagacha district in Bangladesh. *J. Electr. Eng. Electron Control. Comput. Sci.* 2022b; 8(30): 1-10.

Hanifi S, Liu X, Lin Z and Lotfian S. A critical review of wind power forecasting methods - past, present and future. *Energies*, 2020; 13 (15): 3764.

He X, Nie Y, Guo H and Wang J. Research on a novel combination system on the basis of deep learning and swarm intelligence optimization algorithm for wind speed forecasting. *IEEE Access*, 2023; 8: 51482-51499.

Hong YY and Rioflorido CLPP. A hybrid deep learning-based neural network for 24-h ahead wind power forecasting. *Appl. Energy*, 2019; 250: 530-539.

Islam F, Ahshan R and Habib MA. *Feasibility analysis of large-scale utility-connected solar power generations in Bangladesh*. In: Proceedings of the 6th International Conference on Electrical Information and Communication Technology (EICT); 2023.

Islam MS, Islam F and Habib MA. Feasibility analysis and simulation of the solar photovoltaic rooftop system using PVsyst software. *Int. J. Educ. Manag. Eng*. 2022a; 12(6): 21-32.

Islam MS, Noman NA and Habib MA. The best techno-economic aspects of the feasibility study concerning the proposed PV-wind-hydro hybrid system in Nilphamari, Bangladesh. *Int. J. Educ. Manag. Eng.* 2022b; 12(5): 24-37.

Jacobson M, Draxl C, Jimenez T, O’Neill B, Capozzola T, Lee JA, Vandenberghe F and Haupt SE. Assessing the wind energy potential in Bangladesh: Enabling wind energy development with data products. Technical Report No. NREL/TP-5000-71077. A Product of the USAID-NREL Partnership, 2018.

Keyhani A, Ghasemi-Varnamkhasti M, Khanali M and Abbaszadeh R. An assessment of wind energy potential as a power generation source in the capital of Iran, Tehran. *Energy*, 2010; 35(1): 188-201.

Lipu MSH, Miah MS, Hannan MA, Hussain A, Sarker MR, Ayob A, Saad MHM and Mahmud MS. Artificial intelligence-based hybrid forecasting approaches for wind power generation: Progress, challenges and prospects. *IEEE Access*, 2021; 9: 102460-102489.

Liu H and Chen C. Data processing strategies in wind energy forecasting models and applications: A comprehensive review. *Appl. Energy*, 2019; 249: 392-408.

Marugan AP, Marquez FPG, Perez JMP and Ruiz-Hernandez D. A survey of artificial neural networks in wind energy systems. *Appl. Energy*, 2018; 228: 1822-1836.

Mazumder GC, Ibrahim MAS, Shams SN and Huque S. Assessment of wind power potential at the coastline in Bangladesh. *Dhaka Univ. J. Sci.* 2019; 67: 27-32.

Noman NA, Islam MS, Habib MA and Debnath SK. The techno-economic feasibility serves to optimize the PV-wind-hydro hybrid power system at Tangail in Bangladesh. *Int. J. Educ. Manag Eng.* 2023; 13(3): 19-32.

Rahaman A, Bhuiyan A, Habib MA and Mozumder ZH. Modeling and threshold sensitivity analysis of computer virus epidemic. *J. Comput. Eng.* 2015; 17(1): 43-7.

Rahman MS, Ferdous J, Aurpa TT, Haque MM, Azad MAK and Habib MA. Statistical trends in wind speed for Khulna, Bangladesh: An analytical approach. *J. Sci. Rep*. 2024; 7(1): 213-225.

Ramirez P and Carta JA. Influence of the data sampling interval in the estimation of the parameters of the Weibull wind speed probability density distribution: a case study. *Energy Convers. Manag.* 2005; 46: 2419-2438.

Rashid MMU, Habib MA and Hasan MM. Design and construction of the solar photovoltaic simulation system with the implementation of MPPT and boost converter using MATLAB/Simulink. *Asian J. Curr. Res.* 2018a; 3: 27-36.

Rashid MMU, Rahman MM, Habib MA and Hasan MM. Study and analysis of hybrid energy options for electricity production in Muktagacha district. *Asian J. Curr. Res.* 2018b; 3(1): 9-14.

Redclift M. Sustainable development and global environmental change: Implications of a changing agenda. *Glob. Environ. Change,* 2002; 2(1): 32-42.

Sinha S and Chandel SS. Review of recent trends in optimization techniques for solar photovoltaic-wind based hybrid energy systems. *Renew. Sustain. Energy Rev*. 2015; 50: 755-769.

Wang J, Wang S and Yang W. A novel non-linear combination system for short-term wind speed forecast. *Renew. Energy*, 2019a; 143: 1172-1192.

Wang Y, Hu Q, Li L, Foley AM and Srinivasan D. Approaches to wind power curve modeling: A review and discussion. *Renew. Sustain. Energy Rev.* 2019b; 116: 109433.

Wang Y, Zou R, Liu F, Shang L and Liu Q. A review of wind speed and wind power forecasting with deep neural networks. *Appl. Energy*. 2021; 304: 117799.

World Weather Online. Country weather information [Internet]. [cited 2025 May 12]. Available from: https://www.worldweatheronline.com/country.aspx

Yan J and Ouyang T. Advanced wind power prediction based on data-driven error correction. *Energy Convers Manag*. 2019; 180: 302-311.

Yuan X, Chen C, Jiang M and Yuan Y. Prediction interval of wind power using parameter optimized beta distribution based LSTM model. *Appl. Soft Comput. J.* 2019; 82: 105583.

Zhang J, Yan J, Infield D, Liu Y and Lien FS. Short-term forecasting and uncertainty analysis of wind turbine power based on long short-term memory network and Gaussian mixture model. *Appl. Energy,* 2019; 241: 229-244.

J. Bangladesh Acad. Sci. 49(1); 137-146 June 2025 DOI:https://doi.org/10.3329/jbas.v49i1.76826

Journal of Bangladesh Academy of Sciences

Journal homepage: http://www.bas.org.bd/publications/jbas.html

Research Article

Individual and combined effects of bicarbonate and calcium on phosphate adsorption to ferric (hydr)oxides

Rashedul Islam, Md Aktaruzzaman Sorid[1], Md Takibul Azad[1], Sumon Ganguli[2], Ashok Kumar Chakraborty[3], Mahbub Kabir[1] and Md Abdus Sabur[1*]

Department of Chemistry, Jashore University of Science and Technology, Jashore, Bangladesh

ARTICLE INFO

Article History

Received: 15 October 2024
Revised: 14 May 2025
Accepted: 15 May 2025

Keywords: Competitive effect, Adsorption, Desorption, Static and dynamic pH, Phosphate and ferric (hydr)oxides.

ABSTRACT

This study investigates how HCO_3^- and Ca^{2+} influence PO_4 adsorption onto ferric (hydr)oxide under static and dynamic pH conditions. Results show that HCO_3^- competes with PO_4 for surface binding sites, decreasing PO_4 adsorption under static pH conditions, while Ca^{2+} enhances PO_4 adsorption under alkaline conditions. At pH 8.0, 0.25 mM HCO_3^- reduces PO_4 adsorption, with a K_d value (the aqueous to solid-phase PO_4 ratio) 1.7 times higher than that observed in 10 mM NaCl. However, adding Ca^{2+} minimizes this effect of HCO_3^-, reducing K_d from 0.66 to 0.55, 0.37, and 0.24 with 0.05, 0.1, and 0.25 mM Ca^{2+}, respectively. Experiments under dynamic pH conditions show a similar trend, with K_d values approximately 84% lower than under static conditions, suggesting PO_4 immobilization on solid surfaces over time. These results indicate that elevated HCO_3^- concentrations may increase PO_4 mobility by reducing adsorption, while Ca^{2+} counteracts this effect under alkaline conditions.

Introduction

Phosphorus (P), in the form of phosphate ($H_nPO_4^{n-3}$, n=0, 1, 2, 3; hereafter PO_4), is an essential and often limiting nutrient for biological production (Smith and Schindler, 2009; Smolders et al., 2006). Phosphorus can be introduced to an aquatic environment from various points and nonpoint sources or can be released from bottom sediment into the overlying water column, a process known as internal P loading (Matisoff et al., 2016; Paytan et al., 2017; Smolders et al., 2006). This release typically occurs via mineral dissolution, desorption, and hydrolysis of organic P compounds (Joshi et al., 2015; Orihel et al., 2017). The solubility of both externally derived and sediment-released PO_4 in the water column is controlled by various biogeochemical factors, such as pH, redox potential, microbial activity, and the chemical composition of sediments and porewater (Filippelli, 2008; Ruttenberg, 2003; Sabur, 2019).

Naturally occurring anions such as bicarbonate (HCO_3^-), sulfate (SO_4^{2-}), and silicate (SiO_4^{4-}) may compete with PO_4 for the mineral binding sites, thereby increasing PO_4 concentrations in the aqueous phase (Antelo et al., 2007; Geelhoed et al., 1997; Sabur, 2019; Sabur et al., 2022; Smolders et al., 2006). Among these competitive anions, the HCO_3^- concentration is generally higher than PO_4 in natural waters (Sabur, 2019) and has been shown to promote PO_4 release from sediments (Smolders et al., 2006). However, in natural waters, particularly in systems buffered by carbonate minerals like calcite and

---

[*] Corresponding author:<sabur@juniv.edu>

[1] *Dept. of Chemistry, Jahangirnagar University, Dhaka, Bangladesh*

[2] *Biomaterials Research Laboratory, Dept. of Applied Chemistry and Chemical Engineering, University of Chittagong, Chittagong, Bangladesh;* [3] *Dept. of Applied Chemistry and Chemical Engineering, Islamic University, Khustia, Bangladesh*

dolomite—cations such as Ca^{2+} and Mg^{2+} are major chemical constituents alongside HCO_3^- (Langmuir, 1997b). Dissolved Ca^{2+} and Mg^{2+} have been shown to decrease the solubility of PO_4 in the aqueous phase through precipitation or co-precipitation as well as co-adsorption with PO_4 on mineral surfaces, particularly under alkaline conditions (Atouei et al., 2016; Rietra et al., 2001; Spiteri et al., 2008; Talebi et al., 2016).

While previous studies have explored the individual effects of bicarbonate and divalent cations (Ca^{2+}/ Mg^{2+}) on the mobility of PO_4 at the sediment-water interface, their combined effects of HCO_3^- and Ca^{2+} in regulating PO_4 mobility has not been comprehensively examined. The simultaneous effects of HCO_3^- and divalent cations such as Ca^{2+} and Mg^{2+} on PO_4 mobility at the sediment-water interface can be evaluated through experiments using natural sediments. While using natural sediments in experiments offers greater environmental realism, their inherently complex chemical and biological compositions can lead to numerous overlapping processes. Therefore, the HCO_3^- induced release of PO_4 from natural sediments, especially in the presence of divalent cations, may not fully capture the mechanisms by which HCO_3^- influences PO_4 mobility. These mechanisms can often be more effectively isolated by conducting experiments with clean minerals, such as ferric (hydr)oxides, rather than with natural sediments.

In this study, we examine the competitive effect of HCO_3^- on PO_4 adsorption onto ferric (hydr)oxide in both the absence and presence of dissolved Ca^{2+} across a range of static pH conditions. We also assess the effectiveness of HCO_3^- as a competing ion through PO_4 adsorption experiments conducted under static and dynamic pH conditions, with and without the presence of Ca^{2+}. Lastly, we compare the experimental results with water quality data from the US National Water Information Monitoring Database (NWIS) to identify aquatic environments that may experience HCO_3^- induced PO_4 mobility. We hypothesize that the cationic Ca^{2+} will counteract the anionic bicarbonate-induced PO_4 mobilization at the sediment-water interface.

Materials and Methods

Ferric (hydr)oxide synthesis

Ferric (hydr)oxide was synthesized by rapidly raising the pH of an acidic Fe^{3+} solution, following the method described by Schwertmann (1991). In brief, an acidic $FeCl_3$ solution was neutralized to pH 6.5 by the rapid addition of 1.0 M NaOH under continuous stirring at 100 rpm using an orbital shaker (Model: SO1). After 6 hours, the pH of the suspension dropped to 6.0 and was subsequently adjusted to pH 7.0 by adding 0.1 M NaOH. The resulting ferric (hydr)oxide precipitate was collected using a suction funnel, air-dried, and then oven-dried at approximately 105 °C. The dried material was ground with a mortar and pestle, sieved, and characterized using X-ray diffraction (XRD) and Fourier-transform infrared (FTIR) spectroscopy. The point of zero charge (PZC) of the synthesized ferric (hydr)oxides was determined to be 8.1 by potentiometric titration (Vakros et al., 2002). This dried and ground ferric (hydr)oxide was used in the PO_4 adsorption experiments.

Adsorption at static pH

First, a 0.25 mM phosphate (PO_4) solution (1.0 L) was prepared in 10 mM NaCl. This solution was divided into seven 100 mL aliquots, and the pH of each aliquot was independently adjusted within the range of 6.0 to 10.0 using dilute and concentrated HCl and NaOH. Next, 25 mL of each pH-adjusted PO_4 solution was added to a 50 mL polypropylene tube containing 0.0125 g of ferric (hydr)oxide (accurately weighed to four decimal places). The mixtures were shaken at 100 rpm on an orbital shaker (Model: SO1) for 2 hours to reach equilibrium, with pH adjustments made as needed during this period. Following equilibration, the suspensions were passed through a 0.45 µm syringe filter, and the phosphate concentrations in the filtrates were determined.

Additional pH-dependent PO_4 adsorption experiments were conducted using two other background solutions apart from 10 mM NaCl: (i) three $NaHCO_3$ solutions with concentrations of 0.25, 0.50, and 1.00 mM, and (ii) three $NaHCO_3$ (0.25 mM) solutions with varying Ca^{2+} concentrations of 0.05, 0.1, and 0.25 mM. The degree of PO_4 adsorption is expressed in the distribution constant (K_d), which represents the ratio of PO_4 in the aqueous phase to that in the solid phase. Lower K_d values indicate more effective removal of PO_4 from the aqueous phase, reflecting higher adsorption.

Adsorption at dynamic pH

Three sets of phosphate (PO_4) adsorption experiments were conducted under dynamic pH conditions. Set 1: Ferric (hydr)oxide (0.125 g) was equilibrated with 250 mL of a 0.25 mM PO_4 solution, prepared in 10 mM NaCl, for 4 hours. The pH of the suspension was initially adjusted to 5.0 using dilute and concentrated HCl and NaOH, creating a mildly acidic environment favorable for PO_4 adsorption. The pH was then adjusted to 6.0 and equilibrated for 4 hours, with periodic adjustments every 30 minutes to counter any drift. Following this, the pH was incrementally increased from 6.0 to 10.0 in one-unit intervals by adding NaOH. After 4 hours of equilibration at each pH level, samples were collected, filtered (0.45 µm pore size filter), and analyzed for aqueous PO_4 concentration. Set 2: To examine the effect of HCO_3^- on PO_4 adsorption, a 0.2275 mM PO_4 solution prepared in 10 mM NaCl and 225 mL was introduced into a reactor containing 0.125 g of ferric (hydr)oxide. Subsequently, 25 mL of a 2.5 mM $NaHCO_3$ solution was added, resulting in both PO_4 and HCO_3^- concentrations reaching 0.25 mM in the suspension, assuming no adsorption occurred. The pH was adjusted, and the suspension was equilibrated. Samples were then collected, filtered, and analyzed for PO_4 concentration following the same procedures as in Set 1. Set 3: The competitive effect of HCO_3^- on PO_4 adsorption was further evaluated in the presence of Ca^{2+}. Ferric (hydr)oxide (0.125 g) was equilibrated with 225 mL of a solution (225 mL) containing 0.2275 mM PO_4 and 0.28 mM Ca^{2+}, prepared in 10 mM NaCl. Then, 25 mL of a 2.5 mM $NaHCO_3$ solution was introduced to the system and equilibrated for 4 hours at pH 6. The procedures for adding HCO_3^-, adjusting the pH, and collecting and analyzing samples followed the same protocol described in Set 1.

Aqueous phosphate analysis

Phosphate concentrations in all experiments were determined spectrophotometrically by the molybdenum-blue method with maximum absorbance at 890 nm (Barman et al., 2024; Murphy and Riley, 1962; Nagul et al., 2015). For each set of experiments, the PO_4 concentrations were quantified by referencing them to a calibration curve constructed using a mixed matrix solution.

Results

Ferric (hydr)oxides characterization

The XRD pattern of the synthesized ferric (hydr)oxide (Fig. 1a) does not display distinctive features of mineral phases, suggesting that the product is primarily amorphous or poorly crystalline. However, a weak peak around ~35° 2θ may indicate the presence of ferrihydrite (Parmar and Parmar, 2020; Rani and Tiwari, 2017; Zhou et al., 2018). Fig. 1b and 1c show the FTIR spectroscopic data for the synthesized ferric (hydr)oxide, which exhibits several notable spectral bands. The peaks at 1489, 1339, and 446 cm^{-1} are characteristic spectral features of ferrihydrite (Liang et al., 2020). The 1628, 1070, 893, and 797 cm^{-1} peaks are associated with goethite (Liang et al., 2020; Liu et al., 2023). Additionally, FTIR features at 1628 and 1070 cm^{-1} may indicate hematite's presence, as supported by previous studies (Liu et al., 2023). Taken together with the XRD data, the FTIR spectra suggest that the synthesized ferric (hydr)oxide is predominantly amorphous. However, it may contain minor proportions of crystalline phases such as goethite and hematite.

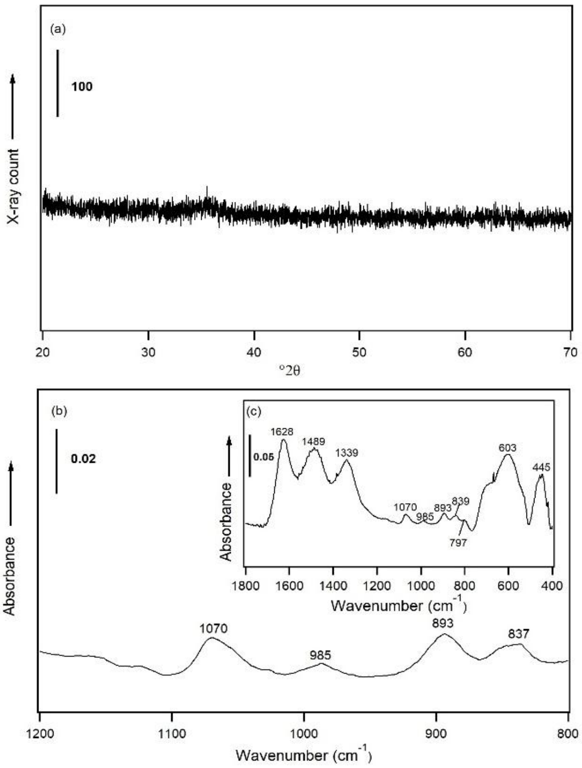

Fig. 1. XRD patterns (a) and FTIR spectra (b, c) of the dried ferric (hydr)oxide.

Adsorption at static pH

The adsorption of PO_4 onto ferric (hydr)oxides is influenced by the aqueous speciation of PO_4 and the protonation state of the solid surface (Gao and Mucci, 2001; Sabur et al., 2022; Spiteri et al., 2008). Generally, acidic pH conditions enhance PO_4 adsorption onto ferric (hydr)oxides compared to alkaline conditions (Li et al., 2016; Sabur et al., 2022). This is due to the increased hydroxyl ions (OH^-) concentration under alkaline conditions can create an unfavorable environment for PO_4 adsorption by acting as a competitive ions and increasing the surface's negative charge through OH^- adsorption (Li et al., 2016). Additionally, the chemical composition of the adsorption medium can affect PO_4 adsorption by altering its aqueous speciation and modifying the surface's electronic environment (Geelhoed et al., 1997; Sabur et al., 2022; Talebi et al., 2016). PO_4 can exist in several forms with different protonation states in aqueous solutions, such as H_3PO_4, $H_2PO_4^-$, HPO_4^{2-}, and PO_4^{3-}, depending on solution pH and chemical constituents (Li et al., 2016; Sabur et al., 2022). Consequently, speciation diagrams of PO_4 in different background solutions were generated (Fig. 2) using PHREEQC with the phreeqc.dat database (Parkhurst and Appelo, 2013).

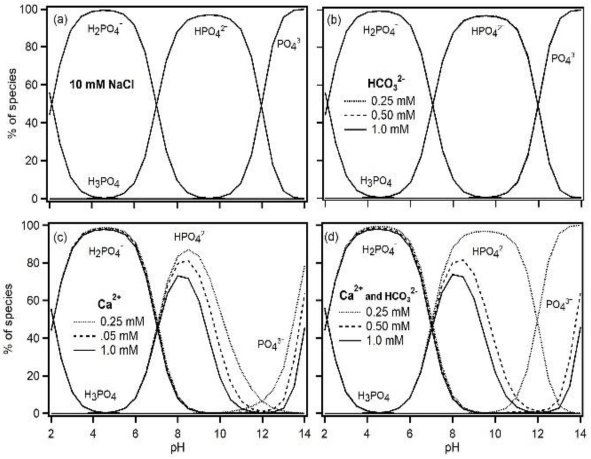

Fig. 2. Speciation of PO_4 (0.25 mM) in (a) NaCl (10 mM), (b) $NaHCO_3$ (0.25 to 1.0 mM) (c) $CaCl_2$ (0.25 to 1 mM), and (d) $CaCl_2$ and $NaHCO_3$ (0.25 to 1.0 mM Ca^{2+} and HCO_3^- ions) across a range of pH values at a temperature of 25 °C.

The phosphate adsorption experiments, both with and without HCO_3^-, reveal that HCO_3^- competes with PO_4 for surface binding sites on ferric (hydr)oxide, resulting in decreased PO_4 adsorption. This competitive effect becomes more pronounced with increasing HCO_3^- concentration, as expected (Fig. 3a). While the competitive effect HCO_3^- on PO_4 adsorption is minimal at or below pH 7.0, HCO_3^- significantly decreases PO_4 adsorption (i.e., K_d increases) as the pH increases from slightly alkaline to strongly alkaline conditions (Fig. 3a). For instance, at pH 8.0, the K_d values for PO_4 adsorption in the presence of three different HCO_3^- concentrations 1.7, 2.1, and 2.3 times higher than those in a 10 mM NaCl solution (0.39). At pH 10.0, these values increase to 3.4, 6.2, and 8.4 times compared to the value in NaCl solution (0.84).

Because with increasing pH, HCO_3^- gradually deprotonates and starts forming fully deprotonated CO_3^{2-} above pH 8.0 (Langmuir, 1997b) and effectively competes with PO_4 for the mineral binding sites (Gustafsson and Antelo, 2022; Mendez and Hiemstra, 2019; Rahnemaie et al., 2007).

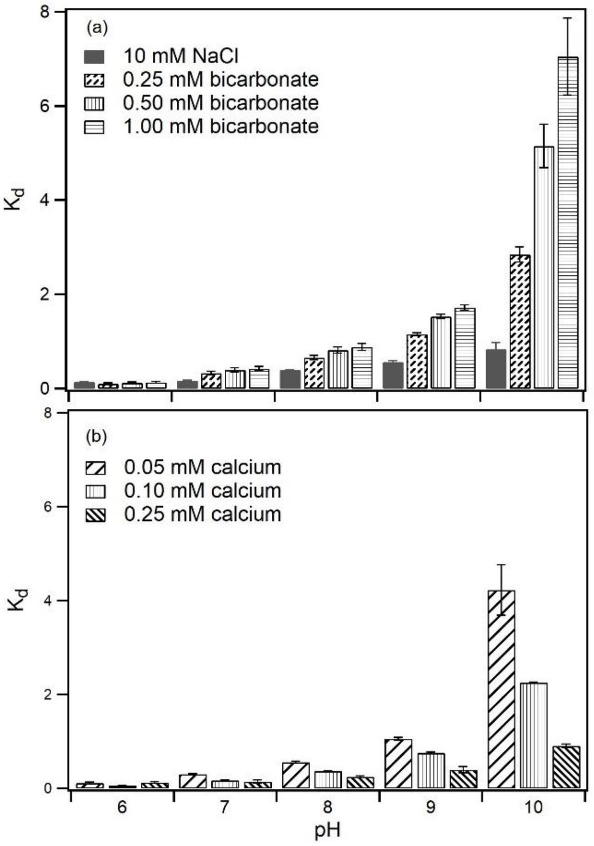

Fig. 3. PO_4 (0.25 mM) distribution constant (K_d) at the ferric (hydr)oxide-water interface in the presence of 0.25 to 1.0 mM HCO_3^- (a), and HCO_3^- (0.25 mM) plus Ca^{2+} concentrations (b) as a function of static pH at room temperature.

Divalent cations such as Ca^{2+} and Mg^{2+} are known to enhance PO_4 binding to ferric (hydr)oxides, particularly under alkaline pH conditions (Antelo et al., 2015; Atouei et al., 2016; Gustafsson and Antelo, 2022; Millero et al., 2001; Rietra et al., 2001). Generally, the adsorption of Ca^{2+} and Mg^{2+} ions to ferric (hydr)oxides increases with rising solution pH due to enhanced electrostatic attraction between the positively charged cations and the negatively charged surface (Spiteri et al., 2008; Talebi et al., 2016). In this study, PO_4 adsorption in HCO_3^- solution increases (i.e., the K_d value decreases) as both the concentration of Ca^{2+} and the pH rise (Fig. 3). The effect of Ca^{2+} on PO_4 adsorption becomes more pronounced with increasing Ca^{2+} concentrations. For example, at pH 8.0, the K_d value for PO_4 adsorption in the presence of 0.25 mM HCO_3^- is 0.66, which decreases to 0.55, 0.37, and 0.24 with the addition of 0.05, 0.1, and 0.25 mM Ca^{2+}, respectively. At pH 10.0, the K_d values for PO_4 adsorption in the presence of 0.25 mM HCO_3^- are 4.23, 2.26, and 0.90 with 0.05, 0.1, and 0.25 mM Ca^{2+}, respectively, compared to 2.85 in the presence of 0.25 mM HCO_3^- alone.

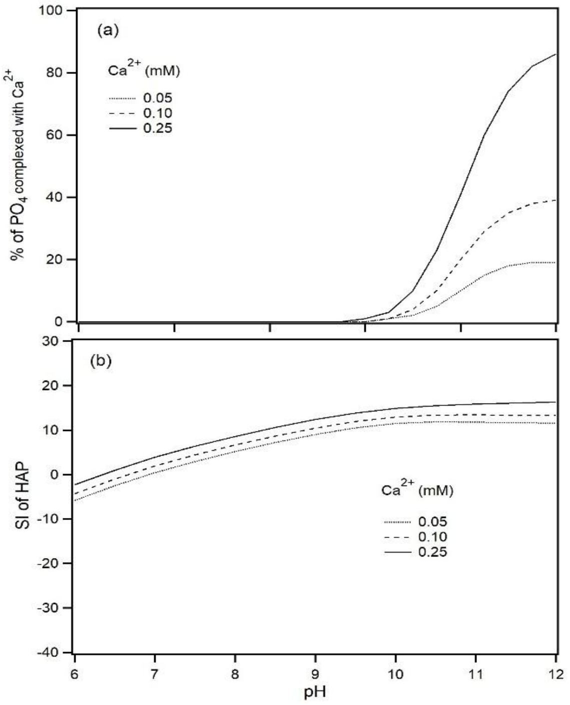

Fig. 4. (a) Percentage of total PO_4 (0.25 mM) complexed with calcium in the presence of 0.05, 0.1, and 0.25 mM Ca^{2+}. (b) Saturation indexes (SI) of hydroxyapatite under the given experimental conditions. The PO_4 speciation and SI values are computed using the PHREEQC Interactive 3.3.7 computer program and *phreeqc.dat* database (Parkhurst and Appelo, 2013), incorporating the dissociation constants of calcium phosphate

mineral phases (Dorozhkin, 2017; Shafii et al., 2024).

The higher K_d observed at pH 10.0 in the presence of both 0.25 mM HCO_3^- and 0.05 mM Ca^{2+}, compared to 0.25 mM HCO_3^- alone (Fig. 3), may be attributed to stronger aqueous complexation of PO_4 with Ca^{2+} (Fig. 4a), which reduces the affinity of PO_4 for the solid ferric (hydro)oxides, or to the precipitation or co-precipitation of PO_4 with Ca^{2+} on the solid surface.

The enhanced PO_4 adsorption with increasing (from 0.05 to 0.1 and 0.25 mM) Ca^{2+} concentrations can be attributed to the formation of calcium-phosphate (Ca-PO_4) phases (Islam et al., 2023), which is followed by the development of ternary surface complexes involving Ca^{2+} adsorbed onto the positively charged surface. Additionally, the removal of PO_4 from the solution via the formation of insoluble Ca-PO_4 complexes at higher Ca^{2+} concentrations is also thermodynamically feasible, as revealed from the calculated saturation index values (Fig. 4b), which increase with rising pH and Ca^{2+} concentrations (Ca/P ratios) (Antelo et al., 2015; Ler and Stanforth, 2003; Spiteri et al., 2008).

Adsorption at dynamic pH

The adsorption experiments were carried out using freshly synthesized ferric (hydr)oxide under controlled, constant pH conditions. In contrast, ferric (hydr)oxides in natural soils and sediments typically possess pre-adsorbed phosphate (PO_4) on their surfaces, and the pH in such environments tends to vary gradually over time. Therefore, we conducted PO_4 adsorption experiments under dynamic pH conditions, progressively adjusting the pH from 6.0 to 10.0. These dynamic pH envelope experiments were conducted in three different types of solution: (i) 10 mM NaCl, (ii) 0.25 mM HCO_3^-, and (iii) an equimolar concentration of HCO_3^- and Ca^{2+} ions (0.25 mM each). The results reveal that the K_d values for PO_4 adsorption under dynamic pH conditions decrease up to pH 8.0, followed by an increase (Fig. 5a), suggesting the release of adsorbed PO_4 occurs after pH 8.0 in the absence of HCO_3^-. Notably, in the presence of HCO_3^-, the K_d value increases with increasing pH, highlighting the competitive interaction of HCO_3^- with PO_4 for surface binding sites, also revealed in the static pH adsorption envelope experiments.

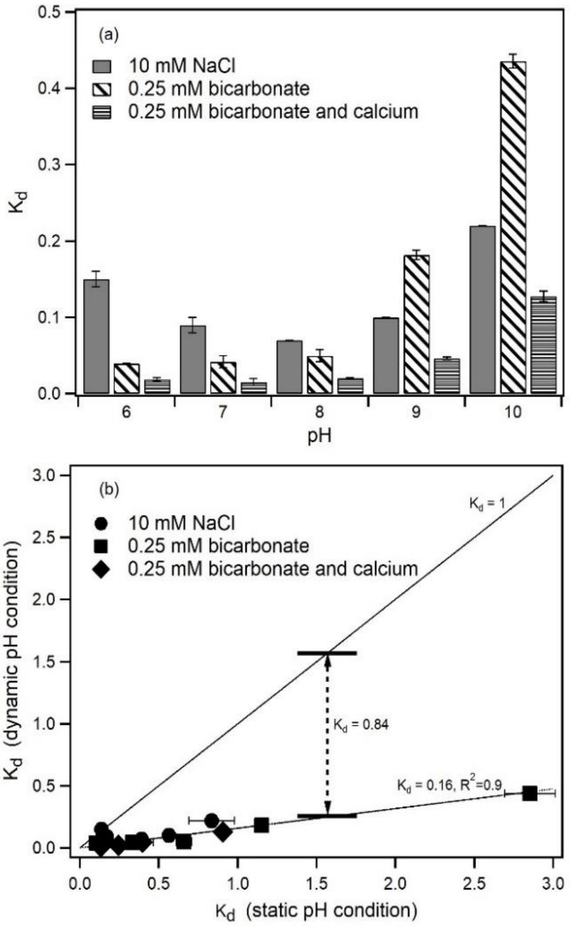

Fig. 5. PO_4 (0.25 mM) distribution constant (K_d) at the ferric (hydr)oxides-water interface under a dynamic pH condition (a). The comparison of K_d values under dynamic and static pH conditions (b).

When both HCO_3^- and Ca^{2+} are present, the K_d values remain relatively stable between pH 6.0 and 8.0 but increase above pH 8.0. Under alkaline conditions, the K_d values are generally higher in the HCO_3^- system than the NaCl system, with the lowest K_d values observed for the combined HCO_3^- and Ca^{2+} system (Fig. 5a), as expected. For example, at pH 9.0

and 10.0, the K_d values in the presence of 0.25 mM HCO_3^- increased to 0.18 and 0.44, respectively, compared to 0.10 and 0.22 in a 10 mM NaCl solution. In contrast, the K_d values for the equimolar concentrations of (0.25 mM) Ca^{2+} and HCO_3^- were 0.05 and 0.13 at pH 9.0 and 10.0, respectively.

The K_d values obtained under static and dynamic pH conditions are compared in Fig. 5b. The results indicate a significant difference between the two sets of K_d values. More specifically, the K_d values obtained from the PO_4 adsorption experiments conducted under dynamic pH conditions are considerably lower than those obtained under static pH conditions. For instance, the K_d (static) to K_d (dynamic) ratio is approximately 0.16, which is substantially less than the expected 1:1 ratio. This result suggests that PO_4 immobilization primarily occurs at the surface, with approximately 84% of the adsorbed-PO_4 remaining immobilized and not being released into the aqueous phase under dynamic pH conditions, in contrast to the observations made in the static pH condition experiments. This result implies that immobilization of PO_4 predominantly occurred on the surface (Ler and Stanforth, 2003; Sabur et al., 2022), possibly facilitated by the formation of stronger binding interactions with surface functional groups. This binding mechanism could hinder the release of adsorbed PO_4 into the aqueous phase. For example, adsorbed-PO_4 may gradually form stronger complexes with ferric iron present on the solid surface (Ler and Stanforth, 2003) or may form stable surface complexes (e.g., bi-dentate) via the transformation of weaker (e.g., outer-sphere and/or mono-dentate) complexes during the pH transition from acidic to alkaline conditions (Sabur et al., 2022; Zhong et al., 2007).

Discussion and significance

Bicarbonate tends to form surface complexes with ferric (hydr)oxide that are less stable than those formed with PO_4, as demonstrated in previous research (Rahnemaie et al., 2007). However, the HCO_3^- concentrations in natural waters are typically higher than PO_4 (Sabur, 2019). Generally, HCO_3 in natural waters is regulated by several factors, including the diffusion of CO_2 from the atmosphere, the dissolution of carbonate minerals (e.g., calcite, aragonite, and dolomite), as well as fluvial input (Langmuir, 1997b). Additionally, the relative rates of photosynthesis and respiration often play a role in controlling HCO_3^- concentrations in surface waters (Langmuir, 1997b; Verspagen et al., 2014). For instance, dissolved CO_2 and HCO_3^- are consumed by primary producers during photosynthesis, with HCO_3^- being generated as a byproduct of organic matter mineralization (Verspagen et al., 2014).

Calcium ions enter aquatic environments through fluvial transport, groundwater flow, and the dissolution of carbonate minerals like calcite and dolomite (Cerar and Urbanc, 2013; Langmuir, 1997a). The dissolution of typical carbonate minerals results in an aqueous phase molar ratio of Ca^{2+} to HCO_3^-/CO_3^{2-} at ~1:1 (Cerar and Urbanc, 2013). However, data from the US National Water Information System (NWIS) indicate that the concentration of HCO_3^- in natural waters is approximately ten times higher than that of Ca^{2+} (Fig. 6). The surface water HCO_3^- and Ca^{2+} concentrations (ponds, impoundments, and lakes) indicate the contribution of other sources (e.g., organic matter mineralization) involved for in-situ generation of HCO_3^- (Langmuir, 1997b). The NWIS data were extracted from the US NWIS database using the USGS parameter codes 00453 and 0915, respectively. The concentrations of HCO_3^- and Ca^{2+} were extracted (between 2010 and 2016) for common sampling stations and dates of sampling from all water depths available in the database.

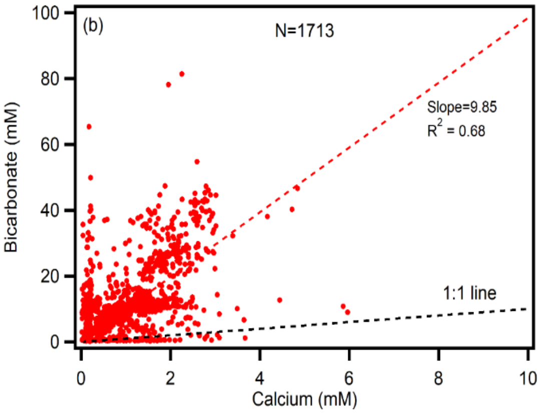

Fig. 6. Concentrations of HCO_3^- with respect to Ca^{2+} in surface waters (ponds, impoundments, and lakes) according to the US NWIS database (2010 - 2016).

Elevated PO_4 concentrations in natural waters often correlate with HCO_3^- (Smolders et al., 2006), indicating that HCO_3^- may slightly enhance PO_4 mobility by reducing its adsorption. However, the release of phosphate (PO_4^{3-}) from mineral surfaces induced by bicarbonate (HCO_3^-) is unlikely, particularly in the presence of naturally occurring cations such as calcium (Ca^{2+}). Nevertheless, in aquatic environments where HCO_3^- primarily arises from the mineralization of organic carbon rather than the dissolution of carbonate minerals, HCO_3^- may contribute to enhanced PO_4 mobility.

Conclusions

In this study, we examine the individual and combined effects of HCO_3^- and Ca^{2+} ions on the mobility of phosphate (PO_4) at the ferric (hydr)oxide–water interface under both static and dynamic pH conditions. Our adsorption pH envelope experiments demonstrate that HCO_3^- can compete with PO_4 for binding sites on mineral surfaces. However, in the presence of Ca^{2+}, this competitive effect is diminished, particularly under alkaline pH conditions.

Results from adsorption experiments under dynamic pH conditions further show that the ability of HCO_3^- to act as a desorbing agent for PO_4 is relatively weak, especially when Ca^{2+} is also present. In natural waters, where HCO_3^- concentrations are significantly higher than those of PO_4^{3-}, HCO_3^- may enhance the mobility of PO_4 by reducing its adsorption to mineral surfaces. Nonetheless, in aquatic systems buffered by carbonate mineral dissolution, the coexistence of Ca^{2+} can mitigate the competitive influence of HCO_3^-, thereby limiting the mobility of dissolved phosphate.

Acknowledgment

The authors are thankful to the University Grants Commission of Bangladesh for financial support.

Disclosure statement

The authors do not have any conflict of interest regarding the publication of this manuscript.

References

Antelo J, Arce F and Fiol S. Arsenate and phosphate adsorption on ferrihydrite nanoparticles. *Chem. Geol.* 2015; 410: 53-62.

Antelo J, Arce F, Avena M, Fiol S, López R and Macías F. Adsorption of a soil humic acid at the surface of goethite and its competitive interaction with phosphate. *Geoderma*, 2007; 138(1-2): 12-19.

Atouei MT, Rahnemaie R, Kalanpa EG and Davoodi MH. Competitive adsorption of magnesium and calcium with phosphate at the goethite water interface: Kinetics, equilibrium and CD-MUSIC modeling. *Chem. Geol.* 2016; 437(25): 19-29.

Barman DK, Islam R, Dash GK, Ganguli S, Chakraborty AK, Kabir M and Sabur MA. Interfering effect of silicate in the quantification of phosphate by the molybdenum-blue method. *Asian J. Water Environ. Pollut.* 2024: 21(6): 195-20.

Cerar S and Urbanc J. Carbonate chemistry and isotope characteristics of groundwater of Ljubljansko Polje and Ljubljansko Barje aquifers in Slovenia. *Sci. World J.* 2013.

Dorozhkin SV. Calcium orthophosphates (CaPO4): occurrence and properties. *Prog. Biomater.* 2017; 5(1): 9-70.

Filippelli GM. The global phosphorus cycle: past, present, and future. *Elements*, 2008; 4(2): 89-95.

Gao Y and Mucci A. Acid base reactions, phosphate and arsenate complexation, and their competitive adsorption at the surface of goethite in 0.7 M NaCl solution. *Geoch. Cosmochim. Acta*, 2001; 65(14): 2361-2378.

Geelhoed JS, Hiemstra T and Van Riemsdijk WH. Phosphate and sulfate adsorption on goethite: single anion and competitive adsorption. *Geoch. Cosmochim. Acta*, 1997; 61(12): 2389-2396.

Gustafsson JP and Antelo J. Competitive arsenate and phosphate adsorption on ferrihydrite as described by the CD-MUSIC model. *ACS Earth*

Space Chem. 2022; 6(5): 1397-1406.

Islam R, Barman DK, Kabir M and Sabur MA. Salinity-induced phosphate binding to soil particles: Effects of divalent cations. *Water Air Soil Pollut.* 2023; 234(11): 697.

Joshi SR, Kukkadapu RK, Burdige DJ, Bowden ME, Sparks DL and Jaisi DP. Organic matter remineralization predominates phosphorus cycling in the mid-bay sediments in the Chesapeake Bay. *Environ. Sci. Technol.* 2015; 49(10): 5887-5896.

Langmuir D. *Aqueous Environmental Geochemistry.* McConnin R., ed., 1st ed., Prentice-Hall. Inc. 1997a. p. 618.

Langmuir D. Carbonate chemistry. In: *Aqueous Environmental Geochemistry.* McConnin R., ed., Prentice-Hall. Inc. 1997b; pp. 193-230.

Ler A and Stanforth R. Evidence for surface precipitation of phosphate on goethite. *Environ. Sci. Technol.* 2003; 37(12): 2694-2700.

Li M, Liu J, Xu Y and Qian G. Phosphate adsorption on metal oxides and metal hydroxides: A comparative review. *Environ. Rev.* 2016; 24(3): 319-332.

Liang C, Tang B, Zhang X and Fu F. Mobility and transformation of Cr (VI) on the surface of goethite in the presence of oxalic acid and Mn (II). *Environ. Sci. Pollut. Res.* 2020; 27: 26115-26124.

Liu R, Kong S, Shao Y, Cai D, Bai B, Wei X and Chorover J. Mechanisms and health implications of toxicity increment from arsenate-containing iron minerals through in vitro gastrointestinal digestion. *Geoderma*, 2023; 432: 116377.

Matisoff G, Kaltenberg EM, Steely RL, Hummel SK, Seo J, Gibbons KJ, Bridgeman TB, Seo Y, Behbahani M, James WF, Johnson LT, Doan P, Dittrich M, Anne M and Chaf JD. Internal loading of phosphorus in western Lake Erie. *J. Great Lakes Res.* 2016; 42(4): 775-788.

Mendez JC and Hiemstra T. Carbonate adsorption to ferrihydrite: Competitive interaction with phosphate for use in soil systems. *ACS Earth Space Chem.* 2019: 3(1): 129-141.

Millero F, Huang F, Zhu X, Liu X and Zhang JZ. Adsorption and desorption of phosphate on calcite and aragonite in seawater. *Aquat. Geochem.* 2001: 7(1): 33-56.

Murphy J and Riley JP. A modified single solution method for the determination of phosphate in natural waters. *Anal. Chim. Acta*, 1962; 27: 31-36.

Nagul EA, McKelvie ID, Worsfold P and Kolev SD. The molybdenum blue reaction for the determination of orthophosphate revisited: opening the black box. *Anal. Chim. Acta*, 2015; 890: 60-82.

Orihel DM, Baulch HM, Casson NJ, North RL, Parsons CT, Seckar DCM and Venkiteswaran JJ. Internal phosphorus loading in Canadian fresh waters: a critical review and data analysis. *Can. J. Fish. Aquat. Sci.* 2017; 74(12): 2005-2029.

Parkhurst DL and Appelo CAJ. Description of input and examples for PHREEQC version 3:A computer program for speciation, batch-reaction, one-dimensional transport, and inverse geochemical calculations. In: *Techniques and Methods.* U.S. Geological Survey, USA, 2013.

Parmar C and Parmar GS. Structural and magnetic properties of six-line ferrihydrite nanoparticles. *J. Supercond. Nov. Magn.* 2020; 33: 441-444.

Paytan A, Roberts K, Watson S, Peek S, Chuang P, Defforey D and Kendall C. Internal loading of phosphate in Lake Erie Central Basin. *Sci. Total Environ.* 2017; 579: 1356-1365.

Rahnemaie R, Hiemstra T and van Riemsdijk WH. Carbonate adsorption on goethite in competition with phosphate. *J. Colloid Interface Sci.* 2007; 315(2): 415-425.

Rani C and Tiwari SD. Phase transitions in two-line ferrihydrite nanoparticles. *Appl. Phys. A*, 2017; 123; 1-4.

Rietra RPJJ, Hiemstra T and Van Riemsdijk WH. Interaction between calcium and phosphate adsorption on goethite. *Environ. Sci. Technol.* 2001; 35(16): 3369-3374.

Ruttenberg KC. The global phosphorus cycle. In: *Treatise on Geochemistry,* Turekian KK, Holland HD, eds., 1st ed., 2003; pp. 585-643.

Sabur MA. *Interactions of Phosphate and Silicate with Iron oxides in Freshwater Environments*. Ph.D. Theis, University of Waterloo, Ontario, Canada, 2019.

Sabur MA, Parsons CT, Maavara T and Van Cappellen P. Effects of pH and dissolved silicate on phosphate mineral-water partitioning with goethite. *ACS Earth Space Chem*. 2022; 6(1): 34-43.

Schwertmann U. Solubility and dissolution of iron oxides. *Plant Soil*, 1991; 130(1-2): 1-25.

Shafii M, Slowinski S, Sabur MA, Arvisais A, Bhusal Y, Withers W, Krogstad JK, Parsons CT and Van Cappellen P. Mineral formation explains the high retention efficiency of dissolved reactive phosphorus in a residential stormwater pond. *Env. Sci.: Adv.* 2024; 3(6): 819-832.

Smith VH and Schindler DW. Eutrophication science: where do we go from here? *Trends Ecol. Evol.* 2009; 24(4): 201-207.

Smolders AJP, Lamers LPM, Lucassen ECHET, van Der Velde G and Roelofs JGM. Internal eutrophication: how it works and what to do about it – a review. *Chem. Ecol.* 2006; 22(2): 93-111.

Spiteri C, Cappellen P Van and Regnier P. Surface complexation effects on phosphate adsorption to ferric iron oxyhydroxides along pH and salinity gradients in estuaries and coastal aquifers. Geochim. Cosmochin. Acta, 2008; 72(14): 3431-3445.

Talebi M, Rahnemaie R, Goli E and Hossein M. Competitive adsorption of magnesium and calcium with phosphate at the goethite water interface: kinetics, equilibrium and CD-MUSIC modeling. *Chem. Geol.* 2016; 437: 19-29.

Vakros J, Kordulis C and Lycourghiotis A. Potentiometric mass titrations: a quick scan for determining the point of zero charge. *Chem. Commun.* 2002; 17: 1980-1981.

Verspagen JMH, Van de Waal DB, Finke JF, Visser PM, Van Donk E and Huisman J. Rising CO2 levels will intensify phytoplankton blooms in eutrophic and hypertrophiclakes. *PloS One*, 2014; 9(8): e104325.

Zhong B, Stanforth R, Wu S and Chen JP. Proton interaction in phosphate adsorption onto goethite. *J. Colloid Interface Sci.* 2007; 308(1): 40-48.

Zhou S, Sato T and Otake, T. Dissolved silica effects on adsorption and co-precipitation of Sb (III) and Sb (V) with ferrihydrite. *Minerals*, 2018; 8(3): 101.

J. Bangladesh Acad. Sci. 49(1); 147-152: June 2025 DOI:https://doi.org/10.3329/jbas.v49i1.76908

Journal of Bangladesh Academy of Sciences

Journal homepage: http://www.bas.org.bd/publications/jbas.html

Short Communication

Influence of supplement liquid manure on snake gourd growth and yield (*Trichosanthes anguina* L.)

AFM Jamal Uddin*, Tamalika Roy[1], Purnima Saha[1], Tamima Dastagir and Fatema Tuz Juhora Chaitee

Department of Horticulture, Sher-e-Bangla Agricultural University, Dhaka, Bangladesh

ARTICLE INFO

Article History

Received: 16 October 2024
Revised: 15 April 2025
Accepted: 16 April 2025

Keywords: Probiotic liquid manure, Snake gourd, Soil health, Microorganism.

ABSTRACT

An experiment was accomplished at the Horticulture Farm, Sher-e-Bangla Agricultural University, Dhaka, from March to June 2024 to study the influence of supplement liquid manure on the growth and yield of snake gourd. Supplement liquid manure applications viz., frequency, T_0: control (BARI recommended fertilizers doses), **T_1**: 100% RFD + Liquid manure (once), and **T_2**: 100% RFD + Liquid manure (twice) were used in this experiment arranged in a Randomized Complete Block Design with three replications. Data on growth, yield, and quality attributes parameters were taken in which all the treatments showed significant variations. The maximum leaves number (10.0), leaf area (147.0 sq.cm), the highest SPAD value (50.1), and maximum female flowers per plant (58.0) were found in twice application (T_2) of liquid manure. Furthermore, the maximum number of fruits per plant (53.0), maximum single fruit weight (0.61g), and maximum snake gourd yield (29.8 t/ha) were found in T_2, whereas the minimum was found from control (T_0) in case of all parameters. Therefore, it can be concluded that the liquid manure supplement applied as **T_2** is an easy and effective liquid manure that can potentially increase the growth and yield of snake gourd.

Introduction

Snake gourd (*Trichosanthes anguina* L.) is a popular vegetable in Bangladesh, and it is valued for its high nutritional content, including vitamins, minerals, and dietary fiber. Organic matter is a vital soil component for improving soil physical properties, and returning organic matter to the soil can increase the soil's active organic carbon content and improve soil vitality (Li et al., 2017). Nowadays, liquid organic manure is used in crop production to increase yield because it is easy to prepare, good for most vegetables, and applied as a top dressing while the crop grows. Unlike conventional organic manure, liquid organic manure contains essential amounts of organic matter and soluble nutrients that help maintain soil health and stability (Somashekar et al., 2018). The specific composition of liquid fertilizers, micronutrients, and beneficial microbes can influence plant resistance to diseases and pests, thus contributing to better yields (Uddin et al., 2023). It is made from domestic cow urine, cow dung, horse gram (Besan), and molasses and is a time-honored agricultural tradition of using cow-based products (Gong et al., 2022). This organic supplement boosts soil fertility, enhances microbial activity, and improves the overall health of plants without the adverse environmental impacts associated with

---

*Corresponding author:<jama14@yahoo.com>

[1] *College of Agricultural Sciences, International University of Business Agriculture and Technology, Dhaka, Bangladesh*

synthetic fertilizers. The present study explored the benefits of liquid manure application frequency in the growth and yield of snake gourd.

Materials and Methods

The field experiment was conducted from March to June 2024 at Sher-e-Bangla Agricultural University, Dhaka. The trial plot was carefully prepared by plowing and cross-plowing with a shovel to ensure good tilth. The area was leveled, and after that, drainage and irrigation channels were built all around the plot. As basal doses, synthetic fertilizers were applied as BARI recommendations (Krishi Projikti Hatboi, 2020). The research was done using a Single-factor experiment. The experiment was conducted in a Randomized Complete Block Design (RCBD) with 3 treatments. The treatments were T_0: control (BARI recommended fertilizers doses), T_1: 100% RFD + Liquid manure (once), and T_2: 100% RFD + liquid manure (twice). A hybrid snake gourd, "Asha," was used in this study, and seedlings of 30 days of age were planted. The plot size was 6 m x 6 m, and the spacing was maintained at 1.5 m x 1.5 m.

Preparation of liquid Manure (PLM)

To prepare the PLM, 10 parts of cow dung mixed with 10 parts of urine, 1 part molasses,1 part of besan flour, and 1 part of virgin soil were mixed in a 100 L drum. This mixture blended well with 100 liters of water (Fresh Cow dung: Urine: Jiggery: Chickpea/ Gram Besan: Soil: Water=10:10:1: 1:1:100). The solution was stirred with a stick, and the drum was covered with a lid (Uddin et al., 2023). It was stirred occasionally with a stick by opening the lid once a day to prepare the PLM well. One part of PLM was mixed with 5 parts water when it was used as the treatment.; 1:5; PLM: Water, V/V).

Data on different morphological characteristics were recorded in visual observation and represented into appropriate categories. Data were also collected based on vegetative growth and yield attributing parameters. Three plants were randomly selected from each plot unit for data collection. Data on vine length (cm), leaves numbers/plant, leaf area (sq.cm), SPAD value, Days to 80% flowering, female flowers/plant, fruits /plant, fruit length (cm), fruit width (cm), average fruit weight (g), and yield (t/ha) were recorded during the study period. The leaf area was calculated using a portable laser leaf area meter. Using a SPAD meter (Plate 2b), the leaf SPAD value was determined.

The statistical analyses were conducted using the STATISTIX 10 statistical program. The analysis of variance (ANOVA) was conducted to assess the differences between treatments. The Least Significance Difference (LSD) test was employed at a significance level of 5%.

Result and Discussion

The research work on "Influence of supplement liquid manure on growth and yield of snake gourd was undertaken in the Horticulture Farm, Sher-e-Bangla Agricultural University, Dhaka. The experimental results on growth, yield, and quality parameters obtained throughout the study period are presented as follows:

Vine length (cm)

Plant vine length of snake gourd showed statistically significant variation with the application of liquid manure (Fig. 1). Vine length increased consistently with the advancement of crop growth with the application of liquid manure.

The maximum vine length (185.6 cm) at 1st flowering stage with T_2 treatment was the lowest (152.6 cm) with control (T_0). At the harvesting stage, the T_1 treatment showed maximum vine length (463.33 cm), and the lowest vine length (423.3 cm) was found with T_0. It was statistically similar to T_1 (463.3 cm) (Fig. 1.). Liquid manure is often derived from animal waste or plant residues that can significantly increase the vine length of snake gourd (or any vining plants) due to its rich nutrient content. Uddin et al. (2024) mentioned that liquid manure provides essential nutrients such as nitrogen, phosphorus, and potassium, which are critical for plant growth.

Leaves number /1 m vine length

Leaves numbers showed a significant variation among the treatments. The maximum leaves number was observed in T_2 (10.0), and the minimum leaves number was observed in T_0 (7.7) in 1m vine length at 46 days after transplanting (Table 1). A result of increased leaf number in organic matter-enriched soil has been observed in cucumber by Adesida et al. (2020). Healthy plants in nutrient-rich, organically enhanced soil are better able to produce growth hormones like cytokinins, which are responsible for stimulating leaf production.

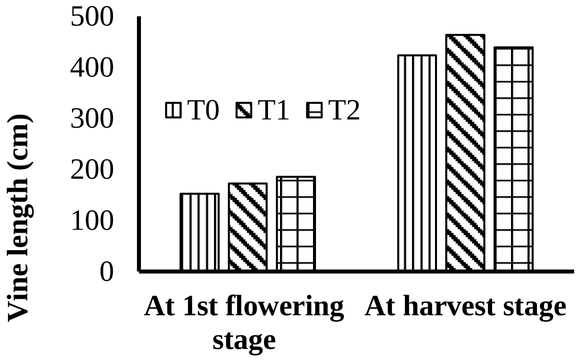

n

plant length of snake gourd (*Trichosanthes anguina* L.) T_0: control (BARI recommended fertilizers doses), T_1: 100% RFD + Liquid manure (once), and T_2: 100% RFD + liquid manure (twice).

Leaf area (sq. cm): Leaf area showed significant variation among the treatments (Table 1). The maximum leaf area (147.0 sq. cm) was observed in T_2, which was identical to T_2, whereas the lowest leaf area (67.9 sq. cm) was found in T_0 (Plate 1). Liquid manure can increase plant leaf area by providing key nutrients and enhancing soil conditions that promote healthy, vigorous leaf growth. Similarly Azeezahmed et al. (2022) also reported a significant increase in leaf area due to liquid manure. Liquid manure increases leaf area by providing essential nutrients, improving water retention, stimulating cell division and expansion, and enhancing plant health.

SPAD Value

SPAD value showed significant variation among the application of liquid manure. The highest (50.1) SPAD value was observed in T_2, and the lowest (40.3) value was observed in T_0 (Table 1). A higher SPAD value indicates a higher concentration of chlorophyll in the leaf. Chlorophyll is vital for photosynthesis, the process by which plants convert light energy into

Table 1. Influence of supplement liquid manure on growth and flowering of snake gourd *(Trichosanthes anguina* L.)

Treatments	Leaves number /1m vine length	Leaf area (sq.cm)	SPAD	Days to 80% flowering	Female flower/ plant
T_0	7.7^{b}	67.9^{b}	40.3^{b}	41.66^{a}	42.3^{b}
T_1	8.3^{ab}	145.1^{a}	41.8^{ab}	38.33^{b}	49.3^{ab}
T_2	10.0^{a}	147.0^{a}	50.1^{a}	30.66^{c}	58.0^{a}
Cv%	9.4	0.7	8.9	3.26	9.1
LSD	1.9	2.0	8.9	2.7	10.3

T_0: control (BARI recommended fertilizers doses), T_1: 100% RFD + Liquid manure (once), and T_2: 100% RFD + liquid manure (twice).

According to the 0.05 threshold of probability, means in a column with similar letters are statistically non-significent, whereas those with differing letters differ significantly.

chemical energy. High SPAD values can suggest that the plant has sufficient nitrogen, a key element for chlorophyll production.

Days to 80% flowering

Significant variation was shown on days to 80% flowering of snake gourd plants due to different treatments and the maximum days (41.66 days) required for flowering of 80% of plants from the control (T_0) treatment. In contrast, the minimum days (30.66 days) to 80% flowering was required in T_2 treatment.

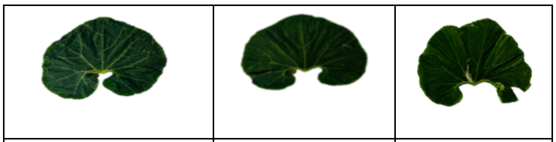

T_0 T_1 T_3

Plate 1. Variation of leaf area with different treatments.

Female flowers per plant

Significant variation of female flower numbers per plant was shown with the different treatments. The highest number of female flowers per plant (58.0) was recorded with the T_2 treatment, and it is statistically identical to T_1 (49.3) and the minimum number of female flowers (42.3) from the T_0 treatment (Table 1). Liquid manure provides essential nutrients, especially nitrogen, phosphorus, and potassium, crucial for flower development and overall plant health. Adequate nutrition can enhance the plant's ability to produce female flowers, which is beneficial for the fruit set and overall yield of snake gourd. A similar result was observed in tomatoes by Shakila and Anburani (2008) and chili, tomato, okra, and cowpea by Mathews et al. (2017).

Fruits per plant

The number of fruits per plant showed significant inequality with different treatments under the study. Among the various applications of liquid manure imposed on the plant, T_2 (Twice) recorded a significant maximum fruit number (53.0) and the minimum fruit number (40.0) from the control (Table 2). Liquid manure is rich in essential nutrients such as nitrogen, phosphorus, and potassium and enhances microbial activity, which is vital for plant growth and development. These nutrients are more favorable environments to promote healthy vegetative growth, flowering, and fruit set. A similar result was reported by Deore et al. (2010), which revealed consistent and significant results for growth and yield parameters due to the application of novel organic liquid manure. Application of panchagavya increased parameters like number of branches per plant, number of flowers per plant, and total yield per plant (Rao et al., 2015).

Single fruit weight

Significant variations in single fruit weight were found with different treatments (Table 2). The maximum average single fruit weight (0.61 g) was recorded in T_2 and the minimum fruit weight (0.39 g) was recorded in T_0.

Yield

Significant differences in yield of snake gourd were observed due to different treatments (Table 2). In the case of different liquid fertilizer applications, the highest result was observed in T_2 (29.8 t/ha) with two applications and the lowest result in T_0 (26.0 t/ha) in the control condition. Probiotic liquid manure can be beneficial in increasing the yield of snake gourd by enhancing soil health and providing essential nutrients in a bioavailable form. Applying probiotic liquid manure at regular intervals throughout the growing period can help sustain beneficial microbial activities, which assist in decomposing organic matter, releasing the essential nutrients like nitrogen, phosphorus, and potassium, that are vital for snake gourd growth and yield. The results are consistent with Somasundaram et al. (2003) and Ali et al. (2011). Mahanta and Dhar (2021) expressed similar opinions that liquid manure enhances soil organic matter content and microbial diversity and stimulates microfauna and enzymes for higher productivity of crops.

Table 2. Influence of supplement liquid manure on yield of snake gourd (*Trichosanthes anguina* L.)

Treatments	Fruits /plant	Fruit length (cm)	Fruits width (cm)	Average fruit wt. (g)	Yield (t/ha)
T_0	40.0 ^{b}	28.3 ^{b}	6.2 ^{b}	0.39 ^{b}	26.0 ^{c}
T_1	51.7 ^{a}	31.7 ^{a}	7.3 ^{a}	0.44 ^{b}	27.8 ^{b}
T_2	53.0 ^{a}	33.3 ^{a}	7.9 ^{a}	0.61 ^{a}	29.8 ^{a}
Cv%	2.9	4.5	4.8	5.62	2.41
LSD	3.2	3.2	0.8	0.07	1.52

T_0: control (BARI recommended fertilizers doses), T_1: 100% RFD + Liquid manure (once), and T_2: 100% RFD + liquid manure (twice).

According to the 0.05 threshold of provability, means in a column with similar letters are statistically non-significant, whereas those with differing letters differ significantly.

Conclusion

The experiment results showed that **T_2** plot plant (Direct use 100% of PLM) treatments more prominently enhanced vegetative growth, SPAD value, and yield attributes of snake gourd. So, we observed that **T_2** treatment was found to perform better regarding vegetative growth, yield, and quality attributes. Therefore, PLM as **T_2** is an effective supplement of liquid manure that has the potential to increase the growth and yield of snake gourd.

Author contribution

AFM Jamal Uddin: Experiment designing and writing, Tamalika Roy: Data collection and analysis, Purnima Saha: Data collection, Tamima Dastagir: writing, Fatema Tuz Juhora Chaitee: Data analysis and writing.

Declaration of conflicting interests

The authors declare that there is no conflict of interest regarding the publication of this paper.

References

Adesida OA, Smart MO, Bamigboye TO, Adedokun TA and Odewale MO. Effect of liquid organic manure and staking methods on the growth and yield of cucumber (*Cucumis sativus* L.) *J. Res. Forest. Wild. Environ.* 2020; 12(2): 148-155

Ali MN, Ghatak S and Ragul T. Biochemical analysis of Panchagavya and Sanjibani and their effect in crop yield and soil health. *J. Crop Weed*. 2011; 7(2): 84-86.

Azeezahmed S, Hardeep S, Sukhbir S, Thayne M and Jacobo S. Liquid organic fertilizer effects on growth and biomass of lettuce grown in a soilless production system. *Hortic.* 2022; 57(3): 447-452.

Deore GB, Limaye AS, Shinde BM and SL Laware. Effect of novel organic liquid fertilizer on growth and yield in chilli (*Capsicum annum* L). *Asian J. Exp. Biol. Sci. Spl.* 2010; 1(4): 15-19.

Gong S, Hodgson JA, Tscharntke T, Liu Y, Van der Werf W, Batary P, Knops JMH and Zou Y. Biodiversity and yield trade-offs for organic farming. *Ecol. Lett.* 2022; 25(7): 1699-1710.

Krishi Projikti Hatboi. Training and communication wing. Joydebpur, Gazipur, Bangladesh. 2020. p. 160.

Li M, Li Q, Yun J, Yang X, Wang X, Lian B and Lu C. Bio-organic-mineral fertilizer can improve soil quality and promote the growth and quality of water spinach. *Canadian J. Soil Sci.* 2017; 97(4): 552-560.

Mahanta D and Dhar S. Liquid organic manure: A boon to organic farmers. *Indian farming,* 2021; 71(11): 47-50.

Mathews NS, Bharani A and Nandhini DU. Influence of organic inputs on growth parameters of vegetable crops under terrace farming. *Int. J. Chem. Stud.* 2017; 5(5): 763-765.

Rao MR, Kumar MS and Jha NK. Comparative yield analysis of chilli (*Capsicum annuum* L.) by application of vermicompost and panchagavya. *J. Chem. Pharm. Res*. 2015; 7(9): 319-323.

Shakila A and Anburani A. Effect of certain organics and pressmud on growth and yield characters of tomato. *Asian J. Hort.* 2008; 3(2): 273-276.

Somashekar G, Ranjit C, Sushmita S and Aradhana S. Prospect of liquid organic manure on organic bitter gourd cultivation. *J Pharmacogn. Phytochem*. 2018; 7(6): 189-193.

Somasunderam E, Chandaragiri K, Meena S, Thiyagarajan TM, Sankaran N and Paneerselvam S. Response of green gram to varied levels of panchagavya foliar spray. *Madras Agric. J.* 2003; 90: 169-172.

Uddin AFMJ, Nahid HM and Husna MA. Impact of different liquid manure on growth and yield of water spinach. *Int. J. Bus. Soc. Sci. Res.* 2023; 11(2): 32-36.

Uddin AFMJ, Nahid HM, Dastagir T, Chaitee FTJ and Husna MA. Liquid manure as a potential alternative nutrient solution for organic strawberry production. *Int. J. Bus. Soc. Sci. Res*. 2024; 12(1): 27-30.

INSTRUCTION FOR AUTHORS

The Journal of Bangladesh Academy of Sciences is published four times a year in March, June, September and December. Original research articles, review articles, and short communications of high standards of all branches of Science and Technology are considered for publication in this journal. Review articles are generally by invited authors; however, the Editor welcomes suggestions of potential topics and potential authors.

The following instructions must be followed while preparing the manuscript intended for publication in this journal:

1. **Research Article:** Manuscripts should be concise and consistent with the style of the journal. The manuscript must be typed using Times New Roman font, size 12 on A4 size page, and wide (1 inch) margins on all four sides. The main text must be typed in a two-column format with 1.5 spacing, and for full papers, it should not exceed 10-20 typed pages, including figures, tables, and references. In general, an article may contain the following sub-titles in sequence: **Title, Abstract, Keywords, Introduction, Materials and Methods, Results and Discussion, Acknowledgement (**if any), and **References.**

A. Title: The first page of the paper, the title page, should have the title and the names of the authors. The title should be brief and specific. Abbreviations and formulae should be avoided where possible. The next line in italics should be the authors' affiliation addresses (where the actual work was done) below the names. Indicate all affiliations with a lowercase superscript letter immediately after the author's name and in front of the appropriate address. The corresponding author, along with email address, should be indicated at the footnote with a proper asterisk.

B. The second page should carry the Title of the paper, Abstract, and Keywords. Author(s) name must not be typed on this page.

- **(i) Abstract:** It should not exceed 150 words and should briefly state the purpose of the research, the significant results, and meaningful conclusions. Nonstandard or uncommon abbreviations should be avoided, but if essential, they must be defined at their first mention in the abstract itself.
- **(ii) Keywords:** Immediately after the abstract, provide a maximum of 6 keywords.

C. The next pages (a maximum of 15 printed pages), will contain the main text of the paper.

(i) Introduction: It should be concise and relevant to the objectives of the study. The importance of the research work described should be pointed out. An appropriate review of the current literature should be made to identify the frontier of existing knowledge and point out the need for further work. The knowledge contributed to the study should be mentioned.

(ii) Materials and Methods: Materials used should be mentioned precisely along with their sources and any pre-treatment undertaken.

The description of methods must be brief but clear enough to enable a reader to reproduce the results. References must be considered sufficient for methods described in earlier publications: only relevant modifications should be described.

It is recommended that authors use the nomenclature and symbols adopted by IUPAC document UIFII (S.U.N. 65-3) 1965, symbols, units, and nomenclature in Physics or by IUPAC Manual of Physiochemical symbols, Terminology and similarly for other disciplines.

(iii) Results and Discussion: This section should include descriptions of results obtained with the help of figures, tables, graphs, and photographs as may be necessary. Tables should have a descriptive title. Large and cumbersome tables should be avoided. Figures and graphs should be prepared and should be properly labelled with bold solid lines such that no further size reduction will be necessary. The paper should contain a minimum number of **Tables, Graphs,** and **Figures.** The same data should not be depicted using both tables and figures. The photographs are to be submitted in JPEG format.

The discussion should include thorough analysis and interpretation of results, and comparison with existing relevant published results, if any, and self-evaluation of the new knowledge contributed, avoiding extensive citations and discussion of published literature.

(iv) Conclusions

The study's main conclusions may be presented in a short Conclusions section, which may stand alone or form a part of the Results and Discussion section.

(v) Acknowledgment: The following support for the research work should be acknowledged:

- Funding by any agency;
- The use of instruments in a laboratory other than those of the authors;
- Individual’s help during the research (e.g., providing an interpretation of results, language help, writing assistance, or proofreading, etc.).

(vi) Author contributions

For transparency, we encourage authors to submit an author contribution statement outlining each author's contributions to the paper. The authors should have participated sufficiently in the work to take public responsibility for appropriate portions of the content.

(vii) References and Text Citations:

In the text, references should be cited within brackets quoting the first author's surname followed by et al. if necessary and the year of publication in the appropriate place, e.g. (Bhuiyan, 2020), Khan et al. (2021) or (Khan et al., 2021). In the case of only two authors, surnames of both need to be mentioned, e.g., (Khan and Rahman, 2021). A semi colon should separate two or more references when putting within the same bracket. At the end of the manuscript, references should be listed and arranged alphabetically according to the first author's surname according to the style described below:

(a) Journal article:

In each reference, names of all authors' will have to be given in the same style, e.g., surname followed by initials, lumped together without using a full stop. The names will be followed by the full title of the article and the journal's abbreviated title (in italics). The year of publication will be given next, followed by volume number (issue number) and page ranges. For abbreviations of the names of journals, authors are advised to follow the *World List of Scientific Periodicals.* For online publications, the URL address must be given. Note: Please list ALL authors’ names in the list of references, do not use (et al.). **Examples:**

Islam S. The Induced Morphological and Root Anatomical Changes in Lentil. *J. Bangladesh Acad. Sci.* 2019; 43(2):107-112.

James BD and Bennett DA. Causes and Patterns of Dementia: An Update in the Era of Redefining

Alzheimer’s Disease. *Annu. Rev. Public Health;* 2019; 40: 65-84.

Moniruzzaman M, Khatoon R and Qamruzzaman AKM. Influence of Plant growth Regulators on Vegetative Growth, Sex Expression and Yield of Summer Bottle Gourd. *Bangladesh J. Agril. Res*. 2019; 44(4): 577-590.

(b) Book or Chapter in a Book:

The place and name of the publisher, year of publication, will have to be given in addition to the name of the author(s), the title of the book (in italics), edition number (if not first), and the number of pages. In the case of an article or chapter in a book or proceedings of a conference, author(s) name and the title of the article or chapter will be followed by the title of the book (in italics), the names of the editors of the book, edition number (if not first), the place and name of the publisher, year of publication and page or page numbers of chapter. **Examples:**

Book:

Carlson BM. *Human Embryology and Developmental Biology*. 4th ed. St. Louis: Mosby; 2009. p. 541.

Cassese A, Acquaviva G, Fan M and Whiting A. *International Criminal Law: Cases and Commentary*. Oxford University Press; 2011, p. 600.

Chapter in an edited book:

Muhammad HFL and Dickinson KM. Nutrients, energy values and health impact of conventional beverages, Chapter 3. In: *The Science of Beverages, Volume 12: Nutrients in Beverages*. Grumezescu AM, Holban AM, eds., Elsevier Science; 2019; pp. 77-109.

Balsam KF, Martell CR, Jones KP, Safren SA. Affirmative cognitive behavior therapy with sexual and gender minority people. In: *Culturally Responsible Cognitive Behavior Therapy: Practice and Supervision*. Iwamasa GY, Hays PA, eds., 2nd edition, American Psychological Association. 2019; p. 287-314.

(c) Proceedings of a Conference:

Luca J and Tarricone P. Does emotional intelligence affect successful teamwork? In: *Meeting at the Crossroads*. Kennedy G, Keppell M, McNaught C (eds.), Proceedings of the 18th Annual Conference of the Australasian Society for Computers in Learning in Tertiary Education, 2001 Dec 9-12; Melbourne: Biomedical Multimedia Unit, The University of Melbourne; 2001. pp. 367-376.

(d) Reports:

Bangladesh Bureau of Statistics (BBS). Population census - 2011. Preliminary report. Bangladesh Bureau of Statistics, Ministry of Planning, Government of the People's Republic of Bangladesh, Dhaka, 2011.

Rowe IL and Carson NE. *Medical manpower in Victoria. East Bentleigh (AU)*: Monash University, Department of Community Practice; 1981. p. 35. Report No.: 4.

2. **Short communication:** Important research findings that may initiate further research in the relevant field may be published in the form of a short communication. This should not exceed three printed pages (900 words), including Graphs, Tables, and Figures. The presentation should be continuous and paragraphed, i.e., without headings like Introduction, Materials, and Methods, etc. A short communication paper should have an **Abstract** containing the gist of the article and should not exceed 60 words, followed by **Keywords.**

3. **Declarations:** While submitting, the corresponding **a**uthor will have to make a declaration mentioning the laboratory/laboratories in which the work was carried out and certifying that the contents of the paper were not published before or submitted for publication in any other journal and that all the co-authors have given their consent for the article to be considered by the Editorial Board for publication in the Journal of Bangladesh Academy of Sciences.

Declaration of conflicting interests

The corresponding author must provide a formal conflict of interest statement for all authors disclosing any financial and personal relationships with other people or organizations that could inappropriately influence (bias) their work. If no conflict exists, please state that 'The author(s) declare(s) that they have no conflicts of interest regarding the publication of this article.'

4. The manuscript should be submitted in pdf or MS Word or LaTex files through online at www.bas.org.bd/publications/jbas.html. Equations generated by using Math Type or Math ML should be incorporated in the text.

   Soft copies of manuscripts with tables, graphs, illustrations, and photographs placed correctly in a printable format are to be submitted. Authors wishing to publish coloured schemes/diagrams/ sketches/photographs in their papers need to pay for the printing charges of one format. This will be charged only after the acceptance of the manuscripts for publication in the JBAS.

   The manuscript submitted should also contain a separate list of tables, figures, illustrations, photographs, and sketches with appropriate captions.

5. Electronic versions of final galley proofs will be sent to authors. No alteration in the title or additions in the text is desirable at this stage.

6. All correspondence for publication should be made on www.bas.org.bd/publications/jbas.html to the **Editor, Journal of Bangladesh Academy of Sciences, National Science and Technology Complex, Agargaon, Dhaka 1207.**

N.B.: No paper will be accepted for publication if it does not conform to the style specified for the journal and approved by the Editorial Board, which has the authority to accept or reject the manuscript of a paper submitted without showing any reason.